ELECTRICAL AND MAGNETIC PROPERTIES OF NANOPARTICLE Mn-Zn FERRITES OBTAINED FROM NOVEL METHOD OF SYNTHESIS

THESIS

Submitted to

GOA UNIVERSITY

For the Degree of

DOCTOR OF PHILOSOPHY

IN

PHYSICS

By

Shri Girish V. S. Kundaiker

Department of Physics

P.E.S S.R.S.N. College of Arts and Science

Farmagudi-Ponda Goa

Girish.kundaikar@gmail.com

December 2011


॥ श्री ॥

॥ श्री शांतादुर्गा देव्याः कृपाशिर्वादैः

मम एषाःप्रकल्पःपूर्णा :अभवत्

अतः अहम् विनम्रभावनया प्रकल्पम्

ईमम् देव्याःचरणेषु समर्पयामी ॥

To……

My Papa

DECLARATION

I hereby state that this thesis for the Ph.D. degree on "ELECTRICAL AND MAGNETIC PROPERTIES OF NANOPARTICLE Mn-Zn FERRITES OBTAINED FROM NOVEL METHOD OF SYNTHESIS" is my original work and that it has not previously formed the basis for the award of any degree, diploma, associate ship and fellowship or any other similar title to the best of my knowledge and information.

Girish V. S. Kundaiker

(Candidate)

CERTIFICATE

As required under the University ordinance, we certify that the thesis entitled "ELECTRICAL AND MAGNETIC PROPERTIES OF NANOPARTICLE Mn-Zn FERRITES OBTAINED FROM NOVEL METHOD OF SYNTHESIS" submitted by Shri. Girish V. S. Kundaiker for the award of Doctor of Philosophy in Physics is a record of research done by the candidate during the period of study under our guidance and that it has not previously formed the basis for the award to the candidate of any degree, diploma, associateship, fellowship or other similar titles.

Date: /12/2011

Prof. R. B. Tangsali
Research guide,
Department of Physics,
Goa University.

Prof. J. S. Budkuley,
Research Co-guide,
Department of Chemistry,
Goa University.

ACKNOWLEDGEMENTS

I bow before Goddess "**Shri Shantadurga**", the most Gracious and Merciful, for her blessings and for giving me the courage and fortitude to complete the research work.

I feel highly privileged and honoured to express my deepest gratitude to Prof. Rudraji B. Tangsali, my research guide, for suggesting this topic and to acknowledge his invaluable inspiring guidance, positive attitude and constant encouragement for completion of this work.

I am extremely grateful to Prof. Jayant S. Budkule, my research co-guide, Dept. of Chemistry, Goa University for his guidance and cooperation, during entire tenure of my research work.

I am grateful to the Management, specially the Chairman of P.E.S.' Society, Shri. Ravi S. Naik for permitting me to carry out research and for his full support.

My sincere thanks to Dr. A.S. Dinge the Principal of P. E. S. R. S. Naik College, for allowing me to carry out research, his constant support and words of encouragement during my entire research tenure.

I am thankful to Shri. Bhaskar Naik, Director, Higher Education, Govt. of Goa for sanctioning me study leave for the purpose. Thanks are due to Prof. E. Desa. Dean of Physical Science and Head, Dept. of Physics, Prof. G. M. Naik former Head of the Dept. Goa University for extending necessary facilities and their full cooperation.

I thank Dr. Kaustub Priolkar, who was my subject expert. I thank my colleague Prof. Vikas Pissurlekar for all the help that he has extended to me during my research work**.**

I express my sincere thanks to Dr. R. K. Kotnala, senior scientist in the National Physical Laboratory, New Delhi, for allowing me to carry out magnetic measurements on V.S.M.

I am proud to express my thanks to the Director of T. I. F. R. Mumbai, Dr. A. K. Nigam, Senior Scientist, Shri. Devendra Buddhikot and Ms. Laxmi Patil, for helping me to use the VSM and the SQUID to carry out magnetic measurements.

My sincere thanks to Dr. Ayub, and Ms. Bhagyashree Chakle, for allowing me to use the HRTEM for particle size measurements.

I am grateful to Director of N.C.O.R., Program Director Dr. Rahul Mohan and Lab. Technician, Ms. Sahina. Gazi for allowing and helping me to use the EDAX and the SEM facilities.

I thank Dr. A. K. Tyagi, Dr. D. B. Naik, Dr. A. Das and Dr. Keka Chakraborty, Scientists from Bhaba Atomic Research Centre (BARC.), Mumbai, for helping me by providing Neutron Diffraction facilities. Thanks to Mr. Sher Singh Meena, S. M. Yusuf of BARC, Mumbai, for helping me to carry out the Mossbaur study of the samples.

I am grateful to Prof. D. C. Khothari, Head Dept. of Physics Mumbai University and in charge of National centre for Nanoscience Nanotechnology for allowing me to carry out few experiments at the centre.

Thanks to all my research colleagues and friends, Mr. Pranav Naik, Mr. M. L. Bosco, Mr. J. Jaison, Mr. Monoj Kotwale, for making my work in the Laboratory comfortable. Thanks to all the teaching and non teaching staff of Dept of Physics, Goa University for all their help.

Thanks to all the teaching and non teaching staff of Dept of Physics, Goa University for all their help.

I thank Dr. S. H. P. Keluskar, the teaching and non teaching staff of the Dept. of Physics of P. E. S's Shree Ravi Sitaram Naik College of Arts and Science, for their cooperation.

I offer my deepest gratitude to my mother, wife and my sisters for their love, support, encouragement and enhancing my confidence.

CONTENTS

CHAPTER I

1. PREAMBLE

1.1 Introduction 1

1.2 Magnetism 3

1.3 Ferrites 20

1.4 Motivation and objective of the work carried out. 27

1.5 Investigative work plan executed 28

1.6 Organization of thesis 30

CHAPTER II

2. LITERATURE SURVEY 35

CHAPTER III

3. PREPARATION OF MATERIALS

3.1 Introduction 61

3.2 Preparation of Magnetic Nanomaterial 61

3.2.1 Ceramic Method 61

3.2.2 Electrochemical Method 62

3.2.3	Spray Pyrolysis Method	63
3.2.4	Hydrothermal Method	63
3.2.5	Co -precipitation Method	64
3.2.6	Sol-gel Method	65
3.2.7	Precursor Method	66
3.2.8	Vapour Phase Method	66
3.2.9	Chimie-Douce Method	67
3.2.10	Plasma Synthesis Method	68
3.2.11	Reverse Micelle Method	68
3.2.12	CTAB Method	70
3.3	Synthesis of $Mn_xZn_{(1-x)}Fe_2O_4$ Mixed Ferrites	71

CHAPTER IV

4. ANALYTICAL TECHNIQUE AND CHARACTERIZATION

4.1	X-ray diffraction	78
4.1.1	X - Ray Diffraction method	79
4.1.2	Instrumentation	80
4.1.3	Effect of crystal size on the powder pattern – particle size measurement	81
4.1.4	Rietveld refinement	82
4.2	Infrared Spectroscopy (IR)	83
4.2.1	Fourier Transform IR spectrophotometer	85
4.2.2	Experimental	87

4.3	Chemical Analysis	87
4.3.1	Energy Dispersive X-Ray Spectroscopy (EDS or EDX)	87
4.3.2	Experimental	88
4.4	Density and Porosity measurements	89
4.5	Results and Discussion	90
4.5.1	X-Ray Diffraction Analysis	90
4.5.2	FTIR Spectroscopy	97
4.5.3	Elemental Analysis	99
4.5.4	Mass Density	102
4.5.5	X-ray density	104
4.5.6	Porosity	105

CHAPTER V

5. INSTRUMENTAL TECHNIQUES FOR PARTICLE SIZE DETERMINATION

5.1	Introduction	108
5.2	Powder X- Ray Diffraction	109
5.3	Scanning Electron Microscope (SEM)	109
5.4	Transmission Electron Microscopy (TEM)	111
5.4.1	High Resolution Transmission Electron Microscopy (HRTEM)	114
5.5	Scanning probe Microscope	116
5.6	Experimental	119
5.7	Results and Discussion	121

CHAPTER VI

6. MAGNETIC PROPERTIES

6.1	Introduction	136
6.2	Neutron Diffraction	137
6.3	Hysterisis Loop Tracers	141
6.4	Vibrating Sample Magnetometer	142
6. 5	Superconducting Quantum Interference Device (SQUID)	143
6.6	Mössbauer spectroscopy	145
6.7	A.C. Susceptibility	148
6.8	Initial Permeability	149
6.9	Experimental	154
6.10	Experimental Results and Discussion	158
6.10.1.1	Magnetic properties (Hysteresis loop)	158
6.10.1.2	Hystersis Loss	167
6.10.2	Magnetic properties (Using Vibrating Sample Magnetometer)	169
6.10.3	SQUID	177
6.10.4	Mossbaur	181
6.10.5	A.C susceptibility	187
6.10.6	Initial Permeability	192

CHAPTER VII

7. ELECTRICAL PROPERTIES

7.1	Introduction	216
7.2	Resistivity	217
7.2.4	Experimental Technique	221
7.3	Thermoelectric Effect (Seeback Coefficient Measurements)	223
7.3.1	Experimental technique	223
7.4	Dielectric constant	224
7 .4.1	Experimental Technique	226
7.5	Result and Discussion	227
7.5.1	Resistivity	227
7.5.1.5	Analysis of Resistivity at room temperature, at Resistivity maximum and at highest temperature (500^0C)	235
7.5.2	Seeback coefficient	238
5.7.3	Dielectric constant	239
7.5.4	Temperature dependence of Dielectric constant	245
7.5.5	Dielectric Loss Factor	250

CHAPTER VIII

8. PRECIS AND CONCLUSIONS

8. 1	Summary	259
8.2	Conclusions	265
8.3	Scope for future work	266

LIST OF FIGURES

CHAPTER I

Fig. 1.1 (a) Electron orbit around the axis (b) Electron spin.

Fig. 1.1 (c) Diamagnetism

Fig. 1.1 (d) Paramagnetism

Fig. 1.1 (e) Ferromagnetism

Fig.1. 2 (a) Antiferromagnetism

Fig. 1.2 (b) Ferrimagnetism

Fig 1.2 (c) Hysteresis Loop

Fig. 1.2 (d) Variation of coercivity with particle size

Fig. 1.3 (a) Ferrospinel structure

Fig. 1.4 (a) Structure of spinel ferrite

CHAPTER IV

Fig. 4.2 (a) XRD pattern for the sample $Mn_{0.65}Zn_{0.35}Fe_2O_4$ prepared by auto combustion method.

Fig. 4.2 (b) XRD pattern for the sample $Mn_xZn_{(1-x)}Fe_2O_4$

Fig. 4.2 (c,d) Rietveld Refinement of X-ray powder diffraction pattern: (c) $Mn_{0.6}Zn_{0.4}Fe_2O_4$ (d) $Mn_{0.7}Zn_{0.3}Fe_2O_4$

Fig. 4.3 (a) Variation of lattice constant with Mn concentration of Nanoparticle sample.

Fig.4.3 (b) Williumson Hall Plot for $Mn_xZn_{(1-x)}Fe_2O_4$ (x=0.6, 0.65, 0.7, 0.8)

Fig.4.4 (a) IR Spectra for $Mn_xZn_{(1-x)}Fe_2O_4$Ferrite Nanoparticles

Fig.4.4 (b,c) IR Spectra of nanoparticles (b) $Mn_{0.6}Zn_{0.4}Fe_2O_4$ & (c) $Mn_{0.8}Zn_{0.2}Fe_2O_4$

Fig.4.5 (a) Variation of mass density with Mn conc. of bulk and nanosamples.

Fig.4.5 (b) Variation of X-ray density with Mn. conc. of Nanoparticle sample

Fig.4.5 (c) Variation of porosity with Mn conc. of nanoparticle samples

CHAPTER V

Fig. 5.1 (a) Schematic Diagram of Scanning Electron Microscopy (SEM)

Fig. 5.2 (a) TEM Philip model CM 200, electron beam of 200Kev.

Fig. 5.2 (b,c) The two basic operations of TEM imaging system. (b) Imaging mode and (c) Diffraction pattern

Fig. 5.3 (a) SPM d,I- CALLIBER Model

Fig. 5.3 (b) AFM - non-contact mode.

Fig. 5.4 (a) SEM Micrograph of nanosample $Mn_{0.6.75}Zn_{0.325}Fe_2O_4$

Fig. 5.4 (b) SEM Micrograph of nanosample $Mn_{0.6}Zn_{0.4}Fe_2O_4$

Fig.5.4 (c,d,e,f,g) SEM Micrographs of bulk sample $Mn_{0.675}Zn_{0.325}Fe_2O_4$ (900^oC,1000^oC 1100 ^oC,1200 ^oC,1300 ^oC)

Fig. 5.4 (h,i) SEM micrograph of bulk sample $Mn_{0.6}Zn_{0.4}Fe_2O_4$ (1100^0C, 1300^0C) and 5.4 (j.k)) SEM micrograph of bulk sample $Mn_{0.625}Zn_{0.375}Fe_2O_4$ (1000^0C, 1200^0C)

Fig.5.5 (a,b,c,d,e,f) TEM, HRTEM micrograph and Histogram of (a) TEM $Mn_{0.6}Zn_{0.4}Fe_2O_4$, (b)TEM of $Mn_{0.7}Zn_{0.3}Fe_2O_4$, (c) HRTEM of $Mn_{0.625}Zn_{0.375}Fe_2O_4$, (d) HRTEM of $Mn_{0.675}Zn_{0.325}Fe_2O_4$, (e) HRTEM of $Mn_{0.65}Zn_{0.35}Fe_2O_4$ (f) HRTEM of $Mn_{0.675}Zn_{0.325}Fe_2O_4$

Fig. 5.6 (a,b) HRTEM Micrographs of $Mn_{0.65}Zn_{0.35}Fe_2O_4$

Fig.5.7 SPM Micrograph of nanosample $Mn_{0.6}Zn_{0.4}Fe_2O_4$

CHAPTER VI

Fig. 6.1(a) Neutron Diffraction pattern for $Mn_{0.6}Zn_{0.4}Fe_2O_4$

Fig. 6.1 (b) Neutron Diffraction pattern for $Mn_{0.7}Zn_{0.3}Fe_2O_4$

Fig. 6.1 (c) Block diagram of Pulse Field Hysteresis Loop Tracer (d) Hysteresis Loop obtained using Pulse Field Hysteresis Loop Tracer

Fig. 6.2 (a) Schematic diagram of VSM

Fig. 6.2 (b) Vibrating Sample Magnetometer 12T; 1.8K-300K

Fig 6.2 (c) Cutaway view of the MPMS SQUID

Fig. 6.2 (d) Isomer shift, quadrupole splitting and Magnetic splitting of the nuclear energy levels and corresponding Mössbauer spectra.

Fig. 6.2 (e) Schematic Diagram of High Pulse Field Magnetization System

Fig. 6.2 (f,g) Torroides (f) before and (g) after permeability measurement

Fig. 6.3 (a) Variation of Magnetization with applied field using High Pulse Field Hysterisis loop Tracer for $Mn_xZn_{(1-x)}Fe_2O_4$ nanosamples for x=0.4, 0.5, 0.6, 0.8., 0.7 and 0.65. (b) for $Mn_xZn_{1-x}Fe_2O_4$ nanosamples for x=0.625, and 0.675

Fig. 6.3 (c,d) Variation of Magnetization with applied field using High Pulse Field Hysterisis loop Tracer (c)for bulk sample $Mn_{0.675}Zn_{0.325}Fe_2O_4$ (1000 ^{0}C and 1100 ^{0}C), (d) for bulk sample $Mn_{0.675}Zn_{0.325}Fe_2O_4$(1200 ^{0}C and 1300 ^{0}C),

Fig. 6.3 (e,f) Variation of Magnetization with applied field using High Pulse Field Hysterisis loop Tracer (e)for bulk sample $Mn_{0.8}Zn_{0.2}Fe_2O_4$ (1000^{0}C and 1100^{0}C), (f) for bulk sample $Mn_{0.8}Zn_{0.2}Fe_2O_4$ (1200^{0}C and 1300^{0}C)

Fig. 6.3 (g) Variation of saturation magnetization with concentration of Mn.

Fig. 6.3 (h) Variation of Saturation Magnetization with sintering temperature of $Mn_xZn_{(1-x)}Fe_2O_4$

Fig. 6.4 (a) Variation of Hystersis loss with con. of Mn for unsintered sample

Fig. 6.4 (b,c) VSM measurement of (b) $Mn_xZn_{(1-x)}Fe_2O_4$ at 300K for x=0.4, 0.5, 0.6 and 0.8, (c) $Mn_xZn_{(1-x)}Fe_2O_4$ at 300K for x=0.625, 0.65, 0.675 and 0.7.

Fig. 6.4 (d,e) Low temperature VSM measurement of (d) $Mn_{0.6}Zn_{0.4}Fe_2O_4$ at 5K, 10K, 25K and 50K., (e) $Mn_{0.625}Zn_{0.375}Fe_2O_4$ at 5K, 10K, 25K and 50K

Fig. 6.4 (f) Variation of Saturation Magnetization with temperature for different concentration of Mn.

Fig. 6.4 (g) Room temperature VSM for bulk sample $Mn_{0.8}Zn_{0.2}Fe_2O_4$ (1100^0C and 1300^0C)

Fig. 6.5 (a) Temperature dependence of magnetization for Zero field cooled and field cooled (MPMS, SQUID from quantum Design USA) Nanoparticle $Mn_{0.8}Zn_{0.2}Fe_2O_4$. 1000, 5000 Oe

Fig. 6.5 (b.c) Temperature dependence of magnetization for Zero field cooled and field cooled (MPMS, SQUID from quantum Design USA) Nanoparticle $Mn_{0.625}Zn_{0.375}Fe_2O4$ at 100 Oe, 500 Oe, 1000 Oe, 5000 Oe.

Fig. 6.5 (d,e) SQUID measurement of $Mn_xZn_{(1-x)}Fe_2O_4$ for x=0.6 (d) and x=0.4 (e)at zero field cooling and field cooling at 100 Oe

Fig. 6.6 Mossbauer spectra of nanosample $Mn_xZn_{(1-x)}Fe_2O_4$ for x= 0.4, 0.5, 0.6, 0.65 and 0.7

Fig. 6.7 (a) A.C. Susceptibility curves of nanosample (a) $Mn_xZn_{(1-x)}Fe_2O_4$ for x=0.4, 0.5, 0.6 and 0.625 and

Fig. 6.7 (b) A.C. Susceptibility curves of nanosample $Mn_xZn_{(1-x)}Fe_2O_4$ for x=0.65, 0.675, 0.7 and 0.8

Fig. 6.7 (c,d,e) A. C. Susceptibility curves, (c) of bulk sample $Mn_xZn_{(1-x)}Fe_2O_4$ (x=0.65, 0.675)(1000^0C), (d) bulk sample $Mn_xZn_{(1-x)}Fe_2O_4$ (x=0.65, 0.675)(1200^0C), (e) bulk sample $Mn_xZn_{(1-x)}Fe_2O_4$ (x=0.65, 0.675) (1300^0C) and (f) bulk samples $Mn_{0.8}Zn_{0.2}Fe_2O_4$ (1000^0C, 1300^0C)

Fig. 6.8 (a,b,c,d) Variation of Permeability with temperature at different frequencies of bulk sample (a) $Mn_{0.5}Zn_{0.5}Fe_2O_4$ (900^0C) and (b)$Mn_{0.4}Zn_{0.6}Fe_2O_4$ (900^0C), (c) $Mn_{0.675}Zn_{0.325}Fe_2O_4$($1000^0$C) and (d) $Mn_{0.6}Zn_{0.4}Fe_2O_4$ (1000^0C)

Fig.6.9 (a,b,c,d,e,f,g,h) Variation of Permeability with temperature at different frequencies of bulk samples (a) $Mn_{0.8}Zn_{0.2}Fe_2O_4$ (1100^0C) and (b) $Mn_{0.675}Zn_{0.325}Fe_2O_4$ (1100^0C), (c) $Mn_{0.8}Zn_{0.2}Fe_2O_4$ (1200^0C) and (d) $Mn_{0.675}Zn_{0.325}Fe_2O_4$ (1200^0C), (e)$Mn_{0.8}Zn_{0.2}Fe_2O_4$ (1300^0C) and (f) $Mn_{0.675}Zn_{0.325}Fe_2O_4$ (1300^0C), (g) $Mn_{0.5}Zn_{0.5}Fe_2O_4$ (1100^0C) and (h) $Mn_{0.5}Zn_{0.5}Fe_2O_4$ (1200^0C).

Fig. 6.10 (a,b,c,d) Variation of permeability with temperature of bulk sample $Mn_xZn_{(1-x)}Fe_2O_4$ (1000^0C, 1100^0C, 1200^0C, 1300^0C)

Fig. 6.10 (e) Variation of Permeability with Temperature of bulk $Mn_xZn_{1-x}Fe_2O_4$ (1300^0C) at 20Hz

Fig. 6.11 (a,b) Variation of permeability with Freq. for different sintering Temperature (a) $Mn_{0.8}Zn_{0.2}Fe_2O_4$ and (b) $Mn_{0.675}Zn_{0.325}Fe_2O_4$

Fig. 6.11 (c,d,e,f,g) SEM Micrograph of bulk $Mn_{0.8}Zn_{0.2}Fe_2O_4$ obtained at c) 900^0C d) 1000^0C e) 1100^0C f) 1200^0C and g) 1300^0C

Fig.6.12 (a,b,c,d,e) Variation of Pemmeability with frequency for bulk samples $Mn_xZn_{(1-x)}Fe_2O_4$ obtained at a) 900^oC b) 1000^oC c) 1100^oC, d) 1200^oC, and e) 1300^oC

Fig. 6.13 (a, b, c,d,e) The variation of the loss factor (tanδ) with frequency for the bulk samples $Mn_xZn_{(1-x)}Fe_2O_4$ obtained at (a) 900°C, (b) 1000°C, (c) 1100°C, (d) 1200°C. and (e) 1300°C.

CHAPTER VII

Fig 7.1(a) Block diagram for resistivity measurement

Fig 7.1 (b) D.C. Resistivity measurement Apparatus

Fig 7.1 (c) Electrode assembly with sample

Fig 7.1 (d) Block diagram of experimental set-up to determine thermo-e.m.f. of the sample

Fig. 7.2 (a) Variation of log ρ versus 1000/ T (K) for nanosamples $Mn_xZn_{(1-x)}Fe_2O_4$

Fig. 7.2 (b,c,d,e,f) Plots of log ρ v/s 1000/ T (K) for bulk samples $Mn_xZn_{(1-x)}Fe_2O_4$ (x=0.4, 0.5, 0.6, 0.65, 0.625, 0.675, 0.7, 0.8) obtained at b) 900 °C, c) 1000 °C, d)1100 °C, e)1200 °C and f)1300°C

Fig. 7.3 (a,b) SEM Micrograph of bulk sample $Mn_{0.6}Zn_{0.4}Fe_2O_4$ (a) 1100°C (b) 1300°C

Fig. 7.3 (c,d) Variation of resistivity with temperature of a) $Mn_{0.6}Zn_{0.4}Fe_2O_4$ and b) $Mn_{0.8}Zn_{0.2}Fe_2O_4$ sintered at different temperatures.

Fig 7.3 (e) Variation of room temperature values of Resistivity with sintering temperature for different concentration.

Fig. 7.3 (f) Variation of Resistivity maximum of all nanoparticle and bulk samples obtained at different temperatures

Fig. 7.3 (g) Variation of resistivity minimum (at 500^{o}C) of nanoparticle and bulk samples with different sintering temperatures.

Fig7.4 (a,b,c,d) Plot of Seeback coefficient (Q) V/S Temperature for nanosample $Mn_xZn_{(1-x)}Fe_2O_4$ (with x=0.4, 0. 5, 0.65and 0.8).

Fig. 7.5 (a,b) Variation of Dielectric constant with frequency for (a) nano sample $Mn_xZn_{(1-x)}Fe_2O_4$ (b) Bulk sample $Mn_xZn_{(1-x)}Fe_2O_4$ (900^{o}C).

Fig. 7.5 (c,d) Variation of Dielectric constant with frequency for bulk sample $Mn_xZn_{(1-x)}Fe_2O_4$ obtained at (a) 1000^{o}C (b) 1100^{o}C.

Fig. 7.5 (e,f) Variation of Dielectric constant with frequency for the bulk sample $Mn_xZn_{(1-x)}Fe_2O_4$ obtained at (a) 1200^{o} C (b) 1300^{o}C.

Fig: 7.6 (a.b) Variation of dielectric constant with frequency of bulk $Mn_xZn_{(1-x)}Fe_2O_4$ (x=0.7, 0.6) obtained at 900^{o}C, 1000^{o}C, 1100^{o}C, 1200^{o}C and 1300^{o}C.

Fig. 7.6 (c,d) Variation of dielectric constant with frequency of bulk $Mn_xZn_{(1-x)}Fe_2O_4$ (x=0.4, 0.8) obtained at 900^{o}C, 1000^{o}C, 1100^{o}C, 1200^{o}C and 1300^{o}C.

Fig. 7.7 (a,b) Dielectric constant vs Temperature at 1MHz for a) Nano sample $Mn_xZn_{(1-x)}Fe_2O_4$and b) bulk sample $Mn_xZn_{(1-x)}Fe_2O_4$ (900^{0}C) at 1MHz.

Fig. 7.7 (c,d) Dielectric constant vs Temperature at 1MHz for bulk sample c) $Mn_xZn_{(1-x)}Fe_2O_4$ (1200^{0}C) and d) $Mn_xZn_{(1-x)}Fe_2O_4$ sintered at 1300^{0}C.

Fig. 7.7 (e) Dielectric constant vs Temperature at 500 Hz. for bulk $Mn_xZn_{(1-x)}Fe_2O_4$ (1300^{0}C).

Fig.7.7 (f) Dielectric constant vs Temperature at 100 Hz. for bulk sample $Mn_xZn_{(1-x)}Fe_2O_4$ (1300^0C).

Fig.7.8 (a,b,c,d,e,f) Variation of dielectric loss factor with frequency for a) nanosample $Mn_xZn_{(1-x)}Fe_2O_4$, bulk sample $Mn_xZn_{(1-x)}Fe_2O_4$ (b) (900^0C), (c) (1000^0C), (d) (1100^0C), (e) (1200^0C) and (f) (1300^0C).

Fig.7.9 (a,b) Loss factor with frequency for a) $Mn_{0.4}Zn_{0.6}Fe_2O_4$ and b) $Mn_{0.8}Zn_{0.2}Fe_2O_4$ sintered at different temperature.

Fig.7.10 (a,b) Dissipation vs. Temperature at 1MHz. frequency for bulk sample a) $Mn_xZn_{(1-x)}Fe_2O_4$ (1300^0C) and b) $Mn_xZn_{(1-x)}Fe_2O_4$ (1200^0C).

LIST OF TABLES

CHAPTER III

Table 3.1 Stiocheometric proportion of metal oxides.

Table 3.2 Expected, Experimental and percentage yield of $Mn_xZn_{(1-x)}Fe_2O_4$

CHAPTER IV

Table 4.1 Variation of lattice constant 'a' and particle size of nanosample $Mn_xZn_{(1-x)}Fe_2O_4$

Table 4.2(a) EDS Results of nanosample (a) $Mn_{0.7}Zn_{0.3}Fe_2O_4$, (b) $Mn_{0.65}Zn_{0.35}Fe_2O_4$, (c) $Mn_{0.6}Zn_{0.4}Fe_2O_4$, (d) $Mn_{0.8}Zn_{0.2}Fe_2O_4$

Table 4.3(a) Estimated percentage error of the elements Mn, Zn and Fe in the nanosample $Mn_xZn_{(1-x)}Fe_2O_4$

Table 4.3(b) Probable error of Mn, Zn, and Fe in the nanosample

CHAPTER V

Table 5.1(a) Particle size for unsintered samples using XRD and TEM

Table 5.1(b) Estimated cation distribution for $Mn_xZn_{(1-x)}Fe_2O_4$ using X-ray results.

Table 5.1(c) The bond length of A-sites d_{AL} and B-sites d_{BL}, the tetrahedral edge d_{AE}, the shared and unshared octahedral edges, d_{BE} and d_{BEU}, and the hopping length at A-site L_A and at B-site L_B for each sample

CHAPTER VI

Table 6.1(a) Neutron Diffraction data for $Mn_{0.6}Zn_{0.4}Fe_2O_4$

Table 6.1(b) Neutron Diffraction data for $Mn_{0.7}Zn_{0.3}Fe_2O_4$

Table 6.2(a) Saturation Magnetization, Retentivity and Coercivity values of unsintered samples using Hysteresis loop tracer

Table 6.2(b) Saturation Magnetization, Retentivity and Coercivity values samples sintered at 1300^0C

Table 6.3(a,b) Low temperature VSM data for (a) $Mn_{0.6}Zn_{0.4}Fe_2O_4$ (b) $Mn_{0.625}Zn_{0.375}Fe_2O_4$

Table 6.3(c) Saturation Magnetization, Retentivity, Squareness and Coercivity values of nanosample samples using VSM.

Table 6.4 Mössbauer parameter for the nanosample $Mn_xZn_{(1-x)}Fe_2O_4$ obtained at room temperature.

CHAPTER I

PREAMBLE

1.1 INTRODUCTION

Nanomaterial in general is defined as material with particles or crystallites having one or more dimensions below 100 nm. At these length scales, a large fraction of the atoms of these particles are at or near the surface which provides the particles with unique properties. In magnetic nanoparticles, crystal symmetry breaking at the surface has profound ramifications [1]. Due to reduced dimensions, nanomaterials have large surface to volume ratio and therefore they often display very interesting and fascinating properties which are substantially different from bulk. Lattice distortion, broken bonds and spin freezing at the surface are rampantly present in such materials.

There is a curiosity to understand the behavior of materials in nano length scale and to exploit the properties exhibited by these materials. If the crystallites are in the nanometer range, the grain will contain only a few unit cells. When the particle size goes below a critical value, domain structure changes and causes drastic modification in magnetic properties such as saturation magnetization and anisotropy. This all together opens up a different advance area of application in the field of modern technology and medicine. It is because of these reasons nanomagnetic materials have fascinated present day researchers. Broadly speaking, there are three different major methods of creating nano materials:

1. Top to down approach
2. Bottom to top approach

3. Virtual fabrication

Top-down is the traditional approach to miniaturization by sculpting via lithographic tools. Bottom up is self assembly from molecular precursor building blocks. In Virtual fabrication method, theorists and computationalists create material with new properties in computer simulations or analytically. But the main advantage of Virtual fabrication is to have the ability to obtain a fundamental understanding and to explain the guiding principles [2].

In respect of emergent technologies, nanomagnetism has taken a prime place in research in magnetic materials, which has evolved new ideas in the field of nanoscience. In last few decades interest in nanoscience and nanotechnology has increased manifold due to its promising technological applications. Consequently the research in the field of nanoscience got a tremendous boost in both the developed as well as the developing nations.

Study of nanomagnetic materials is a remarkable field at the frontiers of Physics and Chemistry. The domain structure, magnetic interactions and the basic properties of these materials are of considerable importance to modern technology. Developing various methods to generate nanostructures and understanding their complex phenomenon with supporting analysis has been a challenging field in research and development. Some important factors like, rich surface/interface effects, including symmetry breaking, electronic environment/charge transfer and magnetic interaction, differentiate nonmagnetic materials from conventional magnetic materials [3].

Nanosized magnetic oxides are becoming important materials due to their micro magnetic properties like superparamagnetism, giant magnetic resistance, magneto optic, magneto caloric effect, etc. These materials are

useful in variety of applications in electronic industries due to their high saturation magnetization, high resistivity, high permeability and low loss [4]. There is a great demand for high performance and miniaturization of electronic devices. Soft ferrite nanomagnetic materials are extensively used in inductors, transformers, antennas, electromagnetic interference, etc. With development of technology, nanomagnetic materials find important applications, in targeted drug delivery system, hyperthermeia [5,6], various medical and industrial sensors, magnetic thin films, MRI suppressors, microwave absorbers etc.

1.2 MAGNETISM

Magnetism has always fascinated mankind. Magnetism was first observed in a form of the mineral magnetite called lodestone, having chemical formula Fe_3O_4 [**7**]. The ancient Greeks were the first known to have used this mineral, which they called a magnet because of its ability to attract other pieces of the same material and iron. The modern understanding of magnetic phenomena originates from the work of Pierre Curie, and Pierre Weiss. Curie examined the effect of temperature on magnetic materials and observed that magnetism disappeared suddenly above a certain critical temperature in materials like iron. Weiss proposed a theory of magnetism based on an internal molecular field proportional to the average magnetization that spontaneously align the electronic micromagnets in magnetic matter. D. U. Bois made the saturation magnetization measurements of magnetite in 1890 [8]. The magnetic properties were studied by Pierre Weiss [9].

The present day understanding of magnetism is based on the theory of the motion and interactions of electrons in atoms (called quantum electrodynamics) and which originates from the work and theoretical models of two scientist Ernest Ising and Werner Heisenberg [10]. Using the concept of electron spin introduced by Goudsmit and Uhlenbeck, the origin of magnetism was explained. The origin of magnetism lies in the orbital and spin motions of electrons and how the electrons interact with one another. The magnetic moment is associated with the spinning charge and, therefore, the electron behaves like a magnet with its poles along the axis of rotation. Since the electron has a magnetic moment due to its spin and also due to its orbital motion around the nucleus, it has a total magnetic moment equal to the vector sum of these two magnetic moments. Hence the net magnetic moment of an atom is the vector sum of the individual spin and orbital magnetic moments of the electrons in the outer shells [11]. Figures 1.1 (a), 1.1 (b) illustrate these two phenomena. An electron of charge **e** revolving in a orbit with velocity **v**, making **n** revolution per second is equivalent to a current loop, and behaves like a magnetic dipole possessing a orbital magnetic moment μ_l=nev. The electron spins around itself and gives rise to spin magnetic moment μ_s. The electron spin is represented in two modes pointed up or down. In an atom, the opposed paired spins cancel and do not result in magnetic moment, while the unpaired spins give rise to a net magnetic moment.

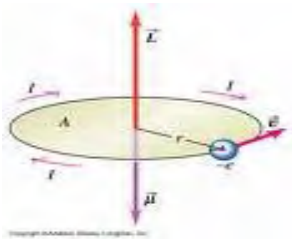

Fig. 1.1 (a) Electron orbit around the axis

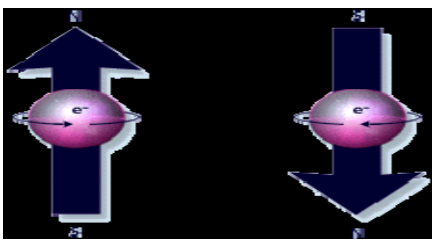

Fig 1.1 (b) Electron spin.

Magnetic materials are Classified into different groups on the basis of their magnetic properties and their temperature dependence viz: Diamagnetic, Paramagnetic, Ferromagnetic, Anti ferromagnetic, and Ferrimagnetic**.**

1.2.1 Diamagnetic Material:

Diamagnetic substances are composed of atoms which have no net magnetic moments i.e. all the orbital shells are filled and there are no unpaired electrons. However, when the material is exposed to a non uniform magnetic field, the orbital speed of electrons undergoes a change due to which a moment is developed in a direction opposite to the applied field. An electron in a magnetic field, will precess around the field with a Larmor frequency

$$\nu = eB/2m$$

This precession is known as Larmors precession. Since the magnetic moments induced by the applied magnetic field always oppose the applied field i.e. there is repulsion, the diamagnetic material has a negative susceptibility.

The M vs. H plot, shows that when the field is zero the magnetization is zero. The other characteristic behavior of diamagnetic materials is that the susceptibility is temperature independent. Some well known diamagnetic substances include: quartz (SiO_2), Calcite ($CaCO_3$), Bismuth, Mercury, water etc.

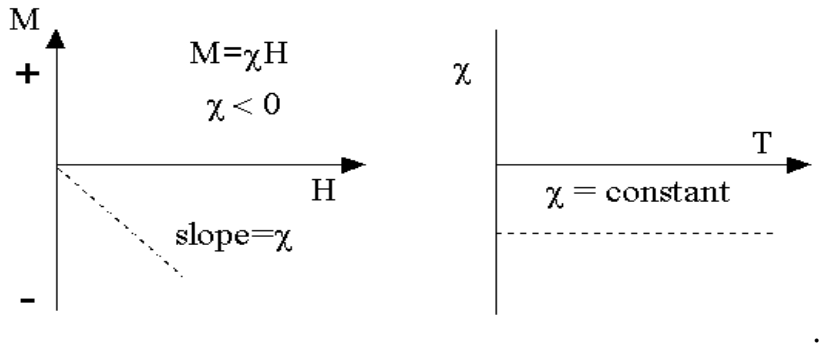

Fig. 1.1(c) Diamagnetism

1.2.2 Paramagnetic Materials:

The atoms or ions of these materials have a net magnetic moment due to unpaired electrons in partially filled orbital. However, due to thermal agitation, these magnetic moments are oriented in a random direction at room temperature. In presence of magnetic field, there is a partial alignment of the atomic magnetic moments in the direction of the field, resulting in a net positive magnetization and positive susceptibility. Since the applied field has to overcome the thermal motion, the paramagnetic susceptibility decreases with increase in temperature. The magnetization disappears when the field is removed.

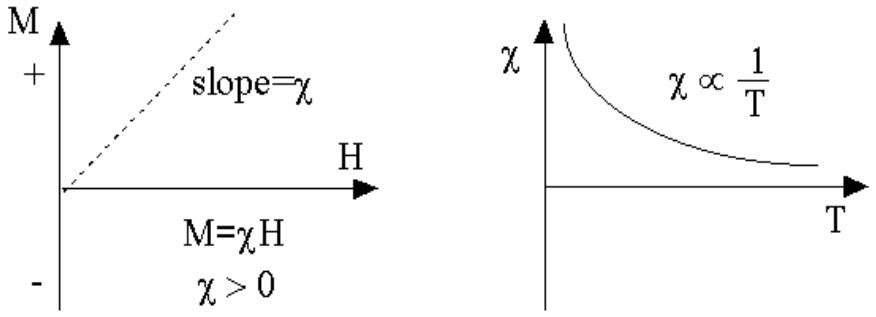

Fig. 1.1 (d) Paramagnetism

The efficiency of the field in aligning the moments is opposed by the randomizing effects of temperature. This results in a temperature dependent susceptibility, which is known as the Curie Law. At normal temperatures and in moderate fields, the paramagnetic susceptibility is small .Unless the temperature is very low (<<100K) or the field is very high paramagnetic susceptibility is independent of the applied field. Examples of paramagnetic substances are Aluminum, Oxygen, Platinum etc.

1.2.3 Ferromagnetic Material:

In these materials the major contribution to the total magnetic moment comes from spin magnetic moment. In ferromagnetic materials the magnetic moments of neighbouring atoms are aligned parallel to each other as shown in fig. 1.1(e), which forms a small region called domain. This behavior is the result of strong exchange coupling between the atoms. The interaction arises due to coupling of spins on adjacent atoms. The atomic moments in these materials exhibit very strong interactions. These interactions are produced by electronic exchange forces and result in a parallel or anti parallel alignment of the atomic moments. Ferromagnetic materials exhibit parallel alignment of moments resulting in large net magnetization even in the absence of a magnetic field.

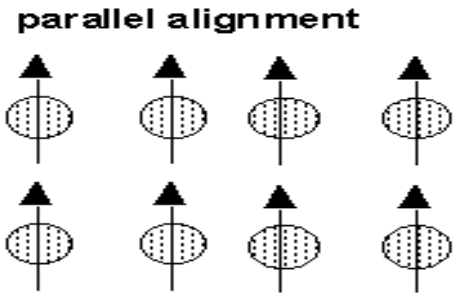

Fig. 1.1(e) Ferromagnetism

Examples of Ferromagnetic substances are Iron, Nickel, cobalt etc.

1.2.4 Antiferromagnetic materials

When the magnetic moments of the two sublattices are exactly equal in magnitude but aligned antiparallel to each other, then the net moment is zero and the material is said to be antiferromagnetic. These materials also have zero remanence, no hysteresis, but a small positive susceptibility that varies in a peculiar way with temperature. The uniqueness of antiferromagnetism is the behavior of susceptibility above a critical temperature, called the Néel temperature (T_N). Above the Néel temperature (T_N) the material behaves like paramagnetic [12] and susceptibility obeys the Curie-Weiss law but with a negative intercept indicating negative exchange interactions . Slight deviations from ideal antiferromagnetism can exist if the anti-parallelism is not exact. When neighboring spins are slightly tilted (<1°) or canted, a very small net magnetization can be produced. Hematite is a well known example of canted antiferromagnetism.

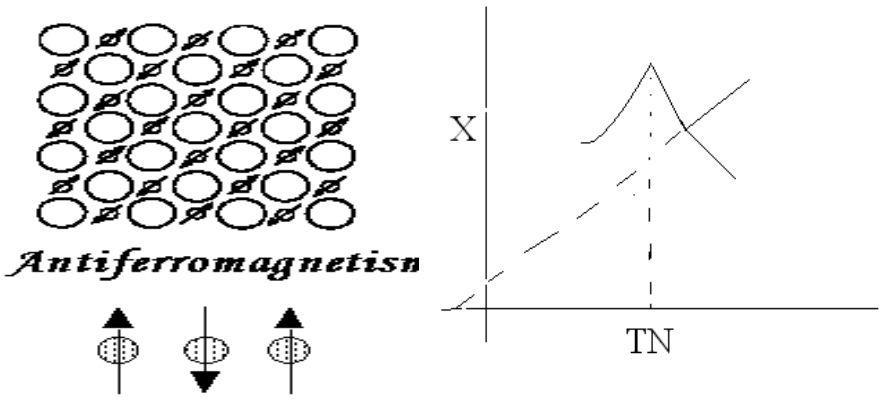

Fig.1. 2 (a) Antiferromagnetism

Examples of Antiferromagnetic substances are Chromium, Manganese Oxide etc.

1.2.5 Ferrimagnetic materials

The magnetic material is composed of two magnetic sublattices (called A and B) separated by oxygen ion. The exchange interactions are mediated by the oxygen anions, and the interactions are called indirect or superexchange interactions. The strongest superexchange interactions result in an antiparallel alignment of spins between the A and B sublattice. In ferrimagnetism, the magnetic moments of the A and B sublattices are aligned antiparallel but not equal in magnitude as shown in fig. 1.2 (b) which results in a net magnetic moment. Ferrimagnetism is therefore similar to ferromagnetism. It exhibits all the characteristics of ferromagnetic behavior such as spontaneous magnetization, Curie temperature, hysterisis, Remenance.

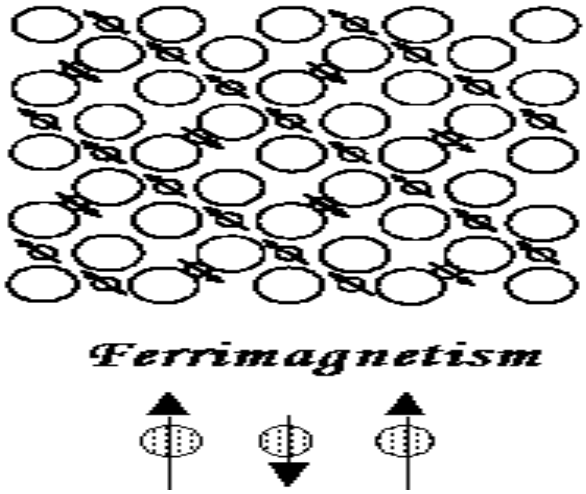

Fig. 1.2 (b) Ferrimagnetism

Some examples of ferrimagnetic substances are Manganese ferrite, Nickel ferrite etc.

1.2.6 The Hysteresis Loop and Magnetic Properties of magnetic materials.

B-H hysteresis loop shown in fig1.2 (c) depicts the relationship between the induced magnetic flux density (**B)** and the magnetizing force **(H).**

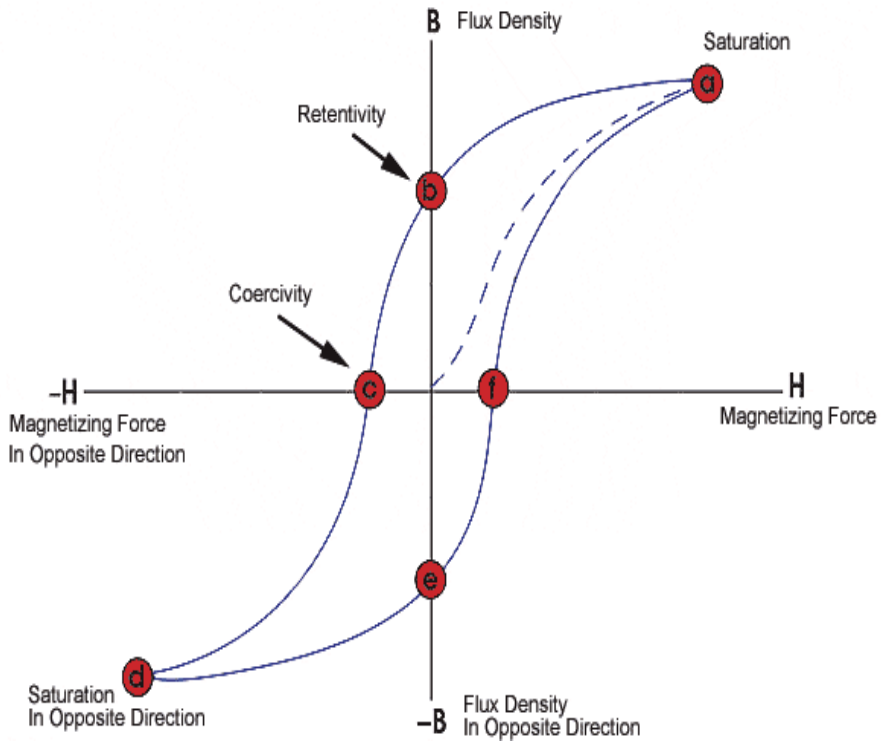

Fig 1.2 (c) Hysteresis Loop

The loop is generated by measuring the magnetic flux of a ferromagnetic material when the magnetizing force is changed. A ferromagnetic material which is thoroughly demagnetized, when placed in the presence of a sufficiently large external magnetic field, the spins in each domain rotate parallel to the direction of the applied magnetic field and follows the dashed line as **H** is increased**.** At point "a" almost all of the magnetic domains are aligned and an additional increase in the magnetizing force will produce very little increase in magnetic flux. At this point material has reached the point of magnetic saturation. When **H** is reduced to zero, the

curve will move from point "a" to point "b." At this point, some magnetic flux remains in the material even though the magnetizing force is zero. This is referred to as the point of retentivity on the graph and indicates the remanence or level of residual magnetism in the material. (At this point some of the magnetic domains remain aligned but some have lost their alignment.). As the magnetizing force is reversed, magnetic induction B decreases and at a point c the flux is reduced to zero. At this point reversed magnetizing force has flipped sufficient number of domains so that the net flux within the material is zero. This is called the point of coercivity on the curve. The force required to remove the residual magnetism from the material is called the coercive force or coercivity of the material.

As the magnetizing force is increased in the negative direction, the material will again become magnetically saturated but in the opposite direction (ie, at point "d"). Reducing **H** to zero brings the curve to point "e." It will have a level of residual magnetism equal to that achieved in the other direction. Increasing **H** back in the positive direction will return **B** to zero. The curve did not return to the origin because some force is required to remove the residual magnetism. The curve will take a different path from point "f" back to the saturation point where it completes the loop. From the hysteresis loop, a number of magnetic properties of a material can be determined.

1. Retentivity; A measure of the residual flux density corresponding to the saturation induction of a magnetic material. It is a material's ability to retain a certain amount of residual magnetic field when the magnetizing

force is removed after achieving saturation. It is the value of **B** at point b on the hysteresis curve.

2. Residual Magnetism or Residual Flux; the magnetic flux density that remains in a material when the magnetizing force is zero. Residual magnetism and retentivity are the same when the material has been magnetized to the saturation point. But, the level of residual magnetism may be lower than the retentivity value when the magnetizing force did not reach the saturation level.
3. Coercive Force; The amount of reverse magnetic field which must be applied to a magnetic material to make the magnetic flux return to zero. It is the value of **H** at point c on the hysteresis curve.

4. Saturation Magnetization; The saturation magnetization is the maximum induced magnetic moment that can be obtained in a magnetic field (Hsat), beyond this field no further increase in magnetization occurs. The spontaneous magnetization is the net magnetization that exists inside a uniformly magnetized microscopic volume in the absence of a field. The magnitude of this magnetization, at 0^o K, is dependent on the spin magnetic moments of electrons.

1.2.7 Anisotropy

The dependence of magnetic properties on a preferred direction is called magnetic anisotropy. The anisotropy is of several types:

1. Magneto crystalline anisotropy:
2. Shape anisotropy:
3. Stress anisotropy:

Magnetic anisotropy affects the magnetic behavior of the material**.** In case of nano-structured materials the important anisotropy types are magneto crystalline and shape anisotropy.

Magnetic anisotropy strongly affects the shape of hysteresis loops and controls the coercivity and remanence. Anisotropy in magnetic materials has considerable practical importance because it is exploited in the design of most magnetic materials that are of commercial importance.

Magneto crystalline Anisotropy

Magneto crystalline anisotropy is an intrinsic property of a ferrimagnet, independent of grain size and shape. Depending on the crystallographic orientation of the sample in the magnetic field, the magnetization reaches saturation in different fields.

For example in magnetite, above 130 K,

<111> is the easy direction of magnetization

<100> is the hard direction of magnetization

<110> is the intermediate direction of magnetization.

Magneto crystalline anisotropy is the energy necessary to deflect the magnetic moment in a single crystal from the easy to the hard direction. The easy and hard directions arise from the interaction of the spin magnetic moment with the crystal lattice (spin-orbit coupling). In cubic crystals, like magnetite, the magnetocrystalline anisotropy energy is given by **a** series expansion in terms of the angles between the direction of magnetization and the cube axes.

1.2.7.2 Stress Anisotropy

In addition to magneto crystalline anisotropy, there is another effect related to spin-orbit coupling called magnetostriction. It arises from the strain dependence of anisotropy constants. When a magnetic field is applied, to a demagnetized crystal it experiences a strain that can be measured as a function of applied field along the principal crystallographic axes. A magnetic material will therefore change its dimension when magnetized. There is also an occurrence of inverse affect or the change of magnetization with the stress. A uniaxial stress can produce a unique easy axis of magnetization if the stress is sufficient to overcome all other anisotropies.

1.2.7.3 Shape Anisotropy

Shape anisotropy is essentially due to the shape of a grain. A magnetized body produces magnetic charges or poles at the surface. This surface charge distribution, acting in isolation, is itself another source of a magnetic field, called the demagnetizing field. It is called demagnetizing field because it acts in opposition to the magnetization that produces it. For example, in a long thin needle shaped grain, the demagnetizing field will be less if the magnetization is along the long axis of needle rather than along one of the short axes. This produces an easy axis of magnetization along the long axis. Spherical grain has no shape anisotropy. It is found that the magnitude of shape anisotropy is dependent on the saturation magnetization. For magnetite, smaller than about 20 microns, shape anisotropy is the dominant form of anisotropy. In larger sized particles, shape anisotropy is less important compare to magneto crystalline anisotropy.

1.2.7.4 Temperature Dependence of Anisotropy

Both the magnetocrystalline and magnetostriction constants are dependent on temperature. In magnetite, at room temperature, the sign of the anisotropy constant K_1 is negative. However, at isotropic point, the anisotropy constant K_1 goes through zero and becomes positive when the magneto crystalline anisotropy vanishes, and therefore the original remanence carried by grains is lost**,** as the remanence is controlled by magnetocrystalline anisotropy. This provides a simple method for distinguishing different domain states. In grains where the remanence is controlled by shape anisotropy (i.e. small grains) or stress anisotropy, no remanence should be lost upon cooling through the isotropic point. Above room temperature, the magneto crystalline and magnetostriction constants decrease with temperature and vanish at the Curie temperature.

1.2.7.5 Domains

As per Wiess [13] the magnetic materials consist of physically distinct regions called domains each of which is magnetized in different directions. Although each domain is magnetized in a particular direction, a multinomial material may have zero net magnetization.

The magnetic behavior of a magnetic material can be explained on the basis of magnetic domains [13] Ferrimagnetic grains can be (i) multidomain (MD) (ii) single domain (SD) and (iii) Super paramagnetic (SP). A large crystallite may consist of many domains resulting in multidomain state but for ultrafine particles there can be only one domain in a crystallite**,** called SD state. SD particles at a particular temperature can have randomly oriented fluctuating domain moments and this state is called super paramagnetic

(SP).The magnetic energy reduces as number of domains in crystal increases. The adjacent domains are magnetized in opposite direction. The energy required to rotate magnetization through an angle θ made by magnetization in a preferred direction in the absence of magnetic field is called Anisotropy energy. A Bloch wall in a crystal is the transition layer that separates adjacent domains, magnetized in different directions. The entire change in spin direction between these domains does not occur in one discontinuous jump across a single atomic plane, but takes place in a gradual way over many atomic planes. For multi domain grains change in magnetization takes place by displacement of domain walls and therefore low field is required, i.e. coercivity is small**.** Change in magnetisation of a single domain arises due to rotation of the spins within the domain and thus results in a higher coercivity and remanance.

The demagnetized state of a ferrimagnetic or ferromagnetic body is normally presumed to be due to subdivision of the body into Weiss domains with Bloch walls between them. Grains which have domain walls in them are known as multidomain. Magnetic grains with dimension of few A^o or larger, which are acicular cannot contain domain wall due to energy consideration and they are termed as single domain for which magnetization direction is fixed in space. However, if the temperature of SD is increased, thermal energy becomes comparable to effective magnetic anisotropy energy and magnetization direction starts fluctuating between easy axes of the grains. In such a case it is said to be exhibiting superparamagnetism (SP). This mechanism can be expressed in terms of an equation $V J_b Hc = 2k T_b$ where J_b is saturation intensity, Hc is coercive field, k is Boltzman constant, 'V' is

volume of the grain, the temperature T_b is referred as blocking temperature which is less than Curie temperature Tc. Magnetic states SD and MD are interchangeable by temperature. A polycrystalline magnetic material may consist of three types of states SD, MD, and SPM, any one of them may predominate depending on condition at the time of sample preparation.

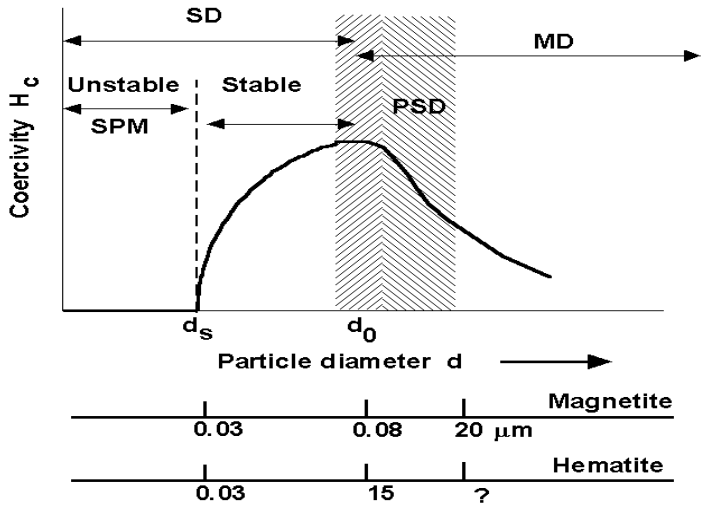

Fig 1.2 (d) Variation of coercivity with particle size.

Fig 1.2 (d) depicts variation of coercivity with particle size. The large coercive force in single domain particles is due to magnetocrystalline and shape anisotropies for non spherical grains. The coercive force is dependent on particle size. As particle size of this single domain particles decrease, the coercive force decreases as shown in the figure. Moreover, the shape anisotropy increases as the aspect ratio of a particle increases. Therefore, elongated single-domain particles can display large coercive forces [14,15].

The boundaries between domains are not sharp on atomic scale but are spread over a finite thickness within which the direction of spins changes gradually from one domain to next [16]. The width of the domain wall varies due to the

two opposing energies namely magnetocrystalline anisotropy energy and the exchange energy. The exchange energy (E_{ex}) tries to align the spin in a direction parallel to the direction of domain, while anisotropy energy (E_a) tries to make the wall thin to minimize misalignment within the easy direction. The actual thickness of domain wall is determined by counterbalance of exchange energy and anisotropy energy. For a simple cubic structure domain wall energy $E_w = E_{ex} + E_a$

Several researchers, using a variety of techniques have investigated the causes for the observed reduction in magnetization in fine magnetic particles. In 1960s Coey and Berkowitz stated that the observed decrease in magnetization is due to the existence of non-collinear spins and high effective anisotropy fields in the surface and non- magnetic dead layers [17,18].

In a nanosized magnetic particle there are two types of contributions, namely contribution from the highly aligned core of the particle and the contribution from canted spins on the surface of the particle. There are two opinions

1. Sato *et al*. suggest that the loss of magnetization as the particle size decreases depends largely on the crystalline magnetic anisotropy energy constant K. Smaller K constants display lower relative magnetization values [19].

2. Experimental analysis including microscopy, XRD and magnetometry studies suggests that the reduced magnetization is due to surface characteristics of nanoparticles. Specifically, the loss of magnetization may be due to the existence of a magnetically dead layer. ~1 nm thick caused by an

asymmetric environment effect of the surface atoms [19]. Saturation magnetization depends on method of sample preparation.

1.2.7.6 Superparamagnetism:

Superparamagnetism is a form of magnetism, which appears in small ferromagnetic or ferrimagnetic nanoparticals. In small enough nanoparticles, magnetization can randomly flip direction under the influence of temperature. The typical time between two flips is called the Néel relaxation time. In the absence of external magnetic field, when the time used to measure the magnetization of the nanoparticles (T_m) is much longer than the Néel relaxation time, their magnetization appears to be on an average zero and particals are said to be in the superparamagnetic state. In this state, an external magnetic field can magnetize the nanoparticles, similar to a paramagnet. However, their magnetic susceptibility is much larger than that of paramagnets. If the magnetization does not flip during the measurement, which means that the measured magnetization retains the value of the initial instantaneous magnetization, and then the nanoparticle appears to be "blocked" in its initial state. It is known that superparamagnetism occurs in single domain nanoparticles. This is possible when the nanoparticle diameter is approximetely in the range of 3–50 nm [20].

As nanoparticles possess magnetic anisotropy, the magnetic moment has usually only two stable orientations which are antiparallel to each other, separated by an energy barrier. The stable orientations are called as "easy axis". At finite temperature, there is a finite probability for the magnetization to flip and regains its direction. The mean time between two flips is called the

Néel relaxation time T_N and is given by the following Néel-Arrhenius equation:

$T_N = T_0 e^{KV/K_B T}$ where 'v' volume of grain, K anisotropy constant, K_B is Boltzman constant and T_o is a length of time, characteristic of the material, called the attempt time or attempt period (10^{-9}–10^{-10} s). A transition between superparamagnetism and blocked state occurs when $T_m = T_N$. In several experiments, the measurement time T_m is kept constant but the temperature is varied, so the transition between superparamagnetism and blocked state is seen as a function of the temperature. The temperature for which, $T_m = T_N$ is called the blocking temperatureT_B. Where $T_B = KV/K_B \ln(T_m/T_o)$.

1.3 FERRITES

Ferrites are usually non-conductive ferrimagnetic ceramic compounds having general formula $MeFe_2O_4$ where Me represents one or more divalent transition metals[21].They are derived from iron oxides such as hematite (Fe_2O_3) or magnetite (Fe_3O_4). Ferrites are dark grey ceramic materials belonging to ferrimagnetic group, which are hard brittle and chemically inert having magnetic properties. Ferrimagnetic iron oxides inherently display a lower magnetic response than ferromagnetic material such as transition metals [22]. However, the iron oxides are also less sensitive to oxidation and therefore maintain stable magnetic responses. The properties of ferrites are enhanced when the size of the particle reaches the nanometer range. In terms of the magnetic properties, ferrites are often classified as soft ferrites and hard ferrites, which respectively refers to their low and high coercivity of their magnetism.

Ferrites that are used in transformers or cores contain nickel, zinc, or manganese compounds which usually have a low coercivity and are called soft ferrites. Because of their comparatively low losses at high frequencies, they are extensively used in the cores of Switched-Mode Power Supply (SMPS) and RF transformers and inductors.

Permanent ferrite magnets or "hard ferrites" have a high coercivity and high remanence after magnetization. They are composed of iron and barium or strontium oxides. In a magnetically saturated state they conduct magnetic flux proficiently and have a high magnetic permeability**.** They are the most commonly used magnets in radios.

Ferrites with high electrical resistance with very low eddy current are commonly seen as a lump in a computer cable, called a ferrite bead, which helps to prevent high frequency electrical noise. Ferrite particles are also used as a component of radar-absorbing materials or coatings used in stealth aircraft and in the absorption tiles lining the rooms used for electromagnetic compatibility measurements.

Depending upon crystal structure they are classified as

1) Ferrospinel $M_eFe_2O_4$,

2) Garnets $Me_3Fe_5O_{12}$

3) Orthoferrites $MeFeO_3$

4) Hexagonal (Magnetoplumbite) $MeFe_{12}O_{19}$

1.3.1 Ferrospinel $M_eFe_2O_4$,

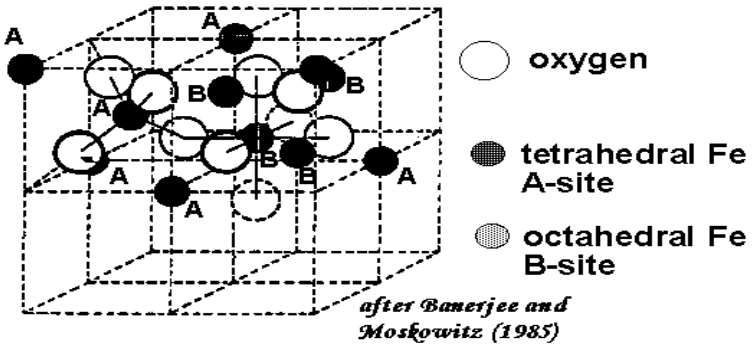

Fig 1.3 (a) Ferrospinel structure

Ferrospinels have the general formula $M_eFe_2O_4$, [4] where M_e is divalent transition metal ion like Mn, Zn, Co, Ni etc. with valency 2 or mixture of divalent transition ions with valency 2. Oxygen ion forms close packed F.C.C. structure where the metal ions are distributed over tetrahedral and octahedral sites. Tetrahedral sites are surrounded by 4 oxygen ions. Octahedral sites are surrounded by 6 oxygen ions. In a unit cell out of 64 tetrahedral sites 8 are occupied and out of 32 octahedral sites 16 are occupied [23]. Manganese-zinc ferrite is a ferrospinel belongs to the group of soft ferrite having chemical formula $Mn_xZn_{(1-x)}Fe_2O_4$.

1.3.2 Garnet

They have the general formulae $Me_3Fe_5O_{12}$ where Me is a trivalent ion such as rare-earth. The unit cell is cubic and contains eight molecules of $Me_3Fe_5O_{12}$. In addition to tetrahedral and octahedral sites, such as those seen in spinels, garnets have dodecahedral (12-coordinated) sites. The net ferrimagnetism is thus a complex result of antiparallel spin alignment among

the three types of sites. A well known garnet, yttrium iron garnet $Y_3Fe_5O_{12}$(YIG) is shown in figure1.3(b). The coordination of the cations is considerably more complex than spinal,with $24Y^{+3}$ in dodecahedral sites, $24Fe^{+3}$ ions in tetrahedral sites and remaning 16 Fe^{+3} in octahedral sites.A wide range of transition metal ions cations can substituteY^{+3}or Fe^{+3}, especially rare earth ions may replace the ions on octahedral and dodecahedral sites. Each type of lattice site will accept other metal ions with suitable size. Example, dodecahedral sites accept ions having size $0.9A^0$ to$1.05A^0$, octahedral sites accept ions having size $0.65A^0$ to $0.8A^0$ and tetrahedral sites accept ions having size $0.4A^0$ to $0.64A^0$. Garnets are magnetically hard and are well known for their microwave applications.

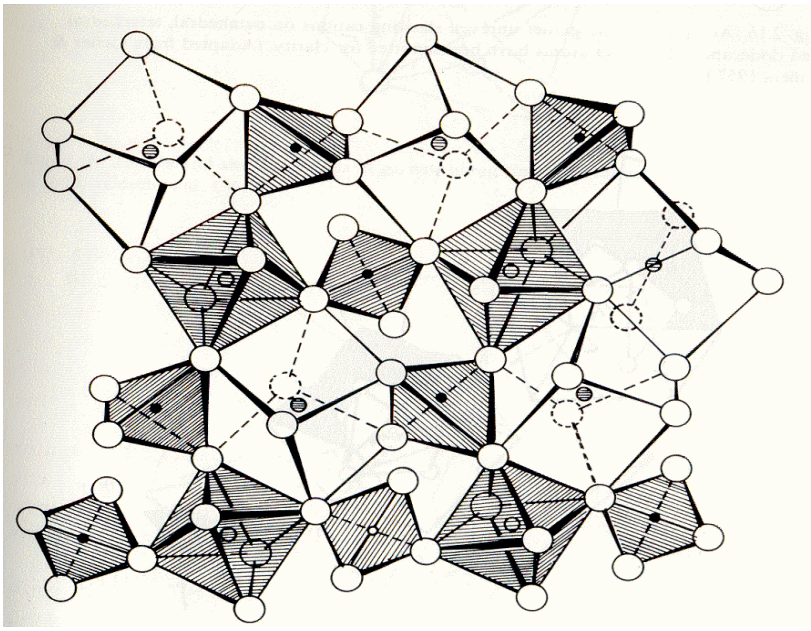

Fig.1.3 (b) Garnet

1.3.3 Orthoferrite

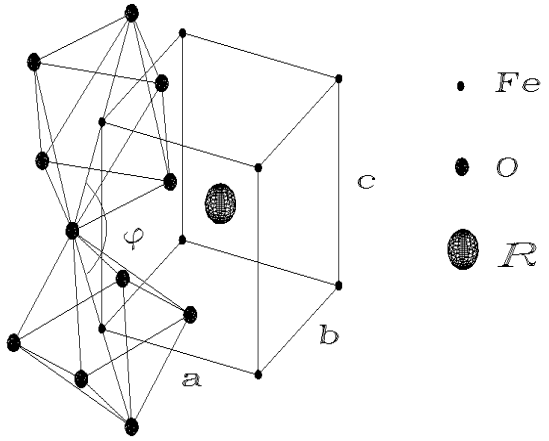

Fig. 1.3 (c) Orthoferrite

Orthoferrites have the general formulae $MeFeO_3$ where Me is a trivalent ion such as rare-earth. They crystallize in a distorted perovskite structure with a orthorhombic unit cell. They are used for bubble domains. Orthoferrites belongs to a space group Pbnm and most of them are weakly ferromagnetic. At the Neel temperature T_N the subsystem of iron ions orders into a slightly canted antiferromagnetic structure with antiferromagnetic moment G and a weak ferromagnetic moment F. The rare-earth ion subsystem acquires magnetization m due to an interaction with the iron subsystem. The orthoferrites are particularly interesting because of the presence of an antisymmetric exchange interaction which involves the vector cross product of neighboring spins as opposed to the usual scalar product. In the absence of this interaction, the orthoferrites would be antiferromagnetic. Interaction leads to a small canting of the sublattices, making the orthoferrites "weak" ferromagnets. Example of cubic pervoskite at room temperature is $BaTiO_3$.

1.3.4 Hexagonal

They have the general formulae $MeFe_{12}O_{19}$ where Me is a divalent metal ion with large atomic radius, usually barium (Ba), strontium (Sr), or lead

(Pb). They crystallize in hexagonal structure. The crystal structure is complex, but it can be described as hexagonal with a unique *c* axis, or vertical axis. This is the easy axis of magnetization in the basic structure. Because the direction of magnetization cannot be changed easily to another axis, hexagonal ferrites are referred to as "hard." The most typical hexaferrites are the so-called M-type ($AFe_{12}O_{19}$), W-type ($AMe_2Fe_{16}O_{27}$), X-type ($A_2Me_2Fe_{28}O_{46}$), Y-type ($A_2Me_2Fe_{12}O_{22}$), Z-type ($A_3Me_2Fe_{24}O_{41}$) and U-type ($A_4Me_2Fe_{36}O_{60}$). The numerous ferrite chemical compositions and crystal structures make it possible to tailor their electromagnetic properties, such as the saturation magnetization, the magneto-crystalline anisotropy, the permittivity, and the permeability.

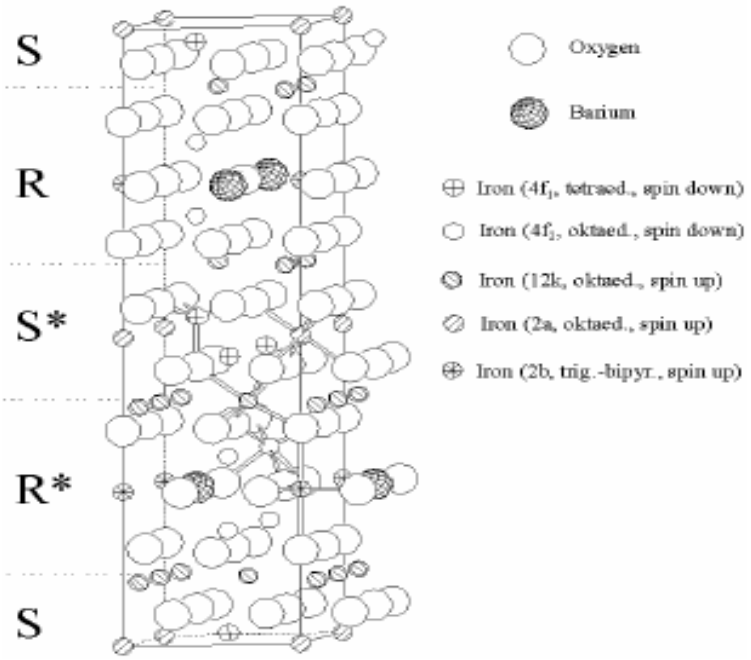

Fig. 1.3 (d) Hexagonal structure of ferrite

1.3.5 Structure of Spinel.

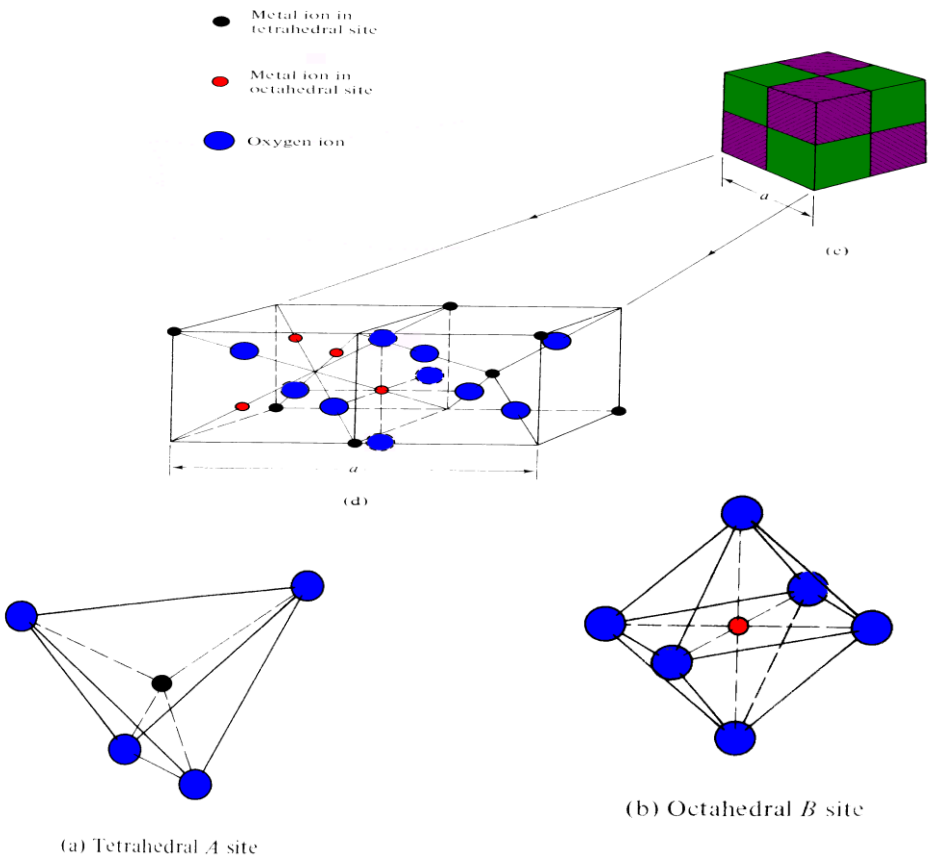

Fig. 1.4 (a) Structure of spinel ferrite

On the basis of cation distribution ferrites are classified as

1.3.6 Normal Ferrites

In which 8 divalent metal ions occupy 'A' sites and 16 trivalent Fe ions occupy 'B' sites. Example: In $Zn^{2+}[Fe_2^{3+}]O_4$, Zn^{+2} have strong affinity towards tetrahedral site (A); therefore they enter the A-site of the lattice, giving rise to normal ferrites.

1.3.7 Inverse Ferrite

All 8 divalent metal ions are in the eight of sixteen octahedral sites and 16 trivalent Fe ions are in eight octahedral and eight tetrahedral sites

Example; Cobalt Ferrite $Fe^{+3}[Fe^{+3}Co^{+2}]O_4$

1.3.8 Mixed Ferrite:

All divalent metal ions and Fe ions are uniformly distributed over A and B site. In Mn-Zn Ferrite $Zn^{+2}{}_{x}Fe_{(1-x)}{}^{+3}[Fe^{+3}{}_{(1+x)}\ Mn_{(1-x)}{}^{+2}]O_4$ Zn occupy tetrahedral site, Mn occupy Octahedral site whereas Fe^{+3} ions occupy tetrahedral and Octahedral sites.

1.4 MOTIVATION AND OBJECTIVE OF THE WORK CARRIED OUT.

The very fact that materials composed of nanoparticles, exhibit newer and at times fascinating properties is an interesting conjuncture. This is because the properties of such materials are driven by number of factors and particle size happens to be a major one. Preparation of Mn-Zn ferrite has been always a challenge to numerous researchers and technologists. Preparing nanoparticles of these materials with particle size in the vicinity of 10nm is a challenge of immense potential. Moreover development of newer methods of nanomaterial preparation is always welcomed in the area of research. Literature survey confirmed that method of preparation of nanoparticles using oxides as starting material was limited to ceramic method followed by grinding of the bulk material using ball mill for long duration at high speeds. The fact that all presently available chemical methods employ metal salts other than oxides happened to be an impending motivation of searching and developing a simple chemical method to prepare nanoparticle Mn-Zn ferrite materials.

It is well known that metal oxides are used in ceramic method of preparation, as the solid state reaction occurs at elevated temperatures of about 900^0C. Since reduced particle size increases the reactivity of the particle, it was felt that if we could reduce the particle size of the oxides, with suitable fuel and complexing agent it may be possible to prepare nanoparticle Mn-Zn ferrite material at low temperatures using simple method. The very fact of increase in reactivity at small dimensions triggered the idea, and accordingly with the objective of devising a new simple method to prepare nanoparticles from oxide materials, the work was taken up. Since nanoparticles exhibit extraordinary properties it was thought that bulk materials prepared from nanoparticles may be different from bulk materials prepared by conventional techniques and would also show some property changes due to various factors that govern nanoparticle behavior. Thus it was felt necessary to carry out detailed investigations on the nanomaterials as well as on the bulk materials obtained from nanomaterials prepared using innovative technique. The investigative work was taken up, keeping this aim and objective in mind. Accordingly the following investigative work plan was executed.

1.5 INVESTIGATIVE WORK PLAN EXECUTED

Since design and execution of a new preparative method using metal oxides as raw materials for wet chemical method was a major part of the work, lots of trial work towards formulation and optimization of the method was carried out in the initial stages of research. Although preparing nanoparticles at low temperature using metal oxides was almost an impossible task, the work was taken up as a challenge. Numerous trial samples, $Mn_xZn_{(1-x)}Fe_2O_4$

with x=0.4, 0.6, were synthesized using the new formulated method and characterized for confirmation of the sample. The method was finally optimized after careful analysis and minute considerations of several factors which were actually influencing the formation of the final product. The final products synthesized were found to fulfill all the necessary requirements of nanoparticle Mn-Zn ferrite materials. The method was then adopted to prepare materials for proposed studies which included.

1.5.1 Studies on nanomaterials

1. Synthesis of ultrafine nanoparticle $Mn_xZn_{(1-x)}Fe_2O_4$ ferrites samples with x=0.4, 0.5, 0.6, 0.625, 0.65, 0.675,0.7, 0.8.
2. Characterization of ferrite nanocrystals from structural, compositional and morphological point of view using XRD, IR and EDS techniques.
3 Estimation of grain size using advanced techniques namely, XRD, TEM, HRTEM, SEM and SPM.
4. Estimation of cation distribution of nano samples using XRD and Neutron diffraction.
5. Study of room temperature magnetic properties like saturation magnetization, coercivity, retentivity of nanoparticles $Mn_xZn_{(1-x)}Fe_2O_4$ using VSM and Hysteresis loop tracer.
6. Study of low temperature magnetic properties of nanosample using VSM.
7 A.C susceptibility and Curie temperature measurements of nano samples.
8. Temperature dependence of magnetization of nano samples using SQUID.

9. Mossbaur and neutron diffraction studies of nano samples to determine magnetic structure and other magnetic parameters.
10. Measurement of electrical properties like Resistivity, Seeback coefficient, Dielectric constant of nano samples as a function of temperature and frequency.

1.5.2 Studies on bulk materials made from nanomaterials.

1. Preparation of bulk material by sintering nanomaterial at different sintering temperature, in presence of nitrogen.
2. Characterization of bulk samples from structural, compositional and morphological point of view using XRD and SEM.
3. Study of room temperature magnetic properties like saturation magnetization, coercivity, retentivity of bulk samples $Mn_xZn_{(1-x)}Fe_2O_4$ using VSM and Hysteresis loop tracer.
4. A.C susceptibility and Curie temperature measurements of bulk samples.
5. Initial permeability measurements of bulk samples as a function of temperature and frequency.
6. Measurement of electrical properties like Resistivity, Dielectric constant of bulk samples as a function of temperature and frequency.

1.6 ORGANIZATION OF THESIS

The thesis is divided into eight chapters.

Chapter I:

The present chapter includes brief introduction of nanomaterials, magnetism, different types of magnetic materials, ferrites and its classes, motivation for the proposed work, and objective of the work.

Chapter II:

Detailed literature survey with reference to theoretical background of MnZn ferrite and their properties are given in this chapter.

Chapter III:

Different methods of preparation of nanoferrites and the mechano-chemical auto-combustion method developed for the synthesis of nanoparticle Mn-Zn is elucidated in this chapter.

Chapter IV:

This chapter is devoted to characterization of materials prepared. Different techniques like X-ray powder diffraction and Rietveld refinement of XRD pattern, Infrared spectroscopy (FTIR), and chemical analysis using titrimetry, EDAX studies and Density employed for measurements have been discussed.

Chapter V:

This chapter involves the study and particle size of the nanoparticle ferrite samples prepared. It focuses on particle size estimation from XRD data, Scanning electron microscope SEM, low and high resolution Transmission electron microscope (HRTEM) and Scanning probe microscopy SPM.

C**hapter VI**:

In this chapter experimental results obtained from magnetic measurements are presented in detail. Different experimental techniques used for measurements of magnetic properties of nano and bulk Mn-Zn ferrites using pulse field hysteresis loop tracer, Vibrating sample magnetometer, SQUID, Mossbaur etc are discussed.

Neutron diffraction studies of nano samples to determine magnetic structure are also included in this chapter. All experimental results obtained on the samples under investigations are presented here.

Chapter VII:

This chapter includes electrical properties of the nano and bulk samples. The details of different experimental technique used for measurements are described along with the experimental results obtained on the materials under study.

Chapter VIII:

This chapter discusses all the results at length, draws conclusions, summarizes all the results obtained, and proposes future investigations.

References

[1] M. A. Willard, L. K. Kurihara1, E. E. Carpenter, S. Calvin and V. G. Harris, International Materials Reviews, 49, (3-4),(2004)125-170.

[2] S. D. Bader: Colloquium: Opportunities in nanomagnetism Rev. Mod. Phys., Vol. 78, No.1, (2006).

[3] Nanomatrerials and nanostructure, page199, Dominant publisher New Delhi, (2007), I S B N no.81-7888-465-8.

[4] M. Sugimoto, J. Am. ceram. soc. 82O (1999)269-280.

[5] Q. A. Pankhurst, Connolly, S. K. Jones, and J. Dobson, "Application of magnetic nano materials in Biomedicine", Journal of Physics D, Vol.36 (2003) No.13, pp. R167-R181.

[6] R. Jurgons, C. Seliger, A. Hilpert, L. Trahms, S. Odenbach, and C. Alexiou, Journal of Physics Condenced matter, vol.18 (2006) no. 38, pp. S2893-S2902.

[7] M. R. Ananthraman, K. Seshan, D. K. Chakrabarty and H. V. Keer, Bull. Mater. Sci., 3(3) (1981) 275.

[8] H. E. Du Bois, Phil Mag., 29 (1890) 293.

[9] P. J. Weiss, J. Phys., 6(4) (1907) 66.

[10] www.buzzle.com/articles/history-of-magnetism.html

[11] B. Jeyadevan, C. N. Chinnasamy, K. Shinoda, K. Tohji, J. Appl. Phys., vol. 93 (2003) pp. 8450-8452.

[12] William. F. Smith, "Principle of material science and engineering" 2nd Edition, McGraw Hill Co. Publishers) New York, (1986).

[13] P. Weiss, Journal of Physics 6 (1907) 667.

[14] M. Ozaki, (Ed.: T. Sugimoto), Marcel Dekker, Inc., Vol. 92 New York, 2000.

[15] E. P. Wohlfarth, Journal of Magnetism and Magnetic Materials 39(1983) 39.

[16] S. Chickazumi and S. H. Charap, "Physics of magnetism" Krieger Malabar (1978), pp 248.

[17] J. M. D. Coey, Physical Review Letters 27 (1971)1140.

[18] A. E. Berkowitz, W. J. Schuele, P. J. Flanders, Journal of Applied Physics 39 (1968) 1261.

[19] T. Sato, T. Iijima, M. Sekin, N. Inagaki, J. Magn Magn Mater 65 (1987) 252.

[20] E. J. W Verwey., P. W Haayaman., F. C. Romejin and Van Cosferhout G. W. Phil, Res.173,(1950)

[21] E. C. Snelling, "Soft ferrite, Properties and application" Butterworth and co Publishers P Ltd, London, (1988).

[22] R. M. Cornell, U. Schertmann, The Iron Oxides: Structure, Properties, Reactions, Occurrence and Uses, VCH Publishers, Weinheim, 1996.

[23] J. Smith and H. P. Wijn, "Ferrites" Philips Tech. Library, Eindhoven, The Netherlands, (1959)137.

CHAPTER II

LITERATURE SURVEY

Over the last few decades the interest towards soft magnetic materials has substantially increased due to increasing demand for improved performances of electromagnetic gadgets, memory or data storage devices, sensors etc.[1]. Oxide based soft magnetic ferrite are one of the major contenders in this field of application [1]. Consequently, the properties of magnetically disorder ferrites have remained a subject of considerable interest for the last 40 years [2]. But it was hardly a decade ago that the importance and possible advantage of nanocrystalline ferrites was understood [3,4]. In particular, nanosized mixed ferrites containing zinc have attracted considerable attention [5]. Among them MnZn ferrites constitute technologically the most important material for their high magnetic permeability, high saturation magnetization, and low core losses [6].

The forceful demands on the quality of high performance ferrites, especially for applications requiring low loss at high frequencies have created the need for a more appropriate method for preparing compositionally and structurally perfect ferrites exhibiting low magnetic and electrical losses.

The search for better product to meet the application oriented requirements and optimum performance is a never ending process. Attempts have been made to present a systematic review of various experimental and theoretical observed facts in the context of the present study.

As far as materials preparation is concerned, different wet chemical methods such as citrate precursor, sulphite hydrazinate, oxalate hydrazinate etc have been reported by different investigators. Wet chemical processes

developed for preparation of Mn-Zn ferrite nanoparticles employ metallic salts as raw materials for synthesis [7-10]. Metal Oxides are usually used in ceramic method of preparation to produce bulk ferrite materials which is then down sized to nanoparticles by ball milling [11-14]. This is done as the temperature required to initiate solid-state reaction in oxides is quite high. But solid state reaction at elevated temperatures does not essentially produce nanoparticle materials. Moreover the nanoparticles obtained from bulk material by ball milling suffer from different micro strain defects and do not exhibit enhanced magnetic properties [15].

Precursor methods are simple, inexpensive, do not require elaborate experimental setup and is less time consuming. The ferrites prepared by this method are found to exhibit better properties then those prepared by ceramic method [16].

A variety of synthetic ferrites were prepared by Hilpert in 1909 by using precursor method, who suggested the basic formula for ferrites as MFe_2O_4, where M is a divalent metal ion [17]. Hilpert described the preparation of stoichiometric ferrites by thermal decomposition of crystalline salts $M_3Fe_6(CH_3CO_2)17O_3OH.12C_5H_5N$. The structural studies on ferrites were done by some researchers [18,19] who reported spinel structure for ferrites. Barth and Posnjak in 1932, discovered normal and inverted spinel structures of ferrites on the basis of X-ray analysis [20]. They found that in the case of ferrites, it was necessary to assume that the divalent and trivalent metal ions interchange positions in the crystal. Thus they discovered “the inverse spinel. Verwey [21] in 1950, reported investigations on the ordering of divalent and trivalent iron ions in magnetite and suggested that the existence

of neighboring Fe^{2+} and Fe^{3+} ions can give rise to higher conductivity because of the exchange of electrons between adjacent ions.

The basic theory of spin-spin interaction in ferrites was developed by Neel [22] in 1948, who introduced the idea of magnetic sublattice. A more detailed examination of the basic interaction of the spin system was made by Anderson [23] in 1951 and van-vleck [24]. Yafet and Kittle [25] in 1952, extended the theory of magnetic sublattice by postulating a triangular arrangement of the three sublattice, when antiferromagnetic exchange interactions between sublattice is comparable to that among the spin moments within the sub lattice formed by Fe^{3+}ions on tetrahedral and octahedral sites. The performance of ferrites at high frequencies was studied by Snoek [26]. Koop [27] in 1951, gave the theory of low frequency dispersion by assuming that polycrystalline sintered ferrites consist of large domains of well conducting grains separated by relatively thin poor conducting layers producing interfacial polarization of Maxwell- Wagner type. It was reported that the dielectric constant varied inversely as the square root of the conductivity [28].

Spinel ferrites of different composition have been studied and used for a long time. Existence or production of an ideal ferrite material which can replace the low performing one in every set-up as per the requirements is unattainable as each one has its own marginal advantages and disadvantages.

Due to rapid development of nanotechnology and the unique features of Mn-Zn ferrite materials, several different methods have been proposed and adopted to prepare these ferrite materials.

These are mainly divided into two types:

1. Conventional ceramic method, i.e. solid state reaction technique, involves milling of the reactants followed by heating at elevated temperature range.
2. Non conventional process involves producing the powdered material by wet chemical method.

E. Auzans and co-workers [29] used Coprecipitation method for the synthesis of MnZn ferrites. Material preparation methods like hydrothermal precipitation process [30] Sol-gel synthesis [31] and the microemulsions approach [32] have been often used to synthesize the Mn-Zn ferrite nanosized materials. Xian- Ming Liu et.al [33] has synthesized Mn-Zn ferrites by precursor method. Shunli Hao et.al [34] have used citrate precursor method to synthesize Mn-Zn ferrites. Daun and co-workers [35-37] have designed novel synthesis route of pure MFe_2O_4 (M=Mg, CO, Ni) spinel ferrites using a single molecular precursor.

Among these methods of preparation, the precursor method of the synthesis of inorganic solid has attracted the attention of solid state chemists for the fact that the product formed is of high purity and homogeneity on an atomic scale in precursor itself thereby decreasing their diffusion distance of reactive cations during the formation of the product and thus lowering the temperature of formation.

Solid solution precursor technique has been used to prepare fine particle ferrites MFe_2O_4, where M= Mg, Mn, Co, Ni, and Zn [38] and Ni-Zn ferrites [39] which were sintered at low temperature to give dense ferrites. Using this technique fine particle Mg-Mn ferrites (Mg_{1-x} Mn_x Fe_2O_4) were

prepared [40] for x = 0.5, 0.62 by thermal decomposition of hydrazinium metal hydrazine carboxylate precursor.

The crystallographic, electrical and magnetic properties depend upon the chemical composition as well as on the various heat treatments during the course of preparation [41]. It is reported [42] that Zinc ferrite prepared by twin roller quenching method has improved microstructure and magnetization. The parameters like lattice constant, x-ray densities, bulk densities, porosity, resistivity [43,44], oxygen positional parameter, degree of inversion and saturation magnetization [45] all change with the heat treatment.

Density plays an important role in changing the electrical and magnetic properties of the ferrites. Density of ferrites, measured in air, is found to be dependent upon the composition and method of preparation [46]. It has been reported that density increases with sintering temperature in the range 800-1000^{o}C and remains fairly constant thereafter for Zn-ferrites [38] and Mn-Zn-ferrites [47]. It is reported that high density Mn-Zn ferrite prepared by this method shows room temperature saturation magnetization M_s =55.85 emu/g at 5.4 kOe [48]. The grain size of Mn-Zn ferrites depends on the method of preparation, and it increases with increase in sintering temperature [47]. Ni-Zn and Li-Zn ferrites have been found to posses' low porosity [49]. Porosity at the grain boundaries and within the grain causes hindrance to the domain wall motion and is damaging to the initial permeability [47]. Particle size significantly affects the magnetic properties of ferrites. Z.X. Tang et.al [50] observed the changes in saturation magnetization with particle size.

Research work carried out in ferrites in last several decades has shown that MnZn ferrites have been the subject of intensive experimental and

theoretical investigations. In France, Guillaud and Pauthernet have studied the saturation magnetization and Curie temperature of Manganese-Zinc ferrites. In Japan, Okamura and his Co-workers have investigated the resonance characteristic of these materials. Several investigators, in the United States, Japan and USSR have contributed to the understanding of the magnetic properties of manganese ferrites [51-57].The dependence of magnetic performance on microstructure and composition of Mn-Zn ferrites prepared by different techniques was reported by Rosales et. al [58]. The influence of segregation in Mn-Zn ferrites [59], deviation from stoichiometry [60] and grain size [61-65] on properties such as initial permeability losses, magnetoelastic energies and others has been continuously studied in the last twenty years. These processes also affect the microstructure and initial permeability of Mn-Zn ferrite [66]. The reactive (hasty or quick) sintering of manganese ferrite has been studied using several raw materials accompanied by expansion of the product and such processing invariably results in a less dense end product [67-69]. Some researchers [70] found hot pressing technique very useful to prepare high permeability and high density ferrite which also helped to lower the porosity in the material.

Mustaffa-Hj et al. [71], prepared several samples of Mn-Zn Ferrites, $Mn_xZn_{1-x}Fe_2O_4$ with $0<x<1.0$ by conventional sintering method. It was reported that the density of the ferrite decreases with increase in concentration of Zn [71]. SEM results indicate that sintered ferrites are granular, polycrystalline containing voids. The increase in concentration of manganese favors the formation of Mn-Zn ferrites with lesser voids, larger grains, and higher density and gives hardness to the bulk materials.

Reports show that $Mn_{0.6}Zn_{0.4}Fe_2O_4$ ferrite has a better combination of electrical and magnetic properties [72] among various combinations of Mn-Zn ferrites. The d.c. resistivity of indium doped Mn-Zn polycrystalline ferrite has been investigated as a function of composition, temperature, applied voltage by Rao.et.al in 1980 [73]. Furthermore, Pannaparayil et.al [74] showed the usefulness of Mn-Zn ferrites in electrical and electronic inductors, especially in high frequency applications up to 10 MHz.

The magnetic susceptibility of $Mn_{(1-x)}Zn_xFe_2O_4$ with $0<x<0.20$ ferrite system has been studied by Mazhar-ur-Rana et.al. [75] using a mutual inductance technique in the temperature range 255 to 600K. It was found that, at temperature above 450 K, the susceptibility follows a Curie Wiess behavior with negative Curie temperature and below 450K shows marked deviation from Curie law.

The modern trend in ferrites involves the study of disordered magnetic phases [76-78]. As reported by Dorman et.al., a randomly ordered structure appears in two magnetic sub lattice system, due to random substitution of non magnetic ions. It has been reported that magnetization in nanomagnetic material is reduced due to canting (disorder) at high temperature from which complex properties arise.

X- ray diffraction study of the cation distribution in the MnZn ferrites was carried out by Abbas et. al [79] . According to these investigators, structural study of a spinel should involve the determination of the lattice parameters, the oxygen positional parameters and the cation distribution at the tetrahedral and octahedral sites. The studies of these parameters show that in $Mn_xZn_{(1-x)}Fe_2O_4$, lattice constant increases with increase in Mn concentration

[79]. It has been observed that Zn^{+2} ions prefer the tetrahedral sites in the spinal structure.

Study of cation distribution of Mn-Zn ferrite using Mossbauer spectra was done by S.M. Attia [80]. Analysis of Mossbauer spectra shows that Zn^{+2} ions preferably occupy A-site while Mn and Fe ions are distributed between A-and B- sites. Existence of superparamagnetic and magnetically ordered particles in the Mn-Zn ferrite samples at different temperatures are also studied by different researchers [81-83] using Mossbauer spectra. It is reported that, population of magnetically ordered particles is more in the samples at lower temperatures compared to the room temperature.

Neutron diffraction studies have been also carried out to determine the magnetic structure and cation distribution in $MnFe_2O_4$ nanoparticles [84]. The magnetic structures for these materials clearly indicate antiferromagnetic exchange nature for the magnetic coupling between tetrahedral and octahedral lattice sites. The temperature dependent magnetization of nanoparticle manganese ferrites using Super conducting quantum interference device (SQUID) investigated by Chao Liu and Z. John Zhang [85] shows that the blocking temperature of these samples increases with increasing mean size of the particles and decreases with increase in applied field. This is attributed to the interplay of both thermal activation and applied magnetic field to overcome the magnetic anisotropy barrier. [85]

Electrical transport properties of Zn substituted Mn ferrite has been studied by Ravinder and Reddy [86]. Ravinder and his coworkers [87,88] observed that the values of electrical conductivity of Mn-Zn ferrites vary from $2.28x10^{-9}ohm^{-1}cm^{-1}$ to $6.82x10^{-6}ohm^{-1}cm^{-1}$. They have also investigated the

thermoelectric power characteristics of cerium substituted Mn-Zn ferrites from the room temperature to well beyond the Curie temperature by different methods. It was observed that the Seeback coefficient is negative for all the compositions showing that these ferrites are n-type semiconductors. On the basis of these results, an explanation for the conduction mechanism in Mn-Zn-Ce mixed ferrites was suggested.

In ferrites, the metallic ions occupy two crystallographically different sites namely octahedral (B) and tetrahedral (A) sites. Three types of magnetic interactions are possible between metallic ions, through the intermediate O^{2-} ions by superexchange mechanism. These are A-A interactions, A-B interactions and B-B interactions [89]. Interaction energy between the two metallic ions Me^{I} and Me^{II} depends upon two factors.

1) Distance 'r' of this ions from oxygen ions

2) Angle ϕ between Me^{I}-O- Me^{II} ions

Based on the distance and angle φ it is concluded that A-B interaction is strongest and A-A is weakest. For A-B interaction the angle A-O-B is fairly large and r is small. But for A-A interaction the angle A-O-A is small and r is comparatively large

A – O – A =79º, B – O – B =90º and A – O – B =125º

Interaction is stronger when angle between Me^{I}-O- Me^{II} is between 126^{0} to 154º.

In general magnetic moment on B sites (M_B) is greater than the magnetic moment on A sites (M_A). Therefore the resultant saturation magnetization is given by $Ms = M_B - M_A$ [90].

Magnetic characteristics of ferrites depend upon the concentration of magnetic and non-magnetic ions in mixed ferrites [91].

In $Zn^{+2}{}_xFe_{(1-x)}{}^{+3}[Fe^{+3}{}_{(1+x)}Mn_{(1-x)}{}^{+2}]O_4$, Zn^{+2} is non magnetic and Mn^{+2} is magnetic ion. With the addition of small concentration of non-magnetic Zn^{+2} ion, saturation magnetization of mixed ferrite is found to increase. This Phenomenon can be easily explained on basis of Neel's theory of ferrimagnetisms [92]. But at higher concentration of Zn ions, deviations occur due to the weakening of A-B interaction and the consequent stronger B-B interaction. Though an increase in the value of Ms is observed with the substitution by divalent non-magnetic ions, the Curie temperature is decreased, as the reduced value of M_A weakens the A-B interaction, which is responsible for the observed ferrimagnetisms. Therefore it is clear that in spinel ferrites, the value of magnetization and of Curie temperature can be conveniently varied by suitable variation in composition.

It is reported that the factors responsible for the variation of magnetization with temperature are (1) the magnitude of sub lattice magnetization. at 0^OK. and (2) the ratio of the magnitude of exchange interaction between (A-A, B-B & A-B)

Both M_A and M_B decrease with temp. Therefore Ms also decreases with temperature, the dependents of M_A and M_B on temperature is complex. Magnetization due to A lattice is not much affected by temperature and decreases slowly and drops to zero sharply at curie temperature but B lattice magnetization falls steeply at low temperature and approaches to zero slowly [89].

The cation distribution in a spinel ferrites is based on factors such as i) electrostatic energy due to repulsion and attraction between the anions and cations, ii) anion polarization energy, iii) electronic configuration and crystal field stabilization energy, iv)ordering energy between different ions on the same sublattice which results in gain of electrostatic energy and v) magnetic ordering energy. The site preference for individual cations is generally expressed in terms of particular site stabilization energy i.e. crystal field stabilization energy (CFSE).

Theoretical values of CFSE for various ions were calculated by Maclure [93], Dunitz and Orgel [94]. These values explained the site preference by the cations in the spinel to a good approximation. Miller [95] extended CFSE calculations incorporating Madelung constant, as well as, short range Coulomb and valence energy terms. It was shown that from site preference energies it is possible to predict the ionic distribution in the spinels.

E. J. W. Verwey and T. J. H. de Boer proposed that the electrical conductivity of spinel ferrites is known to be low as compared to other magnetic materials. Low resistivity in ferrites is caused in particular by simultaneous presence of ferrous and ferric ions on equivalent lattice sites [96]. This factor is responsible for the wide use of ferrites at microwave frequencies. A. Broese and other researchers [97, 98] concluded that, Spinel ferrites in general are semiconductors with their conductivity values varying between 10^{2} and $10^{-11}ohm^{-1}cm^{-1}$. The variation of resistivity and thermoelectric power with temperature of manganese ferrite was studied by Rosenberg et.al. [99] who observed ferromagnetic transition near Curie temperature. Simsa and Simosova [100] have studied high temperature

behavior of electrical conductivity and seeback effect in $MnFe_2O_4$ single crystal. The influence of cation migration between the tetrahedral and octahedral sites of spinel lattice on electrical properties of manganese ferrite was demonstrated.

L.R. Maxwell [101] has reported that the conduction mechanism in ferrites is quite different from that in semiconductors. The resistivity of ferrites is very sensitive to temperature. Ferrites are insulator but they show semiconductor like behavior with the rise of temperature. Their resistivity varies with temperature according to Arrhenius equation $\rho = \rho_o \exp(-\Delta E/kT)$ [102]

Where, ρ_o = Temperature dependent constant, ΔE = activation energy,

K = Boltzmann constant and T = Absolute temperature.

Invariably the resistivity of ferrites has been explained on the basis of Hopping model and Polaron model.

Jonker [103] derived an expression for mobility from hopping conduction model, based on the localized levels for electrons. Band Polaron model was suggested [104] to supplement explanation of resistivity which is based on electron transition between localized cells. Small Polaron model was also introduced to explain resistivity by Haubenreisser [105]. Lorentz and Ihle [106,107] have explained the electrical properties on the basis of thermally activated motion of electrons. Electrical properties of ferrites have been explained by Srinivasan and Srivastava [108], on the basis of tunneling of electrons amongst Fe^{+2} and Fe^{+3}atoms on B sites.

Investigations done on ac susceptibility of nanoparticle Mn-Zn ferrite, reported by some workers [109, 110, and 111] found co-existence of multidomain (MD), single domain (SD) and super paramagnetic (SP) particles in the material.

Thermoelectric measurement usually describes the conduction mechanism in semiconductors and ferrites. S. Mandal, D. Banerji and others [112] have suggested two methods of thermopower measurements, i) Integral method, ii) Differential method. D. P. Rao, B. Ramesh, P. R. M. Rao and others reported that the thermo e.m.f. is proportional to the difference in temperature (ΔT) at the two ends of specimen and is given by the relation $Vs=Q*(\Delta T)$, where 'Q' is the seeback coefficient[113]. Srinivasan and Srivastava [114] have reported that the Seebeck coefficient for cubic system, Q = total number of iron on B- site / total number of Fe^{2+} ions on B- site.

A survey of the literature reveals that studies of thermoelectric power in Mn-Zn ferrites are very limited. However some studies were reported [115–117] for Li-Zn, Li-Cd and Li-O ferrites. D. Ravinder and Latha [118] have reported that substitution of Zn in Mn-Zn ferrite resulted in a continuous decrease of thermoelectric power (Q) with the increase in Zn concentration. Variation of thermo electric power with temperature was observed by several investigators in various ferrite systems [119-122].

S. Mahalakshmi, S. A. Mazen and others have reported that the dielectric properties of ferrites depend upon method of preparation, chemical composition, Temperature, frequency and grain size [123, 124].

Koops gave a phenomenological theory of dispersion [125], based on Maxwell-Wagner interfacial polarization model for inhomogenous dielectric

structure. This model explains a strong dispersion in dielectric constant ε and a relaxation peak in dielectric loss at low frequencies. N. Rezlescu and F. Rezlescu [126] studied the composition, frequency and temperature dependence of copper containing mixed ferrites such as copper manganese ferrites and copper zinc ferrites. They have explained the composition dependence of the dielectric constant by making the assumption that the mechanism of dielectric polarization is similar to conduction process. It was concluded that electron exchange between Fe^{+3} and Fe^{+2} results in local displacement of charges in the direction of electric field; which determines the polarization of the ferrites. C.B. Korekar and others have reported that the magnitude of electronic exchange depends on ratio of Fe^{+3} and Fe^{+2} ions present in Octahedral B sites [127].

Rabinkin and Novikova observed that the electronic exchange between Fe^{2+} and Fe^{3+} results in local displacements of charges in the direction of electric field which determine the polarization of the ferrite. [128]. A similar interpretation was proposed by Reddy and Rao [129] for the nickel substituted lithium ferrites. Ramana Reddy et al (1999) have investigated the dielectric behavior of Ni-Zn ferrites as a function of temperature and frequency [128]. Iwauchi (1971) reported a strong correlation between the conduction mechanism and the dielectric behavior of the ferrites [128].

Globus [130,131] has developed a model for initial permeability which relates reversible domain wall motion under very small magnetic field to initial permeability, neglecting the contribution of the spin rotation as it is negligible. Globus and co-workers [131,132] in their later work realized that in polycrystalline ferrites the magnetization mechanism might be different due

to granular structure of ferrites. Johnson has developed the non-magnetic grain boundary model [133]. This model accounts for the grain size dependence of μ_i, at low anisotropy. Smit and Wijn [134] have explained the extension of the total power loss over a relatively broad frequency region in terms of additional effects upon the resonance condition due to demagnetizing field in the domain structure.

Some studies [135–137] have been reported on the effect of nonstoichiometry on the magnetic properties of nanoparticle MnZn ferrites. Morita and Okamoto [135] reported that the initial permeability (μ_i) of $(Mn_{0.215}Zn_{0.082}Fe_{0.703})_{(3-\delta)}\ O_4$ ferrite increased with increasing nonstoichiometry (δ). Tanaka [136] investigated the initial permeability of MnZn ferrites with different nonstoichiometry to find that the initial permeability at low frequencies either decreased or showed a maximum with increasing nonstoichiometry (δ) based on cationic composition. Inaba [137] reported that the initial permeability of $(Mn_{0.227}Zn_{0.087}Fe_{0.697})_{(3-\delta)}\ O_4$ becomes maximum at the stoichiometric composition (δ=0) and explained it on the basis of point defects. Tanka (1975) studied the effects of oxygen non stiochiometry as well as composition on several magnetic and mechanical properties of MnZn ferrites. In a later paper (1978), he looked at effects of oxygen non-stiochiometry on initial permeability, the frequency and temperature responses of initial permeability, as well as on the domain structure [136].

Power loss studies on Mn-Zn ferrites done by C. Guillard (1957) showed that addition of CaO to the ferrites in small quantities, could produce significant decrease in power losses. This decrease in losses has been attributed to the large reduction in the eddy current in the ferrite cores.

Thus, in-depth literature survey carried out has provided valuable information about different researchers who have synthesized nanoferrites and the bulk ferrites using different methods and studied the same. Most of the workers have used metal salts to prepare nanoparticle Mn-Zn ferrites and have shown that the electrical and magnetic properties of nanoferrite material depend on the composition, method of preparation and particle size. Some workers have prepared bulk Mn-Zn ferrite materials from metal oxides using conventional ceramic method. Many researchers have used conventional ceramic method of preparations of ferrites. In this case the resultant products are not necessarily stoichiometric and homogeneous on microscopic scale and do not always results in reproducible products. There is also possibility of presence of un-reacted phases in the finished product. This also results in loss of fine particle size. Thus it is evident that there is lot of scope for preparing Mn-Zn ferrite nanoparticles using new and innovative methods. The wet chemical method of preparation overcomes the drawbacks of conventional ceramic methods.The wet chemical method of preparing nanomaterials wherein metal salts like nitrates, carbonates, sulphates etc are used, is sometimes tedious and time consuming process. It is reported that there are other process of preparing nanoferrites, but the methods are not simple and are difficult to scale up.

Thus, it was felt to go for a new method of preparation of ultrafine MnZn ferrite material which is cost effective, simple and yield highly homogeneous nanocrystalline Mn-Zn ferrite materials at a lower reaction temperature. The mechano-chemical autocombustion method of synthesis of MnZn ferrites using metal oxides as starting materials developed has been

described and discussed in the next chapter. This method is innovative, newly evolved and found to give good quality fine particles (nano size) ferrites.

References

[1] C. Kittel, Introduction to solid state Physics, 7th ed, John Wiley and Sons Inc., 1996.

[2] A. H. Morrish, P. E. Clark, Phys. Rev. B 11 (1975)278.

[3] J. Ding, W. M. Miao, P. G. McCormick, R. Street, Appl. Phys. Lett. 67 (1995) 3804.

[4] J. Campbell, W. A. Kaczmarck, G. Wang, Nanostruct. Mater. 6(1995) 735.

[5] J. Wang, C. Zeng, Z. Peng, Q. Chen, Physica B 349(2004) 124.

[6] C. Rath, K. K. Shahu, S. Anand, S. K. Date, N. C. Mishra, R. P. Das, J. Magn. Magn. Mater. 202 (1999) 77.

[7] S. Lorentzou, K. Karadimitra, C. Agrafiotis and A. G. Konstandopoulos, partec, 2004.

[8] P. C Fannin., S. W Charles. and J. L. Dormann, J. Magn. Magn. Matter. 201(1999) 98.

[9] T. Pannaparayil, S. Komarneni, R. Marande and M. Zadarko , J. Appl. Phys. 67(1990) 5509.

[10] Z. Yue, J. Zhou, L. Li, H. Zhang and Z. Gui., J. Magn. Magn. Matter, 208 (2000) 55.

[11] M. Mozafari, F. Ebrahimi, S. Danishfozon, J. Amighian, Journal of Alloys and Compounds 449(2008) 65-67.

[12] Z. G. Zang, X. C. Zhong, Y. H. Zhang, Y. H. Yu, D. C. Zeng, Journal of Alloys and Compounds 466(2008) 377-382.

[13] D. Arcos, R. Valenzuela, M. Vazquez and M. Vallet-Regi, Journal of Solid State Chemistry 141(1998)10-16, Article No. SC987882.

[14] E. P. Wohlfarth, Ferromagnetic materials (North Holland Publishing Co.) Vol. 1 and 2, 1980.

[15] G. Vaidyanathan, R. Arulmurugan, S. D. Likhite, M.R. Anantharaman, Milind Vaidhya, S. Sendhilnathan, N. D. Senthilram, Indian Journal of Engineering and Material Science,Vol.11(2004) 289-294.

[16] K. C. Patil, S. Sudar Manoharan and D.Gajapathi, 'Handbook of Ceramics and Composites' (eds. Nicholas P.Cheremisinoff, Marcel Dekker, INC, New York) vol. 1 pp.469.

[17] S. Hilpert, Ber. Deut. Chem.Ges., 42 (1909) 2247.

[18] Y. Kato and T. Takei, J. Institute of Electrical Engineers, Japan, 53 (1953) 408.

[19] H. Forestier, Ann. Chemie Xe Series Tome, 9 (1928)353.

[20] T. F. Barth and E. Posnjac, Z. Krist, 82 (1952) 325.

[21] E. J. W. Verwey, P. W. Haayaman, F. C. Romejin and G. W. Van Cosferhout Phil, Res. 173 (1950)

[22] L. Neel, Proc. Soc. London A-65, 869 (1952)

[23] P. W. Anderson, Phys. Rev. 79 (1950) 350

[24] J. H. Van-Vleck, Phys. Rev. 78 (1950)266

[25] Y. Yafet, C. Kittel Phys. Rev. 87 (1952)290

[26] J. L. Snoek in 'New Development in Ferromagnetic Materials' Elsevier Press. Inc, New York. (1947).

[27] C. G. Koops, Phys. rev., 83 (1951) 121.

[28] Ramachandra Bhat, H. V. Keer, P. Raj, A. Sathamoorty, ICF-5(1989) 49-53.

[29] E. Auzans, D. Zins, R. Massart, J. Mater. Sci. 34 (1999)1253.

[30] M. Rozman, M. Drofenic, J. Am. Ceram. Soc. 78 (1995) 2249.

[31] A. Thakur, M. Singh, Ceram. Int. 29 (2003) 505.

[32] D. Makovec, A. Kosak, M. Drofenic, Nanotechnology 15 (2004) 160.

[33] Xian- Ming Liu, Shao-Yun Fu, J. Magnetism and Magnetic materials 308 (2007) 61-64.

[34] Shunli Hao, Xin Wang, Yu Wei, Yongming Wang and Chunjing Liu, Vol. 25, issue 6, Supplement 1 (2006) 466-470.

[35] F. Li, J. J. Liu, D. G. Evans, X. Daun, Chem. Mater, 16 (2004) 1597.

[36] J. Leu, F. Li, D. G. Evans, X. Daun, Chem. Commen. 4 (2003) 242.

[37] W. Meng, F. Li, D.G. Evans, X. Duan, Mater. Chem. Phys. 86 (2004)1.

[38] P. Ravindranathan, K. C. Patil, Bull Amer, Ceram. Soc. 66, 4(1987)688-692.

[39] P. Ravindranathan, K. C. Patil, J. Mater. Sci. 22: 3261 (1987).

[40] S. Sunder Manoharan, K.C. Patil. Proc. ICF-5 India (1989) 43-47.

[41] T. Abhas, M.U. Islam, M. Ashraf Ch., Mod Phy. Letts. 9,22, (1995) 1419-1426.

[42] K. Tanaka, Y. Nakahara, K. Hirao, N. Soga, J. M. Ag. Mag. Mater.131 (1994) 120-128.

[43] L.G. van Uitert, J. Chem. Phys. 24 (1956) 20.

[44] A. B. Niak, J. I. Power, Indian J. Pure and Appl. Phys, 23 (1985)436-437

[45] J. Smith, H. P. J. Wijn "Ferrites", J. Wiley and Sons, New York (1959)155-156.

[46] H. T. Hahn, J. Appl. Phys. 69(8) (1991)6195-6197.

[47] T. Pannaaparayil, R. Marande and S. Komarneni, J. Appl. Phys. 69(7) (1991)5349.

[48] K. Suresh, K. C. Patil, Proc., ICF-5 (1989)103-107.

[49] Jan Verweel. IEEE. Trans. Magn. MAG-5, 3(1988)pp.622.

[50] Z. X. Tang, C. M. Sorensen, K. J. Klabunde and G. C. Hadjipanayis, J. Appl. Phys. 69(8), (1991).

[51] R. S. Tebble and D. J. Craik, "Magnetic materials", John Wiley and Sons, New York, (1969).

[52] R. Justin Joseyphus, A. Narayanasamy, B. Jeyadevan, K. Shinoda1 and K., Tohoko- University, Japan, 51-53 , (2004).

[53] Tohji1 Jiwei Fan, N.G Foong-Kee, R. Frank Sale, Rare Matals, Vol. 25, 6(2006) 445-449.

[54] H. Inaba, T. Abe, Y. Kitano, J. Shimomura, Journal of Magnetism and Magnetic materials, Vol. 133, 1-3,(1994) 487-489.

[55] Y. Yamamoto, A. Makino, J. of Magnetism and Magnetic materials, vol. 133, 123, (1994) 500-503.

[56] S. G. Dahotre et al Arch. Phy. Res., 2 (1)2011 81-89.

[57] A. C. Razzitte, S. E. Jacobo, and W. G. Fano J. Appl. Phys. 87, (2000) 6232.

[58] M. I. Rosales, A. M. Plata, M. E. Nicho, A. Brito, M. A. Ponce and V. M. Castano, J. Mater. Sci., 30 (1995)4446-4450.

[59] I-Nan Lin, R. K. Mishra and G. Thomas, IEEE. Trans. Mag. 18 (1982) 1544-1546.

[60] A. Gobus and R. Valenzuela, IEEE. Trans. 11(1982)1300.

[61] S. H. Chen, S. C. Chang, I-Nan Lin, M. J. Tung and W. B. Shu, IEEE. Trans. Magn. 28 (1992)2436.

[62] R. L. White, J. Appl. Phys. 40 (1969)1061.

[63] E. Takama, S. Mishima and S. Kawahara, J. Physique Cl. 38, 349(1977).

[64] T. Takada and M. Kiyama, Proc. ICF. Edited by Y. Hoshino, S. Iida, M. Sugimoto (1971) p. 71.

[65] Y. Schichijo and E. Takama, ibid p. 210.

[66] Z. Krysicki , T. Lubanska, J. Mag. Mater. 19 (1980)107-108.

[67] F. J. C. M. Toolennar, M. T. J. Van Lierop- verhees, J. Mater.Sci. 24 (1989)402-408.

[68] ibid- J. Mater. sci. 23 (1988)856.

[69] M. N. Rahman, L. C. de Jonghe, J. Amer, Ceram, Soc. 76(1993)1739-1744.

[70] M. Sugimoto, AIP. Conf. Proc. No. 10. part-2 (1972)1335-1349.

[71] Hj. Mustaffa- Abdullah, Sahrim-Hj, Ahmad, Sains-Malaysiana, 22(2) (1993) 1-7.

[72] J. Smith and H. P. J. Wijn, “Ferrites” John Wiley and Sons, NewYork, 1959.

[73] K. H. Rao, S. B. Raju, R. G. Gupta and R. G. Mendiratta, Solid state communication, 36 (9). (1980) 777-780.

[74] T. Pannaparayil, R. Marande, Journal of Applied Physics, 69, 8(1991).

[75] Mazhar-U-Rana, Tr. Journal of Physics, 19(1955) 1137-1144.

[76] J. L. Dorman, Hyperfine interactions 68(1991) 47-58.

[77] J. L. Dorman, Journal of Phys Codens Matter 2 (1990) 1223-1237.

[78] J. L. Dorman, Solid state Phys. 20(1987) 161-166.

[79] Tahir Abbas, Solid state Communication, 82(9), (1992) 701-703.

[80] S. M. Attia, Egypt. J. Solids, Vol. (29),No.(2), (2006).

[81] M. Petrera, A. Gennaro, N. Burriesci, Journal of Material Science 17 (1982) 429-437.

[82] P. Muthukumarasamy, T. Nagarajani and A. Narayanasamy, J. Phys. C: Solid State Phys., 15 (1982) 2519- 2528. Printed in Great Britain.

[83] R. Justin Joseyphus, A. Narayanasamy, K. Shinodab, B. Jeyadevan, K. Tohji, Journal of Physics and Chemistry of Solids 67 (2006) 1510–1517.

[84] Chao Liu, Bingsuo Zou, Adam J. Rondinone and Z. John Zhang, J. of Physical ChemistryB,Vol.104,No.6, (2002)pp 1141-1145.

[85] Chao Liu and Z. John Zhang, Chem. Mater., 13, (2001)2092-2096.

[86] D. Ravinder and A. V. Ramana Reddy, Materials Letters, 38 (4), (1999) 265-269.

[87] D. Ravinder and B. Ravi Kumar, Material Letters, 57(11), (2003) 1738-1742.

[88] D. Ravinder and B. Ravi Kumar, Materials Chemistry and Physics, 82 (2), (2003) 321-326.

[89] B. Vishwanathan, V. R. K. Murthy. Ferrites materials, Science and Technology, Narosa Publishing House, 1990.

[90] E. W.Gorter, Philips Res. Rept. 9 (1954) 321.

[91] K. J. Standley, 'Oxide Magnetic Materials' (Oxford: Claredon Press, 1972).

[92] L. Neel, Ann.Phys. 3(1948)137.

[93] D. S. Maclure, J. Phys. Chem. Solids, 3 (1957) 311.

[94] J. D. Dunitz and L. E. Orgel, J. Phys. Chem. Solids, 3 (1957)20.

[95] A. Miller, J. Appl. Phys. 30 (4) (1959) 245.

[96] E. J. W. Verwey and T. J. H. de Boer, Rec. Traw. Chim. Phy. Bas; 55; 531(1936).

[97] J. Smith and H. P. J. Winj, "Ferrites" Philips Tech, Libr, Eindhovel, The Netherlands, (1959)137.

[98] A. Broese van Groenev, P. F. Bongers and A. L. Stuyts, Materials Science and Engineering, 3(1968-69) 317.

[99] M. Rosenberg, P. Nicolau and I. Bunget, Phys., Stat. Sol., 4, K 121(1964)

[100] Z. Simsa and J. Simosova, Czech. J. Phys., B24, 439(1974).

[101] L. R. Maxwell and S. J. Pickart, Phys. Rev. 96 (1954) 1501.

[102] E. J. Verway, Heilman, J. Chem. Phys. 15 (1947) 174.

[103] G. H. Jonker, J. Phys. Chem. Solids, 9, (1959) 165.

[104] R. R. Dogoadge, A. A. Cherenko and A. Chimodzhev Yu, Sov, Phys. Solid State, 3, (1961)2698.

[105] W. Haubenreisser, phys. Stat. Solidi, 21, (1961)390S.

[106] B. Lorentz and D. Ihle, Phys. Stat. Solidi, 63, (1974)599.

[107] B. Lorentz and D. Ihle, Phys. Stat. Solidi, 69, (1975)451.

[108] G. Srinivasan , C. M. Srivastava, Phys. Stat. Solidi (b) 108 (1981)665

[109] C. Radhakrishnamurthy, J. Goel Soc. India 26 (9) (1985) 640.

[110] R. V. Upadhyay, G. J. Baldha and R. G. Kulkarni, Mater.Res.Bull. 21 (1986) 1015.

[111] G. J. Baldha and R. G. kulkarni, Solid Stat. Commun. 53 (1985) 11.

[112] S. Mandal, D. Banerji, R. N. Bhattacharya and A. A. Ghosh, J. Phys; Condence Matter 8, (1996), 2865-2868.

[113] A. D. P. Rao, B. Ramesh, P. R. M. Rao, S. B. Raju, Journal of Material Science 34 (1999) 621– 623.

[114] G. Srinivasan , C. M. Srivastava, Phys. Stat. Solidi (b) 108 (1981)665

[115] D. Ravinder, Cryst. Res, Technol 27 (4) (1992)545.

[116] D. Ravinder, S. Rao, Cryst Res., Technol, 25(8) (1990)963.

[117] J. M. Song and J. G. Koh, J. Mag and Matter. 152 (1996) 383.

[118] D. Ravinder and Latha, J. Appl. Phys. 75 (10) (1994) 6118.

[119] D. Ravindar, J. Alloys Compd. 291 (1999) 208.

[120] T. E. Wall, N. Saleno, Y. G. Proykova, K. A. Mirza and S. Mazen, Phil. Mag. B 53 (1986) L107.

[121] D. Ravinder, Material Letters 43 (2000) 129.

[122] Md. Abdul Malk, V. D. Reddy, P. Venugopal Reddy, D. R. Sagar and Prankishan, Mod. Phys. Letts.16 (1994) 947.

[123] S. Mahalakshmi, K. S. Manja, J. All. Comp. vol. 457(2008) 522.

[124] S. A. Mazen, S. F. Mansour, E. Dhahri, H. M. Zaki, A. Elmosalami, J. All. Comp. vol. 470(2009)294.

[125] C. G. Koops, Phys. rev., 83 (1951) 121.

[126] N. Rezlescu, F. Rezlescu , Phys. Status. Solidi. A 23, (1974) 575

[127] C. B. Korekar, D. N. Kambli, S. G. Kulkarni and Varangankar, Journal of material science,30(1995)5784.

[128] D. Ravinder and K. Vijaya Kumar, Bull Mater. Sci., Vol. 24, No. 5, (2001) pp. 505-509.

[129] P. V. Reddy, T. S. Rao, J. Less- Common Met, 86 (1982) 255.

[130] A. Globus J. Physique Coll., Cl (1963) C1.1-C1.15.

[131] A. Globus Cardiff Conf.USA, (1975).

[132] A. Globus and P. Duplex Phys. Stat Solidi, 31 (1968) 75.

[133] M. T. Johnson and E. G.Vissar IEEE Trans. Magn. MAG-26 (1990) 1987.

[134] J. Smit and H. P. J. Wijn “Ferrites” John Wiley, New York, (1959).

[135] A. Morita and A. Okamoto, Ferrites-Proceedings of the Third International Conference on Ferrites ~Japan Society of Powder and Powder Metallurgy, Tokyo, (1980) pp. 313–316.

[136] T. Tanaka, Jpn. J. Appl. Phys. 17, (1978)349.

[137] H. Inaba, J. Am. Ceram. Soc. 78, (1995)2907.

CHAPTER III

PREPARATION OF MATERIALS

3.1 INTRODUCTION

Material scientists have made significant contributions in development of novel and convenient methods of synthesis of ferrite nanomaterials. As mentioned in Chapter one, Mn-Zn ferrite materials belong to technologically important class of oxide compounds. Accordingly, a major focus of research has been in development of newer methods of synthesis of these materials and also fabrication processes leading to their better performance. Standardization of methods for tailor-made materials of the desired structure and properties is the main aim of material scientists, which may sometimes be difficult to achieve. But one can always evolve a rational approach to the synthesis of solid material [1].

3.2 PREPARATION OF MAGNETIC NANOMATERIAL

Numerous physical and chemical routes have been tried and standardized to synthesize ferrite nanoparticles. Ceramic method, Electrochemical method, Hydrothermal [2,3] method, Co-precipitation [4,5] method, Sol-gel [6] method, Vapour phase method, Chimie-Douce method, Precursor [7] method, Plasma Synthesis, Reverse Micelle technique, water CTAB, Microemulsion method- are some of the most commonly used methods of preparation of ferrites.

3.2.1 Ceramic Method

This is one of the common methods employed for preparing mixed metals oxides and other solid materials. This method requires very high

temperatures, which are generally attained by resistance heating [8] and therefore may affect the fineness of the product material thus produced [9]. The procedure involves grinding of powders of oxides, carbonates, oxalates or other compounds containing the relevant metals in appropriate proportions; followed by heating of the mixture at a desired temperature, generally after palletizing the material. Several mixed metals sulphides, oxides, phosphides materials have been prepared by this method. Platinum, silica and alumina containers are used for the synthesis of oxide materials, while graphite containers are used for sulphides and other chalcogenides.

This method has many disadvantages. There is no simple way of monitoring the progress of reaction in ceramic method. It is only by trial and error that one decides on appropriate condition that leads to the completion of the reaction. Because of this difficulty, there is no phase purity of the product. One frequently ends up with mixtures of reactants and products. Separation of the desired product from such mixtures is generally difficult. Also sometimes it becomes difficult to obtain the compositionally homogeneous products by the ceramic techniques even if the reaction proceeds almost to completion [8].

3.2.2 Electrochemical Method

Electrochemical methods have been employed for the synthesis of many solid materials. Typical materials prepared in this manner are metal borides, carbides, silicides, oxides and sulphides. Vanadate spinels of the formula MV_2O_4 as well as tungsten bronzes, A_xWO_3, have been prepared by electrochemical method. Tungsten bronzes are obtained at the cathode when current is passed through two inert electrodes immersed in a molten solution of alkali metal tungstate, A_2WO_4 and WO_3, Oxygen is liberated at the anode

[10]. Oxides containing metals in high oxidation states are conveniently prepared electrochemically. Superconducting $La_2CuO_{(4+\delta)}$ has been recently prepared by electro chemical oxidation [11]

3.2.3 Spray Pyrolysis Method

In this process, microsized liquid droplets of precursor or precursor mixture are converted into solid particles through heating. In practice spray pyrolysis involves several steps: (i) generating microsized droplets of liquid precursor or precursor solution, (ii) evaporation of solvent, (iii) condensation of solute, (iv) decomposition and reaction of solute, and (v) sintering of solid particles [12].

3.2.4 Hydrothermal Method

One of the techniques in synthesis of materials is hydrothermal oxidation. The method is based on the fact that many oxides are soluble in an alkali solution. The method has been most successfully applied to prepare ferrites. The advantage in the hydrothermal method is that it permits the recrystallization of the powder. It is also possible to monitor the grain size and shapes. However this method is time consuming.

Hydrothermal synthesis can be defined as a method of synthesis of single crystals that depends on the solubility of minerals in hot water under high pressure. The crystal growth is performed in an apparatus consisting of a steel pressure vessel called autoclave, in which a nutrient is supplied along with water. A gradient of temperature is maintained at the opposite ends of the

growth chamber so that the hotter end dissolves the nutrient and the cooler end causes seeds to take additional growth.

Possible advantages of the hydrothermal method over other types of crystal growth include the ability to create crystalline phases which are not stable at the melting point. Also, materials which have a high vapour pressure near their melting points can also be grown by the hydrothermal method. The method is also particularly suitable for the growth of large good-quality crystals while maintaining good control over their composition. Disadvantages of the method include the need of expensive autoclaves, and the impossibility of observing the crystal as it grows.[13].

3.2.5 Co -precipitation Method

In Co-precipitation method, the required metal cations, taken as soluble salts (e.g. nitrates), are coprecipitated from a common medium, usually as hydroxides, carbonates, oxalates or citrates. In actual practice, one takes oxides or carbonates of the relevant metals, digests them with an acid and then the precipitating reagent is added to the solution. The precipitate obtained after drying is heated to the required temperature in appropriate atmosphere to produce the final product. The decomposition temperatures of the precipitates are generally lower than the temperatures employed in the ceramic method. If all metal ions do not form insoluble precipitates, it becomes difficult to control the stoichiometry.

Co-precipitation is a very simple method for the synthesis of powders. There are two co-precipitation routes possible for the preparation of Mn-Zn ferrites:

(i) The calcination route. The co-precipitation of hydroxides of Mn^{2+}, Zn^{2+} and Fe (usually Fe^{3+}) in the first stage is followed by calcination of the hydroxide precursors in the second stage:

$$\tfrac{1}{2}\,Mn^{2+} + \tfrac{1}{2}\,Zn^{2+} + 2Fe^{3+} + 8OH \rightarrow \tfrac{1}{2}\,Mn(OH)_2 + \tfrac{1}{2}\,Zn(OH)_2 + 2Fe(OH)_3$$

$$\xrightarrow{600^{\circ}C} Mn_{0.5}\,Zn_{0.5}\,Fe_2O_4 + 4H_2O$$

(ii) The oxidation of Fe (II) hydroxidetakes place. The co-precipitation of hydroxides of Mn^{2+}, Zn^{2+} and Fe^{2+} in the first stage is followed by the oxidation of Fe (II) hydroxide in the second stage, which directly results (in situ) in the formation of the spinel ferrite according to Shikorr's reaction [14]

$$\tfrac{1}{2}\,Mn^{2+} + \tfrac{1}{2}\,Zn^{2+} + 2Fe^{2+} + 6OH^{-} + \tfrac{1}{2}\,O_2 \rightarrow Mn_{0.5}\,Zn_{0.5}\,Fe_2O_4 + 3H_2O.$$

One of the drawbacks of the co-precipitation method is the difficulty of controlling the particle size and morphology. The problem of controlling the particle size and morphology during the synthesis is overcome by using a microemulsion method, which involves co-precipitation in water-in-oil microemulsions [15]. This method has been successfully used for the precipitation of spinels also [12].

3.2.6 Sol-gel Method

Sol-gel method is one of the most important methods of preparing inorganic oxides. It is wet chemical method and a multi step process involving both chemical and physical process such as hydrolysis, polymerization, gelation, drying, dehydration and densification. The name "Sol-gel" is given to the process because of the distinctive viscosity increase that occurs at particular point in the sequence of the steps. A sudden increase in viscosity is the common feature of the sol gel processing, indicating the onset of gel formation. In the sol-gel process, synthesis of inorganic oxides is achieved

from inorganic or organo-metallic precursors (generally metal alkoxides). The important features of the sol-gel method are better homogeneity compared to the traditional ceramic method, high purity, lower processing temperature, more uniform phase distribution in multi component systems, better size and morphological control [12] and possibility of preparing new crystalline and non crystalline materials.

3.2.7 Precursor Method

A precursor method involves preparation of an easily decomposable compound of metals and mixed metals, which yield the desired oxides on heating. One can obtain homogeneous, fine particle, high purity oxide materials from precursors. The preparation of ferrites from solutions of water soluble salts of the corresponding metals fall under wet chemical method category. These methods are reported to yield ferrite powders having molecular level homogeneity, smaller grain size, low porosity and larger surface area [16].

In the recent years, special focus has been placed on obtaining ferrite as a particulate environment through unconventional methods, especially chemical methods [17, 18, 19.]. There are many methods that can be used to obtain the systems consisting of nano-particles [20-25], but their application on a large scale is limited by their cost and the high purity of the starting materials.

3.2.8 Vapour Phase Method

Schafer in 1971 developed method of chemical transport via the vapour phase. This method is used for the synthesis of new compounds, for the

growth of single crystals or for the purification of a compound. This method is used for preparing binary ternary and quaternary compounds where the gas phase is used as a transporting agent and has influence on reaction rates. Gases react much more quickly than solids because mobilities are increased. In addition, the gaseous phase is often important in normal solid state reactions under isothermal conditions, where it may act as a rapid means of transporting matter from one crystal to another [12]

3.2.9 Chimie-Douce Method

Reaction takes place at much lower temperatures in precursor method compared to the normal solid state reaction procedures. Another use of precursor methods is in the synthesis of new, metastable phases which cannot be prepared by other routes. Although these phases are thermodynamically metastable they are often kinetically stable to quite high temperatures. There is a close structural relationship between the precursor phase and final product. Often new phases, therefore, have unusual structures and interesting properties. French have coined the term chimie-douce [12] for this method of preparation.

Crystallite sizes of the powder specimen can be obtained on calcinations at various temperatures. It is observed that the size increases with calcination temperature. As the calcinations temperature affects the particle size, all parameters like Curie temperature, permeability, saturation magnetization dielectric properties, resistivity etc. are also affected accordingly. The ferrites have gained importance due to their microstructures. The magnetic properties of Mn-Zn ferrites depend on the microstructures. The

microstructure of Mn-Zn ferrites is greatly influenced by sintering conditions as well; therefore it is extremely important to control the same.

Chemical methods of synthesis play a crucial role in designing and discovering new and novel materials and in providing less cumbersome methods for preparing known materials. Chemical methods also enable the synthesis of metastable materials, which are otherwise difficult to prepare.

3.2.10 Plasma Synthesis Method

This method yields nano size Mn-Zn ferrites [**26**]. Nanocrystalline powder of Mn-Zn ferrite has been synthesized using 50KW-3MHZ rf induction plasma torch. High energy ball milled (Mn + Zn) + Fe powders, <10 micrometers in size and in the stoichiometric ratio 1:2 were used as metal species in the plasma. Argon gas is used as plasma gas and plasma stream gas consists of mixture of argon and hydrogen gas. All precursor powder is injected through plasma jet stream by argon, a carrier gas. After the induction plasma is established, compressed air is also introduced in the reactor as an oxidizer [27-30]. This method of preparation is highly complex and involves complex systems.

3.2.11 Reverse Micelle Method

Reverse micelle technique is used to obtain manganese–zinc ferrite nanoparticles [31, 32]. Wet chemical synthesis performed in Reverse micelle, in which pools of water are encased by surfactant molecules in an excess volume of oil, provides the greatest control over size and morphology. During synthesis, surfactant molecules keep particles separated and restrict particle growth this keeps control on size and shape of particles. The basis for the technique is the use of a surfactant to stabilize varying aqueous droplet sizes in

hydrocarbon medium. Metal salt precursors are contained in the aqueous portion and are transformed by a reactant from the hydrocarbon phase. Both the structure of the surfactant and the steric size are able to produce metals having a wide range of grain sizes**.** In this synthesis, two reverse micellar solutions are prepared, the first using the metal solution and the second one using ammonium hydroxide. Stock solutions of 0.5 M sodium dioctylsulfosuccinate (AOT) are prepared in 2, 2, 4-trimethylpentane - isooctane! It has been observed that precipitation of metals is influenced by the pH and the electrochemical potential of the solution; therefore, the initial ratio of metal precursors is modified to account for the reduction of metals in the precipitate and subsequently in the fired samples.

In this method the micelle size can be controlled by the molar ratio of water to AOT, which is chosen to yield a fine particle size in namometer. The volume of aqueous solution and desired particle sizes are used to determine the amount of the precursor solution to be used. The ammonia solution is then added to the metal–salt solution under constant stirring. The reaction is allowed to proceed for about 2 hrs, until particle flocculation is induced by adding excess methanol. The particles are then collected using centrifugation and washed using methanol to remove excess surfactant, followed by a methanol-water solution to remove any additional unreacted ions. After final centrifugation, the material is dried overnight under a dynamic vacuum, and subsequently fired at 525 °C for 5 hrs. under inert atmosphere to obtain the required product.

3.2.12 CTAB Method

Magnetic Mn-Zn ferrite nanoparticles with a narrow size distribution can be prepared in water–CTAB–hexanol microemulsions [33]. In this, ferrite-nanoparticles are synthesized in the water pools of reverse micelles in a microemulsion system consisting of an aqueous phase, n-hexanol as the oil phase and n-hexadecyl trimethylammonium bromide (CTAB) as the surfactant. The synthesis of the magnetic ferrite occurs in situ with the coprecipitation of hydroxides of $Mn^{2+,}$ Zn^{2+} and Fe^{2+} ions in the first stage, followed by the oxidation of Fe(II) hydroxide in the second stage. The influence of the pH value after the precipitation of hydroxides on the nature of the product is determined.

The microemulsion containing an aqueous solution of the corresponding metal ions is mixed with a microemulsion containing an aqueous solution of precipitating agent. By varying the amount of the later microemulsion, different pH values between 4 and 13 can be set. The pH value needs to be approximately 8 and above to produce the spinel ferrite product after the oxidation of Fe (II) hydroxide; at lower pH values, FeOOH is obtained as the major product. Although the spinal product is obtained at room temperature, temperature has a large influence on the particle size [34]. Mn-Zn ferrite nano particles have been prepared with micro emulsion method using the coprecipitation routes i. e. calcinations [35,36] and oxidation of Fe^{+2} hydroxide [37,34].

The structural as well as magnetic properties of ferrite material have been found to depend upon particle size, which depends entirely on method of synthesis [38].

It may be observed that many of the methods briefed mentioned above yield nanoparticle ferrites. These methods involve sophisticated instrumentation techniques, require expensive high purity starting materials, constant monitoring of temperature and other preparative conditions, and are time consuming. Some of these methods involve use of ball-milling. In the present work, an alternate route for synthesis has been employed which uses low cost, moderate (AR) grade chemicals to yield Mn-Zn ferrite. Thus it was felt necessary to look for a simple alternate method to produce Mn-Zn ferrite fine particle using metal oxides as raw material. In the present study, $Mn_xZn_{(1-x)}Fe_2O_4$ (with x=0.4, 0.5,0.6,0.625,0.65.,0.675,0.7,0.8) ferrite material samples have been prepared by using oxides as starting material and a simple inexpensive auto combustion method, conveniently.

3.3 SYNTHESIS OF $Mn_xZn_{(1-x)}Fe_2O_4$ MIXED FERRITES:

Ferrite samples of Mn-Zn mixed metal oxides having general formula $Mn_xZn_{(1-x)}Fe_2O_4$ (where x = 0.4, 0.5, 0.6, 0.625, 0.65, 0.675, 0.7, 0.8) were synthesized by using mechano – chemical process. In this method stoichiometric amounts of oxides of Mn (i.e. MnO_2), Zn (i.e. ZnO), and Fe (i.e. Fe_2O_3), as given in the table 3.1**,** with purity of about 99.9 % were taken as starting materials. The mixture of these oxides was than ball milled with ball to material ratio of 10, in Acmos technocracy make model (ACM-8290), for 10 hours at a speed of 80 rpm. The ball milled mixture of oxides obtained was then treated with a predetermined amount of a carboxylate based aqueous ligand of dihydrazimium nitrilotriacetate, and it was homogenized to obtain a

thick paste. This dihydrazimium nitrilotriacetate precursor of mixed metals was slowly dried on a hot plate using conventional method of heating to obtain a dry paste. The dried paste was then ignited to form the desired products.

Titrimetric chemical analysis was carried out on all the samples to confirm the composition and to estimate the sample yield. Formation of the desired oxide materials was confirmed from the experimental yield of the samples in comparison to the theoretical values. The theoretically calculated yield as per the quantity of raw material taken and experimental yield based on actual quantity of sample obtained showed that there was negligible discrepancy. Percentage yield is calculated using the formula,

Percentage yield = (Experimental yield / Expected yield) x 100.

Experimental yield, expected yield and percentage yield for various compositions of $Mn_xZn_{(1-x)}Fe_2O_4$ samples are shown in Table. 3.2.

Table 3.1: Stiocheometric proportion of metal oxides.

Composition $Mn_xZn_{(1-x)}Fe_2O_4$	Molecular wt. of MnO_2	Molecular Wt. of ZnO	Molecular Wt. of Fe_2O_3	Total Starting Material
X=0.4	1.3910	1.9531	6.3876	9.7317
X=0.5	1.7388	1.6276	6.3876	9.7540
X=0.6	2.0866	1.3021	6.3876	9.7763
X=0.625	2.1735	1.2207	6.3876	9.7818
X=0.65	2.2604	1.1393	6.3876	9.7873
X=0.675	2.3474	1.0579	6.3876	9.7929
X=0.7	2.4343	0.9766	6.3876	9.7985
X=0.8	2.7821	0.6510	6.3876	9.8207

Table 3.2 Expected, Experimental and percentage yield of $Mn_xZn_{(1-x)}Fe_2O_4$

Composition $Mn_xZn_{(1-x)}Fe_2O_4$	Expected or Theoretical Yield	Experimental or Actual Yield	% Yield
X=0.4	9.4757	9.3904	99.10
X=0.5	9.4340	9.3019	98.60
X=0.6	9.3923	9.2984	99.00
X=0.625	9.3818	9.3217	99.36
X=0.65	9.3713	9.3469	99.74
X=0.675	9.3609	9.3197	99.56
X=0.7	9.3505	9.2859	99.31
X=0.8	9.3087	9.1560	98.36

The samples obtained by this method were used for characterization and to study their physical, electrical and magnetic properties

References

[1] R. Roy, Solid state ionics, 32-33(1989)3.

[2] M. Rozman and M.Drofenik , J. Am. Ceram. Soc. 78 **(**1995) 2449.

[3] S. Komarneni, E. Fregeau, E. Breval and R. Roy, J. Am.Ceram. Soc., 71 **(**1988) C26.

[4] A. Goldman and A. M. Laing., J. Phys. Coll. 4 **(**1977) C1 297.

[5] A. Attaie, M. R. Piramoon, I. R. Harris, C. B. Ponton, J. Mater. Sci.30(1995)5600.

[6] M. Seki, T. Sato and S. Usui, J. Appl. Phys. 63 **(**1988) 1424.

[7] A. Thakur and M. Singh, Ceram. Int. 29 **(**2003) 505.

[8] Chemical Approach to synthesis of Inorganic materials, C. N. R. Rao, Solid state structural chemistry unit, I. I. Sc. , Jahwaharal Nehuru Center for Advanced Scientific Research.

[9] E. P. Wohlfarth, 'Ferromagnetic Materials' (North- Holland Publishing Co.) Vol. 1 and 2, (1980).

[10] Guozhong Cao; Nanostructures and nanomaterials, synthesis, properties and applications, Imperial College Press, (2004).

[11] J. C. Grenier, A. Wattiaux, N. Lagueyte, J. C. Park, E. Marquestaut, J. Etoumeau and M. Pouchard, Physica C, 173 (1991) 139.

[12] A. R. West, Solid state chemistry and its applications, John Wiley and sons (1984).

[13] Mohammad AkhyarFarrukh, Boon-Tech Heng, Rohana Adnan, Truk. J. Chem. 34(2010)537-550.

[14] G. Schikorr, Z. Allg. Chem., 212 (1938) 33.

[15] M. P. Pileni, J. Phys., Chem. 97 **(**1993) 6961.

[16] K. C. Patil, S. Sudar Manoharan and D.Gajapath, 'Handbook of Ceramics and Composites' vol.1 (eds. Nicholas P.Cheremisinoff, Marcel Dekker, INC, New York) p.469.

[17] P. C. Fannin, S. W Charles. and J. L. Dormann, J. Magn. Magn. Mater. 201 (1999) 98

[18] T. Pannaparayil, S. Komarneni , R. Marande and M. Zadarko, J. Appl. Phys. 67, (1990)5509.

[19] Z. Yue, J. Zhou, L. Li, H. Zhang and Z. Gui, J. Magn. Magn.Mater. 208 (2000) 55.

[20] B. Martinez, A. Roig, E. Molins and C. Monty, J. Appl. Phys. 79 **(**1996) 2580.

[21] F.del Monte, M. P. Morales, D. Levy, A. Fernandez, M. Ocana, A. Roig, E. Molins, K. O'Grady and C. J. Serna, Langmuir, 13 **(**1997) 3627.

[22] C. Cannas, D. Gatteschi, A. Musinu, G. Piccalunga and C. Sangregorio, J. Phys. Chem., B 102**(**1998) 7721.

[23] J. S. Jiang, L. Gao, X. L.Yang, J. K. Guo and H. L. Shen, J. Mater. Sci. Lett., 18 (1999) 1781.

[24] C. Caizer, M. D. Stefanescu, C. Muntean and I. Hrianca 2000 , 3rd Int. Edition of Rom. Conf. on Advanced Materials (Bucharest, Romania, October 23–25) Contribution p 85.

[25] C. Savii, M. Popovici, M. Enache, I. Hrianca, A. Zanfir, R. Turicin and C. Caizer, Int. Conf. on Chemical Sciences for Sustainable.Development (Halkidiki, Greece, June 6–9) Contribution, (2000) 276.

[26] S. Son, R. Swaminathan, and M. E. McHenry, Journal of applied phys. 93, 7495 (2003).

[27] Z. Tugut, Ph. D. Thesis CMU 2000.

[28] M. I. Boulos, J. High Temp. Chem. Processes 1 (1992) 401.

[29] S. Son et al., J. Appl. Phys. 91 (10) (2002) 7589.

[30] S. Yamamoto, N. Tanamachi, H. Kurisu, M. Matsuura and K. Ishida, 21 Aa I-6 digest 8th Int. Conf. on ferrites Kyoto Japan.

[31] P. Poddar, J. L. Wilson, H. Srikanth , S. A. Morrison and E. E. Carpenter, Nanotechnology (IOP publishing) 15 (2004) S570–S574.

[32] S. A. Morrison, C. L. Cahill, E. E. Carpenter, S. Calvin, and V. G. Harris, Journal of applied physics 93 (10) 2003.

[33] D. Makovec, A. Kosak and M. Drofenik, Nanotechnology (IOP Publishing) 15 (2004) S160–S166.

[34] A. Kosak, D. Makovec and M. J. Drofenik, Metastab. Nanocryst. Mater. (2004).

[35] D. O. Yener and H. Giesche, J. Am. Ceram. Soc. 84 (9) (2001), pp. 1987–1995.

[36] J. Wang, P. F Chang, S. C. Nig. and L. M. Gan, Mater. Letter. 30, (1997) 217.

[37] A. Kosak, A. Znidarsic and M. Drofenik, J. Eur. Ceram. Soc., at press. (2004).

[38] P. P. Hankare, P. D. Kamble, M. R. Kadam, K. S. Rane, and P. Vasambekar, Material Lett., 61,2769(2007).

CHAPTER IV

ANALYTICAL TECHNIQUE AND CHARACTERIZATION

Characterization of materials is essential not only to fix the compositions but also to determine the parameters and functions by means of which mechanical, electrical, magnetic, optical and other properties of materials can be described. Characterization of materials plays an important role in systematic development of materials and in understanding their behavior. Material characterization and analytical techniques provide detailed information about products formed. This information may be used to explain their behavior and develop materials with new improved properties to suit the particular requirement. One of the principal objectives in the experimental study of bulk solids is the characterization of lattice structure and investigations of other physical properties.

There are two classes of properties which are important in material characterization. One is compositional (elemental) characterization and molecular or crystal structure of the material, and second is the geometrical properties of the materials such as size, shape, and surface characteristics of particulate matter. Among these, the compositional characteristics in general are independent of the microscopic form of the material, while the geometric parameters are dependent on the microscopic form and decide final properties of the product and its applications.

The recent thrust in advancement of material science in general and nanostructure in particular is due to the discovery and development of

supportive modern characterization equipments. Characterization of nanomaterials and nanostructures has been largely based on surface analysis techniques and conventional characterization methods for bulk materials [1].

In this chapter different experimental techniques employed for the characterization of fine particle Mn-Zn mixed ferrites have been discussed. The results of the various techniques used are presented in the later sections along with the relevant discussion. The following techniques were used for the material characterization:

(i) X-ray Diffraction Spectroscopy (XRD)

(ii) Infra Red Spectroscopy (IR)

(iii) Chemical analysis (EDS)

(iv) Density measurement

4.1 X-RAY DIFFRACTION

XRD is a very important experimental technique that is used for characterization of crystalline materials, determination of crystal structure of solids, lattice constants, orientation of single crystal, preferred orientation of crystals in poly-crystalline materials, crystal defects, stresses, etc.

Each crystalline solid has its unique characteristic X-ray powder pattern, which may be used as a "fingerprint" for its identification. The size and the shape of the unit cell for any compound can be determined most easily using the diffraction of X-rays.

X-ray diffraction technique is used to confirm the formation of any material, to determine interplanar atomic distances, and also the size of the crystallites in case of fine powdered materials.

As the crystallites are randomly oriented, a reflection at the particular position is due to a set of atomic planes satisfying Bragg's condition.

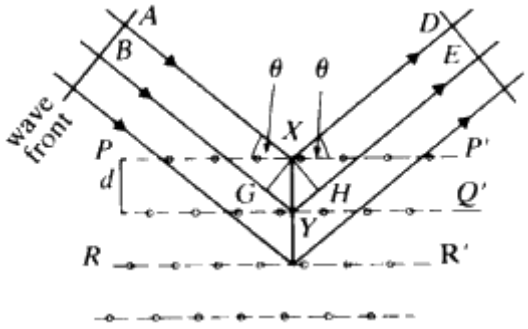

$$n\lambda = 2d_{hkl}\sin\theta$$

where d_{hkl} is the interplanar spacing of crystal planes of miller indices (hkl), θ is the glancing angle , λ is the wavelength of X-ray radiation and 'n' is the order of diffraction.

For a cubic lattice, the interplanar distance, d_{hkl} , lattice parameter 'a' and the miller indices(hkl) are given by relation,

$$d_{hkl} = a \Big/ \sqrt{h^2 + k^2 + l^2}$$

4.1.1 X - Ray Diffraction method.

In case of rotating crystal method, a crystal is mounted with one of its axes, or some important crystallographic direction, normal to monochromatic X – ray beam. As crystal rotates, a particular set of lattice planes will make the correct Bragg angle for reflection of the monochromatic incident beam. The peak intensities are determined by the atomic position within the lattice planes.

4.1.2 Instrumentation

The X -ray diffraction experiment consists of an X-ray source, the sample under investigation and a detector to pick up the diffracted X-rays. Fig 4.1 (a) is a schematic diagram of a powder X-ray diffractometer.

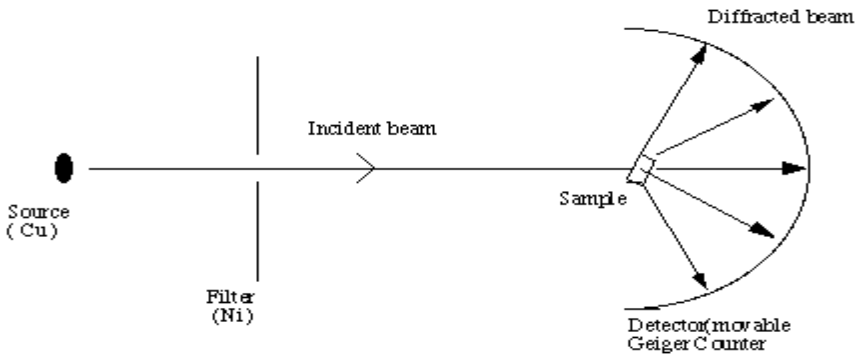

Fig.4.1 (a) Schematic of an X-ray powder diffractometer

The X-ray radiation emitted by copper target, has characteristic wavelength Kα =1.5418Å. (Weighted mean) When the incident beam strikes a powder sample, diffraction occurs in every possible orientation of 2θ. The diffracted beam is detected by using a moveable detector such as a Geiger counter, which is connected to a computer. The counter is set to scan over a wide range of 2θ values from 10 to 90 or more depending upon the equipment make.

Fig 4.1 (b) Righaku XRD Diffractometer

4.1.3 Effect of crystal size on the powder pattern – particle size measurement

Small particle size leads to line broadening because of the conditions under which diffraction occurs in the incident angle, which is slightly different from the Bragg angle θ_B.

The Bragg angle represents the condition under which each plane in a crystal diffracts exactly one wavelength later than the presiding plane. All diffracted beams are therefore in phase and constructive interference occurs. For an incident beam at a slightly greater angle θ_1, there is a phase lag of slightly greater than one wavelength, $\lambda+d\lambda$, for rays diffracted from subsequent planes. By the time the $(j+1)^{th}$ plane is reached, incremental phase lag is $\sum d\lambda$, equal to half a wavelength; i.e. $j\delta\lambda=\lambda/2$.

Planes 1 and (j+1) are exactly π, out of phase for radiation that is incident and diffracted at θ_1 and therefore, cancel each other. If the crystal

contains a total of 2j planes, then the net diffracted intensity at θ_1 is equal to zero because the rays diffracted from planes 1 to j exactly cancels the rays diffracted from the planes (j+1) to 2j. The annular range θ_B to θ_1 is the range over which the intensity of the diffracted beam falls from a maximum at θ_B to zero at θ_1. A similar lower limiting angle, θ_2, occurs for which rays diffracted from adjacent planes have a phase difference of λ-$\delta\lambda$. The magnitude of the angular range θ_1 to θ_2, and hence the width of the diffraction peak, is governed by the number of planes 2j, and hence the crystal thickness. If the number of peaks is very large, no significant broadening occurs because $d\lambda$, and therefore, (θ_2 -θ_1) is negligibly small.

4.1.4 Rietveld refinement is a technique devised for use in the characterisation of crystalline materials. The X-ray and neutron diffraction of powder samples results in a pattern characterised by reflections (peaks in intensity) at certain positions. The height, width and position of these reflections can be used to determine many aspects of the materials structure. The Rietveld technique is a procedure to refine structures of powder crystals. A rough idea of the crystal structure must be known. Then the Rietveld technique is used to get an accurate idea of the structure. It is basically a least squares fit of the crude models diffraction pattern provided by the user to the experimental diffraction pattern.

This technique minimizes the difference between the observed patterns to the model pattern produced. In the powder form of the sample the three dimensional crystal structure of the sample produces a one dimensional diffraction pattern. So there is a lot of overlap of peaks especially for low

symmetry crystal structures. The Rietveld technique fits the profile of the pattern to the calculated profile by not trying to separate overlapping peaks. Instead it assumes all possible peaks being diffracted at a certain scattering angle as having Gaussian profiles and minimizes the residue with respect to variable parameters.

4.2 INFRARED SPECTROSCOPY (IR)

Infrared absorption spectroscopy is an important and non-destructive characterizing tool, which provides qualitative information regarding structural details of crystalline materials. IR spectrum is the portion of electromagnetic spectrum from red end of visible spectrum (12,500cm^{-1}; 0.8mm) to the microwave (10 cm^{-1}; 1000mm) and based upon application and instrumentation involved it is conveniently divided into near-IR (12500 to 4000 cm^{-1}), mid- IR (4000 to 400 cm^{-1}) and far-IR (400 to 10cm^{-1}). Mid-IR region is the most important range as it gives the information about the vibrations of molecules, and hence about the structure of molecules. Far infrared absorption spectroscopy is an excellent tool to study the distribution of the cations in the tetrahedral and octahedral sites in ferrite system and also to determine the local symmetry in any crystalline solids. (Waldron 1955; Ravinder and Manga 1999; Ladgaonkar et al 2002 of ferrite systems) [2].

When IR radiation is passed through a sample, certain frequencies are absorbed by the molecule that corresponds to vibrational changes in the molecule. This is possible if there exist a mode of interaction between the incident radiation and the vibrational energy levels. This mode of interaction is an oscillating electric dipole induced by the vibration, which interacts with the

oscillating electric field of the electromagnetic radiation. IR absorption occurs for each vibrational degree of freedom of the molecule provided, that a change in the dipole moment of the molecule takes place during the vibration. For a large molecule with many vibrational degrees of freedom there may be many IR bands observed. Since each molecule has individual sets of energy levels, the absorption spectrum is characteristic of the fundamental groups that are in the molecule [3,4].

For example A carbon-carbon triple bond (-C≡C-) absorbs in the region 2300-2000 cm^{-1}, where as a double bond (C = C) is weaker and absorbs at lower frequency, 1900-1500 cm^{-1}.

In the IR technique the frequency of incident radiation is varied and the quantity of radiation absorbed by the sample is obtained. IR spectra of solids are usually complex with large number of absorption peaks each corresponding to particular vibrational transition. The intensities of overtone, combination, and difference bands are less than those of the fundamental bands. The combination and blending of all the factors normally creates a unique IR spectrum for each compound.

The absorption bands, from which the details regarding functional groups and their linkages can be explored, are found to be dependent on atomic mass, cationic radius, cation–anion bond distances and cation distribution [5]. The characteristic absorption bands authorizes one to obtain useful structural information by comparing absorption bands for a sample to standard tables of functional groups absorption frequencies.

In ferrites, both the absorption bands depend on the nature of octahedral ions, and tetrahedral ions. The band, at around 600 cm^{-1} represents

the intrinsic vibrations of the tetrahedral metal oxygen complexes and the band around 400 cm^{-1} represents the intrinsic vibrations of the octahedral complexes [5]. The difference in the band positions is due to the difference in the Fe^{+3}–O^{+2} distances for the octahedral and tetrahedral complexes. The presence of any splitting or shoulder in the band implies the presence of Fe^{+2} ions [6].

4.2.1 Fourier Transform IR spectrophotometer

Fourier Transform Infrared (FTIR) Spectroscopy is a measurement technique for collecting infrared spectra. Instead of recording the amount of energy absorbed when the frequency of the infra-red light is varied (monochromator), the IR light is guided through an interferometer. After passing through the sample, the measured signal is the interferogram. Performing a mathematical Fourier transform on this signal results in a spectrum identical to that from conventional (dispersive) infrared spectroscopy. Measurement of a single spectrum is faster for the FTIR technique because the information at all frequencies is collected simultaneously. This allows multiple samples to be collected and averaged together resulting in an improvement in sensitivity. FTIR spectrometers have fast speed and high sensitivity and are capable of analyzing samples in many areas.

FTIR spectroscopy offers at least three advantages: 1) multiplex advantage, results from the accumulation and sorting of data. In one second with one scan the FTIR measures a spectrum of all wave numbers.

2) Aperture advantage (throughput Jacqui not advantage), which is created by the large FTIR aperture. FTIR results depend on the aperture area and the

incident angle of light. When a large aperture is used, more of the light source is available to maintain a high – throughput optical system, giving the spectrum a high S/N ratio.

3) The wave number precision, or cones, advantage is the result of the FTIR 8400 He-Ne laser. The laser emits extremely stable monochromatic light, creating a spectrum with high wave number accuracy.

FTIR uses one of the several optical systems; the FTIR – 8400 relies on a Michelson interferometer. After passing through the aperture, light is turned into a parallel beam by the collimator mirrors and enters the beam splitter where it splits the single beam into two, reflecting one to the fixed mirror and transmitting the other to the moving mirror. Both mirrors reflect their beams back to the beam splitter; part of each returning beam is reflected and transmitted. The transmitted light from the fixed mirror and the reflected light from the moving mirror combine and interfere with each other as they travel towards the collecting mirror. The interference is either constructive or destructive.

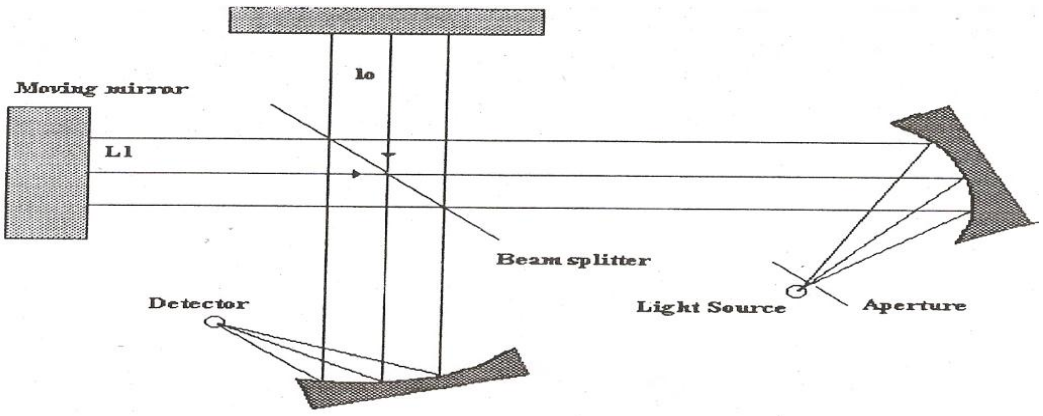

Fig 4.1 (c) Michelson Interferometer

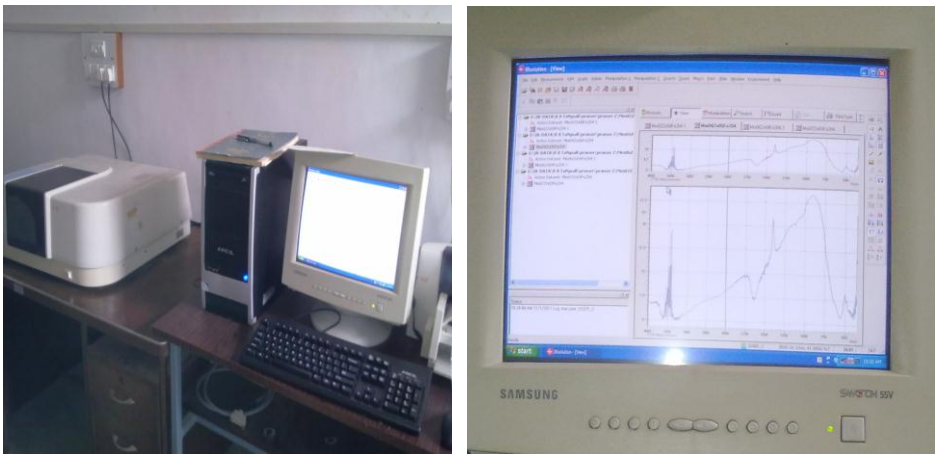

Fig. 4.1 (d) FTIR 8900 assembly

4.2.2 Experimental

FTIR spectra for all the samples were recorded on Shimadzu FTIR 8900 spectrometer. The solid sample was finely ground along with pure and dry KBr, in the ratio 1:100. The mixture was pressed into a pellet using hydraulic press to form a transparent pellet of about 2 to 2.5 mm thickness and 1cm diameter by applying force of 5kN. The pellet was then mounted on the sample holder, placed in the sample chamber of the IR spectrometer. The absorption spectrum for the sample was recorded in the wavelength range of $350cm^{-1}$to $4000cm^{-1}$ as usual. Similar measurements were carried out on all the samples.

4.3 CHEMICAL ANALYSIS

4.3.1 Energy Dispersive X-Ray Spectroscopy (EDS or EDX)

This is a chemical microanalysis technique used in conjunction with scanning electron microscopy (SEM). The EDS technique detects X-rays which are emitted from the sample, when the sample is bombarded by an electron beam. Energy-dispersive X-ray spectroscopy (EDS or EDX) is an analytical technique used for the elemental analysis or chemical

characterization of a sample. The technique relies on the investigation of a sample through interactions between electromagnetic radiation and matter, analyzing X-rays emitted by the matter in response to being hit with charged particles. Its characterization is based on the fundamental principle that each element has a unique atomic structure allowing X-rays that are characteristic of an element's atomic structure to be identified uniquely from one another.

When the sample is bombarded by the SEM electron beam, electrons are ejected from the atoms which are present on the sample's surface. The incident beam may excite an electron in an inner shell, ejecting it from the shell while creating an electron hole pair giving rise to an exciton. An electron from an outer, higher-energy shell then fills the hole, and the difference in energy between the higher-energy shell and the lower energy shell is released in the form of an X-ray photon. The number and energy of the X-rays photons emitted from a sample can be measured by an energy-dispersive spectrometer. The EDS X-ray detector measures the relative abundance of emitted X-rays versus their energy. The spectrum of X-ray energy versus counts is evaluated to determine the elemental composition of the sampled volume.

4.3.2 Experimental

The EDAX spectra of the nanosamples $Mn_xZn_{(1-x)}Fe_2O_4$ (x=0.4, 0.5, 0.62, 0.65, 0.675, 0.7 and 0.8) were obtained on JEOL model 840 and JOEL model JSM 6360LV instruments at the accelerating voltage of 10KV.

The ferrite samples under investigation were sprinkled lightly on adhesive tape with spatula. This adhesive tape was then mounted on cylindrical stubs of diameter around 1 cm. The specimen was fixed on a sample holder and then placed into the sputter coater until a thin layer of

platinum is built up on the surface of the powder sample. A sputter coater produces a nanometer thickness of conductive material on the surface through a cold plasma process that retains the contours of the specimen. The specimen is then placed in the SEM vacuum chamber and the electron gun is switched on for recording the necessary elemental analysis. From the EDS spectra, percentage content of Mn, Zn and Fe were obtained.

4.4 DENSITY AND POROSITY MEASUREMENTS

The density of the powder and sintered samples were measured by pyknometric method. The mass density of each sample was measured in CCl_4 medium (density of CCl_4 =1.529).

The density was calculated using formula:

d= (Weight of the sample /loss of weight in liquid) *density of CCl_4

X-ray densities, were calculated using the expression $d_x = 8M/a^3N$ where M is the molecular weight of the sample and N is the Avogadro's number and '**a'** is the lattice constant.

The porosity of each sample was calculated from the ratio of the values of X-ray density and mass density using the relation [7].

$P = 1 - (d/d_x)$ where d is the mass density and d_x is X-ray density.

4.5 RESULTS AND DISCUSSION

4.5.1 X-Ray Diffraction Analysis

X-ray diffraction method was used to confirm the formation of spinel structure, to determine interplanar distances and the lattice constants of the materials prepared.

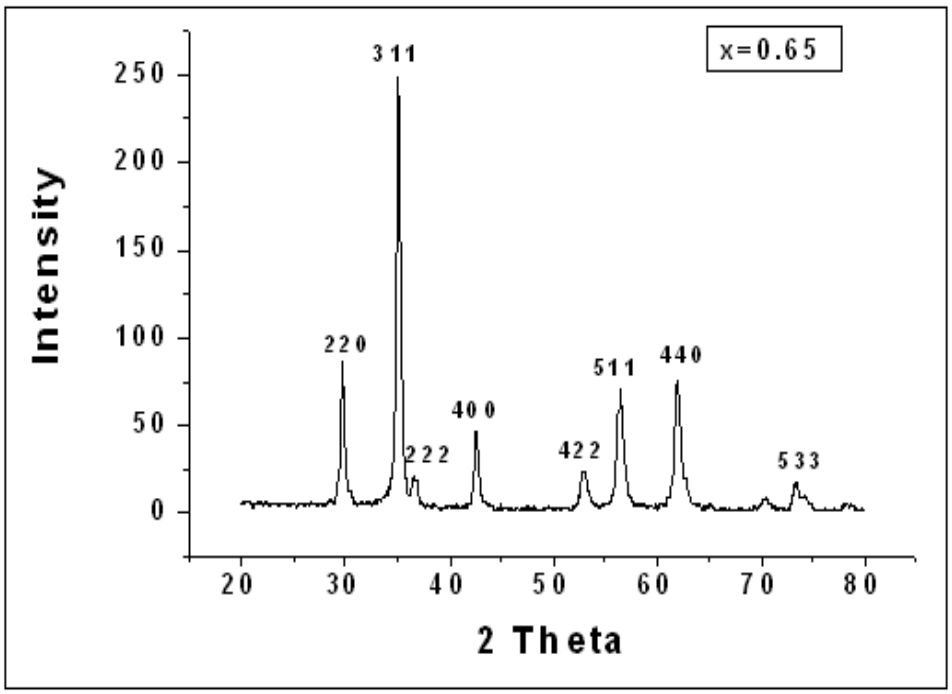

Fig. 4.2 (a) XRD pattern for the nanosample $Mn_{0.65}Zn_{0.35}Fe_2O_4$ prepared by auto combustion method.

A XRD pattern for the sample $Mn_{0.65}Zn_{0.35}Fe_2O_4$ is shown in Fig.4.2 (a) and Fig**.** 4.2 (b) shows the X–ray diffraction patterns of $Mn_xZn_{(1-x)}Fe_2O_4$ samples with different concentrations of Mn and Zn. The patterns obtained are similar to the patterns reported in literature [8]. This confirms formation of monophasic samples.

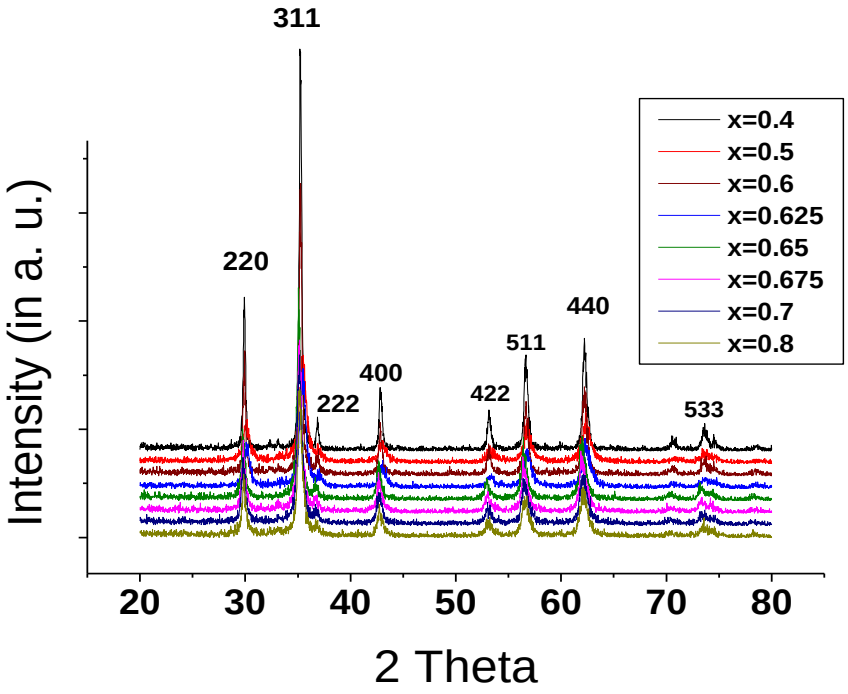

Fig.4. 2 (b) XRD pattern for the nanosample $Mn_xZn_{(1-x)}Fe_2O_4$.

4.5.1.1 Ritveld Refinement

Ritveld Refinement was done to obtain an accurate X ray structure and to fit entire diffraction pattern at once optimizing the agreement between calculated and observed pattern. Inputs needed for Ritveld Refinement were, correct space group symmetry, reasonable accurate unit cell dimension and approximate starting position of atoms.

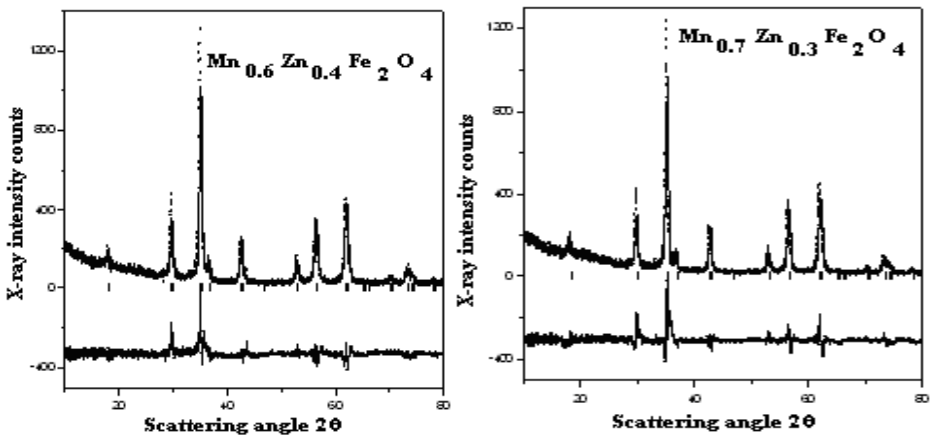

(c) (d)

Fig 4.2 (c, d) Rietveld Refinement of X-ray powder diffraction pattern of nanosamples (c) $Mn_{0.6}Zn_{0.4}Fe_2O_4$ (d) $Mn_{0.7}Zn_{0.3}Fe_2O_4$

XRD and Rietvleld refinement of $Mn_{0.6}Zn_{0.4}Fe_2O_4$ and $Mn_{0.7}Zn_{0.3}Fe_2O_4$ is shown in Fig.4.2 (c) and 4.2 (d). Experimental data is shown as continuous line and computed profile is shown as discrete dots. At the bottom of the figure is shown the residual error between the computed and experimental values. Finally, at the bottom of the diffraction pattern the stick patterns are shown to identify the phases. Once the phases have been identified and the necessary atomic information extracted from the database, a computed profile is calculated. Then, by the use of a least-squares technique, the residual error is minimized by modifying the lattice parameters, the scale factors, atomic parameters such as the thermal vibrations, atomic positions, and occupancies. The recorded XRD data were found to fit well to the space group *Fd-3m.*

So in a diffraction pattern the intensities of a diffraction pattern depend on many variables through the structure factor. The intensity of the profile is calculated through a starting model which depends on the size of the unit cell and the positions of the atoms in the unit cell. In the process of refining, the

peak positions are accurately obtained by varying cell constants and zero of the counter. Next, the intensities of the peaks are fitted to the experimental intensities by varying the atomic positions of the atoms on general sites, after which the occupancies of various atoms in the unit cells are fitted. The various atoms in the unit cell are vibrating at RT and so their vibrations contribute to the experimental Debye- Waller factor. They reduce the peak intensities at high angles.

4.5.1 .2 Lattice constant:

The variation of lattice constant 'a' as a function of Mn concentration is shown in Fig. 4.3 (a). The lattice constant increases with increase in Mn concentration. This increase in lattice constant with Mn concentration arises due to the replacement of Zn^{+2} cations having a smaller ionic radius 0.074nm by Mn cations having larger 0.082nm ionic radius [9].

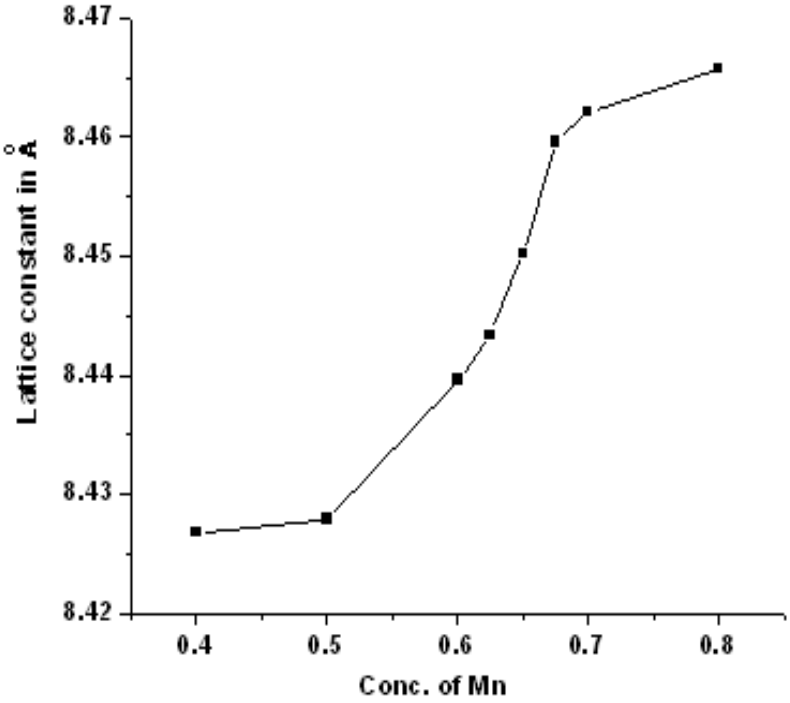

Fig 4.3 (a) Variation of lattice constant with Mn conc.of Nanoparticle sample.

The values of lattice constant "**a**" calculated was found to be in good agreement with reported values [9,10] and is dependent on Mn concentration in samples. The variation of the lattice parameter can be attributed to the ionic radii of the ions and cation distribution in the two sites.

4.5.1.3 Particle Size:

The broadening of X-ray peaks were used to calculate the crystallite size using Scherrer formula;

$$t = (0.9\lambda)/(B \cos \theta_B)$$ [11].

Where t is the particle size (in angstroms), λ the x-ray wavelength and θ_B the Bragg angle.

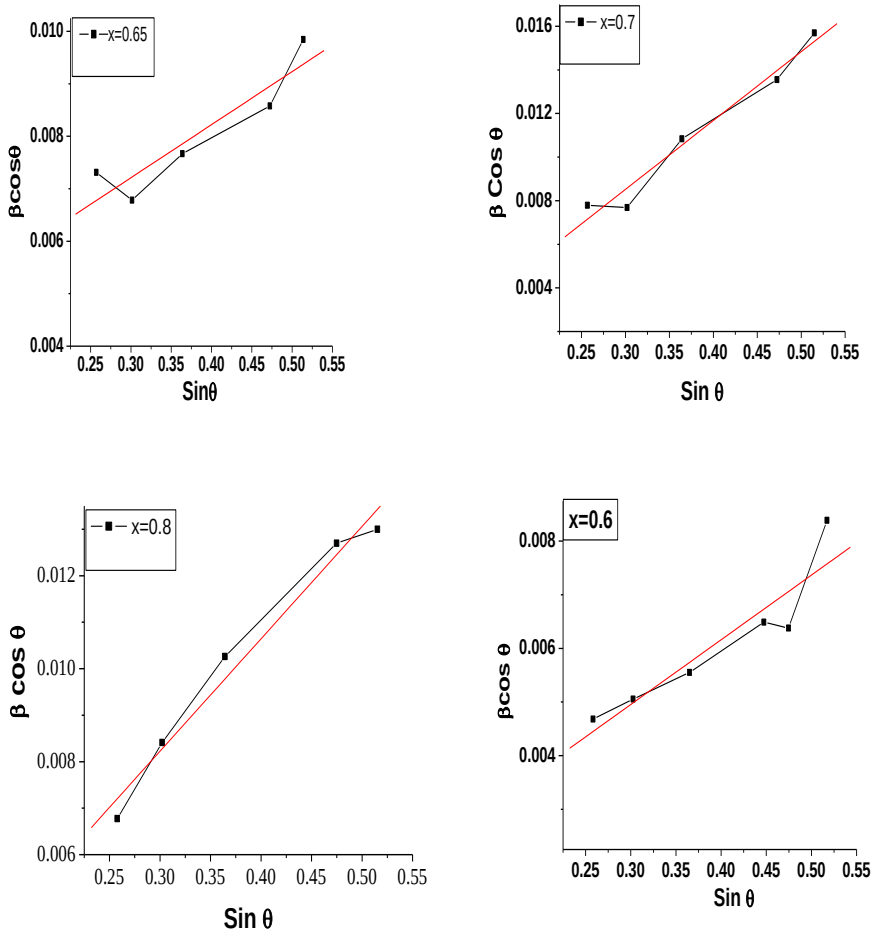

Fig.4.3 (b) Williamson Hall Plot for $Mn_xZn_{(1-x)}Fe_2O_4$ (x=0.6, 0.65, 0.7, 0.8)

The particle size estimates were also done by applying particle strain corrections to FWHM using Williamson's technique.

Table 4.1: Variation of lattice constant and particle size of Nanosample $Mn_xZn_{(1-x)}Fe_2O_4$

Sample	Lattice Constant 'a' in Å	Average Particle size 't' (by Scherrer's Formula) in nm	Average Particle size 't' (by Williamson Hall Plot) in nm
$Mn_{0.4}Zn_{0.6}Fe_2O_4$	8.4268	26.51	36.05
$Mn_{0.5}Zn_{0.5}Fe_2O_4$	8.4279	10.90	10.43
$Mn_{0.6}Zn_{0.4}Fe_2O_4$	8.4396	23.53	34.06
$Mn_{0.625}Zn_{0.375}Fe_2O_4$	8.4434	12.50	12.82
$Mn_{0.65}Zn_{0.35}Fe_2O_4$	8.4502	17.55	21.68
$Mn_{0.675}Zn_{0.325}Fe_2O_4$	8.4596	16.92	20.90
$Mn_{0.7}Zn_{0.3}Fe_2O_4$	8.4622	13.54	22.45
$Mn_{0.8}Zn_{0.2}Fe_2O_4$	8.4657	14.41	21.64

The corresponding particle size values which are in nanometer range are given in table 4.1 above. The calculations show that the particle size of the samples have a reasonably narrow range of distribution which happens to be in the range of 10nm to 36nm with uneven strain distribution depending on several factors.

4.5.2 FTIR Spectroscopy

Infra Red (IR) absorption spectra of the nanosamples $Mn_xZn_{(1-x)}Fe_2O_4$ (x=0.4, 0.5, 0.6, 0.625, 0.65, 0.675, 0.7and 0.8) are shown in Fig 4.4 (a) IR spectra of the samples were recorded in the wavelength range of (4000-400) cm^{-1}.

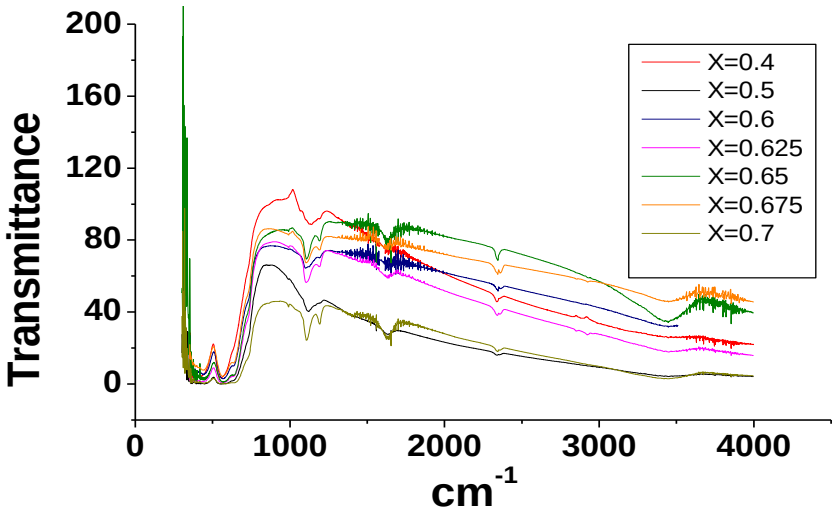

Fig 4.4 (a) IR Spectra for $Mn_xZn_{(1-x)}Fe_2O_4$ Ferrite Nanoparticles

Vibrational bands of the type

(1) (Me_T – O -- Me_o) stretching vibration at 600-550cm^{-1}

(2) (Me_o-O) stretching vibration at 450-385 cm^{-1}

(3) (Me_T-Me_o) stretching vibration at 350-330 cm-1

where O is oxygen, Me_o is the metal ion in octahedral site and Me_T is the metal ion in tetrahedral site, are observed for spinel ferrites in general. Many a times the band (2) and band (3) being very close, combine to show a broad band at 450-330 cm-1.

Infrared absorption spectra of the compositions under investigation reveal the formation of single phase cubic spinel, showing two significant absorption bands (Woldron 1955). The first absorption band, observed at

about 550 cm^{-1} to 600 cm^{-1} is attributed to the tetrahedral site, whereas the second band observed at about 330 cm^{-1} to 425 cm^{-1} is assigned to octahedral group complexes [5].

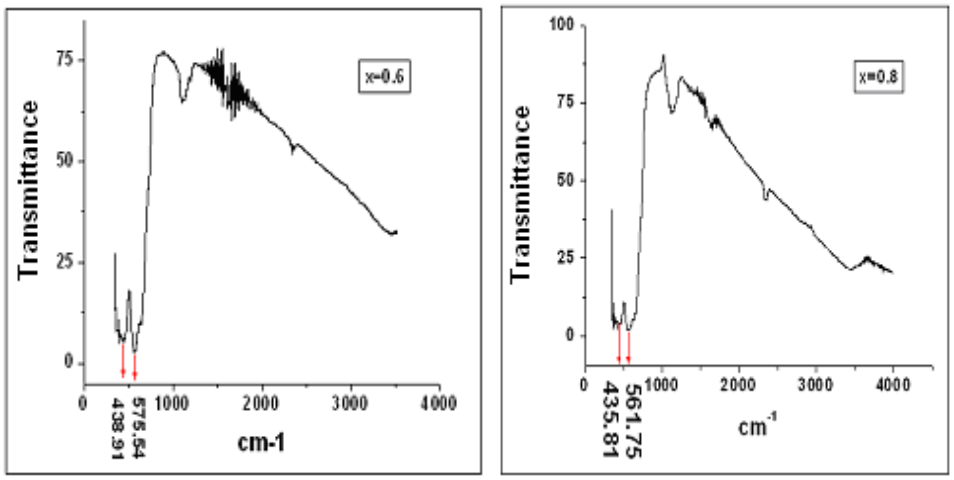

(b) (c)

Fig 4.4 (b,c) IR Spectra of nanoparticles (b) $Mn_{0.6}Zn_{0.4}Fe_2O_4$ & (c) $Mn_{0.8}Zn_{0.2}Fe_2O_4$

The positions of absorption bands are compositional dependent, whose dependence could be attributed to the variation in cation oxygen bond distances [5]. Shift in the position of bands as shown in Fig. 4.4 (b) and 4. 4 (c) depends on cationic distribution in two sites. IR spectra for all the samples under investigation matches with reported one [12, 13].

4.5.3 Elemental Analysis:

Estimation of percentage contents of the elements Mn, Zn, Fe and O are carried out with the help of EDS analysis of all the samples.

EDS Data

Table 4.2 a: EDS Results of nanosample $Mn_{0.7}Zn_{0.3}Fe_2O_4$

Element	Weight %	Atomic %
O K	30.38	54.09
Mn K	16.21	9.08
Fe K	45.03	24.80
Zn K	8.39	3.95
Total	100	

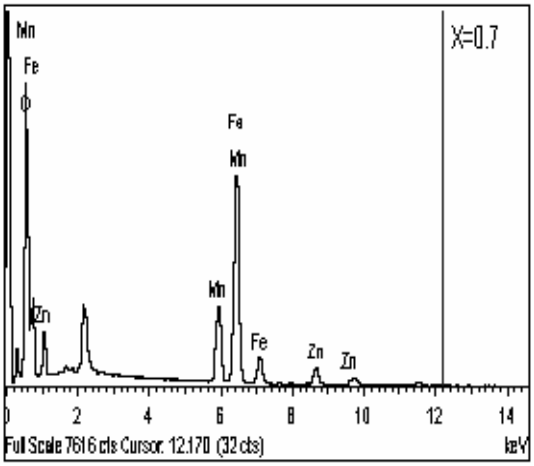

Table 4.2. b: EDS Results of nanosample $Mn_{0.65}Zn_{0.35}Fe_2O_4$

Element	Weight %	Atomic %
O K	30.75	63.91
Mn K	14.96	8.05
Fe K	45.05	23.86
Zn K	9.24	4.18
Total	100	

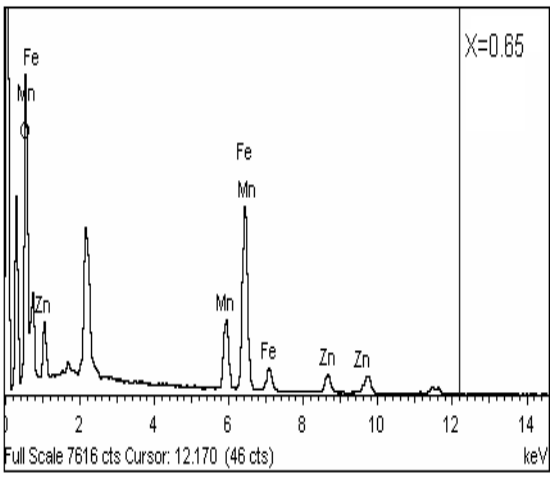

Table 4.2.c: EDS Results of nanosample $Mn_{0.6}Zn_{0.4}Fe_2O_4$

Element	Weight%	Atomic%
Mn K	14.55	9.65
Fe K	50.01	32.66
Zn K	11.45	6.39
O	23.99	52.33
Totals	100.00	

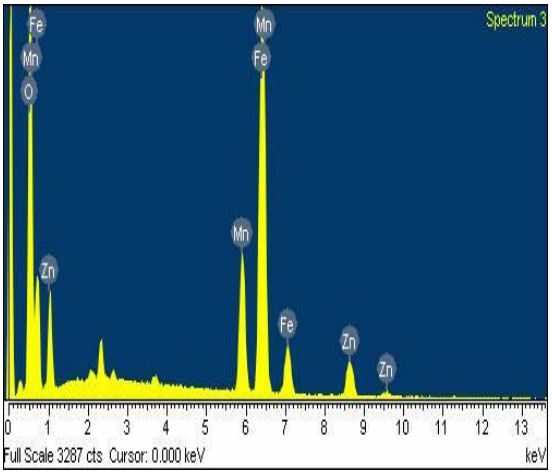

Table 4.2.d: EDS Results of nanosample $Mn_{0.8}Zn_{0.2}Fe_2O_4$

Element	Weight%	Atomic%
Mn K	18.04	11.87
Fe K	53.63	34.70
Zn K	5.56	3.43
O	22.77	50.00
Totals	100.00	

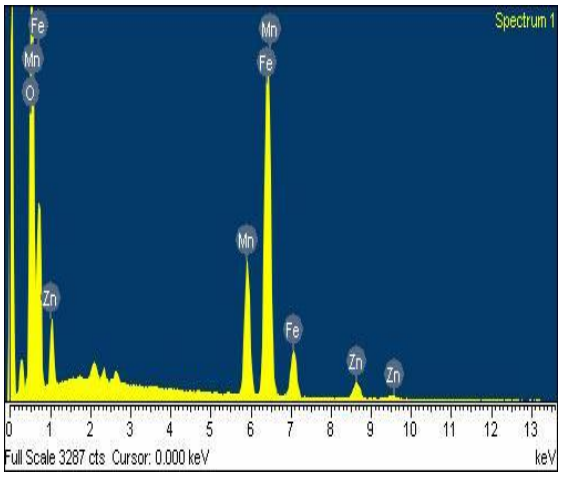

Table 4.3 (a) Estimated percentage error of the elements Mn, Zn and Fe in the nanosample $Mn_xZn_{(1-x)}Fe_2O_4$.

Sample	Mn		Zn		Fe	
	EDAX values	% error	EDAX values	% error	EDAX values	% error
$Mn_{0.4}Zn_{0.6}Fe_2O_4$	0.3759	6.03	0.5691	5.15	2.02	-1.00
$Mn_{0.5}Zn_{0.5}Fe_2O_4$	0.4911	1.78	0.5110	-2.21	1.99	0.5
$Mn_{0.6}Zn_{0.4}Fe_2O_4$	0.6220	-3.66	0.4115	-2.87	2.10	-5.00
$Mn_{0.625}Zn_{0.375}Fe_2O_4$	0.615	1.60	0.3698	2.67	1.88	6.0
$Mn_{0.65}Zn_{0.35}Fe_2O_4$	0.6378	1.88	0.3311	5.4	1.89	5.5
$Mn_{0.675}Zn_{0.325}Fe_2O_4$	0.7220	-6.9	0.327	-0.62	2.09	-4.5
$Mn_{0.7}Zn_{0.3}Fe_2O_4$	0.6899	1.44	0.30	0.0	1.88	6.00
$Mn_{0.8}Zn_{0.2}Fe_2O_4$	0.7641	4.48	0.1979	1.05	2.10	-5.00

Table 4.3(b) Probable error of Mn, Zn, and Fe in the nanosamples.

Sample	Mn	Zn	Fe
$Mn_{0.4}Zn_{0.6}Fe_2O_4$	0.0195	0.0242	0.1169
$Mn_{0.5}Zn_{0.5}Fe_2O_4$	0.0077	0.0565	0.0334
$Mn_{0.6}Zn_{0.4}Fe_2O_4$	0.0759	0.0169	0.0065
$Mn_{0.625}Zn_{0.375}Fe_2O_4$	0.0311	0.062	0.0235
$Mn_{0.65}Zn_{0.35}Fe_2O_4$	0.0074	0.0073	0.1053
$Mn_{0.675}Zn_{0.325}Fe_2O_4$	0.0144	0.0172	0.0476
$Mn_{0.7}Zn_{0.3}Fe_2O_4$	0.0150	0.0094	0.0697
$Mn_{0.8}Zn_{0.2}Fe_2O_4$	0.0182	0.0206	0.0699

Estimated values of Mn, Zn and Fe from EDS analysis are in good agreement with the theoretical values, thus confirming the preservation of

stoichiometry [14]. Slight deviation of Mn, Zn, and Fe contents in the nanosamples calculated from EDS data seem to be reasonable.

The errors in the percentages of various elements calculated from EDS data, though in permissible limits could be due to the fact that the SEM electron beam used for the purpose is a less intensity beam and samples under investigations are strongly magnetic samples. Strong magnetic samples probably need high energy electron beam for reasonably good accuracy.

4.5.4 Mass Density

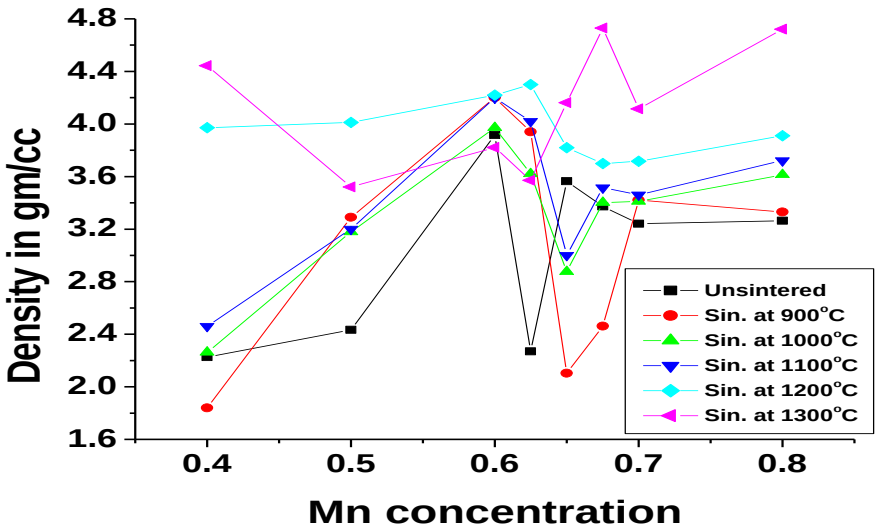

Fig.4.5 (a): Variation of mass density with Mn conc. of bulk samples and nanosamples.

The density measurements were done by pyknometric method. Variation of density of nanoparticle samples and bulk samples $Mn_xZn_{(1-x)}Fe_2O_4$ with Mn concentration **x** is shown in Fig.4.5 (a).All the density patterns show double peaks for nanosamples as well as for sintered samples. Nanosample with Mn=0.6 has a maximum density 3.9245 gm/cc whereas the sample with Mn=0.625 has a minimum density 2.266 gm/cc.

The variation of density of the sintered samples in general is found to follow a non uniform pattern with variation in Mn concentration. Moreover the density of sintered samples with x = 0.8, 0.7, 0.675, 0.65, 0.625, 0.6, 0.5 and 0.4 (fig. 4.5 (a)) was found to be high when sintered at 1200^{o}C and 1300^{o}C, whereas the same was comparatively low when sintered at 900^{o}C, 1000^{o}C and 1100^{0}C respectively. The density for sample with x=0.5. 0.6 and 0.625 exhibits a maxima when sintered at 1200^{o}C, whereas samples with higher concentration i.e. x=0.65, 0.675, 0.7 and 0.8 show high density values for higher sintering temperature (1300^{o}C). The density of samples with x = 0.4, 0.675, 0.7, and 0.8 increases with increase in sintering temperature. This variation can be explained on the basis of the microstructure development of the material while it undergoes sintering process.

The density measurements show an overall increase in the densification with the increase in the sintering temperature. In general, this occurs due to reduction of the number of pores in the samples with increase in effective area of grain-to –grain contact [15, 16]. The density values for sintered samples were found to be in the range of 1.8g/cc, to 4.73 gm/cc. The highest density being 4.73 gm/cc. for the sample $Mn_{0.675}Zn_{0.325}Fe_2O_4$ sintered at 1300^{o}C.

4.5.5 X-ray density:

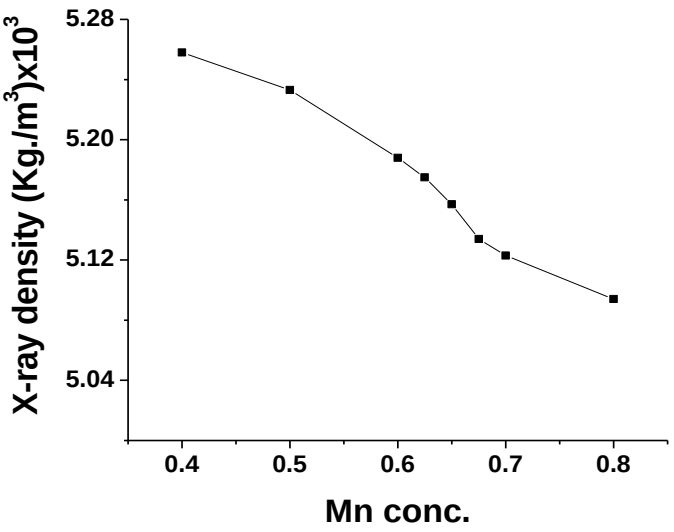

Fig.4.5 (b) Variation of X-ray density with Mn. conc. of Nanoparticle sample.

X-ray density of various samples, so prepared, was calculated from the lattice constant '**a**'. The variation of x-ray density with Mn concentration in the nanosamples is shown in fig.4.5 (b). The X-ray density decreases with increase in Mn content as Lattice constant 'a' for the samples increases with increase in Mn content in the samples as reported earlier [17,18]**.** X-rays density of nanosamples is found to be in the range of 5.094×10^3 Kg./m^3 to 5.258×10^3 Kg./m^3.

4.5.6 Porosity

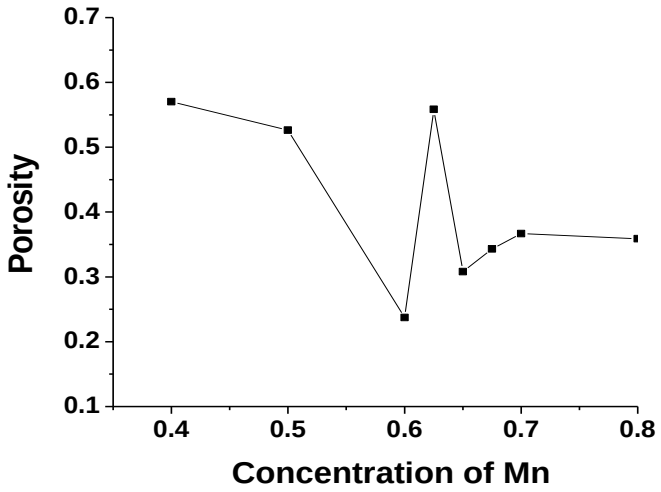

Fig.4.5 (c) Variation of porosity with Mn conc. of nanoparticle samples

The Porosity (P) is calculated by using the formula given in section 4.4 using mass density and X-ray densities of the samples. The variation of porosity with Mn concentration **x** in the samples is shown in the Fig.4.5 (c)**.** The porosity of the samples appears to show a trend, which is opposite to that of density. Any low porosity sample is found to exhibit high density and vice-versa.

References

[1] Guozhonq Cao, Nanostructures and Nanomaterials, synthesis, properties and Applications, publication 2004, Reprinted 2005, 2006, Imperial college press.

[2] R. Iyer, R. Desai, R. V. Upadhyay, Material. Sc., 32 (2) (2009) 141-147.

[3] R. W. Cahn, P. Haasen, E. J .Kramer, Material Science and Technology. Vol. 2A , VCH- Weinheim- Newyork.

[4] R. W. Cahn, P. Haasen, E. J. Kramer, Material Science and Technology Vol. 2B , VCH- Weinheim- Newyork.

[5] B. P. Ladgaonkar, C. B. Kolekar, A. S. Vaingankar, Indian Acamdemy of Science, Bull. Meter. Sci. Vol. 25, No.4, (2004), pp. 351-354.

[6] V. A. Potakova, N. D. Zvev and V. P. Rommanov, Phy. Stat. Sol. A, 12 (1972), p 623 (29).

[7] M. U. Islam, I. Ahmed, T. Abbas and M. A. Chaudhary, 6th international Symposium on advanced Materials (1999)155-158.

[8] L. Nalbandian, A. Delimitis, V. T. Zaspalis, E. A. Deliyanni, D. N. Bakoyannakis, E. N. Peleka, Microporous and Mesoporous materials114,(2008)465-473.

[9] Chandan Rath, S. Anand, R. P. Das, K. K. Sahu, S. D. Kulkarni, S. K. Date, N. C. Mishra, Journal of applied physics, Vol.91, (2002). Number4.

[10] R.G. Welch, J. Neamtu, M. S. Rogalski, S. B. Palmer, Materials Letters 29, (1996) 199-203.

[11] B. D. Cullity, Elements of X-ray Diffraction, 2nd edition, Addison Weseley (1978).

[12] J. Lemcomte, Enciclopedia of Physics, Springer Verlag, Berlin, 26, (1958) 244.

[13] V. C. Farmer, in “The Infrared Spectra of Minerals” ed. V. C. Farmer, Mineralogical Society, London , (1974) 18.

[14] S. Son, R. Swaminathan, and M. E. McHenry J. of Applied Physics 93(10) (2003).

[15] M. K. Moinuddin, S. R. Murthy, J. Alloys Compound.194 (1993)105 (JALCOM539).

[16]Uzma Ghazanfar, S. A. Siddiqi, G. Abbas, Materials Science and Engineering B 118 (2005) 84-86.

[17] E. V. Gopalan, I. A. Al-Omari, K. A. Malini, P. A. Joy, D. S. Kumar, Y. Yoshida and M. R. Anantharaman, J. Magn. Mater, 321(2009)1092 -1099

[18] S. Dasgupta, K. B. Kim, J. Ellirich, J. Eckert and I. Manna, J. Alloys Comp, 424 (2006) 13-20.

CHAPTER V

INSTRUMENTAL TECHNIQUES

FOR PARTICLE SIZE DETERMINATION

5.1 INTRODUCTION

Particle size determination is very essential and important while working with nanomaterials. There are a few good experimental techniques, which are currently used by the researchers worldwide, for particle size determination. XRD, SEM, TEM, SPM, and particle size analyzers are some of the efficient and reliable techniques which can precisely determine particle size of the nanomaterials depending on the type of the material. In the present work, the following techniques have been employed to determine the particle size of the materials prepared, by novel method in present investigation.

Experimental techniques used to determine the particle size of the samples are:

1. X-ray Diffraction.
2. Scanning Electron Microscope (SEM).
3. Transmission Electron Microscope (TEM) and High Resolution Transmission Electron Microscope (HRTEM)
4. Scanning Probe Microscope (SPM).

5.2 POWDER X- RAY DIFFRACTION

From the X-Ray diffraction pattern obtained for the samples the particle size of the crystallites in the sample was determined using Scherrer's formula after applying particle strain corrections using Williamson's Hall analysis. The details of these calculations are as given in Section 4.5.3 of Chapter IV.

5.3 SCANNING ELECTRON MICROSCOPE (SEM)

The Scanning Electron Microscope images of the surface of the sample under measurement by scanning it with a high-energy beam of electrons. SEM gives topographical as well as chemical composition [1]. In SEM, accelerated electrons carry significant amounts of kinetic energy that is dissipated in the sample during the interaction of these electrons with the surface atoms in the sample as a result of which multiple signals are produced. Appropriate signals are collected depending upon the mode of operation of the instrument. Signals produced by SEM are secondary electrons, backscattered electrons (BSE), characteristics X rays, light (cathodoluminescence), specimen current and transmitted electrons. SEM can produce very high-resolution magnified images of a sample surface, revealing details about less than 1 to 5nm in size. SEM micrographs have a large depth of field due to its very narrow electron beam which yields a characteristic three-dimensional appearance useful for understanding the surface structure of a sample. Secondary electrons and backscattered electrons are commonly used for imaging samples.

Since the intensity of the BSE signal is strongly related to the atomic number (Z) of the specimen, BSE images can provide information about the distribution of different elements in the sample.

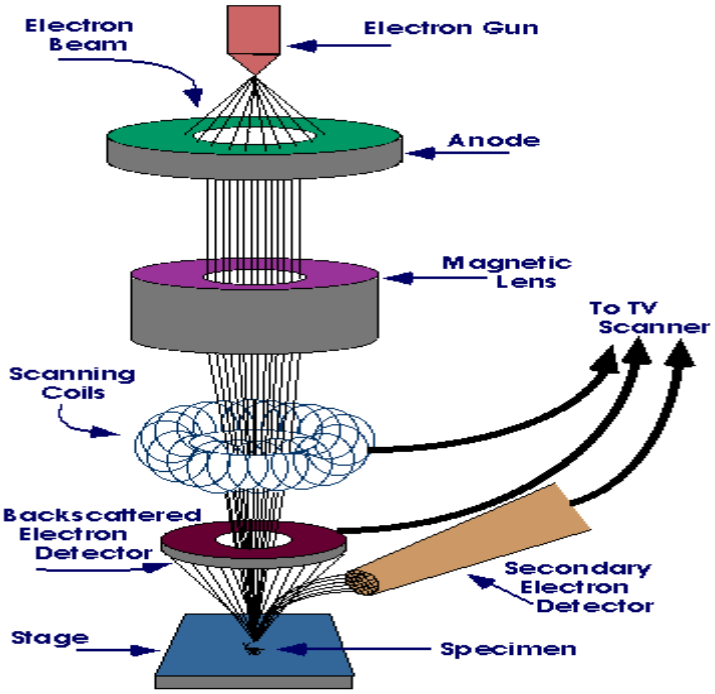

Fig. 5.1(a) Schematic Diagram of Scanning Electron Microscopy (SEM)

Fig.5.1 (b) : JOEL Model JSM 6360LV (SEM)

Fig. 5. 1 (c) JEOL Model 840 (SEM)

A typical photograph of SEM instrument, showing the electron column, sample chamber, EDS detector, electronics console, and visual display monitor is shown in the fig. 5.1 (b, c)

5.4 TRANSMISSION ELECTRON MICROSCOPY (TEM)

The Transmission Electron Microscope (TEM) has emerged as a powerful tool for probing the structure of metals and alloys. It can give morphological information of shape and size of particles in a microstructure. It can also reveal the nature of crystallographic defects. A detail study of both line defects and planar defects can be carried out in the TEM. Indirect structural information is obtained by making use of the various diffraction techniques available in the TEM. It is capable of yielding composition analysis at nanolevel. With its multifaced capabilities such as nano-beam diffraction and composition analysis and imaging abilities at angstrom level, it has emerged as an instrument for complete characterization of microstructure of materials. TEM's are available in several different forms, which are referred by different acronyms such as HRTEM (High resolution TEM), STEM (Scanning TEM) and ATEM (Analytical TEM).

Fig. 5.2 (a) : TEM Philip model CM 200, electron beam of 200Kev

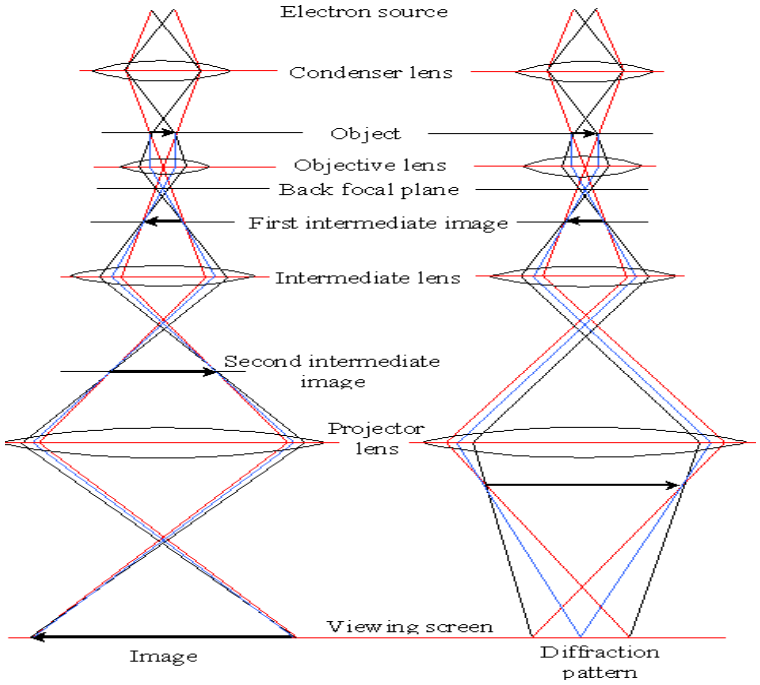

(b) (c)

Figure 5.2 (b,c) The two basic operations of TEM imaging system. (b) Imaging mode and (c) Diffraction pattern

The basic TEM's comprise an electron gun, a vacuum system, electromagnetic lenses, high voltage generator, recording devices and the associated electronics. In order to get the best images, best diffraction effects and the chemical analysis capabilities, the best available electron source needs to be used. The resolution of the modern TEM is under 0.2 nm (point to point) even with a fair amount of specimen tilt. These microscopes are, therefore, capable of resolving the structure of different phases in most metals and alloys.

TEM use low wavelength electron which makes it possible to get a high resolution image. A well focused electron beam obtained from electron gun assembly and electromagnetic condenser lenses is accelerated by an anode, which is typically at +100 keV (in the selective range of 40KeV to 400 keV) with respect to the cathode. The beam is restricted by the condenser aperture, which stops or eliminates un-colliminated electrons. The colliminated high energy (200 Kev and above) beam of electrons strikes the specimen and gets scattered depending upon the thickness and electron transparency of the specimen. Part of the scattered electron beam undergoing phase and amplitude change during scattering is transmitted and the same is focused by the objective lens which forms an image on phosphor screen or charge coupled device (CCD) camera. Adjustable objective apertures can be used to enhance the contrast by blocking out high-angle diffracted electrons.

There are two basic modes of TEM operation: diffraction patterns and imaging modes. As the beam of electrons passes through a crystalline specimen, it is scattered according to the Bragg's law. In order to observe the diffraction pattern, imaging system lenses are adjusted so that the back focal

plane of the objective lens acts as the object plane for the intermediate lens. Then the diffraction pattern is projected onto the viewing screen (Fig.5.2 (c)). While for the imaging mode, the intermediate lens is adjusted so that its object plane is the image plane of the objective lens. The image is then projected onto the viewing screen (Fig 5.2 (b)).

Modern TEM has about five to six image forming lenses. The final image is projected on the screen. The diffraction pattern forms on the back focal plane of the objective lens and the first image forms on the back plane of the objective lens. If the image forming lenses following the objective lens are adjusted in such a way that these see the back focal plane of the objective lens as the object then what one sees on the screen is the diffraction pattern.

However, if the lenses are excited in such a way that these see the back image plane of the objective lens as an object then what we see on the screen is the image of specimen. Therefore, in a modern TEM it is possible to switch from diffraction to imaging and vice-versa by changing the excitation of the lenses following the objective lens. TEM can be used to image the specimen by focusing the final image in the plane of the fluorescent screen or it can be used to image the diffraction pattern from the specimen.

5.4.1. High Resolution Transmission Electron Microscopy (HRTEM)

High-resolution transmission electron microscopy (HRTEM) is an imaging mode of the transmission electron microscope (TEM) that allows the imaging of the crystallographic structure of a sample at an atomic scale [2]. HRTEM can produce images with high resolution below 0.5 Angstrom [3] at magnifications above 50 million times [4]. Because of its high resolution and ability to determine the positions of atoms within materials, it has become a

powerful tool to study nanoscale properties of crystalline materials in nano-technology research and development [5].

The basic working principle of HRTEM is that when a plane wave of electrons is incident on the sample surface, it is attracted by the positive atomic potentials of the atom cores, and channels along the atom columns of the crystallographic lattice. All lattice planes satisfying the Braggs position will diffract the primary beam.The diffraction pattern is the Fourier transform of the periodic potential for the electrons in two dimensions.

In the objective lens, all the diffracted beams and primary beam are brought together and their interference provides a back transformation and leads to enlarged picture of periodic potential. The picture is then magnified by the electron -optical system and finally seen on the screen at a magnefication of around10^6. This imaging process is called phase contrast imaging or high resolution imaging. Due to the inability to record phase of these waves, generally amplitude is measured from these interference pattern. However the phase of the electron wave still carries the information about the sample and generates constrast in the image.

5.5 SCANNING PROBE MICROSCOPE

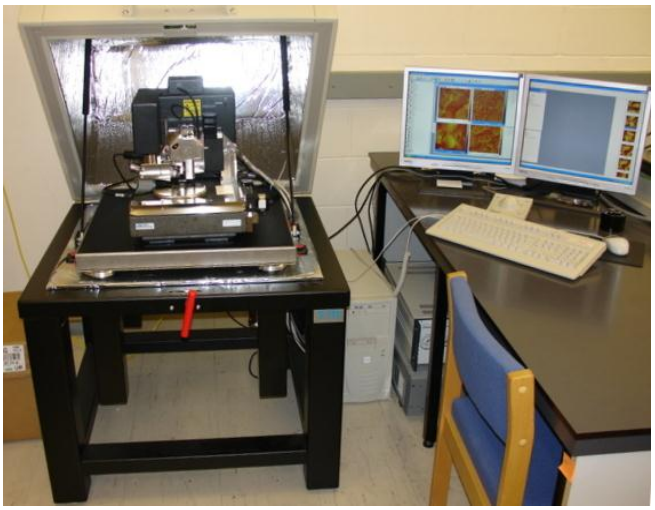

Fig. 5.3 (a) SPM d,I- CALLIBER Model

Scanning probe microscopes (SPM) allows to image, characterize material structures at exceedingly small scales including features of atomic proportions. Scanning probe microscope uses a probe called cantilever that interacts with the sample surface. SPM consist of two major members: Scanning tunneling microscope used for electrically conductive materials, and Atomic Force Microscope for dielectrics.

5.5.2 Scanning tunneling microscope

A Scanning Tunneling Microscope (STM) is an instrument for imaging surfaces at the atomic level. The STM is based on the concept of quantum tunneling. STM can be operated in two modes. In constant current imaging, conductive tip is positioned above the surface of the sample. When the tip moves back and forth across the sample surface at very small intervals, the

height of the tip is contineously adjusted to keep the tunneling current constant. The tip positions are used to construct a topographic map of the surface.

An alternate imaging mode is the constant height operation mode, in which constant height and the bias are simultaneously maintained. As the tip scans the surface, there is a variation in curent due to topographic structure of the sample. Constant current mode produces a contrast directly related to electron charge density profiles of the surface being scanned, whereas the constant height mode permits faster scan rates.

5.5.3 The Atomic Force Microscope

The atomic force microscope (AFM) probes the surface of a sample with a sharp tip, a couple of microns long and often less than 100Å in diameter. The tip is located at the free end of a cantilever that is 100 to 200μm long.

When the tip is brought into proximity of a sample surface, forces between the tip and the sample lead to a deflection of the cantilever. Typically, the deflection is measured using a laser spot reflected from the top surface of the cantilever into an array of photodiodes. Laser light is reflected from the back of the cantilever and is collected by a position sensitive detector (PSD) consisting of two closely spaced photodiodes whose output signal is collected by a differential amplifier. Angular displacement of the cantilever results in one photodiode collecting more light than the other photodiode, producing an output signal which is proportional to the deflection of the cantilever. The measured cantilever deflections allow a computer to generate a map of surface

topography. AFM can be used to study insulators and semiconductors as well as electrical conductors. The primary modes of operation for an AFM are static mode and dynamic mode. In static mode, the cantilever is dragged across the surface of the sample and the contours of the surface are measured directly using the deflection of the cantilever. Static mode AFM is always done in contact where the overall force is repulsive. Consequently, this technique is typically called "contact mode". In contact mode, the force between the tip and the surface is kept constant during scanning by maintaining a constant deflection.

In the dynamic mode or Non-contact mode the cantilever is externally oscillated at or close to its fundamental resonance frequency or a harmonic, where the amplitude of oscillation is typically a few nanometers. The oscillation amplitude, phase and resonance frequency are modified by tip-sample interaction forces. These changes in oscillation with respect to the external reference oscillation allow the scanning software to construct a topographic image of the sample surface.

Dynamic mode operation includes frequency modulation and amplitude modulation. In frequency modulation, changes in the oscillation frequency provide information about tip-sample interactions. In amplitude modulation, changes in the oscillation amplitude or phase provide the feedback signal for imaging. In amplitude modulation, changes in the phase of oscillation can be used to discriminate between different types of materials on the surface. In dynamic contact mode, the cantilever is oscillated such that the

separation distance between the cantilever tip and the sample surface is modulated.

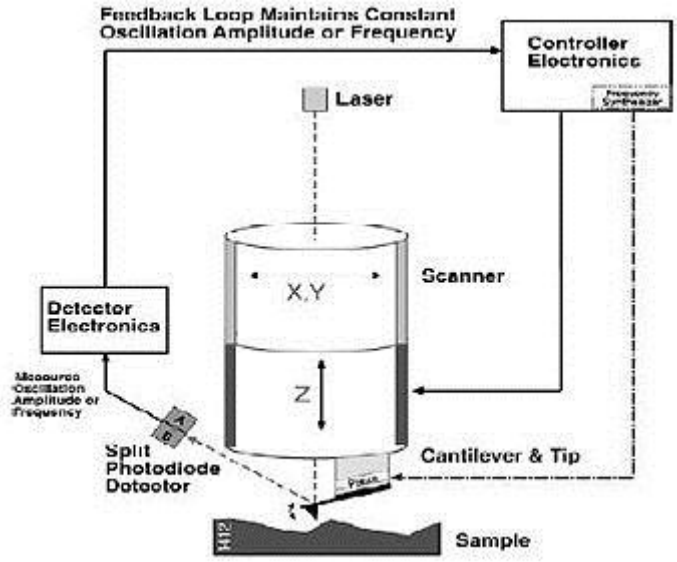

Fig. 5.3 (b) AFM - non-contact mode

AFM has several advantages over the scanning electron microscope (SEM). Unlike the electron microscope, which provides a two-dimensional projection or a two-dimensional image of a sample, the AFM provides a three-dimensional surface profile.

5.6 EXPERIMENTAL

1. XRD Pattern for the powdered samples were obtained on microcomputer controlled Rigaku Diffractometer using Cu K_α(λ=1.5418 Å) from 20^o to 80^o and XRD Desktop miniflex-II (λ=1.5408 Å)

Average particle size estimation was done by substituting XRD peak broadening in Scherrer's formula. Cation distribution, bond length and hopping lengths were calculated using the same.

2. Scanning electron micrograph of powdered sample were obtained on JEOL MODEL 840 and JOEL JSM 6360LV instrument at the accelerating voltage of 10KV

The experimental technique used for determination of SEM micrographs is similar to the one employed for EDS determination, as describe in chapter IV.

3. Transmission electron micrographs are taken on FEI TECNAI 200KV HRTEM and Philip model CM 200 TEM with resolution 0-23nm having an electron beam of 200KeV.

4. Scanning probe micrograph were taken on d- I-CALLIBER SPM and High Resolution Flex AFM

These measurements were carried out to confirm the formation of ultra fine particle size material and to study the surface morphology of sintered samples. Nanoparticles were immobilized on a glass slide on top of a permanent magnet. The particles were imaged by dynamic mode in a High resolution Flax AFM and d, I- CALLIBER SPM.

5.7 RESULTS AND DISCUSSION

5.7.1 Particle Size Estimation

The particle size values obtained for the samples using Scherrer formula after applying Williamson's Hall Plot correction and from TEM are listed in Table 5.1 (a)

Table 5.1 (a): Particle size for nanosamples using XRD and TEM.

Sample	Average particle size 't' (by Williomson Hall Plot) in nm	Average particle size 't' (by using TEM) in nm
$Mn_{0.4}Zn_{0.6}Fe_2O_4$	36.05	30.04(6.43)
$Mn_{0.5}Zn_{0.5}Fe_2O_4$	10.43	10.34(2.20)
$Mn_{0.6}Zn_{0.4}Fe_2O_4$	34.06	39.31(8.44)
$Mn_{0.625}Zn_{0.375}Fe_2O_4$	12.82	11.13(2.17)
$Mn_{0.65}Zn_{0.35}Fe_2O_4$	21.68	8.9(1.71)
$Mn_{0.675}Zn_{0.325}Fe_2O_4$	20.90	13.66(2.69)
$Mn_{0.7}Zn_{0.3}Fe_2O_4$	22.45	15.54(4.06)
$Mn_{0.8}Zn_{0.2}Fe_2O_4$	21.64	21.89(3.86)

5.7.2 Estimation of the Cation Distribution

Spinel ferrite with formula $MeFe_2O_4$ contains two types of sites: tetrahedral site and octahedral sites. The distribution of the cations over these two types of sites can be expressed as [6]

$$Me_{\gamma}\ Fe_{1-\gamma}\ [\ Me_{1-\gamma}\ Fe_{1+\gamma}]\ O_4$$

where the square bracket include the ions at the octahedral sites, and γ is a constant which can determine the cation distribution. For the system under investigation $Mn_xZn_{1-x}Fe_2O_4$, the cation distribution can be expressed as

$$Zn_{\delta}\ Mn_{\gamma}\ Fe_{1-\gamma-\delta}\ [\ Zn_{1-x-\delta}\ Mn_{x-\gamma}\ Fe_{1+\gamma+\delta}\ ]\ O_4$$

Therefore, the mean radius of the ion at the tetrahedral site is given by

$$r_{tetr} = \delta\ r_{Zn} + \gamma\, r_{Mn} + (1-\gamma-\delta)\, r_{Fe}$$

and the mean radius of the ion at the octahedral site is given by

$$r_{oct.} = \frac{1}{2}[\ (1-x-\delta) r_{Zn} + (x-\gamma)\, r_{Mn} + (1+\gamma+\delta)\, r_{Fe}\ ]$$

From the other hand also, the mean radius of the ions at tetrahedral site and octahedral site is given by [**7]**

$$r_{tetr.} = a\sqrt{3}\ (u - 0.25) - R_o$$

$$r_{oct.} = a\ (\frac{5}{8} - u) - R_o$$

where R_o is the radius of the oxygen ion (1.26 Å) and u is the oxygen parameter. Solving above Eqns. both δ and γ can be determined. Table (5.1 (b)) shows the estimated cation distribution for these samples.

Table 5.1 (b): Estimated cation distribution for $Mn_xZn_{(1-x)}Fe_2O_4$ using X-ray results.

Sample	Tetrahedral Site	Octahedral Site
$Mn_{0.4}Zn_{0.6}Fe_2O_4$	Mn(0.363)Zn(0.114)Fe(0.523)	Mn(0.037)Zn(0.486)Fe(1.477)
$Mn_{0.5}Zn_{0.5}Fe_2O_4$	Mn(0.358)Zn(0.126)Fe(0.517)	Mn(0.142)Zn(0.374)Fe(1.483)
$Mn_{0.6}Zn_{0.4}Fe_2O_4$	Mn(0.359)Zn(0.147)Fe(0.494)	Mn(0.241)Zn(0.253)Fe(1.506)
$Mn_{0.625}Zn_{0.375}Fe_2O_4$	Mn(0.360)Zn(0.153)Fe(0.487)	Mn(0.265)Zn(0.222)Fe(1.513)
$Mn_{0.65}Zn_{0.35}Fe_2O_4$	Mn(0.362)Zn(0.163)Fe(0.475)	Mn(0.288)Zn(0.187)Fe(1.525)
$Mn_{0.675}Zn_{0.325}Fe_2O_4$	Mn(0.366)Zn(0.183)Fe(0.452)	Mn(0.309)Zn(0.142)Fe(1.548)
$Mn_{0.7}Zn_{0.3}Fe_2O_4$	Mn(0.366)Zn(0.181)Fe(0.454)	Mn(0.334)Zn(0.119)Fe(1.546)
$Mn_{0.8}Zn_{0.2}Fe_2O_4$	Mn(0.362)Zn(0.192)Fe(0.446)	Mn(0.438)Zn(0.008)Fe(1.554)

5.7.3 The Interionic Distances

The interionic distances *(i.e.* cation–anion distances at A-site, d_{AL}, and B-site, d_{BL}, together with the distance of closest anion–anion approach, tetrahedral edge, d_{AE}, and shared and unshared octahedral edges, d_{BE}, d_{BEU}) are calculated according to the following Eqns. [8]:

$$d_{AL} = a\ \sqrt{3}\left(u - 0.25\right)$$

$$d_{BL} = a\left(3u^2 - \frac{11}{4}u + \frac{43}{64}\right)^{1/2}$$

$$d_{AE} = a\sqrt{2}\left(2u - 0.5\right)$$

$$d_{BE} = a\sqrt{2}\left(1 - 2u\right)$$

$$d_{BEU} = a\left(4u^2 - 3u + \frac{11}{16}\right)^{1/2}$$

The obtained values are listed in Table 5.1 (c)**.** It is clear that the values of d_{AL}, d_{BL}, d_{AE}, d_{BE}, and d_{BEU} increase with increasing Mn ion content. This variation may be attributed to the substitution process and the cation distribution.

The distance L_A and L_B between the magnetic ions at A–site and B–site respectively can be obtained, where, $L_A = a\sqrt{3}/4$**,** and $L_B = a\sqrt{2}/4$ [9]. The obtained values of L_A and L_B are listed in Table 5.1 (c) Maximum value of L_A is 3.666A^o for the sample $Mn_{0.8}Zn_{0.2}Fe_2O_4$ and minimum value of L_A is 3.648 A^o for the sample $Mn_{0.4}Zn_{0.6}Fe_2O_4$ at A-site. Maximum value of L_B is 2.993

Å and minimum value is 2.978 Å at B- site for the samples $Mn_{0.8}Zn_{0.2}Fe_2O_4$ and the sample $Mn_{0.4}Zn_{0.6}Fe_2O_4$ respectively.

Table 5.1 (c): The bond length of A-sites d_{AL} and B-sites d_{BL}, the tetrahedral edge d_{AE}, the shared and unshared octahedral edges, d_{BE} and d_{BEU}, and the hopping length at A-site L_A and at B-site L_B for each sample.

Sample	d_{AL} Å	d_{BL} Å	d_{AE} Å	d_{BE} Å	d_{BEU} Å	L_A Å	L_B Å
$Mn_{0.4}Zn_{0.6}Fe_2O_4$	1.824	2.106	2.978	2.978	2.978	3.648	2.978
$Mn_{0.5}Zn_{0.5}Fe_2O_4$	1.825	2.107	2.979	2.979	2.979	3.649	2.979
$Mn_{0.6}Zn_{0.4}Fe_2O_4$	1.827	2.110	2.983	2.983	2.983	3.654	2.983
$Mn_{0.625}Zn_{0.375}Fe_2O_4$	1.828	2.111	2.985	2.985	2.985	3.656	2.985
$Mn_{0.65}Zn_{0.35}Fe_2O_4$	1.829	2.113	2.987	2.987	2.987	3.659	2.987
$Mn_{0.675}Zn_{0.325}Fe_2O_4$	1.831	2.114	2.990	2.990	2.990	3.663	2.990
$Mn_{0.7}Zn_{0.3}Fe_2O_4$	1.832	2.115	2.991	2.991	2.991	3.665	2.991
$Mn_{0.8}Zn_{0.2}Fe_2O_4$	1.833	2.116	2.993	2.993	2.993	3.666	2.993

5.7.4 SEM Micrograph

SEM Micrograph of nanosamples:

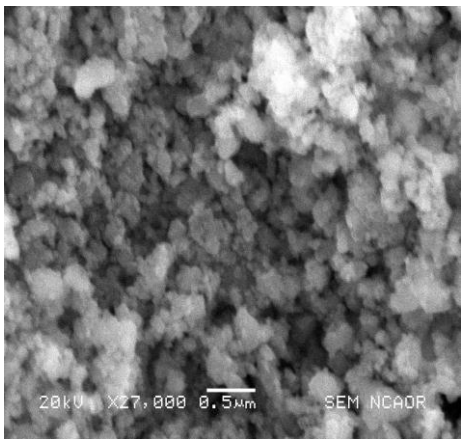

5.4 (a): SEM Micrograph of $Mn_{0.675}Zn_{0.375}Fe_2O_4$

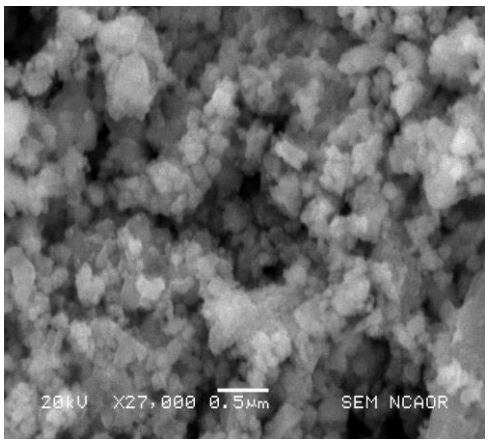

5.4 (b) SEM Micrograph of $Mn_{0.6}Zn_{0.4}Fe_2O_4$

SEM image of nanosamples is not well resolved, because samples are highly magnetic and intensity of electron beam of SEM may not be sufficient to provide the required resolution to make estimates of nanoparticle sizes. Thus the particles are not well resolved and magnified. This fact makes it impossible to make accurate estimates of particle size distribution of SEM image of nanosamples.

SEM Micrographs of sintered samples and the particle size histograms of the same are given in the corresponding figures below:

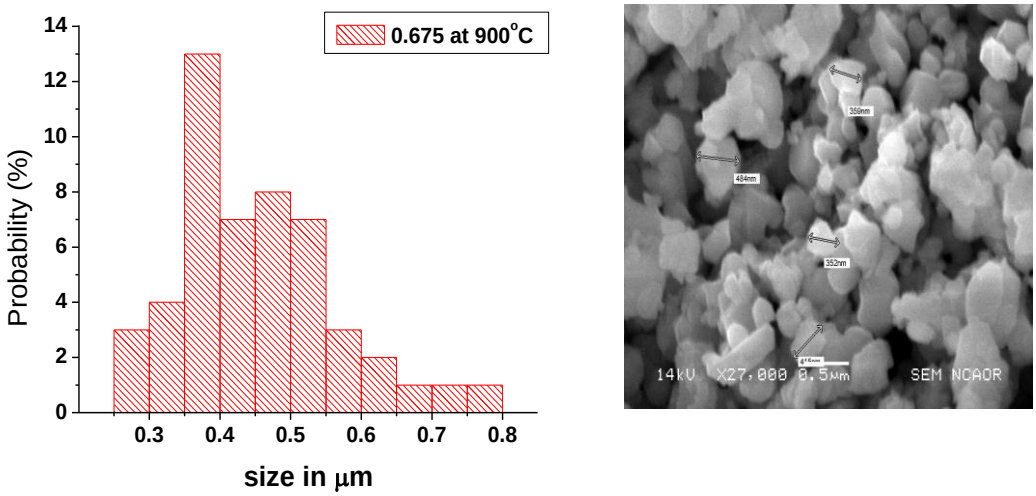

Fig.5.4 (c) SEM Micrograph of bulk sample $Mn_{0.675}Zn_{0.325}Fe_2O_4$ (900°C)

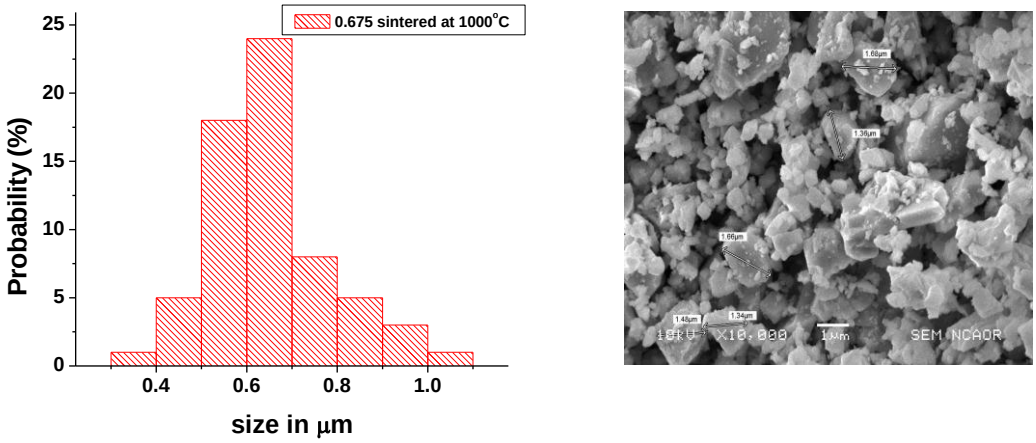

Fig.5.4 (d) SEM Micrograph of bulk sample $Mn_{0.675}Zn_{0.325}Fe_2O_4$ (1000°C)

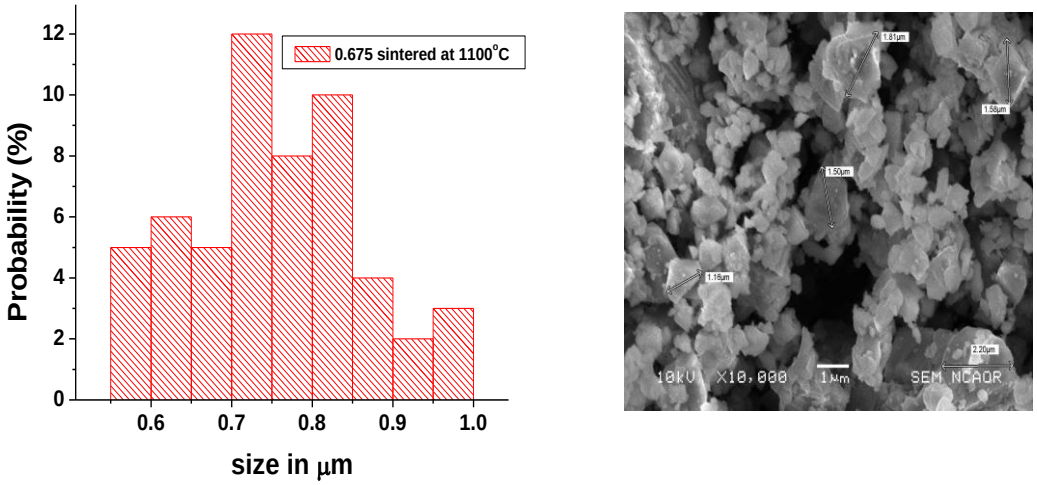

Fig.5.4 (e) SEM Micrograph of bulk sample $Mn_{0.675}Zn_{0.325}Fe_2O_4$ (1100°C)

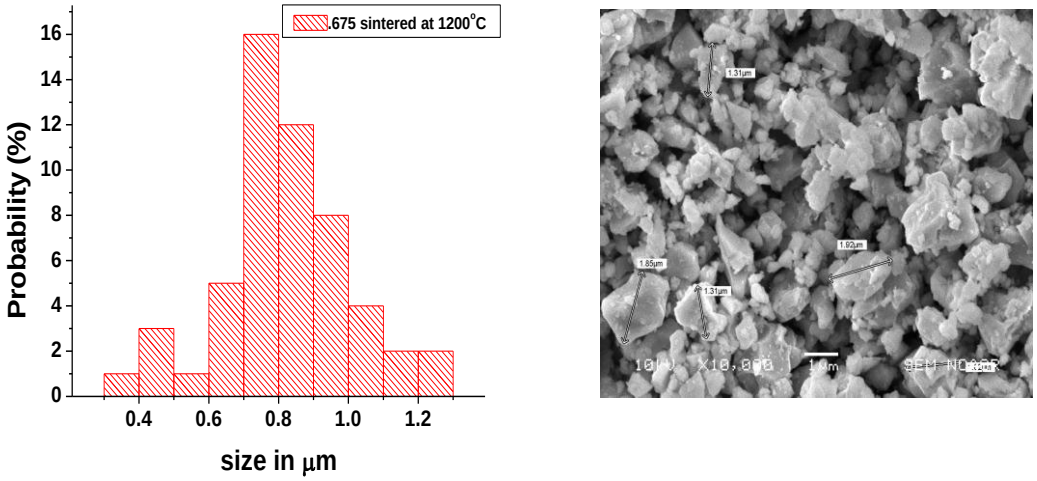

Fig.5.4 (f) SEM Micrograph of bulk sample $Mn_{0.675}Zn_{0.325}Fe_2O_4$ (1200°C)

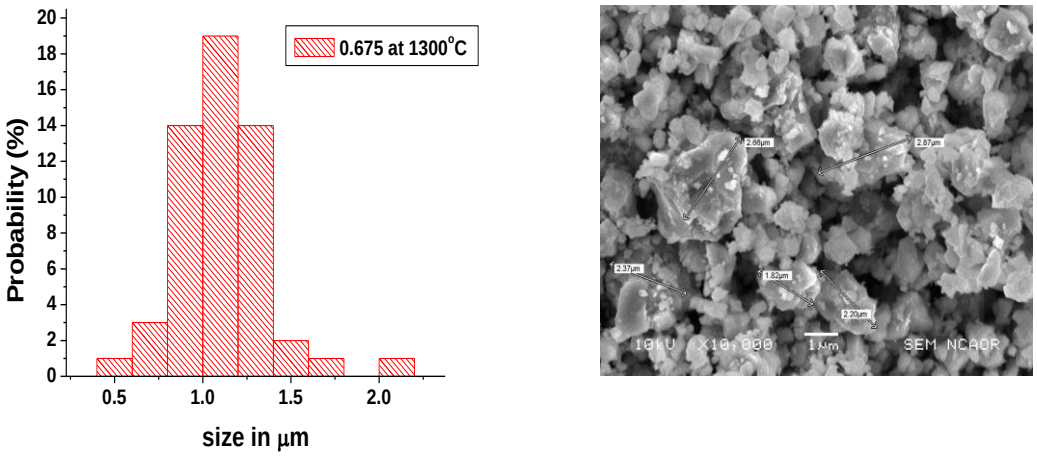

Fig.5.4 (g) SEM Micrograph of bulk sample $Mn_{0.675}Zn_{0.325}Fe_2O_4$ (1300°C)

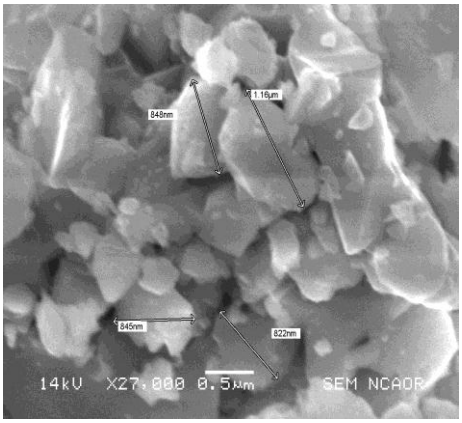

Fig. 5.4(h) bulk sample $Mn_{0.6}Zn_{0.4}Fe_2O_4$ (1100^oC)

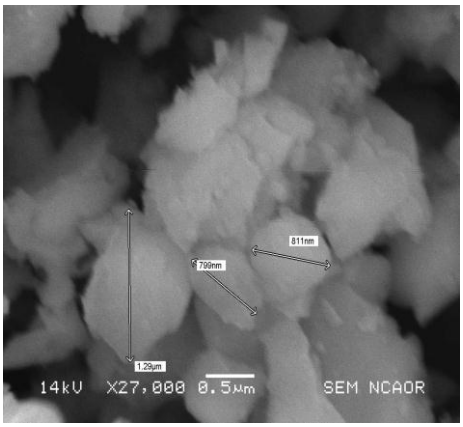

Fig. 5.4(i) bulk sample$Mn_{0.6}Zn_{0.4}Fe_2O_4$ (1300^oC)

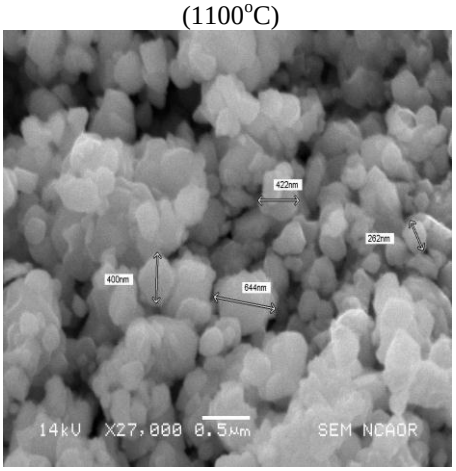

Fig. 5.4(j) bulk sample $Mn_{0.625}Zn_{0.375}Fe_2O_4$ (1000^0C)

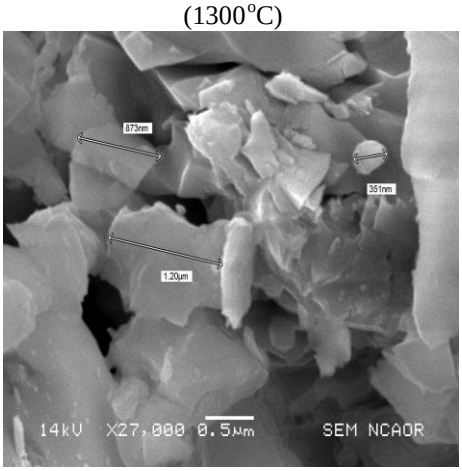

Fig. 5.4(k) bulk sample $Mn_{0.625}Zn_{0.375}Fe_2O_4$ (1200^0C)

Fig. 5.4 (h,i) SEM micrograph of bulk sample $Mn_{0.6}Zn_{0.4}Fe_2O_4$ (1100^0C, 1300^0C) and 5.4 (j.k) SEM micrograph of bulk sample $Mn_{0.625}Zn_{0.375}Fe_2O_4$ (1000^0C, 1200^0C)

Particle size of fifty individual particles was determined using image J software to obtain the histogram for particle size distribution. The histogram of bulk sample $Mn_{0.675}Zn_{0.35}Fe_2O_4$ obtained at 900^oC shows that the maximum size distribution is in the range of 0.35µm to 0.55µm. At 1000^oC, maximum size distribution is in the range of 0.5µm to 0.7µm, which increases to 0.7 µm to 0.9µm at 1200 ^oC, whereas for the same sample sintered at 1300^oC, the

maximum size distribution is in the range of 0.75µm to 1.5µm. These results indicate that particle size of bulk samples increase with increase in sintering temperature as expected.

5.8 TEM Micrograph

Fig. 5.5 (a, b, c, d, e, f) are the TEM Micrographs of samples and the corresponding histograms for particle size.

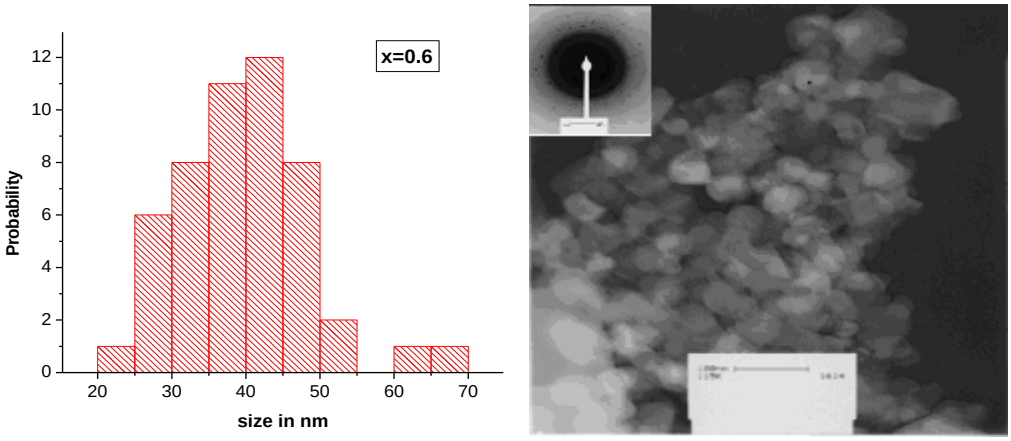

Fig.5. 5 (a) TEM micrograph & Histogram of $Mn_{0.6}Zn_{0.4}Fe_2O_4$

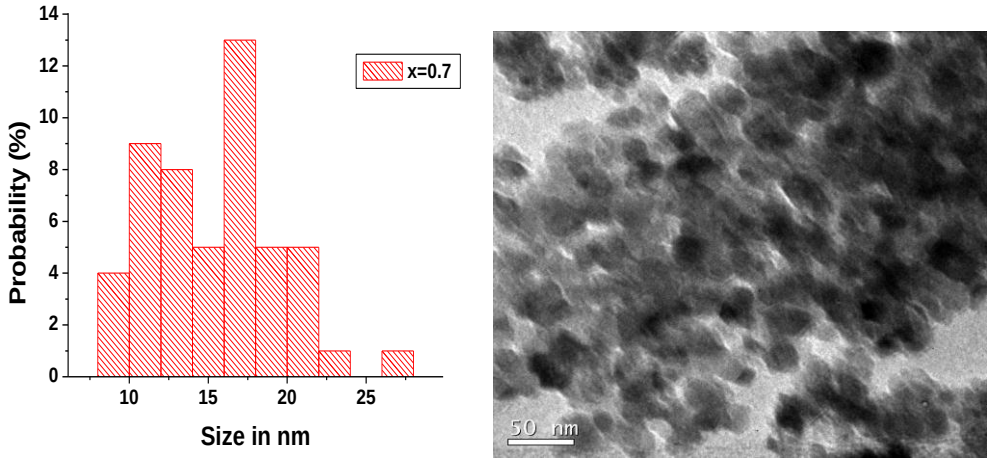

Fig.5.5 (b) TEM micrograph & Histogram of $Mn_{0.7}Zn_{0.3}Fe_2O_4$

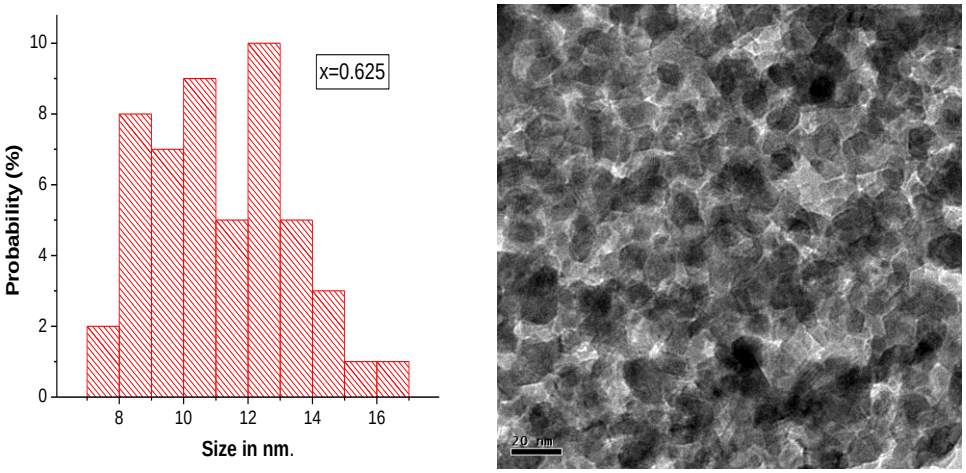

Fig.5.5 (c) HRTEM Micrograph and Histogram of $Mn_{0.625}Zn_{0.375}Fe_2O_4$

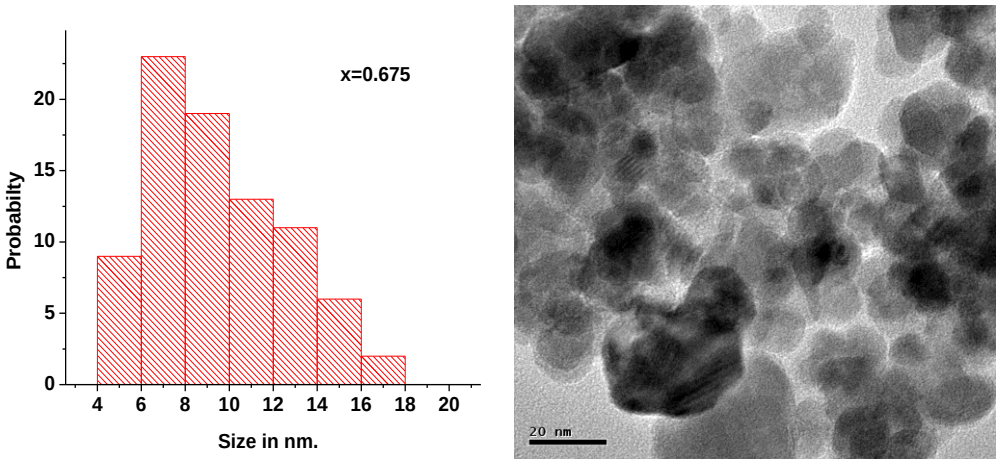

Fig. 5.5 (d) HRTEM Micrograph and Histogram of $Mn_{0.675}Zn_{0.0.325}Fe_2O_4$

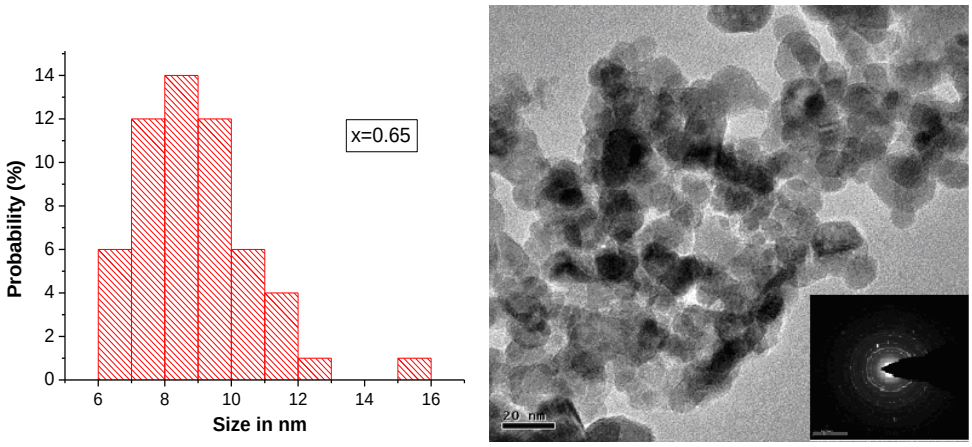

Fig.5. 5 (e) HRTEM micrograph and Particle Size Histogram of $Mn_{0.65}Zn_{0.35}Fe_2O_4$

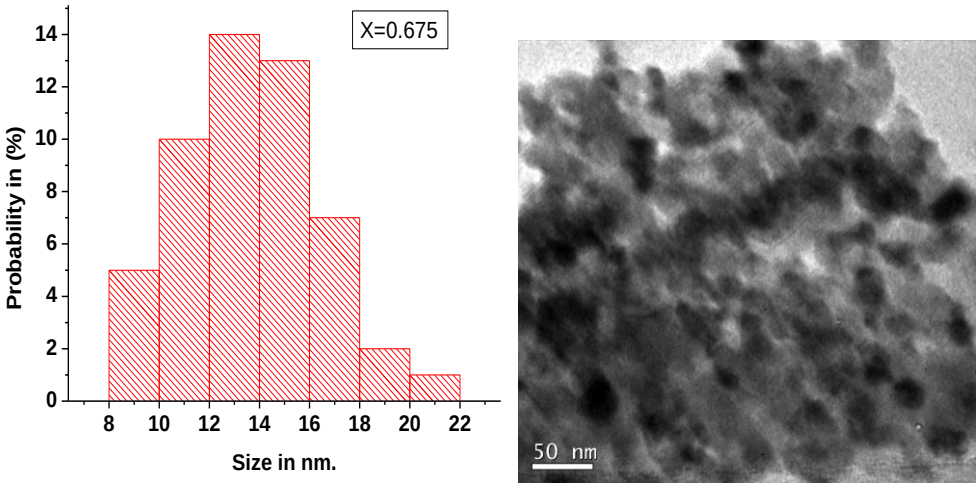

Fig.5. 5 (f) HRTEM Micrograph and Histogram of $Mn_{0.675}Zn_{0.0.325}Fe_2O_4$

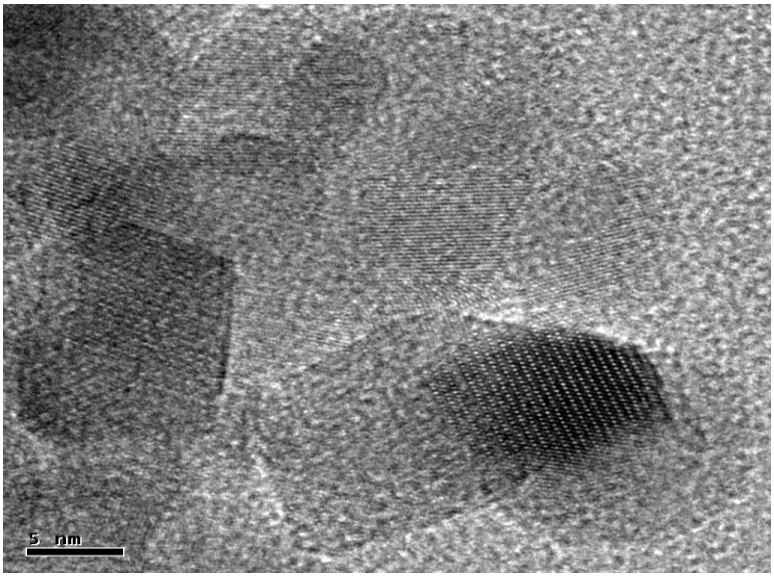

Fig.5.6 (a) HRTEM micrograph $Mn_{0.65}Zn_{0.35}Fe_2O_4$

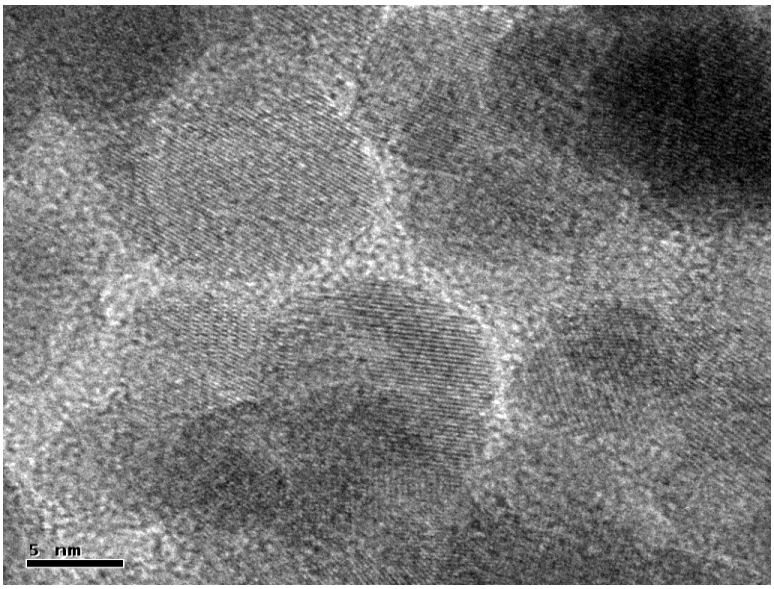

Fig. 5.6 (b) HRTEM micrograph $Mn_{0.65}Zn_{0.35}Fe_2O_4$

The average size of nanoparticles calculated from the peak broadening, and after applying Williamsons Hall Plot correction for particle strain broadening in the x-ray diffraction pattern by using Scherrer formula [10], gives an overall particle size for the samples in the range of 10 nm to 36 nm. However the average particle size of the same samples seen from TEM and

HRTEM is in the range of 8 to 40 nm. This is in good agreement with the particle size estimated from Scherrer formula.

Transmission electron microscopy (TEM) and High Resolution microscopy have been used to confirm the nanoparticle size and to determine the particle size distribution. The size distribution has been determined from the histogram obtained by measuring the size of around sixty individual particles using image J software. The histogram of sample $Mn_{0.60}Zn_{0.40}Fe_2O_4$, shows that the maximum size distribution is in the range of 35nm to 45nm, for the sample $Mn_{0.7}Zn_{0.3}Fe_2O_4$, it is in the range of 16nm to 18nm, for the sample $Mn_{0.625}Zn_{0.375}Fe_2O_4$ it is in the range of 8nm to 13nm, and for the sample $Mn_{0.65}Zn_{0.35}Fe_2O_4$, it is in the range of 7nm to 10nm.The high resolution TEM image of $Mn_{0.65}Zn_{0.35}Fe_2O_4$, shows clearly the lattice fringes of these nanocrystallites (Fig.5.6 (a) & 5.6 (b)).

5.9 Scanning Probe Microscope

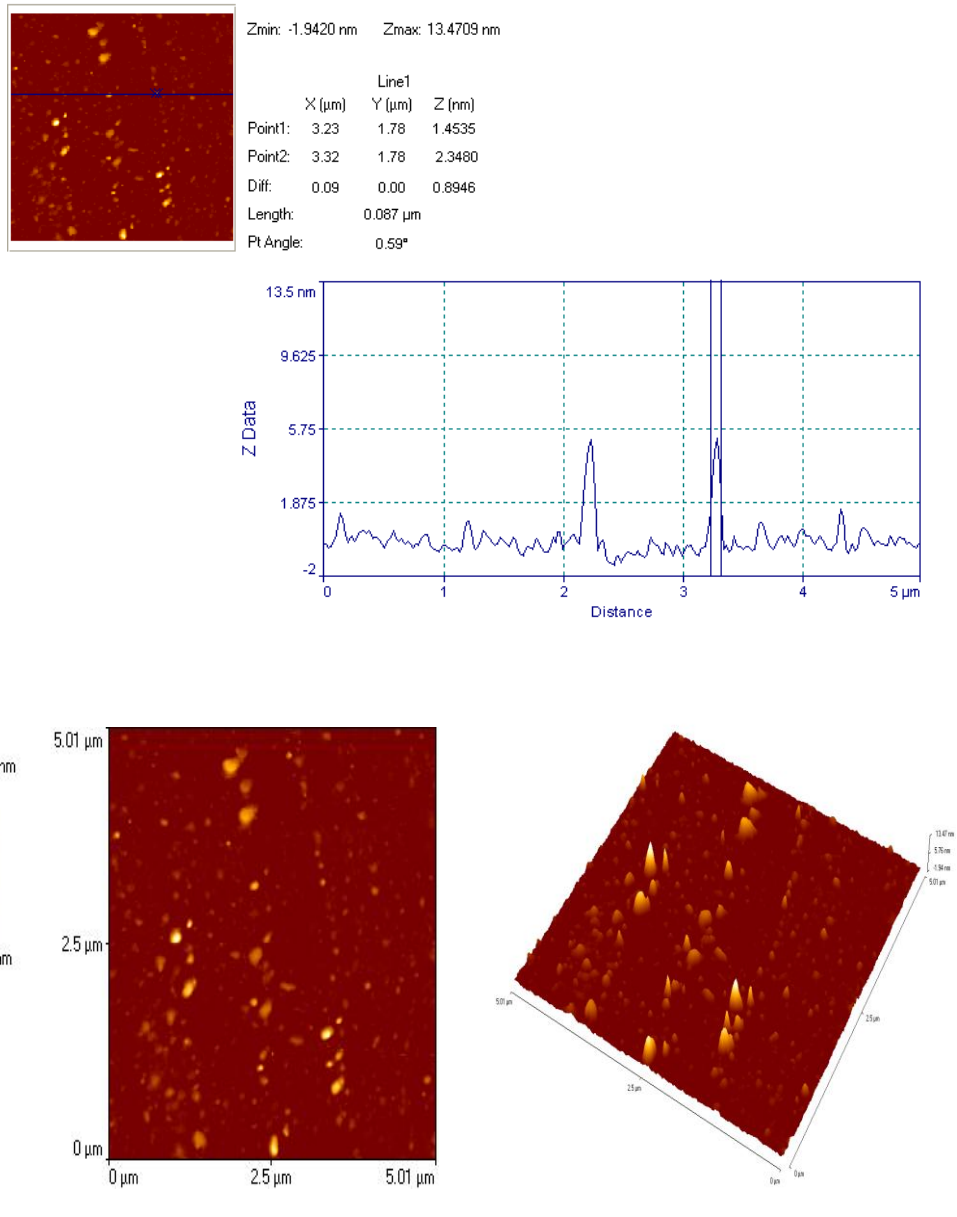

5.7 SPM Micrograph of nanosample $Mn_{0.6}Zn_{0.4}Fe_2O_4$

SPM Micrograph of nanosample $Mn_{0.6}Zn_{0.4}Fe_2O_4$ provides three dimensionional information of the particle size (Fig.5.7). Particle size analysis carried out on SPM micrographs indicates formation of polycrystalline fine grain material with one dimension in nanometer. Particles of different sizes are visible in the Fig.5.7.

In conclusion, the particle size analyses carried with the help of the XRD and the most modern microscopy tools like TEM, HRTEM, and SPM, show that all the samples under investigation, prepared using the new preparative technique are nanoparticle, and some of the samples have a narrow range of particle size distribution. Thus, the new method developed can be used as a potential method for production of nanoparticle Mn-Zn ferrite materials.

References

[1] Guozhonq Cao, Nanostructures and Nanomaterials, synthesis, Properties and Applications, publication 2004, Reprinted 2005, 2006, Imperial college press.

[2] R. W. Cahn, P. Haasen, E. J. Kramer, Material Science and Technology Vol.2A, VCH-Weinheim-Newyork.

[3] R. W. Cahn, P. Haasen, E. J. Kramer, Material Science and technology Vol.2B, VCH-Weinheim-Newyork.

[4] P. J. Goodhew and F. J. Humhreys, Taylor and Francis, Electron Microscopy and Analysis, London ,(1988).

[5] D. B. Williams and C. B. Carter, Transmission Electron Microscopy, Plenum Press, Newyork, (1996).

[6] A. A. Yousif, M. E. Elzain, S. A. Mazen, H. H. Sutherland, M. H. Abdalla, and S. F. Mansour, J. Phys. Condens. Matter **6**, 5717 (1994).

[7] J. Smit and H. P. J. Wijn, "Ferrites", Cleaver-Hume. Press, London, (1959).

[8] C. Otero Arean, E. Garcia Diaz, J. M. Rubio Gonzalez and M. A. Villa Garcia, J. Sol. State Chem. **77** (1988) 275.

[9] B. Gillot and F. Jemmali, phys. stat. sol. (a) **76** (1983) 601.

[10] B. D. Cullity, Elements of X-ray Diffraction, 2nd edition, Addison Weseley (1978).

CHAPTER VI

MAGNETIC PROPERTIES

6.1 INTRODUCTION

In this chapter a systematic presentation of the results of Neutron Diffraction, further confirming the formation of the samples along with cation distribution and magnetic moment calculations per site are presented. A detailed discussion on magnetic properties measurement made on nanoparticle ferrite materials prepared forms the main content of this chapter. The magnetic properties being important in deciding about the importance of the nanomagnetic materials, adequate stress has been given to measure magnetic properties using different modern equipments and to analyze the data and apply the appropriate models wherever possible for the data analysis. The properties under investigation were measured with the following equipments and facilities:

1. Neutron Diffraction using powder Diffractometer
2. Hysteresis Loop Tracer
3. Vibrating Sample Magnetometer (VSM)
4. Superconducting Quantum Interference Device (SQUID)
5. Mossbauer Spectra using Moussbauer spectrometer.
6. A. C. Susceptibility Apparatus
7. Magnetic Permeability using Wayne Kerr Pression component Analyser.

6. 2 NEUTRON DIFFRACTION

Neutron Diffraction data were collected using the powder Diffractometer at the Dhruva Reactor in BARC. The nano-crystalline powders were packed in a Vanadium can with a copper cap. It was held in position in a CCR and was bathed in a neutron beam of wavelength 1.2443 Å. Five linear PSD's recorded the diffraction pattern in an angular range 5°-145°. The data were calibrated and refined using the WinPLOTR suite of programs

Neutron diffraction studies have been carried out to determine the magnetic structure and cation distribution in $Mn_{0.6}Zn_{0.4}Fe_2O_4$ and $Mn_{0.7}Zn_{0.3}Fe_2O_4$ nanoparticles. Figure 6.1 (a) and Fig.6.1 (b) displays the neutron diffraction pattern obtained at room temperature.

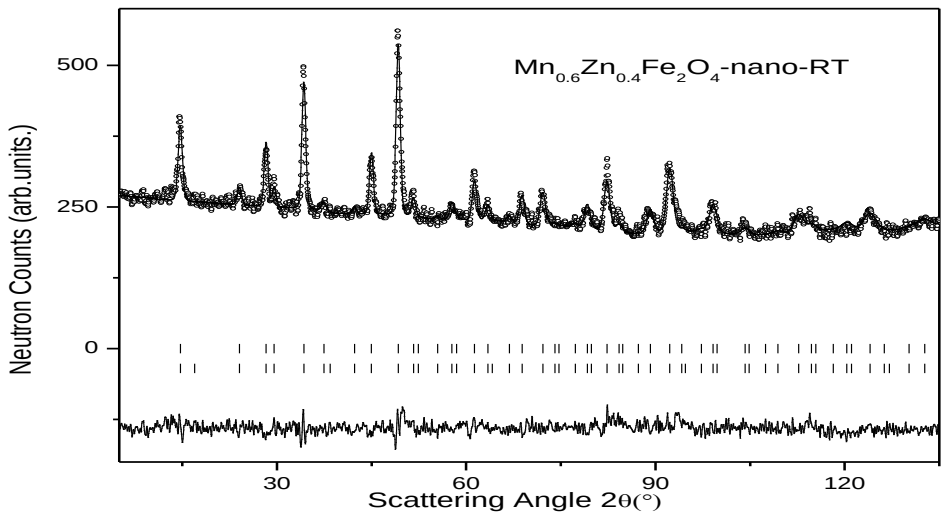

Fig 6.1 (a) Neutron Diffraction pattern for $Mn_{0.6}Zn_{0.4}Fe_2O_4$

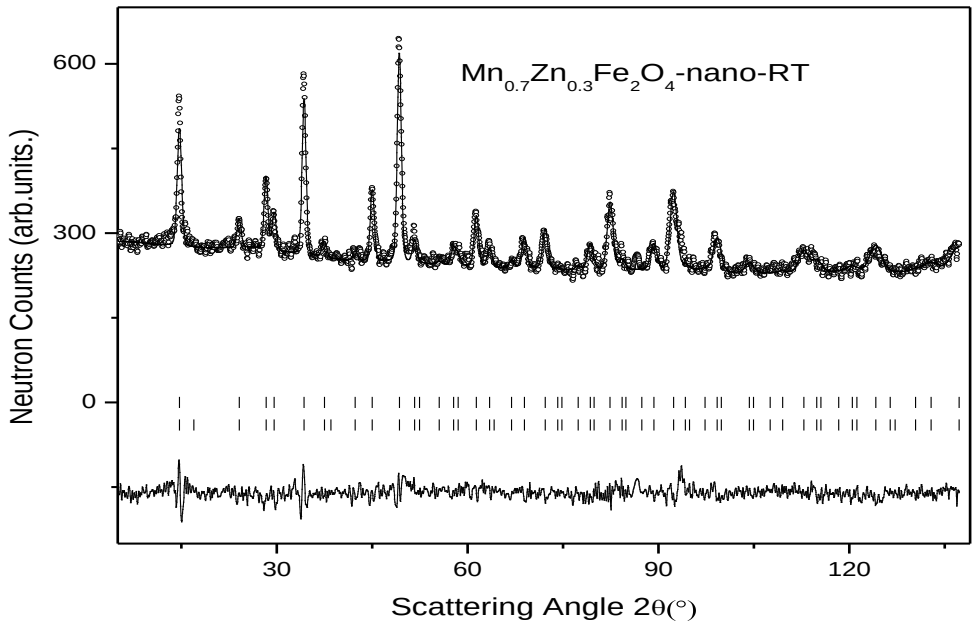

Fig. 6.1 (b) Neutron Diffraction pattern for $Mn_{0.7}Zn_{0.3}Fe_2O_4$.

The recorded diffraction data were found to fit well to the space group Fd-3m. All the recorded peaks were broadened due to particle size effects. Rietveld refinement commenced with varying scale factor with zero point of the detector and cell constants. The background was linearly interpolated between externally provided background points. These points were chosen to lie in non-overlapping peak regions.

Next the u parameter was varied and fixed. After which the cation distribution was determined. Next the magnetic refinement was commenced over and above the nuclear refinement.

Table 6.1(a): Neutron Diffraction data for $Mn_{0.6}Zn_{0.4}Fe_2O_4$

Atom	X	y	Z	Biso(Å2)	n
Mn	0.125	0.125	0.125	0.9(1)	0.3
Zn	0.125	0.125	0.125	0.9(1)	0.3
Fe	0.125	0.125	0.125	0.9(1)	0.4
Fe	0.5	0.5	0.5	0.3(7)	1.6
Mn	0.5	0.5	0.5	0.3(7)	0.3
Zn	0.5	0.5	0.5	0.3(7)	0.1
O	0.2600(2)	0.2600(2)	0.2600(2)	0.61(7)	4.0
a = b = c (Å)	8.4564(2)				
Rp%	2.66				
Rwp%	3.40				
Rexp%	6.44				
RBragg%	13.4				
R-Facto%r	11.5				
χ^2	0.278				
Rmag%	17.1				
µMn µB	3.6(3)				
µFe µB	-2.2(1)				

The results are provided in Table 6.1 (a) and Table 6. 1 (b) for x = 0.6 and 0.7 respectively with a figure of the observed, calculated and difference patterns in Figure 6.1 (a) for x = 0.6, and Figure 6.1 (b) for x = 0.7. The Rietveld refinement shows that there is a well-defined magnetic order.

Table 6.1 (b): Neutron Diffraction data for $Mn_{0.7}Zn_{0.3}Fe_2O_4$

Atom	x	y	z	Biso(Å2)	n
Mn	0.125	0.125	0.125	1.2(1)	0.3
Zn	0.125	0.125	0.125	1.2(1)	0.2
Fe	0.125	0.125	0.125	1.2(1)	0.5
Fe	0.5	0.5	0.5	0.12(7)	1.5
Mn	0.5	0.5	0.5	0.12(7)	0.4
Zn	0.5	0.5	0.5	0.12(7)	0.1
O	0.2586(2)	0.2586(2)	0.2586(2)	0.67(7)	4.0
a = b = c (Å)	8.4511(8)				
Rp%	2.88				
Rwp%	3.72				
Rexp%	6.12				
RBragg%	13.1				
R-Facto%r	9.38				
$\chi 2$	0.371				
Rmag%	16.3				
µMn µB	4.2(2)				
µFe µB	-2.9(1)				

The magnetic moment for the sample $Mn_{0.6}Zn_{0.4}Fe_2O_4$, μ_{Mn}= 3.6(3)µB and μ_{Fe} = -2.2(1)µB. Similarly for $Mn_{0.7}Zn_{0.3}Fe_2O_4$, μ_{Mn}= 4.2(2)µB and μ_{Fe}= -2.9(1)µB. Cation distribution for both the samples is given in the respective table. The lattice constant for the cubic $Mn_{0.6}Zn_{0.4}Fe_2O_4$ spinel unit cell is 8.4564(2) Å. and for $Mn_{0.7}$ $Zn_{0.3}$ Fe_2O_4 it is 8.4511(8)Å.

6.3 HYSTERESIS LOOP TRACER

The system consists of Pulsed Power Supply, Solenoid and Pick-up Coil, Signal Processor and Data Acquisition system. High magnetic field is generated in a solenoid by passing a pulse current of sinusoidal shape, A pickup coil is kept in the solenoid to detect field and magnetization signal of a sample placed in the pickup coil. The signals produced are then processed by an electronic system. These transitory signals are digitized by a micro-controller and then sent to computer for plotting hystersis loop which is observed on the monitor with calculated values of hystersis parameters. The system is useful for samples in powder or pallet form.

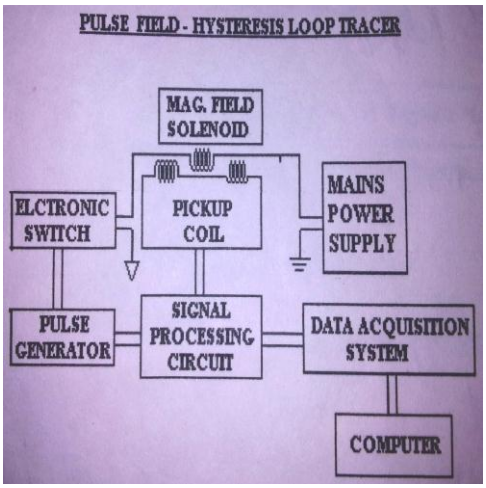

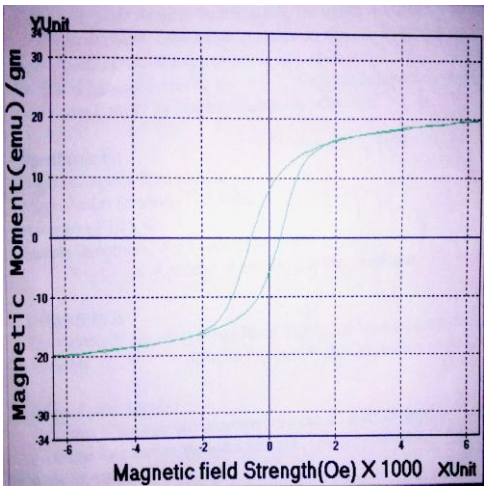

(c) **(d)**

Fig 6.1 c) Block diagram of Pulse Field Hysteresis Loop Tracer d) Hysteresis Loop obtained using Pulse Field Hysteresis Loop Tracer

6.4 VIBRATING SAMPLE MAGNETOMETER

A schematic and a photograph of a typical Vibrating Sample Magnetometer (VSM) is shown in the fig.6.2 (a and b) below. VSM is specialized equipment and is used to measure the magnetic behavior of magnetic materials.

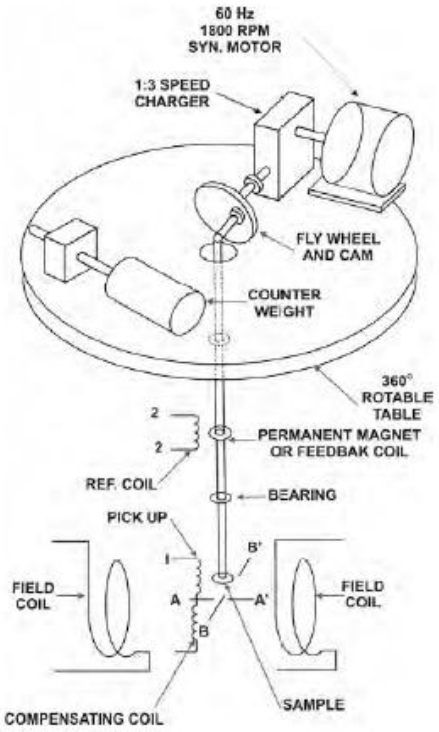

Fig. 6.2 (a) schematic diagram of a VSM 12T

Fig. 6.2 (b) Vibrating Sample Magnetometer 1.8K-300K

It operates on Faraday's Law of Induction. The sample under investigation is placed in the sample holder in a constant magnetic field. The constant magnetic field will magnetize the sample by aligning the magnetic domains in the direction of the field. The strength of the magnetic field will decide the magnitude of magnetization in the sample. The magnetization of the sample will develop a magnetic field around it, sometimes called the

magnetic stray field. When the sample is subjected to vertical vibration (up and down, oscillating) the changing magnetic stray field induces a current in the pick-up coils, proportional to the magnetization of the sample. Information on magnetization of the sample and its dependence on the constant magnetic field is automatically obtained with the help of controlling software on the PC coupled with the instrument. The data collected generates a plot of magnetization (M) versus magnetic field strength (H) for the sample. Magnetic information like saturation magnetization, coercivity, retentivity, hysteresis loss, squareness etc. at various temperatures can be obtained.

6.5 SUPERCONDUCTING QUANTUM INTERFERENCE DEVICE (SQUID)

6.5.1 Low Field and Low Temperature Magnetization Measurements using SQUID

A superconducting quantum interference device (SQUID) is a very sensitive magnetometer used to measure extremely weak magnetic fields, based on superconducting loops containing Josephson junctions. A Josephson junction is made up of two superconductors, separated by an insulating layer so thin that electrons can pass through it.

A SQUID is, basically, a flux to voltage transducer providing an output voltage. It is periodic in the applied flux with a period of one flux quantum of ϕ_o = h/2e. One is generally able to detect an output signal corresponding to flux change of much less than ϕ_o. SQUID is able to measure any physical

quantity that can be converted to flux, ex. magnetic field, magnetic field gradient, current, voltage, displacement and magnetic susceptibility.

There are two types of SQUID. i) (RF) SQUID which is made up of one Josephson junction, mounted on a superconducting ring. An oscillating current is applied to an external circuit, whose voltage changes as an effect of the interaction between current and the ring. The magnetic flux is then measured. ii) A direct current (DC) SQUID, which is much more sensitive, consists of two Josephson junctions employed in parallel so that electrons tunneling through the junctions demonstrate quantum interference, dependent upon the strength of the magnetic field within a loop. SQUID can detect a change of energy as much as 100 billion times weaker than the electromagnetic energy that moves a compass needle. The photograph in the fig. 6.2 (c) gives a cutaway view of a typical Squid equipment.

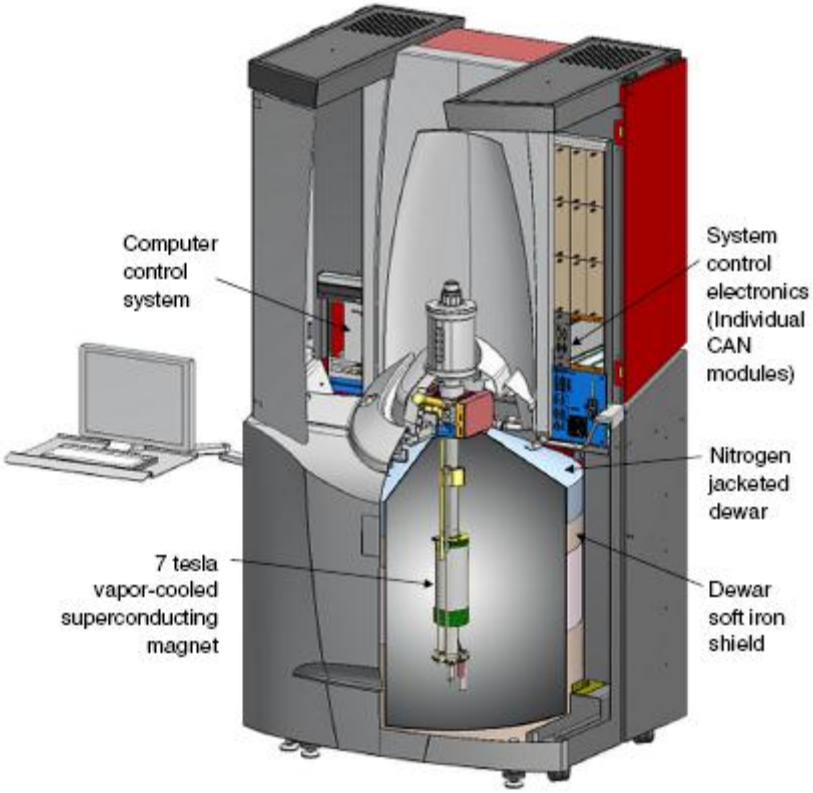

Fig 6.2 (c) Cutaway view of the MPMS SQUID-VSM

6.6 MOSSBAUER SPECTROSCOPY

Mössbauer spectroscopy is a spectroscopic technique based on the recoil-free, resonant absorption and emission of gamma rays in solids. Three types of nuclear interaction may be observed: i) an isomer shift, also known as a chemical shift; ii) quadrupole splitting; iii) magnetic or hyperfine splitting, also known as the Zeeman effect [1]. Due to the high energy and extremely narrow line widths of gamma rays, Mössbauer spectroscopy is one of the most sensitive techniques in terms of energy (and hence frequency) resolution, capable of detecting change in just a few parts per 10^{11}[2].

If the emitting and absorbing nuclei are in identical chemical environments, the nuclear transition energies would be exactly equal and

resonant absorption would be observed with both materials at rest. The difference in chemical environments however, causes the nuclear energy levels to shift in few different ways. Although these energy shifts are tiny (often less than a micro-electron-volt), the extremely narrow spectral line widths of gamma rays for some radio nuclides correspond to large changes in absorbance. A slight change in gamma ray energy is necessary to bring back the two nuclei into resonance which is achieved through Dopplar effect.

Isomer shift is a relative measure, describing a shift in the resonance energy of a nucleus due to the transition of electrons within its '**s**' orbital. The whole spectrum is shifted in either a positive or negative direction depending upon the s electron charge density. This change arises due to alterations in the electrostatic response between'**s'** orbital electrons and nucleus. [1]

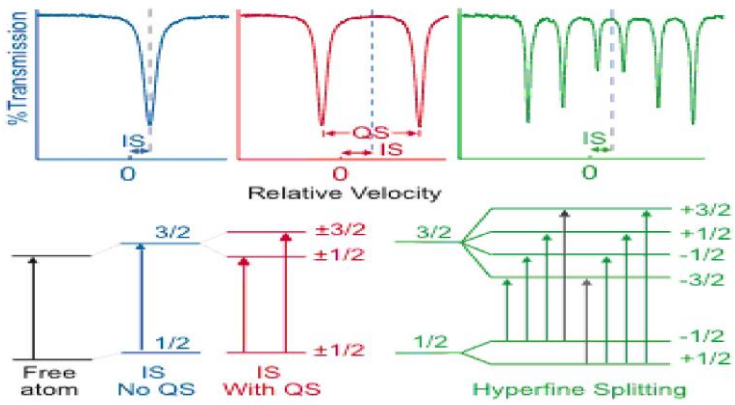

Fig. 6.2 (d) Isomer shift, quadrupole splitting and Magnetic splitting of the nuclear energy levels and corresponding Mössbauer spectra.

Quadrupole Splitting arises due to the interaction between the nuclear energy levels and surrounding electric field gradient (EFG). Nuclei with non-spherical charge distributions, i.e. all those nuclei with total angular momentum quantum number **I** greater than 1/2**,** produce an asymmetrical

electric field which splits the nuclear energy levels. This produces a nuclear quadrupole moment [1].

In the case of an isotope with a I=3/2 excited state, such as ^{57}Fe or ^{119}Sn, the 3/2 to 1/2 transition is split into two substates with m_I=±1/2 and m_I=±3/2. These appear as two specific peaks in a spectrum, sometimes referred to as a 'doublet'. Quadrupole splitting is measured as the separation between these two peaks and reflects the character of the electric field at the nucleus.

Magnetic splitting (hyperfine splitting) is a result of the interaction between the nucleus and surrounding magnetic field. A nucleus with spin I, splits into 2I + 1 sub-energy levels in the presence of magnetic field. For example, a nucleus with spin state I= 3/2 will split into 4 non-degenerate sub-states with m_I values of +3/2, +1/2, -1/2 and −3/2. Each split is hyperfine split, and is in the order of 10^{-7}eV. The restriction rule of magnetic dipoles means that transitions between the excited state and ground state can only occur where m_I changes by 0 or 1. This gives six possible transitions for a 3/2 to 1/2 transition [1]. Therefore, in the majority of cases only six peaks can be monitored in a spectrum produced by a hyperfine splitting nucleus.

The three Mössbauer parameters: isomer shift, quadrupole splitting, and hyperfine splitting can often be used to identify a particular compound by comparing it to known spectra.

In Mössbauer absorption spectroscopy, a solid sample is exposed to a beam of gamma radiation, and a detector measures the intensity of the beam transmitted through the sample. The atoms in the source emitting the gamma

rays must be of the same isotope as the atoms in the sample absorbing them. Mössbauer spectroscopy has an extremely fine energy resolution and can detect even subtle changes in the nuclear environment of the relevant atoms.

During Mössbauer absorption spectroscopy, the source is accelerated through a range of velocities using a linear motor to produce a Doppler effect and scan the gamma ray energy through a given range. A typical range of velocities for ^{57}Fe is ±11 mm/s (1 mm/s = 48.075 neV) [2,3].

6.7 A.C. SUSCEPTIBILITY

The magnetic susceptibility is the degree of magnetization of a material in response to an applied magnetic field. When the magnetic susceptibility is measured in response to an AC magnetic field, it is called AC susceptibility. Curie temperature is one of the important parameters of any ferrite system. The ferrimagnetic materials show quite resemblance in their magnetic properties to those of ferromagnetic class. These materials show hysteresis and susceptibility below transformation temperature i.e. Curie temperature. It is an intrinsic property of the spinel ferrites, which can be controlled by preparation method, sintering temperature and doping of additives [4]. The microstructure, chemical composition, porosity and grain size play a crucial role in deciding the A.C. susceptibility of a material. A.C. Susceptibility studies are normally carried out to investigate the domain nature, and Curie temperature as well as existence of superparamagnetic grains in the material.

AC susceptibility measurement on the samples were carried out using High Pulse field magnetization system shown in fig.6.2 (e).

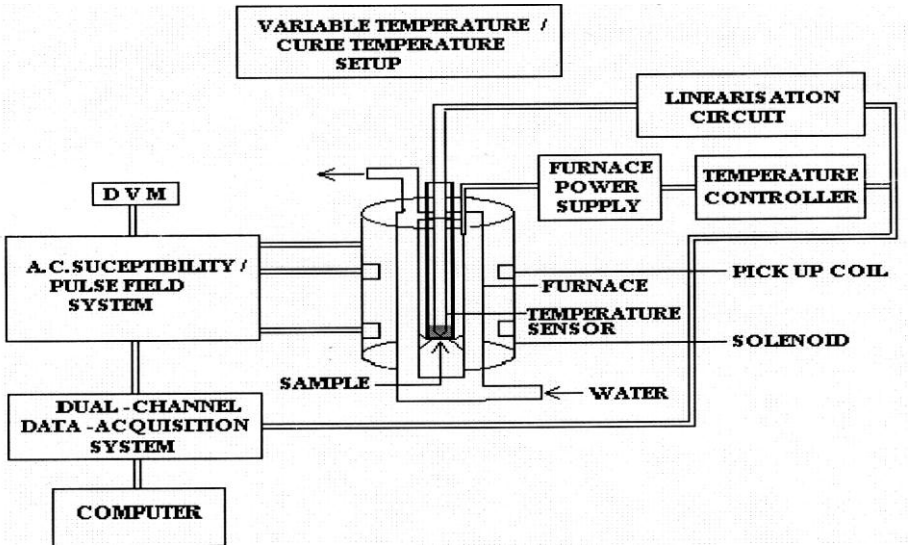

Fig 6.2 (e) Schematic Diagram of High Pulse Field Magnetization System

It consists of solenoid and a pickup coil assembly. A furnace made with platinum wire wound on a quartz tube is placed in the pickup coil. A magnetic sample can be inserted in the furnace and a resistance thermometer is placed in contact with the sample to read its temperature.

A pulse magnetic field of sinusoidal shape is generated in the solenoid of the order of 2.5KOe using a solid state relay circuit. The Pickup coil detects the magnetization signal of the samples. The signal is processed to produce a steady output to be read on digital meter. The temperature of the sample is controlled by a programmable temperature controller. The magnetization signal and the temperature signal are digitalized by a micro-controller at regular intervals and the data is send to a computer. Special software is used to plot magnetization of the sample at different temperature.

6.8 INITIAL PERMEABILITY

Initial permeability is another important magnetic parameter which helps in deciding the suitability of ferrites for particular applications. This

property which is highly influenced by microstructure which in turn depends upon method of preparation. The initial permeability is dependent on grain size, density and porosity of the material [5].

Mainly two processes are responsible for permeability:

(i) rotations of domains

(ii) domain wall displacement

The initial permeability is caused by the reversible displacement of the domain walls, the contribution of rotation of spin inside each domain is negligible due to relatively high crystal anisotropy. In polycrystalline ferrites, due to sintering, certain amount of pores are present and the domain walls extend from pore to pore so that they are not free to move. These pores have a considerable demagnetizing effect, which leads to rather intrinsic pattern of Weiss domains. Hence it is difficult to predict which kind of magnetization process will give the predominant contribution to the initial permeability.

For the reversible rotational process, Chikazumi [6] has given the permeability as

$$(\mu-1) = (\text{constant})\ (Ms)^2\ \text{Sin}\theta\ /K_1$$

where θ is the angle between Ms and μ, for reversible wall processes, permeability is, $(\mu-1) = (\text{constant})\ (Ms)^2 S/\alpha$, where S= wall surface area

α = Second order derivative of wall energy with respect to wall displacement.

At low frequency domain wall motion is a dominant mechanism. Whereas, domain rotation is largely responsible for the high frequency permeability.

6.8.1 Models of Permeability

(i) Globus Model: As per Globus the initial permeability of magnetic material is mainly due to the reversible motion of domain walls under small magnetic field and contribution of the spin rotation is negligible [7,8]. This model considers domain wall to be pinned at the grain boundaries which bulge under the application of magnetic field until the critical field is reached when the walls gets unpinned. Accordingly

$$\mu_i = 3\,[(M_s)^2 D/16\gamma\,] + 1$$

where Ms is saturation magnetization, D is grain diameter and γ is domain wall energy per unit area, as $\gamma \sim \sqrt{}\, AK_1$

$$\mu_i = (M_s)^2 D/\,|\,K_1|$$

Such a model can be extended to the case where the domain walls are pinned at inter-granular pores. According to Globus and co-workers [8,9], in polycrystalline ferrites the magnetization mechanism might be different due to granular structure of ferrites. The other model developed uses domain wall bulging of 180^o instead of domain wall displacement which is considered to be responsible for the initial permeability.

In yet another model Globus and others [10,11] used the existence of easy axis prevalent in each grain. The domain walls, under the influence of

flux forces, tend to align themselves along the director circle as best as they can in order to minimize the demagnetizing field.

(ii) Non Magnetic Grain Boundary Model: Johnson [12] has developed the non-magnetic grain boundary model, which accounted for the entire grain size dependence of μ_i at low anisotropy. This model describes about the dependence of rotational permeability on grain size mostly in polycrystalline materials [13]. According to this model there is almost a linear dependence of permeability on grain size for fine grained polycrystals wherein $D << \mu_i \delta$. It is given by the relation

$$\mu_e = \mu_i D / (\mu_i \delta + D)$$

where μ_e = effective permeability, μ_i = complex permeability,

D= grain size, δ =grain boundary thickness.

For larger grain size where $D >> \mu_i \delta$, the model predicts constant rotational permeability equivalent to that in single crystal of the same material i.e. $\mu_e \sim \mu_{is.}$

(iii) Two Pinning Model: This model assumes that a component that varies with spatial co-ordinates along the grain boundary is responsible for permeability [14-17]. The disorientation of magnetic axis gives rise to microstress on the grain boundary. This magnetostrictional deformation creates the inhomogeneous stress along grain boundary as a result domain wall is formed near grain boundary with the regions of increased anisotropy.

$$\Delta K = (| K| - | K_1|)$$

6.8.1.1 Variation of Initial Permeability

(i) Temperature Dependence

Temperature dependence of initial permeability can be expressed in terms of material parameter called the temperature factor which is defined as

$$Ti = \Delta T / \Delta \mu_i^2$$

Where $\Delta \mu_i$ is the difference in permeability at temperatures T_1 and T_2 respectively and ΔT is the change in temperature.

The temperature factor can be used to predict the variation in magnetic properties of a magnetic component. When temperature is varied from higher temperature above T_c to lower temperature thermal hysteresis is obtained. This is explained by taking into account the domain wall pinning component between the intrinsic parameter M_s and K_1 around the transition point [18].

(ii) Microstructure Dependence

Microstructure plays a very important role in initial permeability. Porosity is another factor that causes hindrance to domain wall motion and in turn effects the initial permeability [19]. Domain walls are energetically favorable in fine grains and in such grains there is a reversal of magnetization by rotation of spins. Increase of porosity increases the coercive force because of internal demagnetizing field which in turn is responsible for decrease in permeability. The larger grain size means multidomain material, so increased number of domain walls; this causes reduction in initial permeability. Secondly the shape of grain may be irregular and may contain voids that induce demagnetizing field, this hampers domain wall motion. Thus the grain

size is a very important parameter in the permeability. A duplex structure is undesirable because it lowers the permeability [20,21].

(iii) Frequency Dependence

At low frequencies the domain wall motion is dominant mechanism and permeability is almost independent of frequency. High frequency permeability depends on the domain structure. At low frequencies, the applied field causes domain wall shift and this motion results in change in net magnetization. At high frequencies, the domain wall inertia prevents any appreciable wall motion but the mechanism can rotate within each domain. This mechanism is similar to ferromagnetic resonance.

6.9 EXPERIMENTAL

6.9.1 High Field Hysteresis Loop Tracer

Saturation Magnetization and Hystersis Loss measurements on the sample were carried out using a high field hystersis loop tracer described by Likhite et al [22]. The pallet of known weight of the sample under investigation was placed in the sample holder of the equipment and high current pulses were passed through the field producing coil which generates high field for the duration of the pulse cycle. Thus the sample undergoes through the entire cycle of the magnetic field. The data acquasition system collects the magnetization data on the sample during this period and it is displayed on the pc screen in the form of a hysteresis loop. The system gives the valus of saturation magnetization, retaintivity and coercive field for the sample.

6.9.2 VSM

The magnetic measurements of as prepared samples were carried out on vibrating sample magnetometer at room temperature, 5K, 10K, 25K, 50K and for sintered samples at 300K, using; OXFORD Instruments, UK at T.I.F.R. Mumbai. Saturation magnetization, coecivity and retentivity values were determined.

6.9.3 SQUID

Temperature dependent magnetization (FC, ZFC) of $Mn_xZn_{(1-X)}Fe_2O_4$ nanoparticles were studied by using a MPMS SQUID from Quantum Design USA. Magnetometer with a magnetic field 100, 500, 1000, 5000 Oersted in the temperature range 5K to 300K at TIFR Mumbai.

6.9.4 Mössbauer Spectroscopy

Mössbauer spectra at room temperature were recorded using a Mössbauer spectrometer at BARC Mumbai. [Mössbauer spectrometer System (Type: MC1002), Nucleonix Systems Pvt. Ltd., Hyderabad, India] operated in constant acceleration mode (triangular wave) in transmission geometry. The source employed is Co-57 in Rh matrix of strength 50 mCi. The calibration of the velocity scale is done by using α-Fe metal foil. The outer line width of calibration spectra is 0.29 mm/s. Mössbauer spectra were fitted by a least square fit (MOSFIT) programme assuming Lorentzian line shapes. The results of isomer shift are relative to α-Fe metal foil.

6.9.5 A.C. Susceptibility

A.C. Susceptibility measurements and Curie temperature were obtained on Likhite's automated Pulse Field A.C. Susceptibility apparatus [23] for nano samples as well as bulk samples obtained at 900^0C, 1000^0C, 1100^0C, 1200^0C and 1300^0C.

6.9.6 Initial Permeability

To measure the initial permeability of the samples, powder samples were pressed into torroids with inner and outer diameter of 1cm. and 2 cms respectively by applying a force of 75KN for duration of 8 minutes. The Torroids were sintered at temperatures 900^oC, 1000^oC, 110^oC, 1200^oC, and 1300^oC in nitrogen atmosphere for four hours in progressive manner by setting heating and cooling rate of 5^0C/min.

(f) (g)

Fig. 6.2 (f, g) Torroides (f) before and (g) after permeability measurement

100 turns of super enameled doubly insulated copper wire of gauge 33 was wounded on each torroid to carry out initial permeability μi and Q factor measurements as function of temperature (ranging from 30^oC to 490^oC) for (20Hz, 100Hz, 500Hz, 1KHz, 10KHz, 100KHz, 500KHz, 1MHz, 2MHz,

3MHz) frequencies and also the same measurement were carried out at room temperature as a function of frequency using Wayne Kerr Precision component Analyser Model 6400.

The initial permeability (μi) was calculated from the formulae

$$L=0.0046\ \mu_i\ N^2\ h\ (\ln OD/ID)$$

Where L is inductance in Henry, N is the number of turns of copper wire on torroid, h is height of the core in metres, OD is outer diameter of torroid in metres, and ID is the inner diameter of torroid in metres

6.10 EXPERIMENTAL RESULTS AND DISCUSSION

6.10.1 Sample preparation (Hysteresis loop tracer)

The nanopowders of the samples were pressed into pellets of diameter 10mm and thickness of 3mm using a hydraulic press. A pressure of 9.554×10^8 Newton / m^2, for duration of 8 minutes was applied for preparation of the pallets. The pallets nanoparticle samples so formed were used for obtaining the magnetic hysteresis loop and hence measuring the related properties. Another five sets of pellets of all the nano samples were prepared and each set was sintered at 900^oC, 1000^oC, 1100^oC, 1200^oC, 1300^oC in nitrogen atmosphere using tubular Carbolite programmable furnace, respectively for four hours by setting heating and cooling rate of 5^0C/min. This process was followed to obtain bulk samples from nanoparticles with different densities and microstructure and was used for relevant investigation. Initially the Magnetic properties like saturation magnetization, retaintivity, coercivity and hysteresis loss were measured on using a pulsed high field hysteresis loop tracer described by Likhite et al [22]. Later similar measurements were carried out for all the samples using VSM at room temperature. In addition to this, measurements on nanoparticle samples were carried out at low temperatures 5K, 10K, 25K, 50K. VSM manufactured by OXFORD Instruments, UK (facility at T.I.F.R. Mumbai) was utilized for this purpose.

6.10.1.1 Magnetic properties (Hysteresis loop)

The fig. 6.3 (a, b) below gives the Hysteresis loops of nanoparticle samples obtained on Pulsed high field hysteresis loop tracer. Magnetic Hysteresis loop is important for any magnetic material as lot of information

about the material can be gained. Magnetic behavior is largely affected by numerous imperfections in the material. Imperfections like surface spin canting, formation of dead layer on the surface, influence of cationic stoichiometry and their occupancy in the specific sites, lattice distortions at the surface of the particles [24] play a major role in deciding the magnetic properties of the material. In nanoparticles contributions from magnetic core and surface of the particle behave differently. The contribution arising from surface is large as the surface to volume ratio is large in nanomaterials. This indeed makes the particle size a very important parameter as the same can change the material properties drastically due to changing surface to volume ratio.

The hysteresis loops obtained for nanoparticle $Mn_xZn_{(1-X)}Fe_2O_4$ samples with x=0.4 , 0.5, 0.6, 0.625, 0.65, 0.675, 0.7 and 0.8, taken on hysteresis loop tracer at room temperature are displayed in Fig 6.3 (a, b). The hysteresis loops are found to be extremely narrow; this is so because the particles are nanoparticles of small average diameter. The squareness ratio for the particles is also extremely small. This factor reflects the nature or gives vital information about the type of domains present in the nanoparticles. The corresponding parameters Saturation Magnetization, Retentivity and Coercivity values obtained from hysteresis loops are tabulated in Table 6.2 (a).

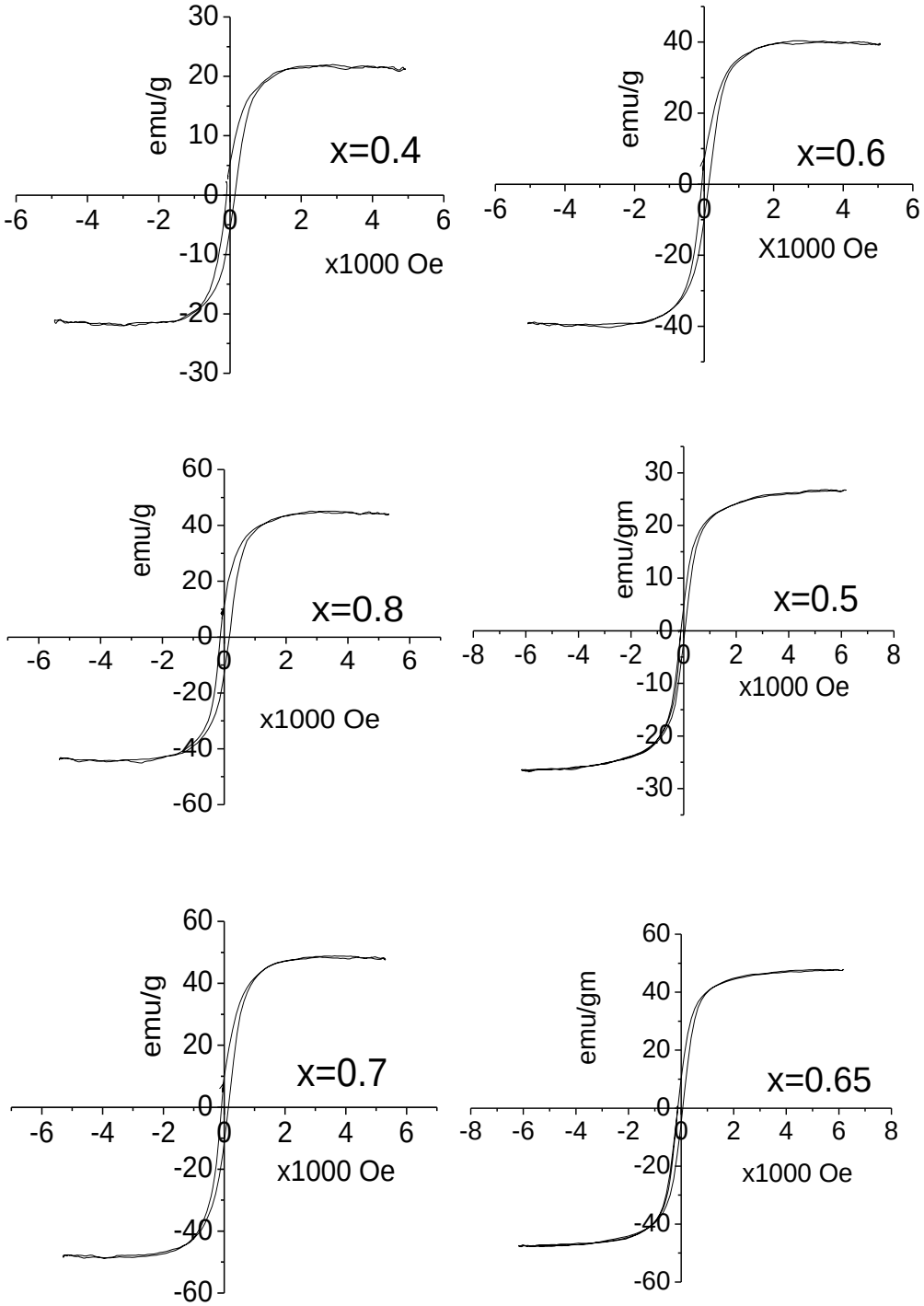

Fig.6.3 (a): Variation of Magnetization with applied field using High Pulse Field Hysteresis loop Tracer for $Mn_xZn_{(1-x)}Fe_2O_4$ nanosamples for x=0.4, 0.5, 0.6, 0.8., 0.7 and 0.65.

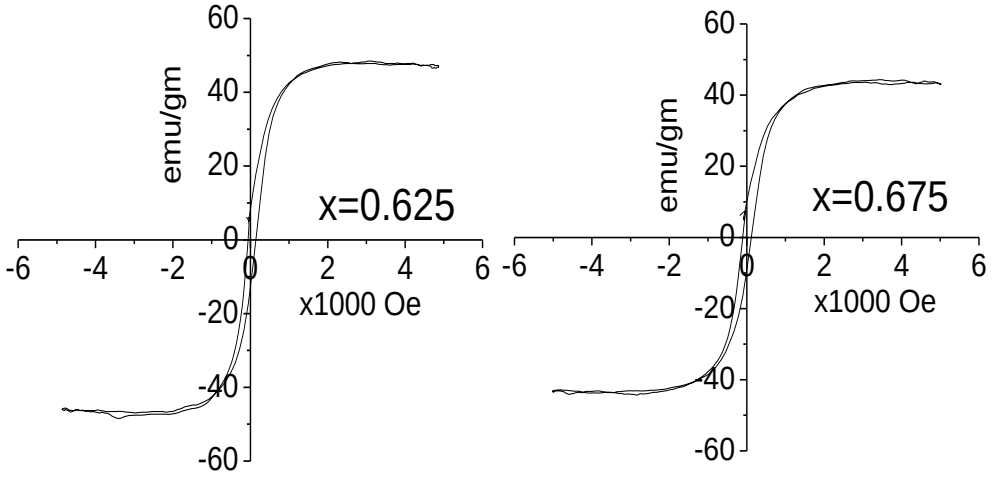

Fig.6.3 (b): Variation of Magnetization with applied field using High Pulse Field Hysteresis loop Tracer for $Mn_xZn_{(1-x)}Fe_2O_4$ nanosamples for x=0.625, and 0.675

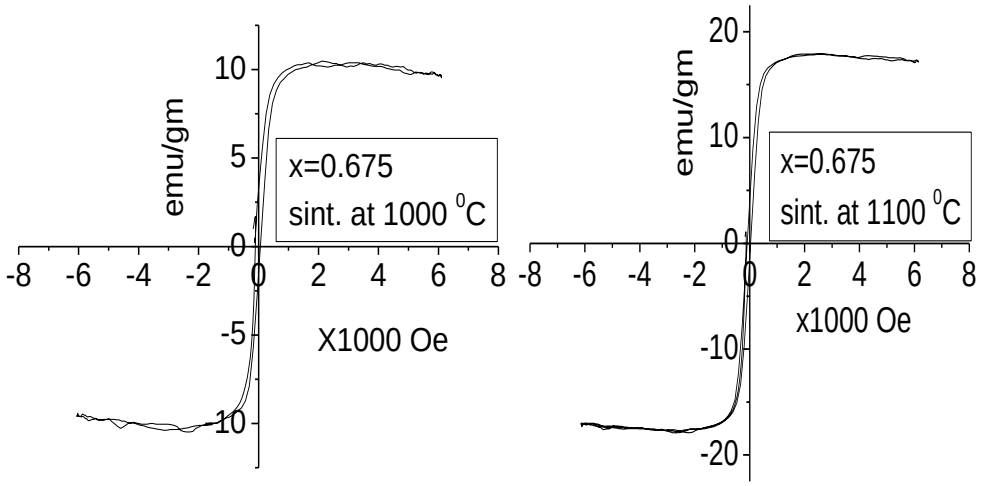

Fig. 6.3 (c) Variation of Magnetization with applied field using High Pulse Field Hysteresis loop Tracer for bulk sample $Mn_{0.675}Zn_{0.325}Fe_2O_4$ (1000 ^{0}C and 1100 ^{0}C)

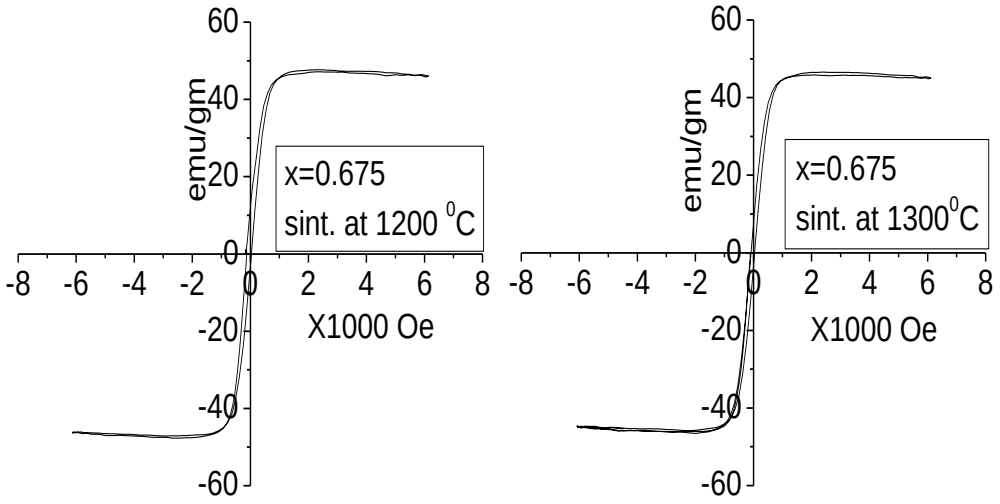

Fig. 6.3 (d) Variation of Magnetization with applied field using High Pulse Field Hysteresis loop Tracer for bulk sample $Mn_{0.675}Zn_{0.325}Fe_2O_4$ (1200 ^{0}C and 1300 ^{0}C)

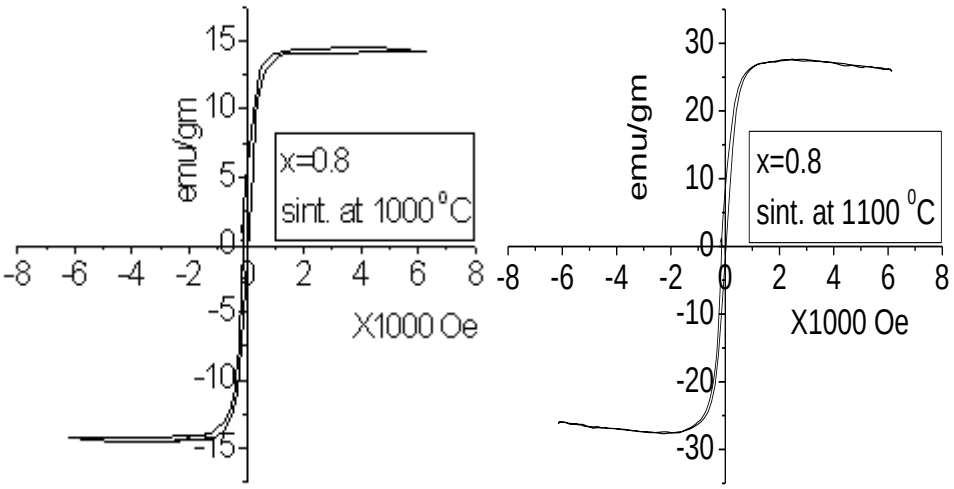

Fig. 6.3 (e) Variation of Magnetization with applied field using High Pulse Field Hysteresis loop Tracer for bulk sample $Mn_{0.8}Zn_{0.2}Fe_2O_4$ (1000 ^{0}C and 1100 ^{0}C)

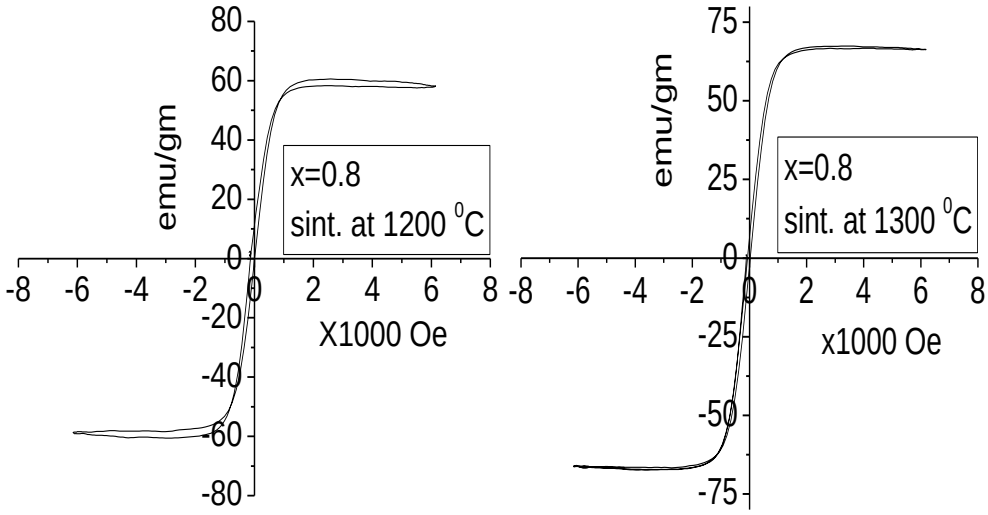

Fig. 6.3 (f) Variation of Magnetization with applied field using High Pulse Field Hysteresis loop Tracer for bulk sample $Mn_{0.8}Zn_{0.2}Fe_2O_4$ (1200 ^{0}C and 1300 ^{0}C)

Table 6.2 (a): Saturation Magnetization, Retentivity and Coercivity values of nano samples using Hysteresis loop tracer

Conc. of Mn	Sat. Mag. (Ms) emu/gm	Coercivity (Tesla)	Retentivity (Mr) emu/gm	Squareness Mr/Ms
0.4	21.86	0.0112	5.55	0.253
0.5	26.83	0.0072	3.21	0.119
0.6	39.85	0.0091	8.22	0.206
0.625	48.35	0.0101	10.55	0.218
0.65	47.81	0.0092	7.51	0.157
0.675	43.74	0.0111	10.00	0.228
0.7	48.12	0.0113	10.61	0.22
0.8	44.32	0.0145	12.21	0.275

Table 6.2 (b): Saturation Magnetization, Retentivity and Coercivity values of bulk samples obtained at 1300^0C

Conc. of Mn	Sat. Mag.(Ms) emu/gm	Retentivity (Ms) emu/gm	Coercivity Tesla	Squareness Mr/Ms
0.4	16.17	3.86	0.0063	0.23
0.5	29.72	3.5	0.005	0.117
0.6	44.33	5.5	0.0076	0.124
0.625	45.91	7.31	0.0085	0.159
0.65	51.73	4.12	0.006	0.079
0.675	48.81	4.21	0.006	0.086
0.7	55.01	7.02	0.007	0.127
0.8	66.28	3.52	0.004	0.053

It is observed that coercivities and squareness as obtained from the hysteresis loops are very low, for both nanoparticle material and bulk material obtained from nanoparticle. A decrease in coercivity value *Hc* and squareness (*Mr* /*Ms*) is observed for sintered samples. This decrease can be attributed to an increase in grain size and decrease in porosity of the sample. Comparatively, larger values of Coercivity *Hc* and retintivity observed for nanoparticle $Mn_xZn_{(1-X)}Fe_2O_4$.(x=0.4, 0.625, 0.675, 0.7,0.8) is indeed a result of single domain (SD) behavior of the material whereas the lower values of retintivity Mr and the corecivity Hc for nanoparticle $Mn_xZn_{(1-X)}Fe_2O_4$ (x=0.5, 0.6, 0.65) indicates MD behavior of the material. As magnetization/ demagnetization due to domain wall movement requires lower field energy compared to that required for domain rotation (SD) [25] *Mr* and *Hc* values in MD samples are lower than the values observed for SD samples.

Sintering of material for production of bulk material is done at the cost of the grain size. Grain size of such materials increase and the material is bound to loose its SD behavior. This phenomenon is observed in most of the bulk samples which exhibit low values for *Mr* and *Hc* compared to corresponding nanoparticle samples.

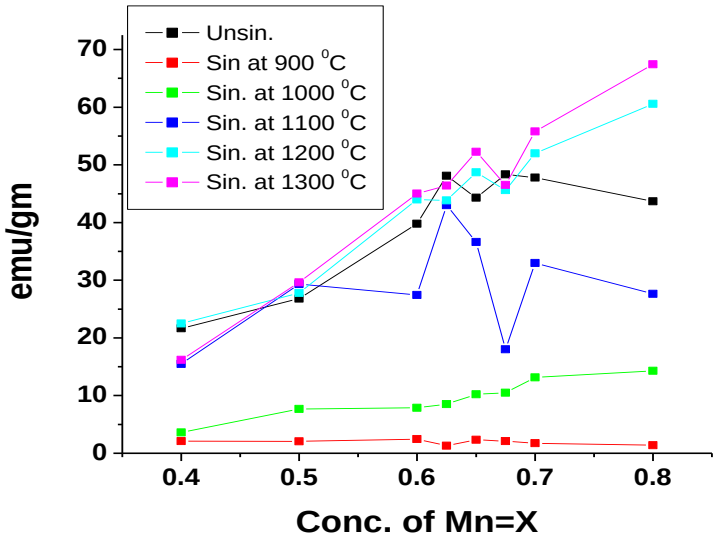

Fig.6.3 (g) Variation of saturation magnetization with concentration of Mn.

Variation of Saturation magnetization for nanoparticle and bulk samples $Mn_xZn_{(1-X)}Fe_2O_4$ with different concentration is shown in fig. 6.3 (g) (measurement made on hysteresis loop tracer). On an average it can be seen that each curve exhibits two maxima points. . In case of nanoparticle samples the first maximum is observed at x=0.625 whereas the other one is observed at x= 0.675. The values of Ms at these positions are 48.8emu/gm. and 48.74emu/gm respectively. The lowest value of Ms for nanoparticle sample is 21.86 emu/gm for x=0.4, whereas the sample with x=0.625 shows highest value of 48.88 emu/gm at room temperature.

The saturation magnetization Ms for the bulk samples is found to show a very unusual pattern. The bulk samples obtained at sintering temperature of 900^{o}C surprisingly show substantial quenching of magnetic moment which is an unexpected result.

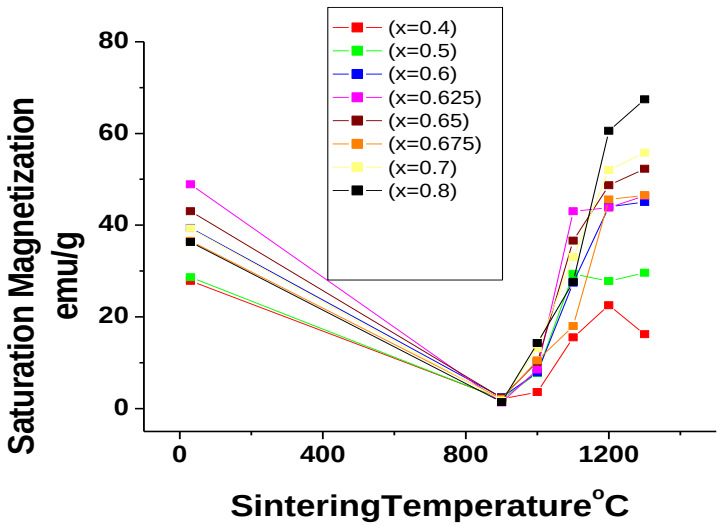

Fig. 6.3 (h) Variation of Saturation Magnetization with sintering temperature of $Mn_xZn_{(1-X)}Fe_2O_4$

It is observed that the saturation magnetization is totally destroyed after sintering the nanoparticle samples at 900^{0}C for all concentrations of Mn. But the same samples regain magnetization when sintered at higher temperatures. This fact is clearly seen in Fig. 6.3 (h). Nanoparticle samples sintered at 900^{o}C exhibit quenching of magnetic moments to the extent of 97 to 99 %. This could be due to the decomposition of the sample at this temperature. Reports [26] show that there may be products of the type Fe_2O_3 with major peak at 2θ =33^{o}C, which is non magnetic material along with Mn_2O_3 and ZnO. This is confirmed with the help of XRD that is carried out on the bulk sample obtained at 900^{o}C. The other possibility may be the formation of magnetically dead layer at the surface of the nanoparticles. This

can happen due to partial evaporation of Zn from the surface of the nanoparticles. This fact can give rise to lattice distortion in the sample sintered at 900^{o}C. As the sintering temperature is increased above 900^{0}C, it is observed that, all the samples show an increase in saturation magnetization, which increases with corresponding rise in sintering temperature. This could be attributed to an increase in crystallinity, improvement on microstructure and crystalline sizes which is in agreement with observations made on SEM micrograph. This could be due to decomposition of nonmagnetic Fe_2O_3 and Mn_2O_3 [26] formed in the sample as a result of previous sintering process at lower temperature. At 1100^{o}C, saturation magnetization curve shows two peaks, one is at x=0.625 and the other one is at x= 0.7 with Ms values 42.32emu/gm and 32.9 emu/gm respectively, with dip appearing at x=0.675. Whereas, samples sintered at 1000^{o}C, 1200^{o}C and 1300^{o}C, show an increasing trend in saturation magnetization with increase in Mn concentration followed by the peaking behavior. This behavior may be attributed to particle size of the sample.

6.10.1.2 Hysteresis Loss

Variation of hysteresis loss with Mn concentration is shown in fig.6.4 (a). Hysteresis loss is found to increase with increasing Mn concentration and show a peak at x = 0.625 followed by a dip at x = 0.65 and increases further with increase in conc. of Mn. This could be attributed to the alignment of surface canted spins at the surface of the particles. A low value of loss at x= 0.65 could be due to variation in the thickness of the canted spin surface layer of the nanoparticles in the sample. Thus the variation of hysteresis loss with the Mn concentration could be attributed to thickness of canted spin surface in

the samples in addition to energy loss in alignment of single domain cores in the sample. The thickness of canted spin layer is dependent on the particle size and Mn concentration in the sample.

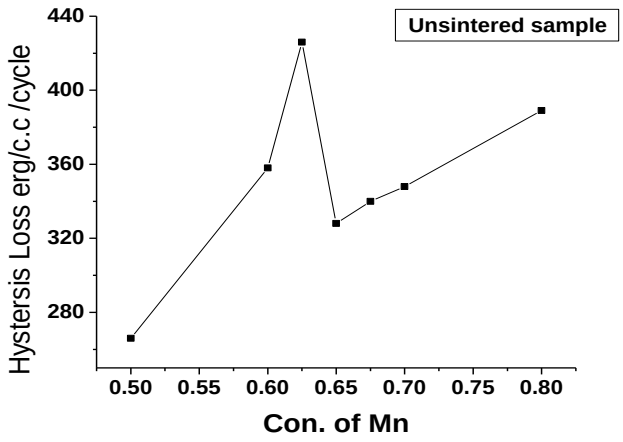

Fig.6.4 (a) Variation of Hysteresis loss with con. of Mn for nano samples.

6.10.2 Magnetic Properties (Using Vibrating Sample Magnetometer)

Magnetic measurements were carried out at room temperature as well as at low temperature (50K, 25K, 10K, 5K) using VSM.

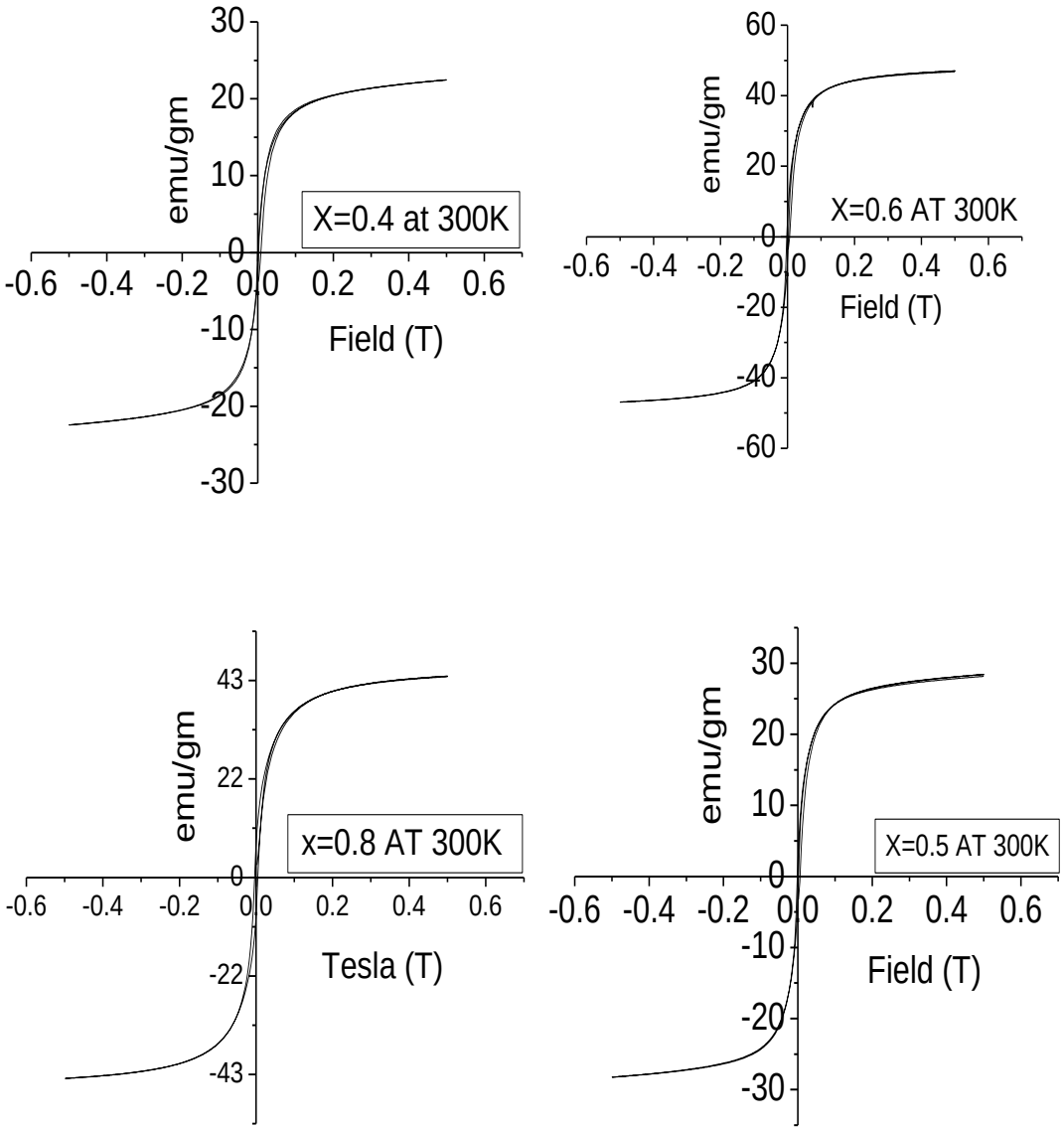

Fig.6.4 (b) VSM measurement of $Mn_xZn_{(1-x)}Fe_2O_4$ at 300K for x=0.4, 0.5, 0.6 and 0.8

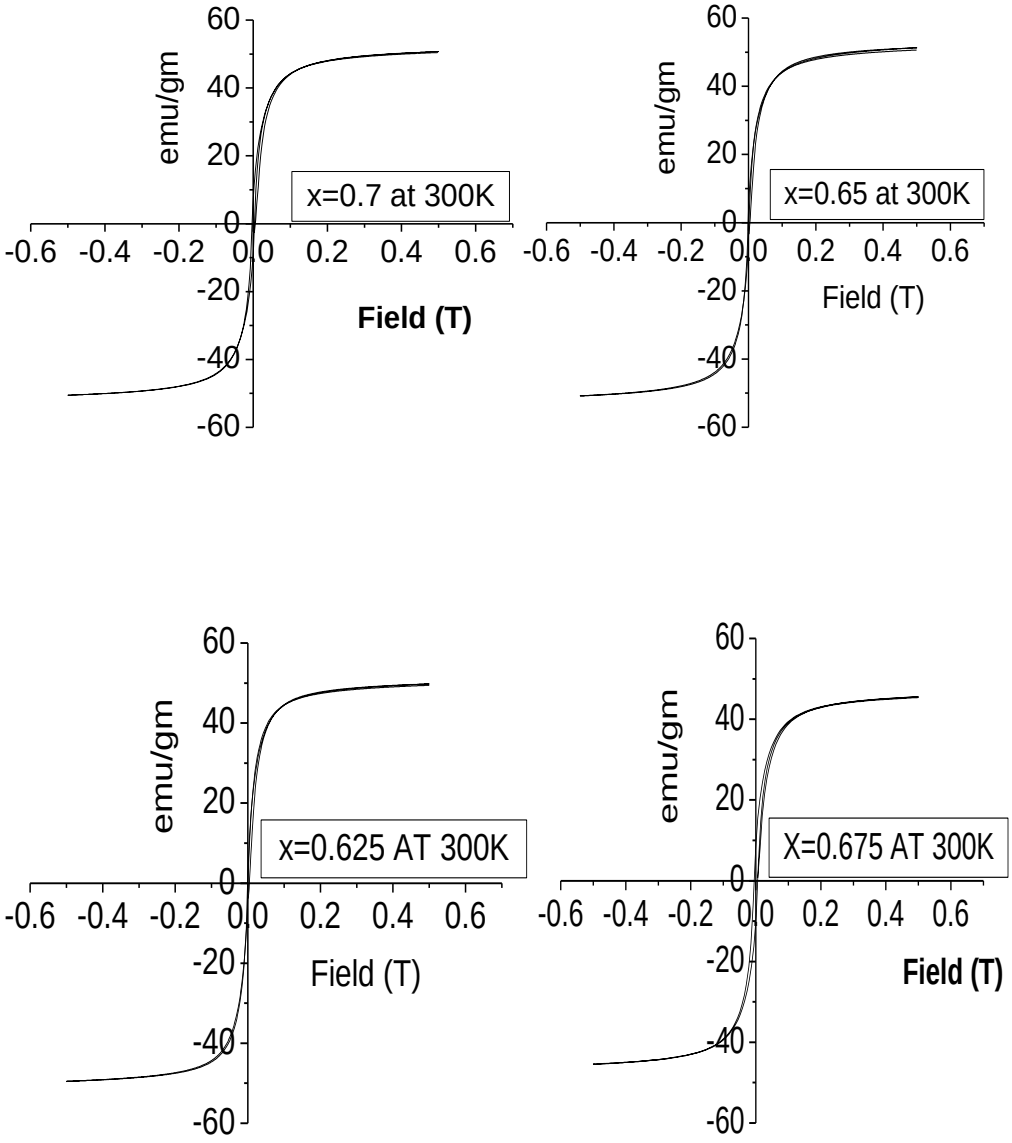

Fig.6.4 (c) VSM measurement of $Mn_xZn_{(1-X)}Fe_2O_4$ at 300K for x=0.625, 0.65, 0.675 and 0.7

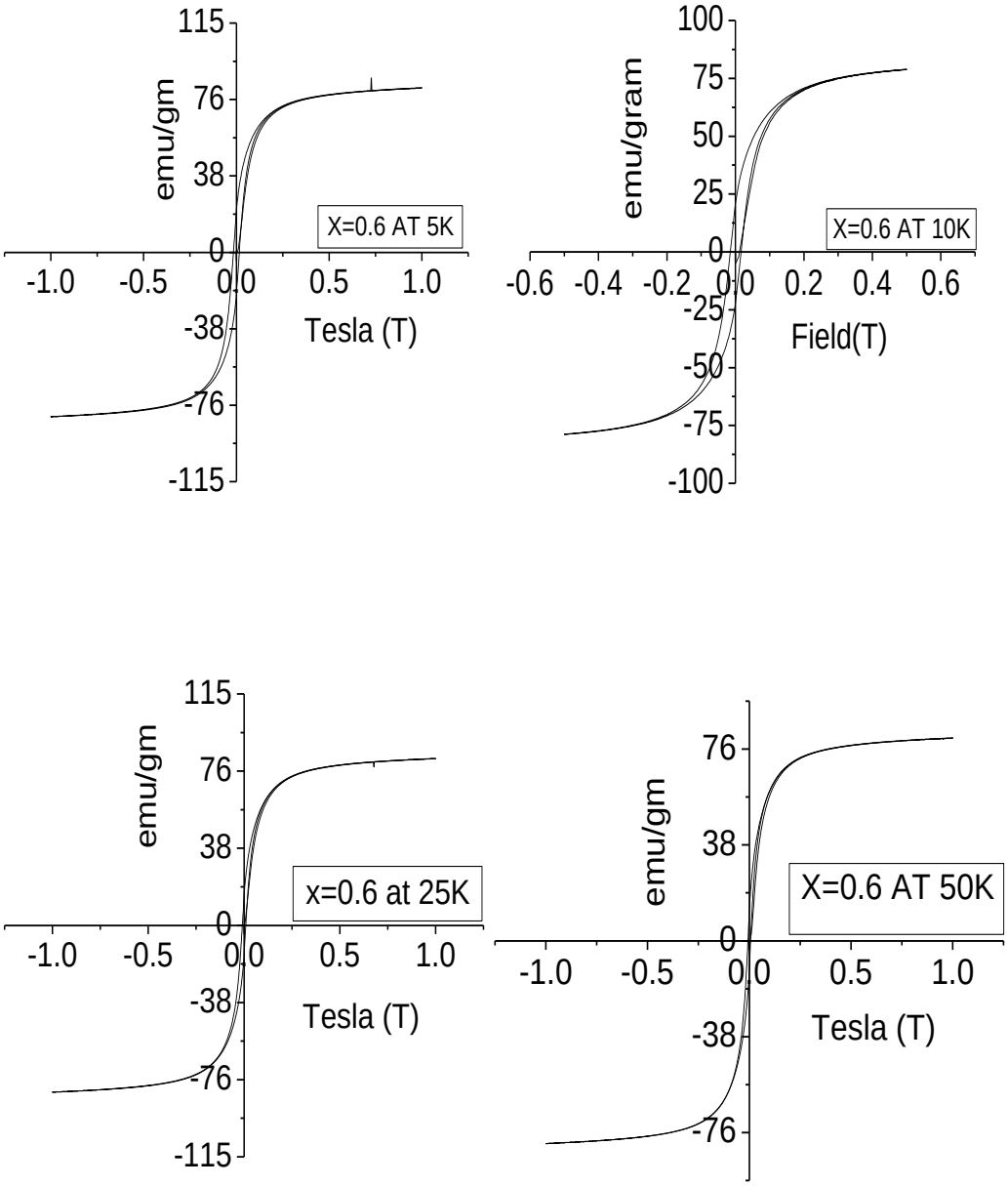

Fig.6.4 (d) Low temperature VSM measurement of $Mn_{0.6}Zn_{0.4}Fe_2O_4$ at 5K, 10K, 25K and 50K.

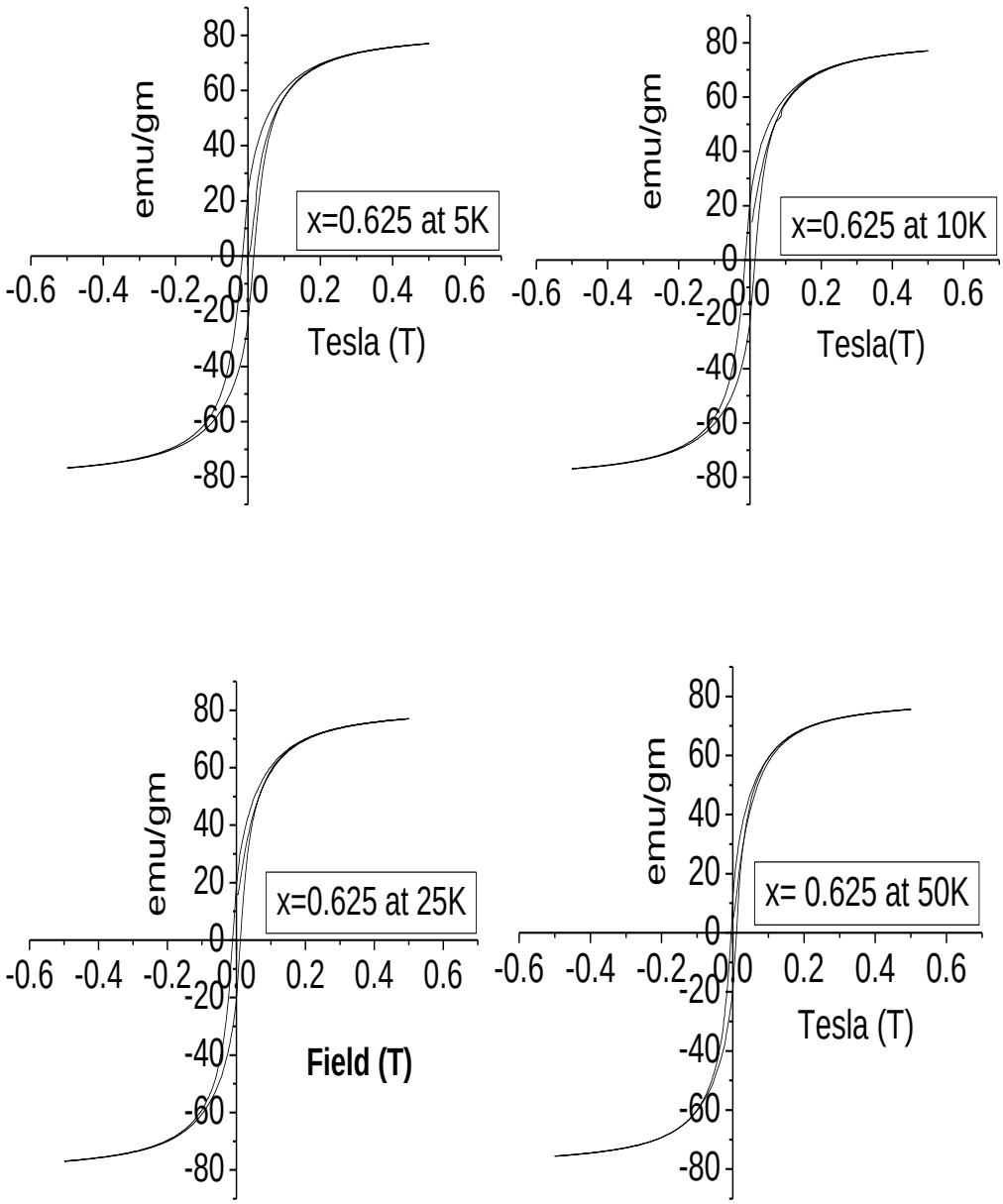

Fig. 6.4 (e) Low temperature VSM measurement of nanosample $Mn_{0.625}Zn_{0.375}Fe_2O_4$ at 5K, 10K, 25K and 50K.

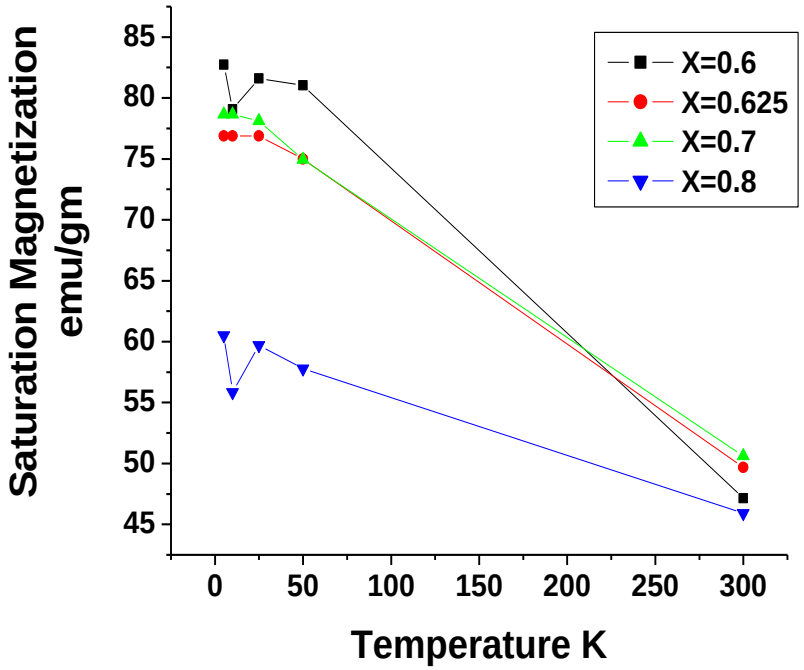

Fig.6.4 (f) Variation of saturation Magnetization with temperature for different concentration of Mn.

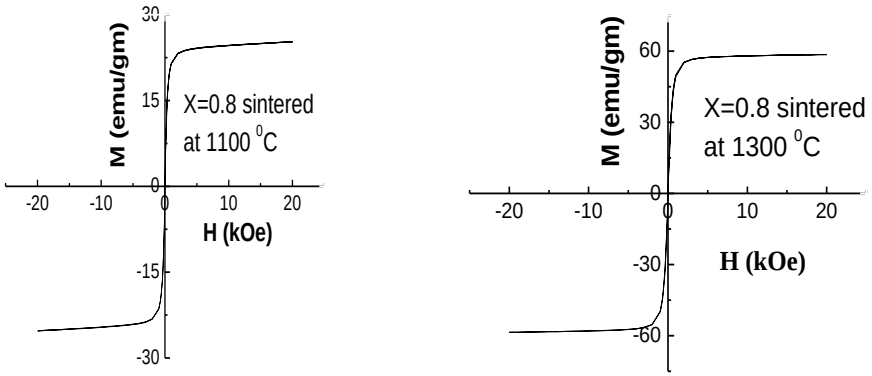

Fig.6.4 (g) Room temperature VSM for bulk sample $Mn_{0.8}Zn_{0.2}Fe_2O_4$ (1100^0C and 1300^0C)

Table 6.3 (a): Low temperature VSM data for $Mn_{0.6}Zn_{0.4}Fe_2O_4$

x=0.6	5K	10K	25K	50K
Sat.mag. emu/gm	82.73	78.55	82.23	80.51
Retentivity emu/gm	20.84	21.66	15.18	12.26
Coercivity In Tesla	0.0155	0.0155	0.009	0.006

Table 6.3 (b): Low temperature VSM data $Mn_{0.625}Zn_{0.375}Fe_2O_4$

x=0.625	5K	10K	25K	50K
Sat.mag. emu/gm	76.89	76.89	76.89	75.51
Retentivity emu/gm	23.32	21.83	19.5	15.00
Coercivity In Tesla	0.015	0.0135	0.011	0.007

Table 6.3 (c): Saturation Magnetization, Retentivity, Squareness and Coercivity values of nanosamples using VSM.

Conc. of Mn	Sat. Mag. (Ms) emu/gm	Coercivity Tesla	Retentivity (Mr) emu/gm	Squareness Mr/Ms
0.4	22.64	0.00015	1.04	0.0459
0.5	28.62	0.0036	2.475	0.086
0.6	47.14	0.0024	5.47	0.116
0.625	49.66	0.0009	2.77	0.557
0.65	50.92	0.0014	4.31	0.0846
0.675	45.25	0.0055	9.4	0.20
0.7	50.62	0.0032	7.76	0.153
0.8	44.13	0.00422	7.24	0.164

Low temperature measurement using VSM shows that Ms increases with decrease in temperature. The saturation magnetization (Ms) at room temperature, for nanoparticle sample $Mn_{0.6}Zn_{0.4}Fe_2O_4$ is 47.14 emu/gm, increases to 82.73emu/gm at 5K and for sample $Mn_{0.625}Zn_{0.375}Fe_2O_4$, the same increases from 49.66 emu/gm, to 76.89 emu/gm at 5K. All the nanoparticle samples show increase in, Coercivity with decrease in temperature. Coercivity values are tabulated in table 6.3 (a), 6.3 (b). A sharp increase in the saturation magnetization at low temperatures, was observed for all the nanoparticle samples. However samples with x=0.6,0.8 show identical trends except that Ms values for the former are higher than the later. Secondly surface spin freezing temperature for samples with x=0.625, 0.7 is around 25K whereas for

sample with x= 0.6 it is 50K. Samples with larger (x=0.6, 0.8) particle size show identical behavior whereas the samples (x=0.625, 0.7) with lower particle size also show identical behavior but the two behaviors are different. This could be attributed to the domain structure of the materials. Material with lower particle size appears to be more superparamagnetic than the other two with larger grain size. The samples with x=0.65, 0.7 exhibit total spin freezing at temperatures below 25K where as samples with (x=0.6, 0.8) do not exhibit such behavior due to different domain structure. Similar sharp increase of Ms for ferrite nanoparticles has been reported [27]. This type of behavior has been attributed to misaligned surface spins due to broken exchange bonds. These spins fluctuate more freely at high temperatures than those from the core and freeze progressively at low temperatures into a disordered structure [28,29]. The coercivity of Nanoparticles is related to the magnetic anisotropy. Coercivity corresponds to magnetic field strength at which magnetic field provides required energy in addition to thermal activation energy to overcome the magnetic anisotropy [30]. At low temperature thermal activation energy is very low, therefore higher magnetic field strength is required to overcome the anisotropy energy. Ms values obtained for nanoparticle samples using VSM at room temperature are in good agreement with the Ms values obtained using hysteresis loop tracer.

Table 6.3 (c) shows all magnetic data recorded using VSM. Magnetic data was also obtained for sintered samples using VSM. The corresponding hysteresis loops are shown in Fig 6.4(g). It is observed that Ms increases for sintered sample. This can be due to increase in particle size and decrease in porosity for sintered samples. For nanosample $Mn_{0.8}\,Zn_{0.2}Fe_2O_4$, the saturation

magnetization Ms at room temperature is 44.13emu/gm. At 900^{o}c Ms is very low; it increases to 25.29 at 1100^{o}C and further increases to 60.42emu/gm sintered at 1300^{o}C.

6.10.3 SQUID

The magnetic properties of the $Mn_xZn_{(1-x)}Fe_2O_4$ (x=0.625, x=0.8) nanoparticle samples were studied by SQUID magnetometer. Fig 6.5 (a) shows the temperature dependence of magnetization for different applied field. The temperature dependence of the magnetization of $Mn_xZn_{(1-x)}Fe_2O_4$ nanoparticles has been studied from 5 to 300K. The nanoparticulate samples were initially cooled to 5 K without any magnetic field applied (ZFC).

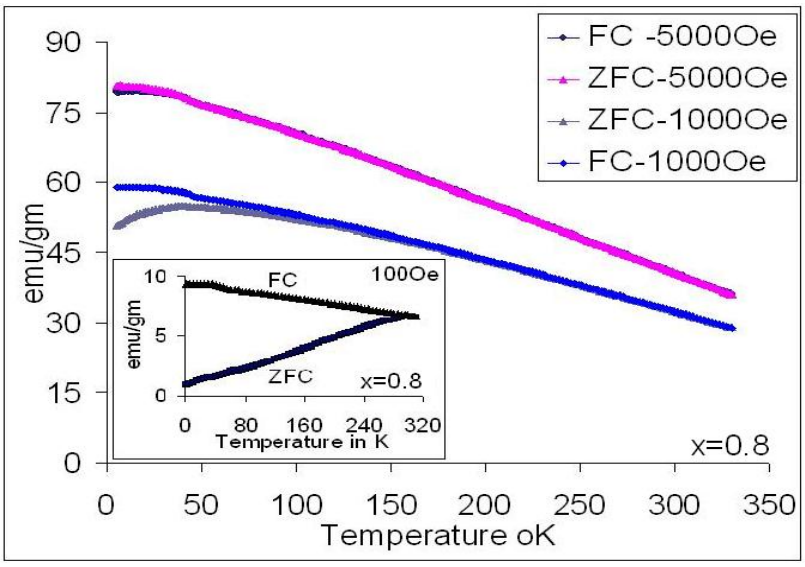

Fig. 6.5 (a): Temperature dependence of magnetization for Zero field cooled and field cooled (MPMS, SQUID from quantum Design USA) Nanoparticle $Mn_{0.8}$ $Zn_{0.2}Fe_2O_4$

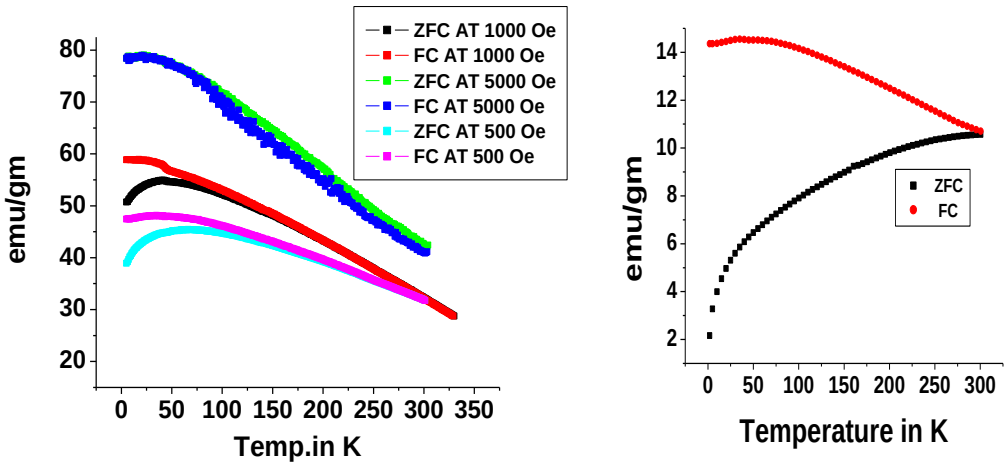

(b) (c)

Fig. 6.5 (b, c) Temperature dependence of magnetization for Zero field cooled and field cooled Nanoparticle $Mn_{0.625}$ $Zn_{0.375}Fe_2O_4$ at 500 Oe, 1000 Oe, 5000 Oe (Fig. 6.5 b) and at 100 Oe (Fig. 6.5 c)

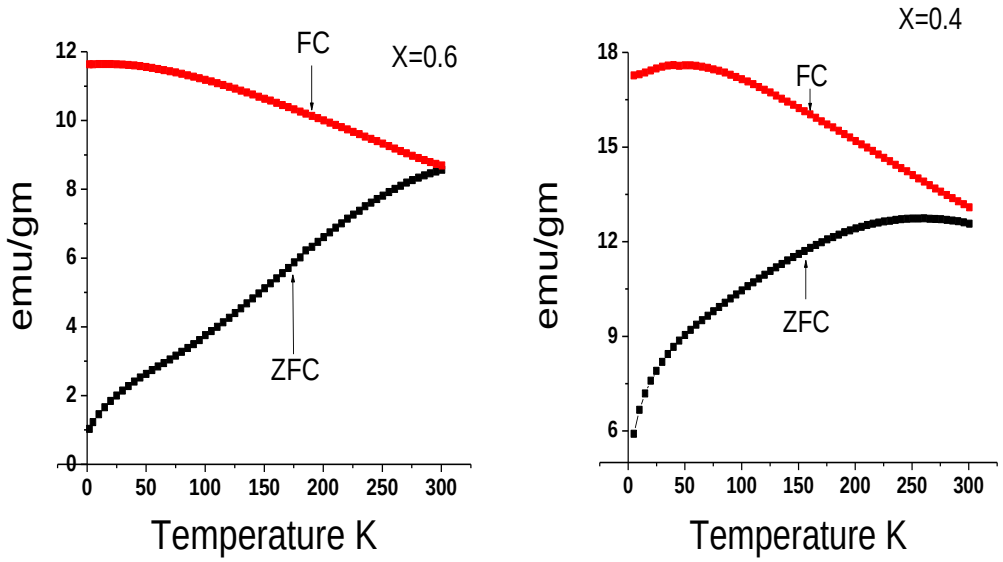

(d) (e)

Fig.6.5 (d,e) SQUID measurement of $Mn_xZn_{(1-x)}Fe_2O_4$ for x=0.6 (d) and x=0.4 (e)at zero field cooling and field cooling at 100 Oe

After cooling a magnetic field of 100 Oe was applied, the magnetization was recorded as the temperature slowly rises. The magnetization initially increases slowly with increasing temperature and eventually reaches the maximum value, at a certain temperature. This temperature is defined as the blocking temperature, T_B. Beyond this temperature T_B, the magnetization falls with increasing temperature and the nanoparticles of $Mn_xZn_{(1-x)}Fe_2O_4$ show paramagnetic features.

In case of Field Cooled (FC) magnetization measurements the samples are cooled in the presence of magnetic field to a temperature of 5K. The magnetization of the sample is then recorded as the temperature increases. The magnetization under the same applied field is maximum at 5 K, and it decreases steadily with increasing temperature. After the temperature rises above the blocking temperature [31] the FC magnetization plot overlaps with the ZFC magnetization plot under the same magnetic field strengths.

The blocking temperature of the $Mn_xZn_{(1-x)}Fe_2O_4$ nanoparticles depends on the strength of the applied magnetic field for the FC process and magnetization measurement (ZFC) process. The blocking temperature observed for $Mn_{0.625}Zn_{0.375}Fe_2O_4$ was 295 K for nanoparticles under an applied field of 100 Oe (Figure 6.5 (c)). The blocking temperature shifts down to 58^oK and $42^oK$and 16^oK when the applied field is increased to 500 Oe, 1000Oe .and 5000 Oe respectively (Figure6.5 (b)). Large discrepancies are also clearly visible in temperature-dependent magnetization between ZFC and FC processes under a field of 100 Oe, 500 Oe and 1000 Oe. At 5000 Oe ZFC and FC almost merge.

The differential behavior in magnetization below the blocking temperature is a characteristic behavior of superparamagnetic nanoparticles having undergone different cooling processes. This difference is due to the magnetic anisotropy energy barrier in $Mn_xZn_{(1-x)}Fe_2O_4$ nanoparticles [32].

The nanoparticles from a ZFC process need to overcome the magnetic anisotropy during the temperature- dependent magnetization measurement. The magnetic anisotropy does not have an effect on the magnetization of the nanoparticles from a FC process. Both thermal activation and applied magnetic field contribute in overcoming the magnetic anisotropy barrier in the zero-field-cooled nanoparticles. When a stronger magnetic field is applied, the magnetization direction of the nanoparticles becomes easier to switch to the field direction, and less assistance is required from thermal [31] activation. Consequently, the blocking temperature shifts to a lower value with increasing strength of the applied field [31] (Figure6.5 (b)).

$Mn_xZn_{(1-x)}Fe_2O_4$ nanoparticles show typical size-dependent superparamagnetic properties. Their blocking temperature increases with increasing mean size of the nanoparticles for a given field strength. For $Mn_{0.8}Zn_{0.2}Fe_2O_4$ (mean size14nm) blocking temperature is 68K and 54K at 500Oe and 1000Oe respectively. For $Mn_{0.625}Zn_{0.375}Fe_2O_4$ (mean size12nm) blocking temperature is 58K and 42K at 500Oe and 1000Oe respectively. The correlation between the blocking temperature and the size of the $MnZnFe_2O_4$ nanoparticles is consistent with the size dependence of the magnetocrystalline anisotropy in the nanoparticles. The blocking temperature is the threshold point of thermal activation, at which magnetocrystalline anisotropy is overcome by thermal activation and the nanoparticles become

superparamagnetic. The larger the nanoparticles are, the higher is the anisotropy energy. Consequently, a larger thermal energy k_BT is required for superparamagnetic transition. Therefore, Blocking temperature increases with increasing nanoparticle size [31]

6.10.4 Mossbauer

The Mössbauer spectra of the nanosamples $Mn_xZn_{(1-x)}Fe_2O_4$ (x=0.4, 0.5, 0.6, 0.65 and 0.7) within the velocity range -10 to 10 mm/s are shown in Fig.6.6.

Appearance of central doublet in all the samples with quadruple splitting is due to the presence of superparamagnetic particles in all the samples. Whereas the occurrence of only the central doublet without any sextet in the samples $Mn_xZn_{(1-x)}Fe_2O_4$ (x=0.4, 0.5), indicates that the long-range magnetic ordering has vanished and all particles in these samples appear to be superparamagnetic and behave like a single domain [33]

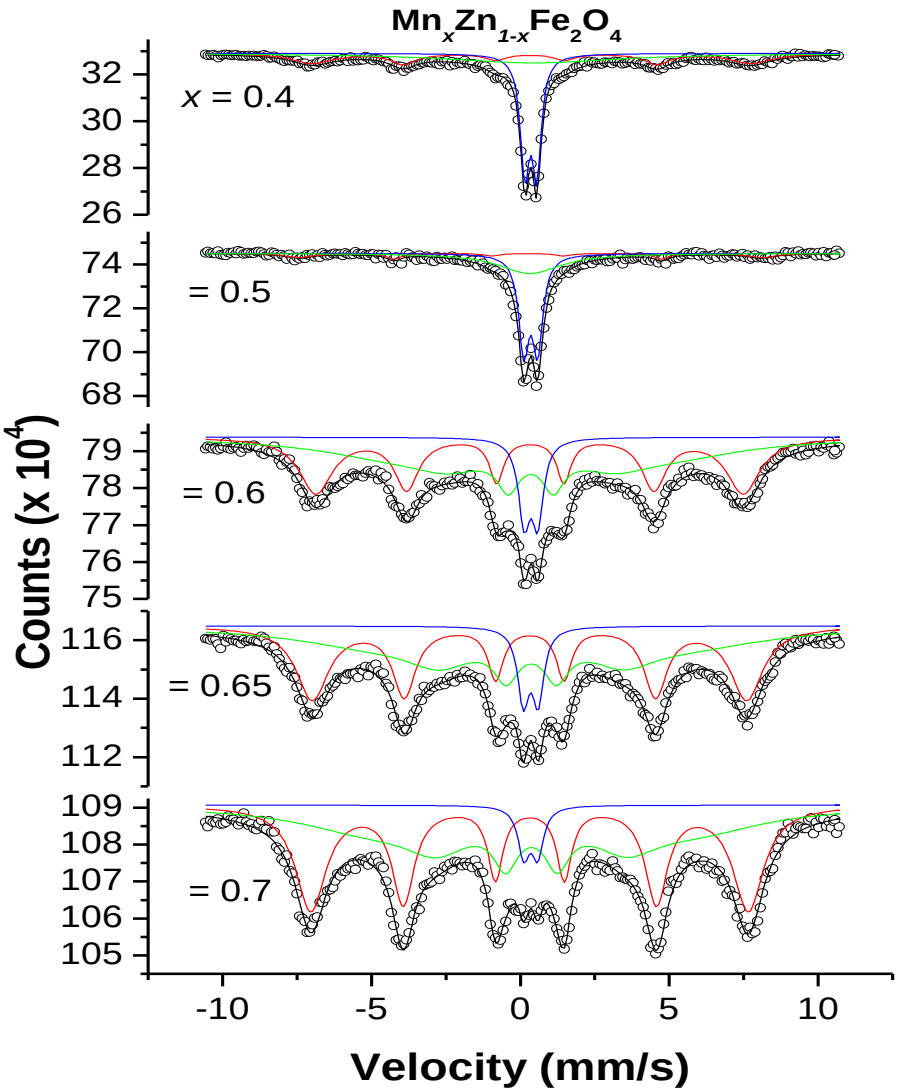

Fig 6.6 Mossbauer spectra of nanosample $Mn_xZn_{(1-x)}Fe_2O_4$ for x= 0.4, 0.5, 0.6, 0.65 and 0.7

It is also observed that significant number of particles in the samples with x=0.6, 0.65, and 0.7, are magnetically ordered at room temperature as seen from the appearance of two sextets corresponding to the A (red) and B (green) sites of the spinel structure which show ferromagnetic behavior, whereas all the particles in samples with x=0.4 and x=0.5 appears to be superparamagnetic. The spectra for the sample with x=0.6 0.65 and 0.7 shows a central paramagnetic phase C (blue), relaxed sextet subspectra combined with a week six line Zeeman pattern. The six line spectra for these samples

were analyzed into two subspectra. The sharper pattern is due to Fe^{3+} ions at A–site while the broader pattern is due to Fe^{3+} and Fe^{2+} ions at B–site. The broadening of the B-pattern is interpreted as being due to the distribution of hyperfine fields at B–site caused principally by random distribution of the cations at A–site [34]. The existence of the paramagnetic phase C in the Mössbauer spectra may be due to the fact that a fraction of Fe ions have few nearest neighbors which possess magnetically ordered spins [34], but the existing of the six– line magnetic pattern is due to the superexchange interaction between the magnetic ions at A– and B–sublattices [35]. Statistical fluctuations in the distribution of the magnetic and non–magnetic ions are believed to be responsible for this behavior [36]. The existence of the quadrupole doublet, in the spectra could be attributed to randomization of cations with different charges and radii at A– and B–sites [37]. The Mössbauer spectra have been fitted in order to get the Mössbauer parameters.

Table 6.4: Mössbauer parameter for the nanosample $Mn_xZn_{(1-x)}Fe_2O_4$ obtained at room temperature.

Conc.of Mn=x	Pattern	H_{hf} k.G.	QS mm/s	IS mm/s	Line width	Area
x=0.4	A	457.0440	-0.0235	0.3224	1.6619	30.71772
	B		0.0486	0.4423	6.9081	30.87082
	C		0.3994	0.3496	0.3610	38.41145
x=0.5	A	481.8470	-0.0427	0.2414	1.1406	13.13901
	B		0.0796	0.3229	2.5069	34.64104
	C		0.4669	0.3480	0.4106	52.21994
x=0.6	A	445.8229	0.0123	0.3330	1.3489	39.75880
	B	297.1112	-0.0121	0.3519	6.0575	50.40716
	C		0.4551	0.3553	0.4590	9.83405
X=0.65	A	453.0443	0.0057	0.3194	1.3136	42.73388
	B	331.4968	0.0203	0.3671	6.6013	49.82127
	C		0.4682	0.3483	0.4620	7.44486
x=0.7	A	456.3996	0.0051	0.3186	1.2457	47.55996
	B	341.4852	-0.0258	0.3701	5.8448	48.34182
	C		0.4682	0.3483	0.4620	4.09822

Some of the Mössbauer parameters are listed in Table 6.4 The results show that the Fe^{3+} isomer shift values *IS* of A–sites (*ISA*) and B–sites (*ISB*) do not vary gradually with Mn ion content. Their values lie between 0.2 and 0.44 mm/s. The values obtained for isomer shift are comparable with those reported previously for spinel ferrites and are characteristic of the high spin Fe^{3+} charge state [37]. The ineffectiveness of the isomer shift to the Mn ion content means that influence of Mn substitution on s–electron charge distribution of Fe ions is negligible. The values of the quadrupole shift *QS* of A and B magnetic pattern for the sample with x=0.4, 0.5, 0.6, 0.65 and 0.7 are low. This shows that, in these samples, the local symmetry of the magnetic phase of A–sites is close to cubic while that of B–site is close to trigonal.

The central doublet with isomer shifts between 0.2 and 0.44 mm/s and very low quadruple splitting (QS) is attributed to the super paramagnetic particles present in the sample [38, 39]. The obtained *QS* values of the magnetic patterns A and B are comparable with that reported previously [34]. In ferrites, the doublet structure of Mössbauer spectra arises from the quadrupole interaction of ^{57}Fe nuclei located on octa points of the spinel lattice with the electric field gradient (EFG) due to the non-spherical distribution of the 3–d electrons of the ion itself and charges on the neighboring ions [36].

The hyperfine fields for the A and B sites are distinctly seen for sample with x=0.6, 0.65 and 0.7 as shown by the splitting of the sextets. The largest hyperfine field with a smaller isomer shift is characteristic of Fe^{3+} ions in tetrahedral A site, whereas the other two sextets with relatively larger isomer shifts represent Fe^{3+} ions at two different environments in B-site. The A-site isomer shift is expected to be smaller than the B-site isomer shift due to a higher degree of covalency at A-site [40]. It is well known that in $MnFe_2O_4$ and Mn–Zn Fe_2O_4 ferrites the A-site hyperfine magnetic field is greater than the B-site hyperfine field [41-44]. The relative magnitudes of the hyperfine fields of two sites depend upon the type of nearest neighbours that the Fe^{3+} ions at these two sites have. A tetrahedral Fe^{3+} ion has all its twelve nearest neighbours from B-site whereas a B-site Fe^{3+} ion has six nearest neighbours from A-site and the other six from B-site itself. In Mn–Zn ferrite, Mn^{2+} and Fe^{3+} ions occupy both A- and B-sites whereas Zn^{2+} ion has a strong preference for A-site. Hence an A- site Fe^{3+} ion has more number of nearest neighbour

Fe^{3+} ions from B site than a B-site Fe^{3+} ion could have. Since the Fe^{3+}(A)–O–Fe^{3+}(B) super exchange interaction strength is stronger than the Fe^{3+}(B)–O–Mn^{2+}(A) super exchange interaction strength and since Fe^{3+} (B)–O–Zn^{2+}(A) bond is nonmagnetic the super exchange interaction strength experienced by a Fe^{3+} (A) ion is greater than that by a Fe^{3+} (B) ion. This results in a higher hyperfine magnetic field at A-site than that at B-site [45]. The average value for the hyperfine fields of A- and B-sites for sample 0.6, 0.65, 0.7 is found to be 37.14T, 39.20T and 39.88 T respectively, which is nearly 44 T for the bulk Mn–Zn ferrite reported in literature [46]. The reduction in the average hyperfine fields for the nanoparticles compared to their bulk values is due to particle size effects [47].

6.10.5 A.C Susceptibility

In the present study, AC susceptibility measurements were carried out on high field A. C. susceptibility equipment. [23]

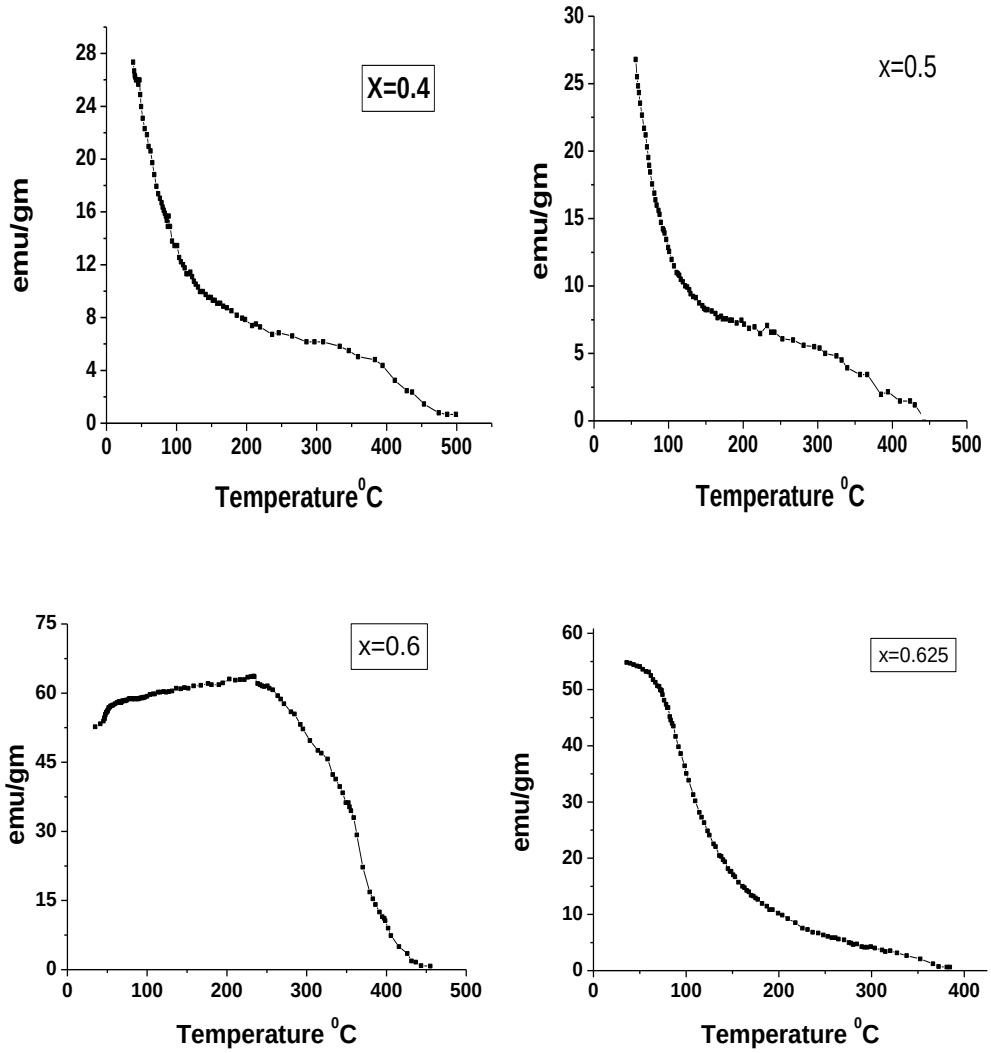

Fig: 6.7 (a) A.C. Susceptibility curves of nanosample $Mn_xZn_{(1-x)}Fe_2O_4$ for x=0.4, 0.5, 0.6 and 0.625

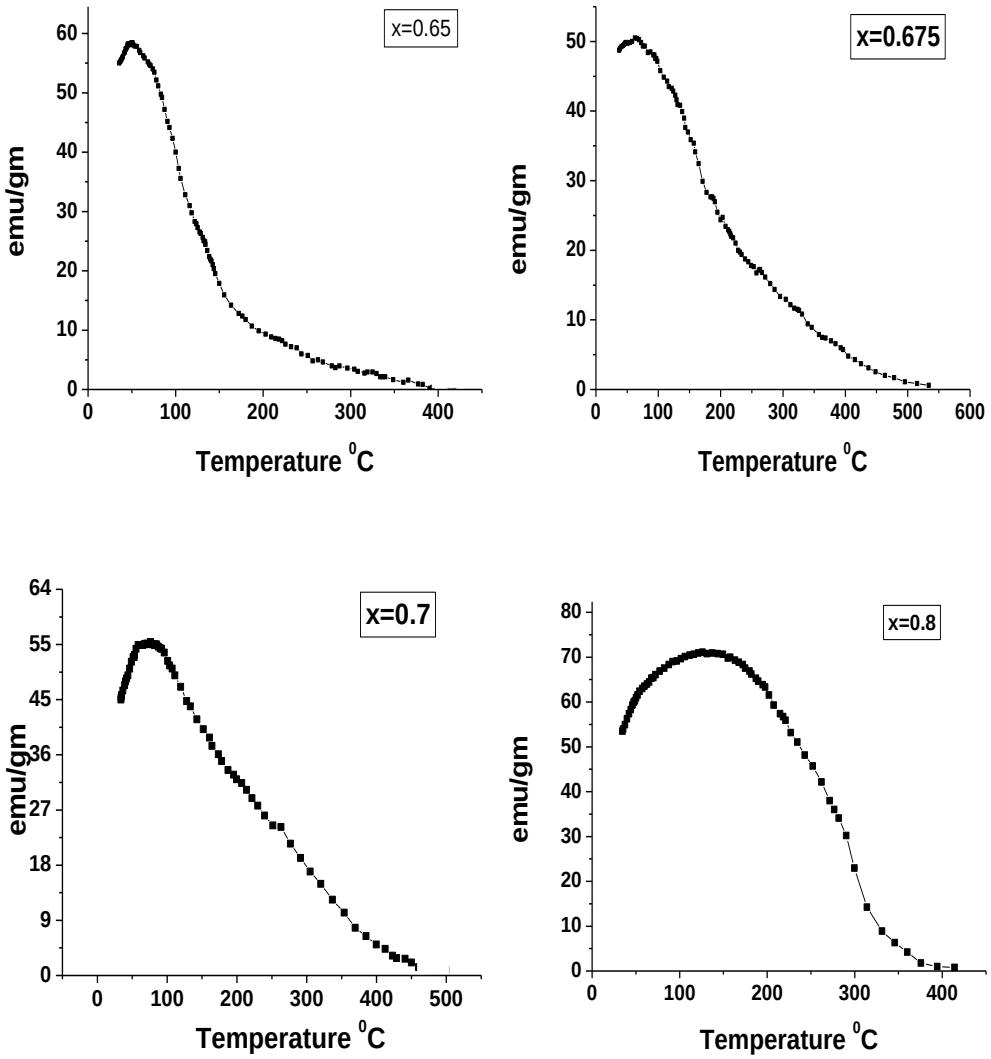

Fig: 6.7 (b) A.C. Susceptibility curves of nanosample $Mn_xZn_{(1-x)}Fe_2O_4$ for x=0.65, 0.675, 0.7 and 0.8

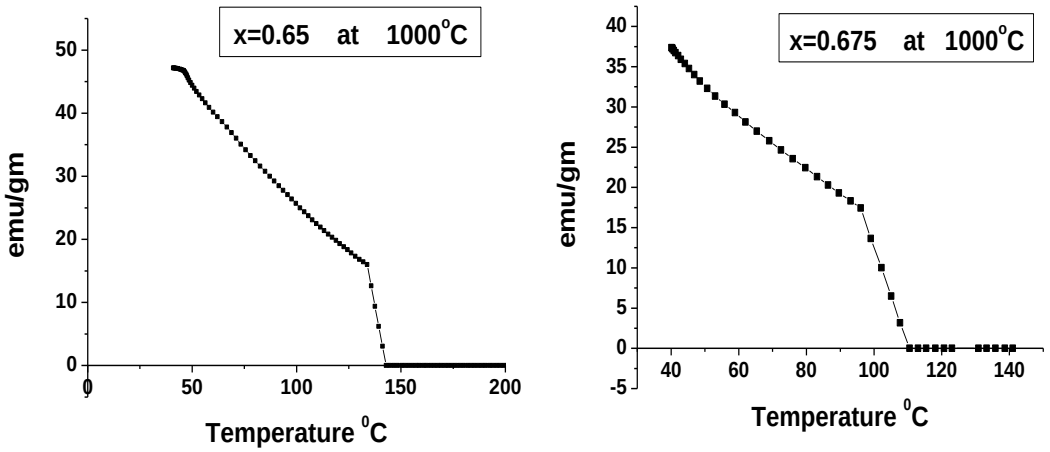

Fig. 6.7 (c): A. C. Susceptibility curves of bulk sample $Mn_xZn_{(1-x)}Fe_2O_4$ (1000^0C)

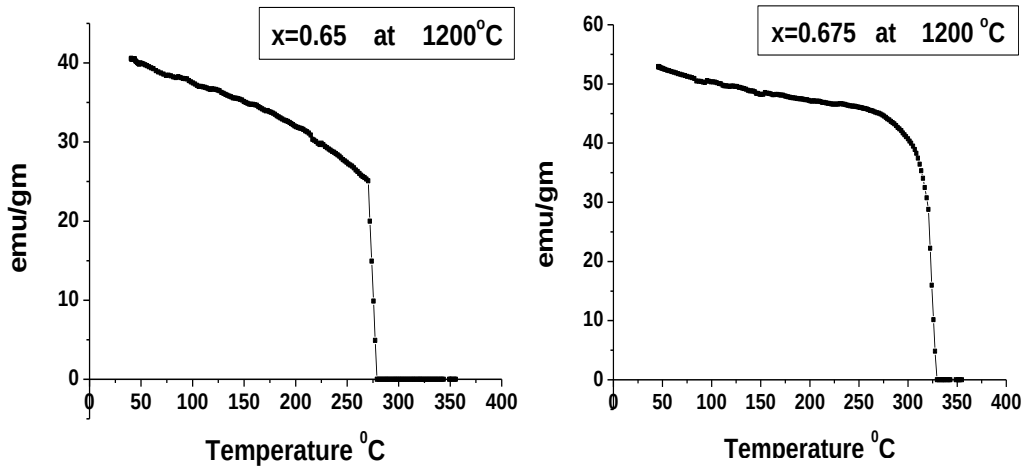

Fig. 6. 7 (d) A. C. Susceptibility curves of bulk sample $Mn_xZn_{(1-x)}Fe_2O_4$ (1200^0C)

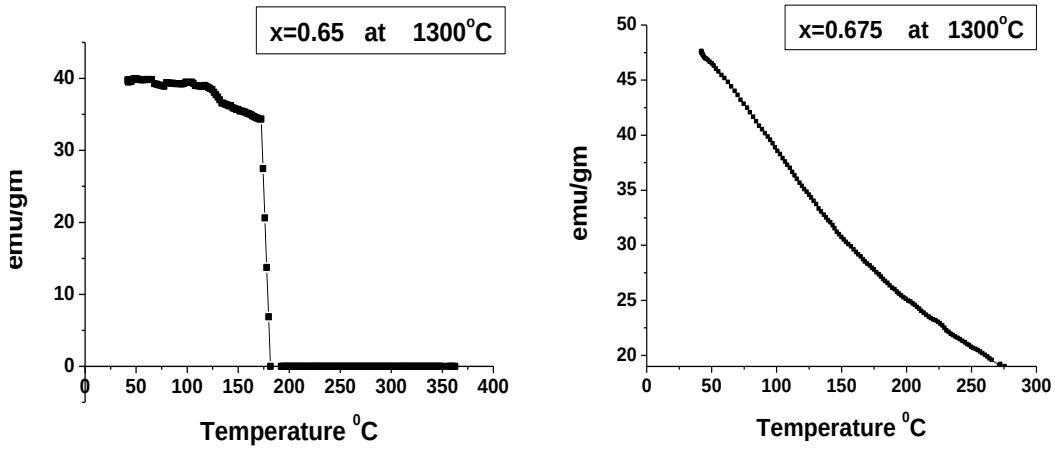

Fig. 6.7 (e) A. C. Susceptibility curves of bulk sample $Mn_xZn_{(1-x)}Fe_2O_4$ (1300^0C)

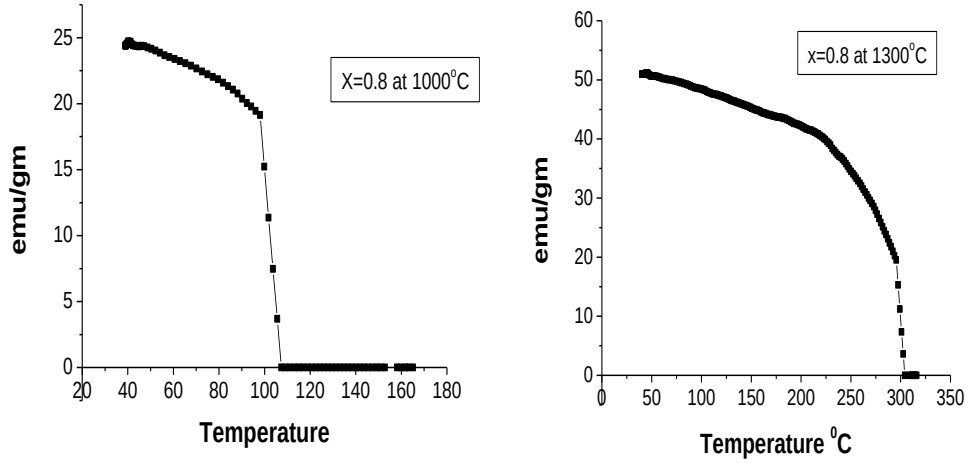

Fig. 6.7 (f) A. C. Susceptibility curves of bulk samples $Mn_{0.8}Zn_{0.2}Fe_2O_4$ (1000 ^{0}C, 1300 ^{0}C)

The variation of a.c. susceptibility with temperature has been reported by many workers [48-50]. From these curves the Curie temperature and domain structure have been estimated. It has also been found that at Curie temperature the curve drops almost to zero. Below Curie temperature, ferrites exhibit ferrimagnetic nature. At Curie temperature, magnetic transition occurs from ferromagnetic to paramagnetic.

AC susceptibility curves for nanoparticle samples indicate that the samples are mixtures of different type's particles except for x= 0.4 and x=0.5 sample. The sample with x= 0.4 and 0.5 is made up of single domain (SD) crystallites [51,52], the magnetization smoothly decreases and goes to zero as the material undergoes from ferromagnetic to paramagnetic transition. The sample with higher values of "x" exhibit a narrow multidomain (MD) character in addition to single domain (SD) behavior [53]. However the quantity of MD grains in the samples appears to depend on Mn concentration in the sample. The samples with x=0.7and x=0.8 appear to have more grains with MD and superparamagnetic (SP) character then samples with x=0.6 where SD character is more predominant. This is due to the increase in the particle size.

The Curie temperature (T_c) for nano sample $Mn_{0.4}Zn_{0.6}Fe_2O_4$ is 475^{o}C, whereas for the sample $Mn_{0.5}Zn_{0.5}Fe_2O_4$ and $Mn_{0.6}Zn_{0.4}Fe_2O_4$ it is 450^{o}C, which decreases to 375^{o}C, 390^{o}C and 425^{o}C for the sample $Mn_{0.625}Zn_{0.375}Fe_2O_4$, $Mn_{0.65}Zn_{0.35}Fe_2O_4$and $Mn_{0.8}Zn_{0.2}Fe_2O_4$ respectively. Highest Tc =540^{o}C is observed for the sample $Mn_{0.675}Zn_{0.325}Fe_2O_4$. AC susceptibility curves for bulk samples also exhibit the SD and MD character. Curie temperature for bulk sample $Mn_{0.65}Zn_{0.35}Fe_2O_4$ obtained at 1200^{o}C and 1300^{o}C is 275^{o}C and 180^{o}C respectively. And for the bulk sample $Mn_{0.675}Zn_{0.325}Fe_2O_4$ obtained at 1200^{o}C and 1300^{o}C, T_c is 325^{o}C, 275^{o}C respectively. Curie temperatures for bulk samples are much less compare to nanoparticle samples.

6.10.6 Initial Permeability

Initial magnetic permeability (μi) is a microstructure sensitive, technologically important extrinsic magnetic property which decides the suitability of a ferrite for particular application, which in turn depends upon the method of preparation. The study of thermal variation of initial permeability of polycrystalline ferrite can be used as quality test in the preparation of ferrite samples [54].

The Variation of permeability with the temperature of bulk samples $Mn_xZn_{(1-x)}Fe_2O_4$ (x= 0.4, 0.5, 0.6, 0.675) obtained at 900^oC and 1000^oC, for various frequencies (100Hz. to 3MHz) are shown in Fig. 6.8 (a,b,c & d). Bulk samples obtained at 900^oC shows very low value of permeability compared to samples obtained at 1000^oC (Fig. 6.8 c & d). Low value of initial permeability of the samples obtained at 900^oC sintering temperature is because of the quenching of magnetic moment. Initially, there is a steady decrease in Permeability with temperature and then it almost remains constant for a wide range of temperature, followed by a sharp drop to a very low value at Curie temperature. The constant value of permeability obtained is due to the fact that the rate of change of M_S and the rate of change of anisotropy field with temperature are the same [55] in all the above bulk samples. We have not observed any profound peak in the μi-T variation. It may be possible to observe this type of peak at a lower temperature below room temperature as observed by some workers [56, 57].

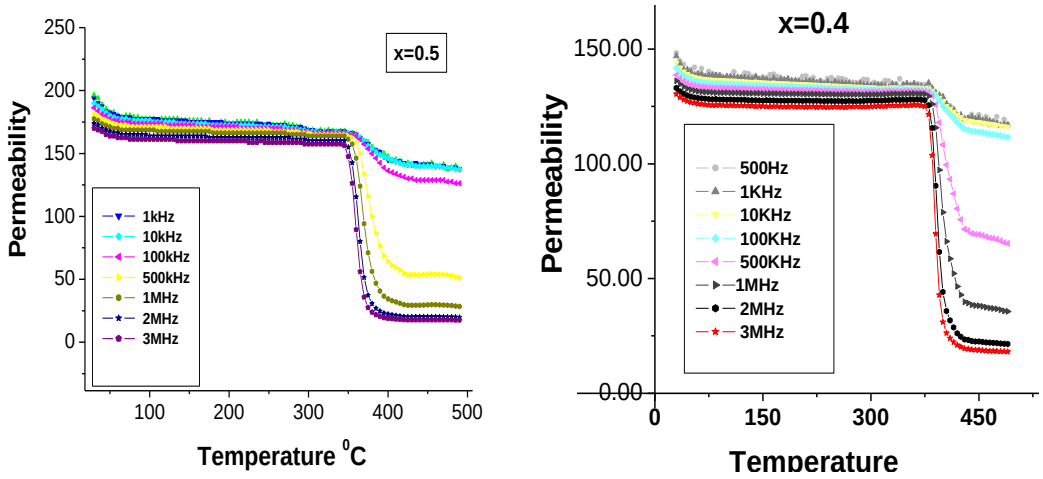

(a) (b)

Fig. 6.8 (a, b): Variation of Permeability with temperature at different frequencies of bulk sample a) $Mn_{0.5}Zn_{0.5}Fe_2O_4$ (900^0C) and b)$Mn_{0.4}Zn_{0.6}Fe_2O_4$ (900^0C)

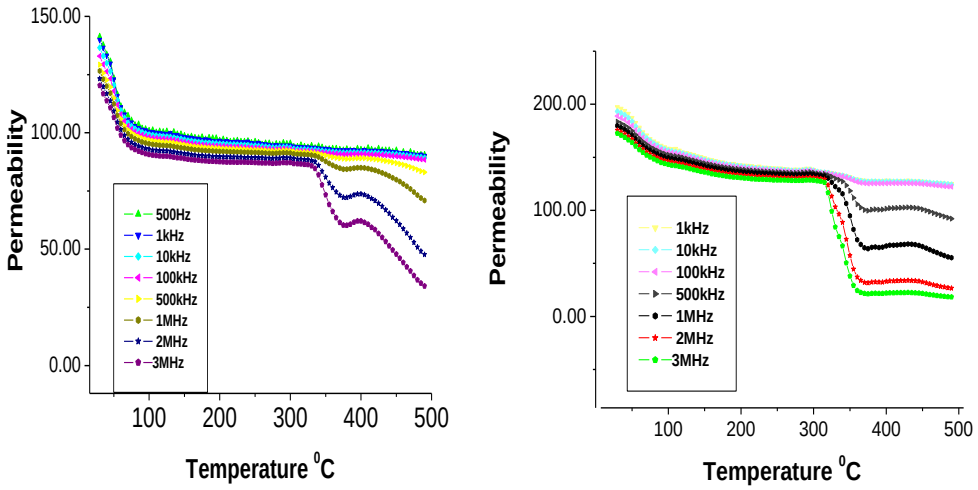

(c) (d)

Fig. 6.8 (c, d) Variation of Permeability with temperature at different frequencies of bulk samples c)$Mn_{0.675}Zn_{0.325}Fe_2O_4$($1000^0$C) and d)$Mn_{0.6}Zn_{0.4}Fe_2O_4$ (1000^0C)

Variation of initial permeability with the temperature for bulk samples $Mn_xZn_{1-x}Fe_2O_4$ (x= 0.5, 0.675 0.8), obtained at 1100°C, 1200°C and 1300°C, at various frequencies (100Hz.to 3MHz) are shown in Fig. 6.9 (a,b,c,d,e,f,g,h) Samples sintered at higher temperatures exhibit different nature of µi-T variation. Permeability is maximum at room temperature, decreases almost exponentially with increase in temperature and then there is a sharp drop at Curie temperature.

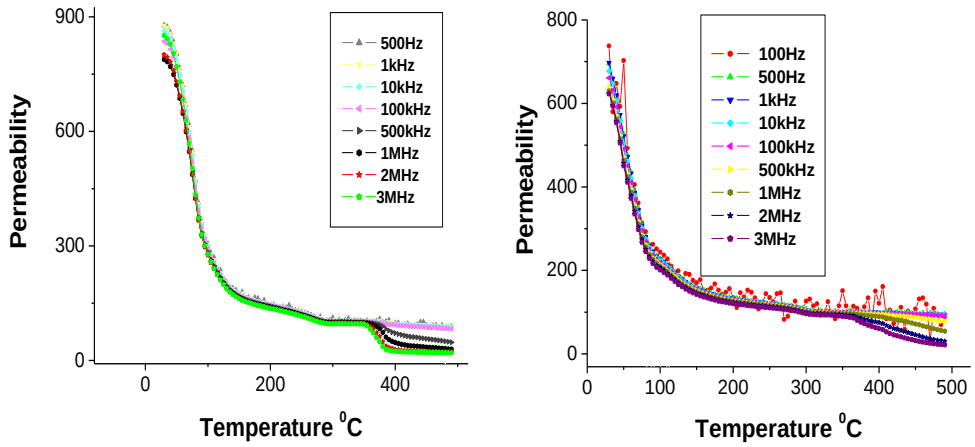

(a) (b)

Fig. 6.9 (a,b): Variation of Permeability with temperature at different frequencies of bulk samples (a) $Mn_{0.8}Zn_{0.2}Fe_2O_4$ (1100^{0}C)and (b) $Mn_{0.675}Zn_{0.325}Fe_2O_4$ (1100^{0}C)

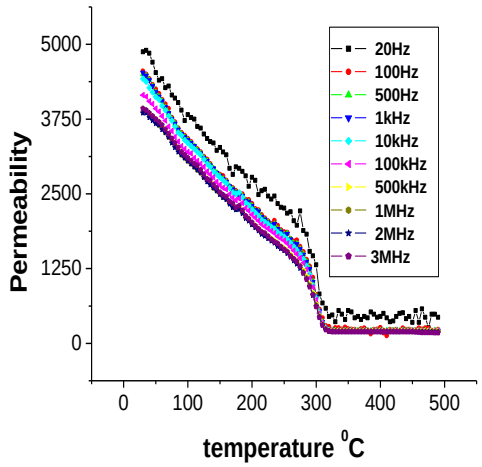

(c)

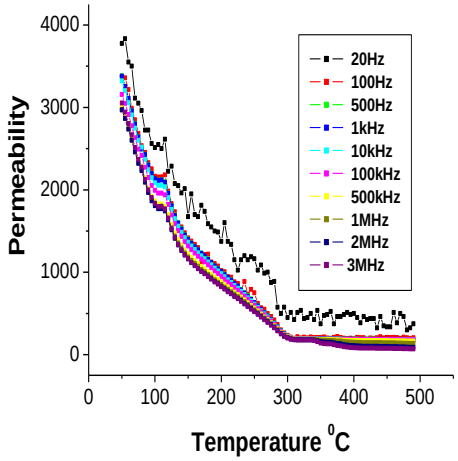

(d)

Fig. 6.9 (c,d): Variation of Permeability with temperature at different frequencies of bulk samples c)$Mn_{0.8}Zn_{0.2}Fe_2O_4$ (1200^{0}C) and d) $Mn_{0.0.675}Zn_{0.325}Fe_2O_4$ (1200^{0}C)

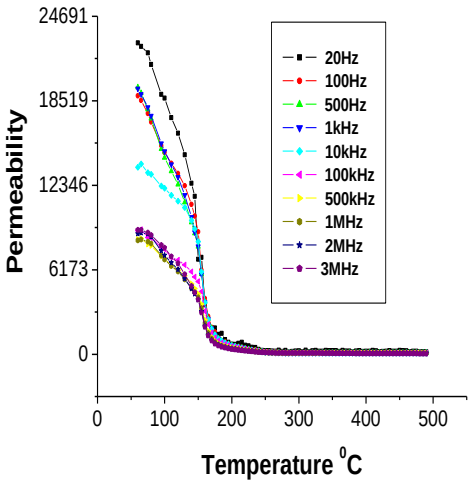

(e)

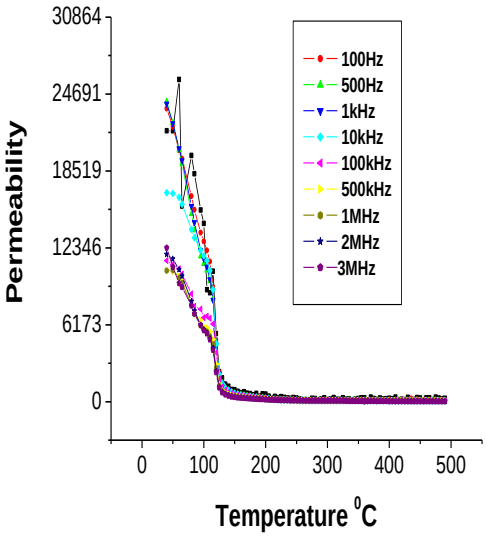

(f)

Fig. 6.9 (e,f): Variation of Permeability with temperature at different frequencies of bulk samples (e) $Mn_{0.8}Zn_{0.2}Fe_2O_4$ (1300^{0}C) and (f)$Mn_{0.675}Zn_{0.325}Fe_2O_4$ (1300^{0}C).

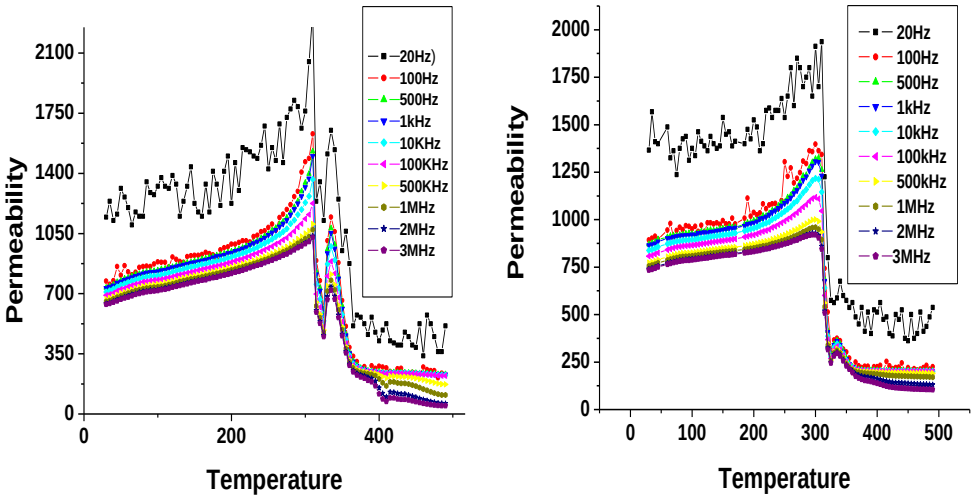

(g) (h)

Fig.6.9 (g, h) Variation of Permeability with temperature at different frequencies of bulk sample (g)$Mn_{0.5}Zn_{0.5}Fe_2O_4$ (1100^0C) and (h) $Mn_{0.5}Zn_{0.5}Fe_2O_4$ (1200^0C)

No sharp Hopkinson peak is observed [56,57,58] in all the samples except in $Mn_{0.5}Zn_{0.5}Fe_2O_4$ in the frequency range 100Hz to 3Mhz. The sample $Mn_{0.5}Zn_{0.5}Fe_2O_4$ shows totally different behavior. For this particular sample, permeability increases with increase in temperature and shows Hopkinson peak near Curie temperature.

Initial permeability is related to Ms and temperature dependence of the effective magnetic anisotropy <K> as

$$\mu i \alpha Ms^2/<K>$$

Any mismatch between the rate of decrease of <K> and Ms^2 will either increase or decrease the permeability with increase in temperature [58]. The increase in permeability with temperature is due to the fact that the anisotropy decreases faster with temperature than the saturation magnetization. The

maxima in initial permeability corresponds to the point of zero anisotropy field.[59] The sharp fall in the value of μi near T_c indicates single phase formation of the ferrite.

Variation of initial permeability with temperature for $Mn_xZn_{(1-x)}Fe_2O_4$ (x=0.4, 0.5, 0.6, 0.625,0.65, 0.675, 0.7, 0.8) sintered at one particular temperature and measured at 100KHz frequency is shown fig.6.10. (a,b,c and d). Variation of permeability with Temperature for $Mn_xZn_{(1-x)}Fe_2O_4$ sintered at 1300 ^{0}C and measured at 20Hz is shown in fig 6.10 (e)

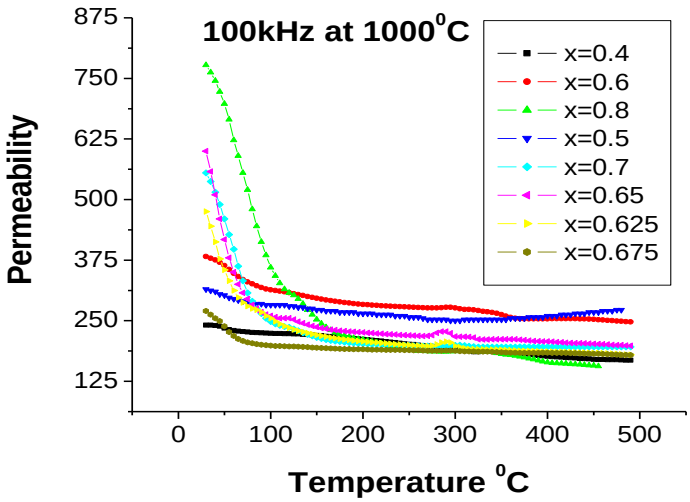

Fig.6.10 (a) Variation of permeability with temperature of bulk sample $Mn_xZn_{(1-x)}Fe_2O_4$ (1000 ^{0}C)

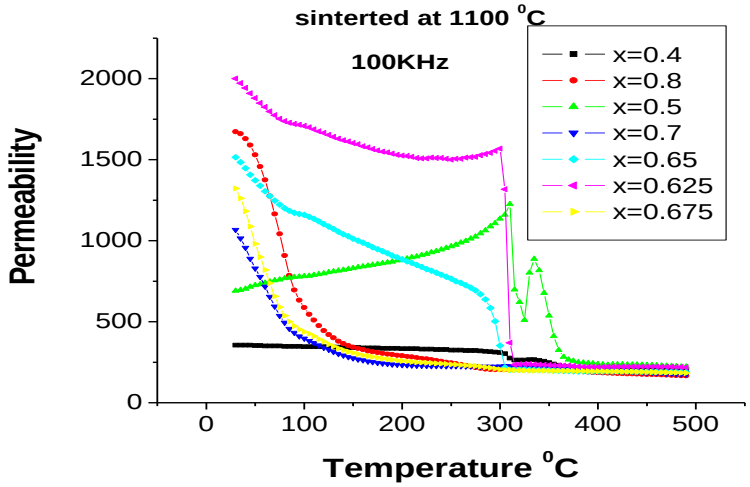

Fig.6.10 (b) Variation of permeability with temperature of bulk sample

$Mn_xZn_{(1-x)}Fe_2O_4$ (1100 ^{0}C)

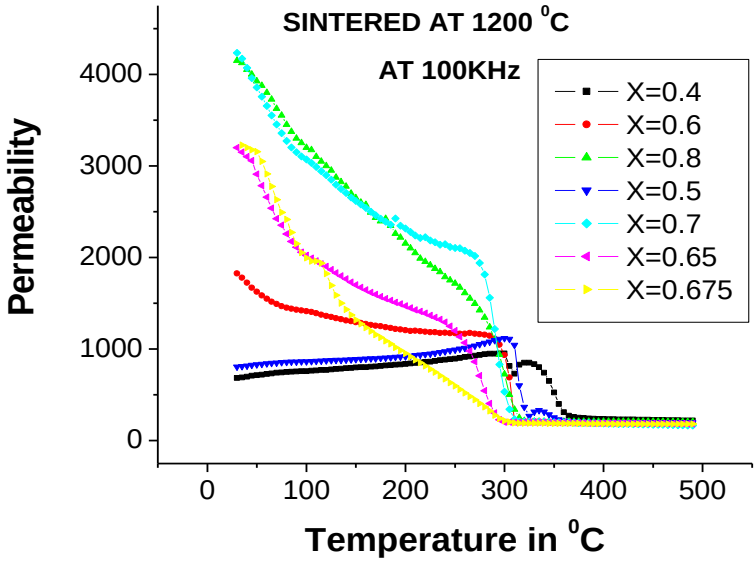

Fig.6.10 (c) Variation of permeability with temperature of bulk sample

$Mn_xZn_{(1-x)}Fe_2O_4$ (1200 ^{0}C)

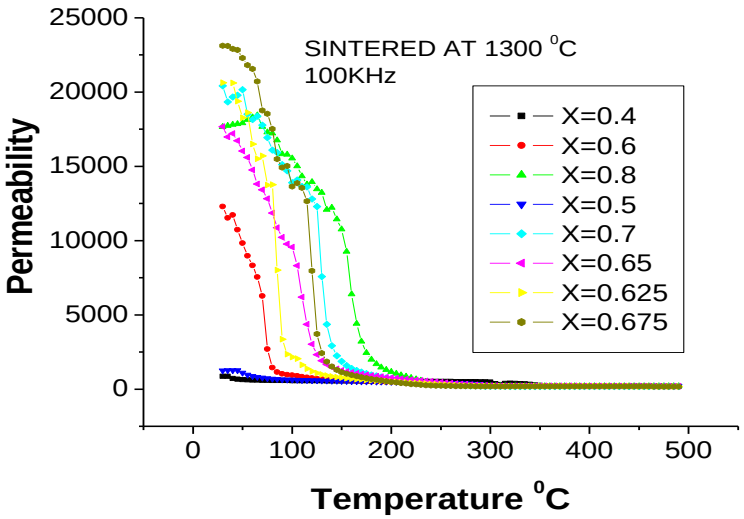

Fig.6.10 (d) Variation of permeability with temperature of bulk sample

$Mn_xZn_{(1-x)}Fe_2O_4$ (1300 ^{0}C)

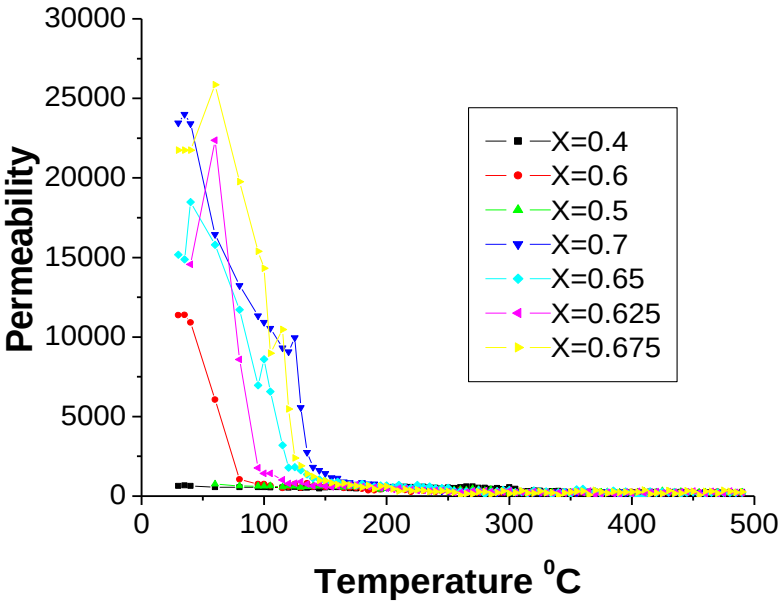

Fig.6.10 (e) Variation of Permeability with Temperature of bulk $Mn_xZn_{(1-x)}Fe_2O_4$ (1300^{0}C)at 20Hz

Room temperature permeability of bulk sample $Mn_{0.8}Zn_{0.2}Fe_2O_4$ (1000^{o}C) is 775 (at 100KHz.) whereas 245 is room temperature permeability

shown by bulk sample $Mn_{0.4}Zn_{0.6}Fe_2O_4$ (1000^0C) (at 100KHz). When the samples are sintered at 1100^oC, $Mn_{0.625}Zn_{0.375}Fe_2O_4$ shows highest value of permeability ie.2000 and lowest is 250 for the sample $Mn_{0.4}Zn_{0.6}Fe_2O_4$ at room temperature. Whereas when the sintering temperature is 1200^oC, $Mn_{0.7}Zn_{0.3}Fe_2O_4$ shows maximum value of permeability i.e. 4070 and minimum is 625 for $Mn_{0.4}Zn_{0.6}Fe_2O_4$. Bulk sample $Mn_{0.675}Zn_{0.325}Fe_2O_4$ (1300^oC) has highest value of permeability i.e. 22000 at 100KHz, and minimum appears in $Mn_{0.4}Zn_{0.6}Fe_2O_4$. Initial permeability measured at 20Hz of the bulk samples obtained at 1300^oC (Fig.6.10 (e)) increases with increase in temperature and shows a peak just before the Curie point, which is Hopkinson peak [58] and then drops to a very small value. Highest value of initial permeability observed was 26,876 for the bulk sample $Mn_{0.675}Zn_{0.325}Fe_2O_4$ (1300^oC) measured at 20 Hz.

Variation of permeability with frequency for the sample $Mn_{0.8}Zn_{0.2}Fe_2O_4$ and $Mn_{0.675}Zn_{0.35}Fe_2O_4$ at various sintering temperature is shown in fig 6.11.(a and b) and SEM Micrograph of bulk sample $Mn_{0.8}Zn_{0.2}Fe_2O_4$ (900^0C ,1000^0C 1100^0C, 1200^0C and 1300^0C) is shown in Fig. 6.11 (c, d, e, f & g).

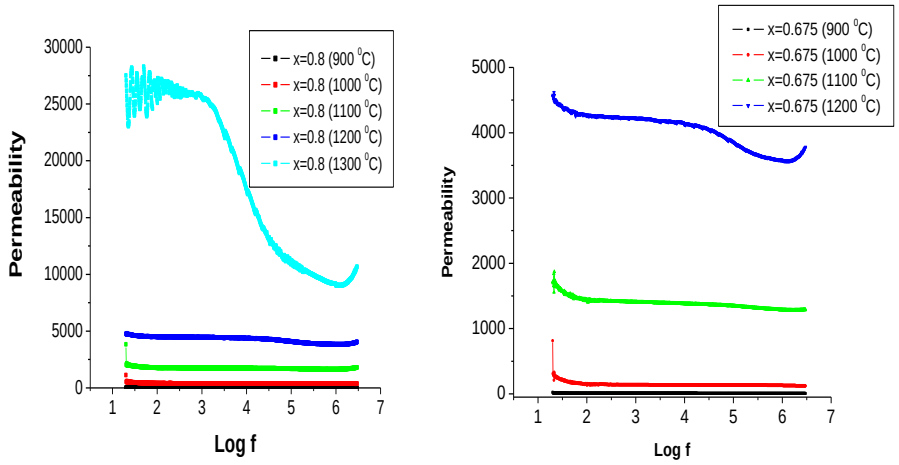

(a) (b)

Fig. 6.11 (a,b) Variation of permeability with Freq. for different sintering Temperature

(a) $Mn_{0.8}Zn_{0.2}Fe_2O_4$ and (b) $Mn_{0.675}Zn_{0.325}Fe_2O_4$

Room Temperature initial permeability for the bulk sample $Mn_{0.675}Zn_{0.325}Fe_2O_4$ (1000°C) measured at 500Hz is 190, increases to 1422 and 4258 at 1100° and 1200°C respectively. Maximum value of initial permeability for the bulk sample $Mn_{0.8}Zn_{0.2}Fe_2O_4$ obtained at 1000°C, 1100°C, 1200°C, 1300°C is 655, 1818, 4509 and 25980 respectively.

Overall permeabilities increase with increase in sintering temperature for all the bulk samples, as depicted in fig 6.11(a,b). Increase in permeability with sintering temperature can be attributed to an increase in density and grain size with sintering temperature [60]. With higher grain size and greater density the grain to grain continuity in the magnetic flux leads to higher permeability. This is evident from the SEM of $Mn_{0.8}Zn_{0.2}Fe_2O_4$ sintered at 900°C, 1000°C, 1100°C, 1200°C and 1300°C **(**Fig**.** 6.11 c, d, e, f & g).

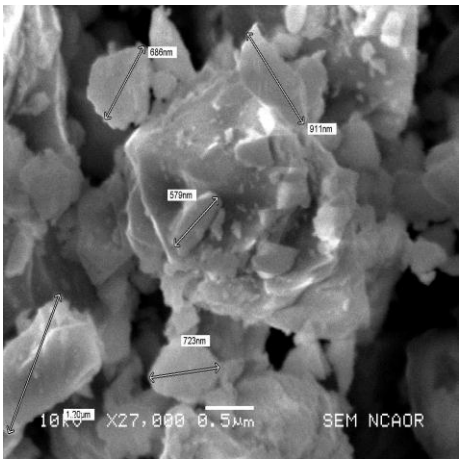

c

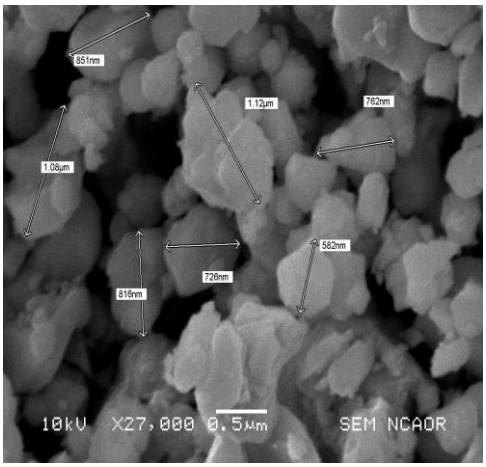

d

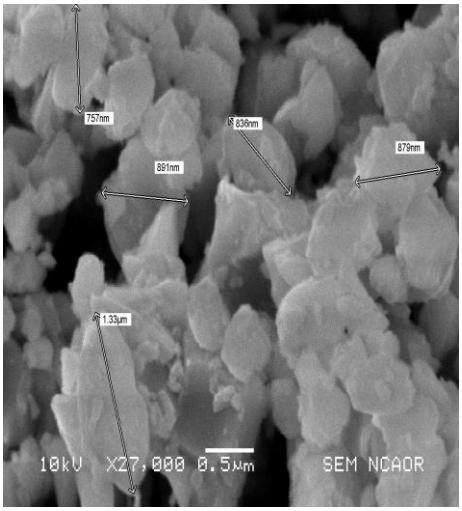

e

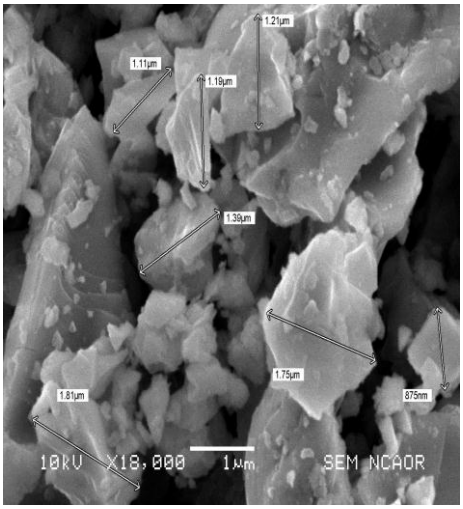

f

Fig.6.11(c,d,e,f) SEM Micrograph of bulk $Mn_{0.8}Zn_{0.2}Fe_2O_4$ obtained at c) 900 ^{0}C d) 1000 ^{0}C e) 1100^{0}C and f) 1200^{0}C

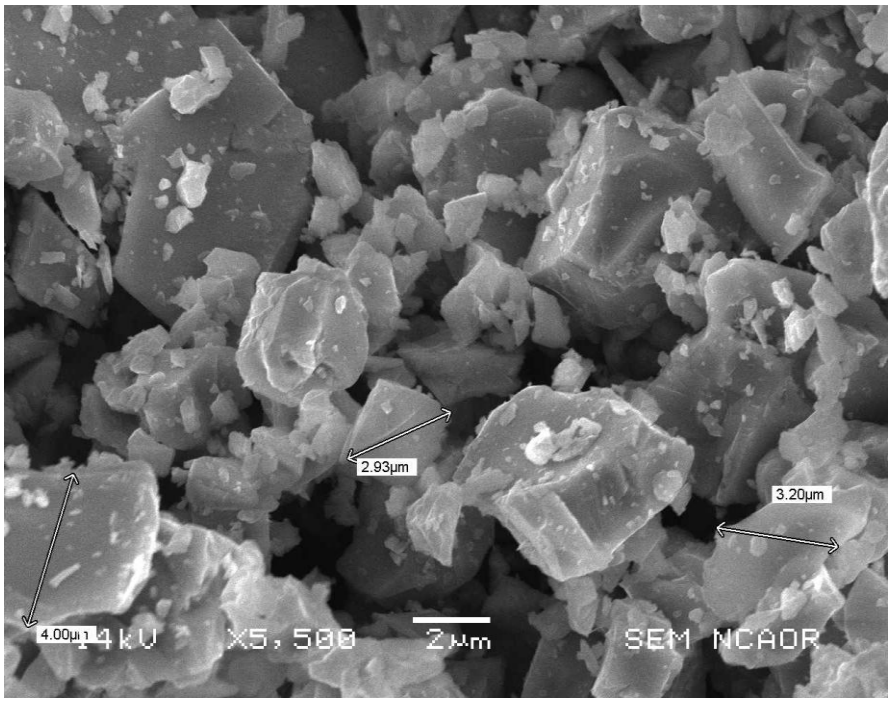

Fig.6.11 (g) SEM Micrograph of bulk $Mn_{0.8}Zn_{0.2}Fe_2O_4$ obtained at 1300 ^{0}C

SEM micrograph of the bulk sample $Mn_{0.8}Zn_{0.2}Fe_2O_4$ (900^{o}C) shows microstructure with well developed grains with grain size around 680 nm, however nonmagnetic voids are also large. The density of this sample is 3.33gm/cc.Hence the permeability of this sample is the lowest one. More over the permeability of this samples is lowest largely due to the fact that it is governed by Ms, and Ms is lowest for this sample. When the sample in sintered at 1000^{o}C the grain size increases to 1.1 µm and the density increases to 3.613gm./cc., shows larger crystalline size and less nonmagnetic voids. As a result permeability is higher as compared to bulk samples obtained at 900^{o}C. The Ms value for these bulk samples is also larger compared to bulk samples obtained at 900^{o}C. Bulk samples obtained at 1100^{o}C and 1200^{o}C shows further increase in grain size and density as well as in Ms value. Grain size increases to 1.3µm, 1.8 µm, density increases to 3.72gm./cc, 3.911 gm/cc and Ms increases from 27 emu/gm. to 58 emu/gm respectively .Accordingly there

is a increase in permeability. The bulk sample obtained at 1300^{o}C shows interesting microstructure. The sample has much larger polycrystalline grains with less nonmagnetic voids and the density is 4.72gm./cc**.** The sample has large crystallites and also exhibits a higher Ms value 66 emu/gm and hence exhibits very high value of permeability.

The initial permeability of high permeability material depends to a large extent on mobility of the Bloch's domain walls. To obtain high permeability it is important to reduce the crystalline anisotropy and the magnetrostriction. Ferrites in particular are burdened with magnetic imperfections. Voids in bodies that are not completely densified, non-magnetic inclusions are ample, these factors, give rise to internal magnetostatic energy. The stable domain configuration in a material is always such is to minimize this energy. The loss that occurs is proportional to imperfections of materials as well its anisotropy, both crystalline and strain. High permeability may be expected in materials that are homogeneous, dense and have composition that has very low value of anisotropy. Anisotropy is temperature dependent property. Effect of this depends on the composition. The anisotropy in Mn-Zn ferrite is highly dependent on the material composition. For some compositions of Mn-Zn, anisotropy takes negative value at room temperature, increases monotonically with temperature to zero at Curie temperature whereas for certain combinations of Mn-Zn it takes a negative value increases to zero, takes a positive value and decreases to attain a zero value at Curie temperature. This behavior is strongly reflected in the initial permeability of the material. The initial permeability rises to maximum at both zero anisotropy points with a saddle corresponding to the temperature

at which anisotropy has a maximum positive value [61,62]. Well-adjusted sintering conditions support the design of microstructure and resulting magnetic properties of the sample.

The variation of initial permeability at room temperature with frequency in the range 20 Hz to 3MHz for the bulk samples $Mn_xZn_{(1-x)}Fe_2O_4$ (x=0.4, 0.5, 0.6 , 0.625, 0.65, 0.675, 0.7, 0.8) obtained at 900^{o}C, 1000^{o}C, 1100^{o}C are shown in Fig. 6.12 (a, b, c)

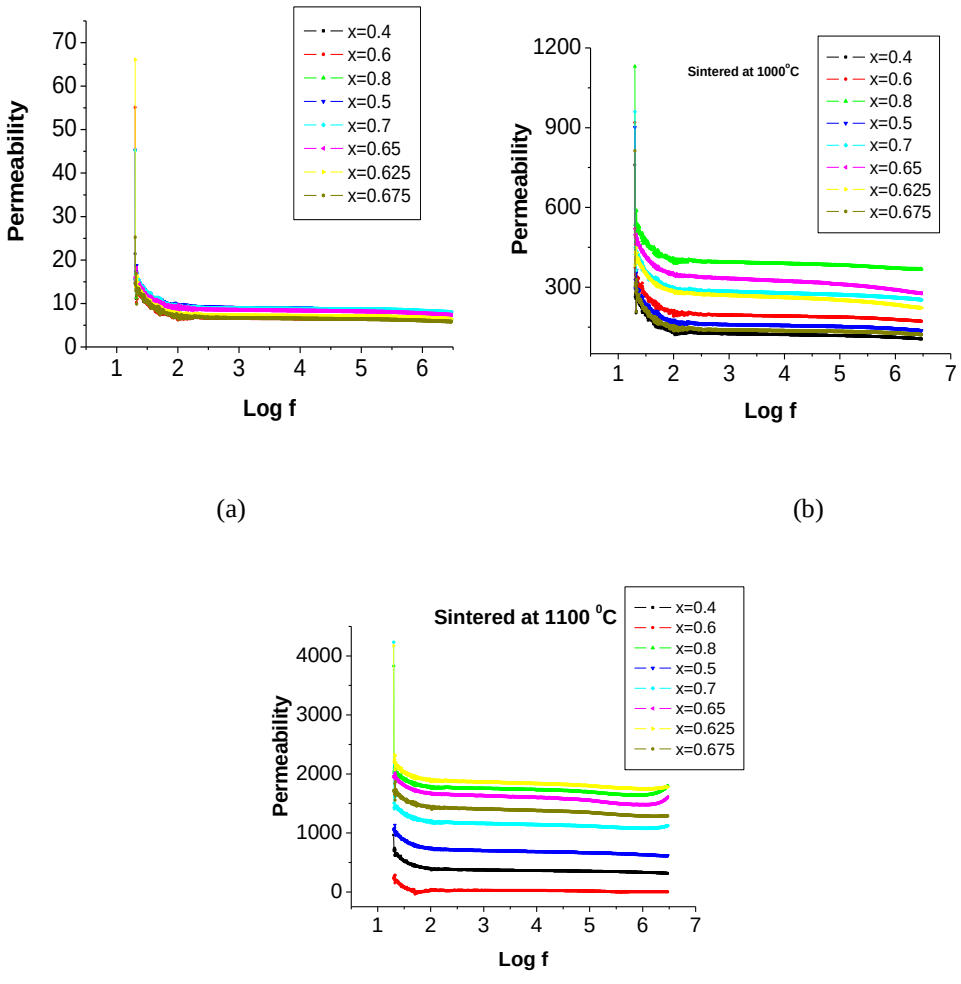

(a) (b)

(c)

Fig.6.12 (a,b,c): Variation of Permeability with frequency for bulk samples $Mn_xZn_{(1-x)}Fe_2O_4$ obtained at a)900^{o}C. b) 1000^{o}C, and c) 1100^{o}C

Initially there is a sharp decrease in the permeability to a low value with increase in frequency from 20Hz to 100Hz, and then it is found to be independent of frequency in the frequency range 100Hz to 3MHz. Bulk sample $Mn_{0.8}Zn_{0.2}Fe_2O_4$ (1100^oC) has permeability 3858 at 20 Hz., decrease to 1769 at 100 Hz., from 100Hz to 3 MHz it is constant. Similarly the bulk sample $Mn_{0.625}Zn_{0.375}Fe_2O_4$ (1100^oC) shows maximum value of permeability 4139 at 20 Hz, decreases to 1896 at 100Hz, from 100Hz to 3 MHz permeability is independent of frequency.

The variation of initial permeability with frequency can be understood on the basis of Globus model [63,64]. According to this model, $(\mu i - 1)^2$ fr = constant, where μi is the static initial permeability and fr is the dispersion frequency. It follows from this equation that dispersion frequency is expected to be lower for specimen of higher permeability. Constant behavior of μi in the frequency range 100Hz to 3 Mhz is attributed to the domain wall motion.

Variation of initial permeability with frequency of the bulk samples $Mn_xZn_{(1-x)}Fe_2O_4$ (x=0.4, 0.5, 0.6, 0.625, 0.65, 0.675, 0.7, 0.8) obtained at 1200^oC and 1300^oC are shown in Fig.6.12 (d, e).

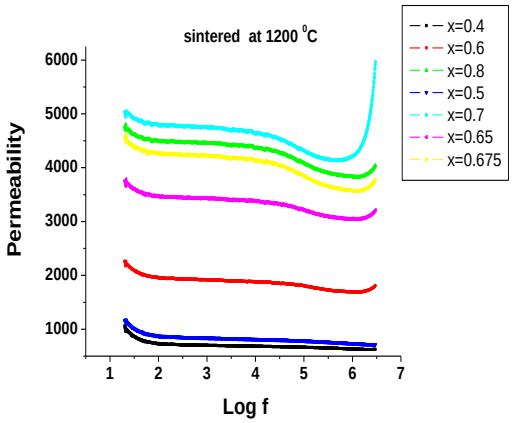

(d)

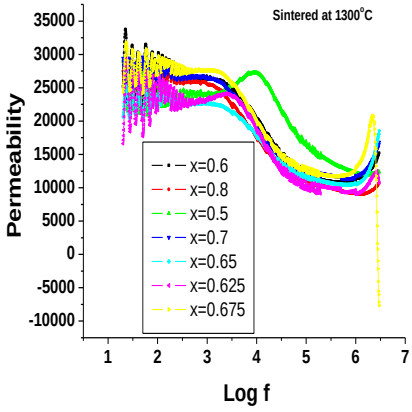

(e)

Fig.6.12 (d,e)Variation of Permeability with frequency for bulk samples $Mn_xZn_{(1-x)}Fe_2O_4$obtained at d) 1200°C, and e) 1300 °C

For bulk sample $Mn_{0.675}$ $Zn_{0.325}Fe_2O_4$ obtained at 1300°C, permeability is 26876 at 20 Hz., decreases to 11815 at 0.398MHz, beyond this frequency µi starts increasing and resonance peak appears at 2.3 MHz. Permeability of bulk sample $Mn_{0.5}$ $Zn_{0.5}Fe_2O_4$ obtained at 1300°C is 24164 decreases to 2400 in the frequency range 20Hz to 750 Hz. Beyond this frequency permeability starts increasing, and exhibits a resonance peak at 10 K.Hz. In general in all bulk samples obtained at 1200°C and 1300°C there is a decrease in permeability with increase in frequency up to certain range of frequency, for higher frequency permeability starts increasing. In most of the samples there is no resonance peak, except for the bulk samples $Mn_{0.675}$ $Zn_{0.325}Fe_2O_4$, $Mn_{0.625}$ $Zn_{0.375}Fe_2O_4$ and $Mn_{0.5}$ $Zn_{0.5}Fe_2O_4$ obtained at 1300°C. Whereas for all the bulk samples obtained at 1200°C show a rise in the permeability at higher frequency but do not exhibit any resonance peaks. The reason for the absence of resonance peak may be that, this peak probably lies beyond the measurable

frequency range. The magnetic spins in the ferrites precesses with a natural frequency known as the Larmor frequency. The resonance peak, occurs when the frequency of applied field equals the Larmor precession of electron spins and the consequent absorption of energy. [65]

The variation of the loss factor (tanδ) with frequency for the bulk samples $Mn_xZn_{(1-x)}Fe_2O_4$ (x=0.4, 0.5, 0.6 , 0.625, 0.65, 0.675, 0.7, 0.8) obtained at 900 ^oC, 1000 ^oC, 1100^oC , 1200 ^oC, 1300 ^oC are shown in Fig.6.13 **(**a,b,c,d,e**).** It is observed that for all the samples loss decreases rapidly to an extremely low value with increase in frequency from 20Hz. to 1 KHz. In the frequency range from 1 KHz to 3MHz. loss remains constant to a low value. Also loss decreases with increase in sintering temperature.

The loss is found to depend on composition and microstructure of the sample, which is decided by sintering profile of the sample. The low losses are result of appropriate control of chemical composition and microstructure of ferrites [66].

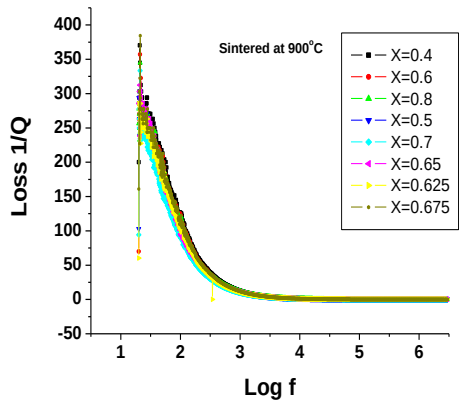

(a)

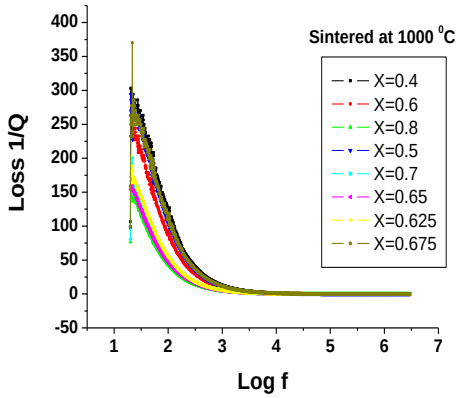

(b)

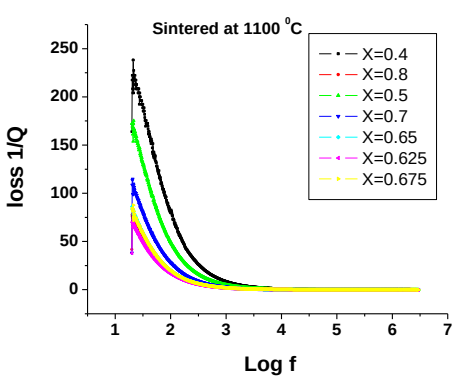

(c)

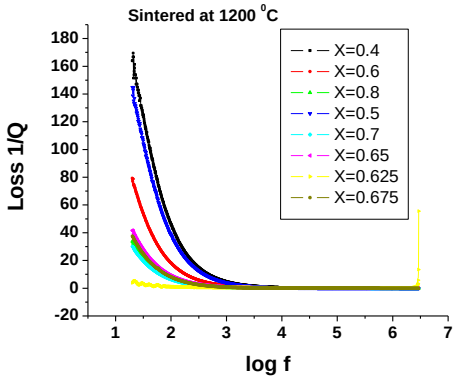

(d)

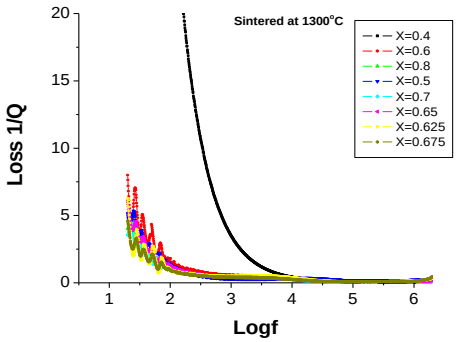

(e)

Fig.6.13(a,b,c,d,e) The variation of the loss factor (tanδ) with frequency for the bulk samples $Mn_xZn_{(1-x)}Fe_2O_4$ obtained at (a) 900 °C, (b) 1000 °C, (c) 1100 °C,(d) 1200 °C, (e) 1300 °C.

The losses and their frequency dependence determine the ultimate operating frequency of magnetic devices. The losses in ferrites are associated with domain wall relaxation and rotational resonance. Domain wall relaxation is usually observed at lower frequency while the rotational resonance is observed in the megahertz range [65].

References

[1] R. Kotitz, P. C. Fannin, L. Trahms, Journal of Magnetism and Magnetic Materials 149(1995) 42-46.

[2] I. S. Jacobs, C. P. Bean, in Magnetism, Vol. III (Eds.: G. T. Rado, H. Suhl), Academic Press, New York, 1963, pp. 271.

[3] T. Sato, T. Iijima, M. Sekin, N. Inagaki, Journal of Magnetism and Magnetic Materials, 65(1987)252.

[4] A. A. Sattar and K. M. El-Shokrofy J. Phys., IV France 7 Colloq (1997), Cl-245.

[5] Goldman, Modern ferrite Technology, Van Nostrand Reihold, New York, 1990.

[6] S. Chikazumi "Physics of Magnetism" Wiely, New York (1996).

[7] A. Globus J.Physique Coll., Cl (1963) C1.1-C1.15.

[8] A. Globus Cardiff Conf. USA, (1975).

[9] A. Globus and P. Duplex Phys. Stat. Solidi, 31 (1968) 75.

[10] A. Globus and M. Gayut, IEEE Transactions on magnetics, 6 (1970) 614.

[11] A. Globus, Thesis, Univ. of Paris, France (1963).

[12] M. T. Johnson and E. G.Vissar, IEEE Trans. Magn. MAG-26, (1990) 1987.

[13] P. J. Vender Zaag, J. J. M. Ruigrok, A. Noordermeer, M. H. W. M. van Deiden, P. J. Por, Recveltk, D. M. Sonnet and J. N. Chapman, J. Appl.Phys,74(6) (1993) 4085.

[14] H. Piscard and A. Globus, Phys. Rev. B 24 (1981) 6610.

[15] G. Rankis Bull. Latv. Acad.Sci., Phys Tech. Sci., N2 (1984) 27.

[16] A. Globus J. Phys. (France) 38 (1977) 1.

[17] J. Gieraltowski, Ferrites, Proc. International Conf., Japan (1980) 277.

[18] H. Rikukawa, IEEE Trans., On Magn., 18 (1982) 1535.

[19] C. Guillaud Proc. IEEE, 704 (B) (1957) 165.

[20] C. Kittel, Physical Reviews, 70 (1946) 965.

[21] C. P. Bean, J. D. Livingston, Journal of Applied Physics 1959, 30, 120S

[22] S. D. Likhite and C. Radhakrishnamurthy and P. W. Sahasrabudhe, Rev.Sci.Instr. 25, (1965), 302.

[23] S. D. Likhite and C. Radhakrishnamurthy, curr.sci. 35 (1966) 534.

[24] D.Santhosh Kumar, K. Chandra Mouli, International Journal of Nanotechnology and applications, ISSN 0973-631X Volume 4,No. 1(2010),pp.51-59.

[25] A. Verma, T. C. Goel, R. G. Mendiratta, P. Kishan, J. Magn. Magn. Mater. 208 (2000) 13-19.

[26] Ping Hu, Hai-bo Yang, De- an Pan, Hua Wang, Jian –jun tian, Shen-gen Zhang, Xin- feng Wang, Alex A. Volinsky, Journal of Magnetism and Magnetic materials 322(2010)173-177.

[27] C. R. Alves, R. Aquino, A. J. Depeyrot, T. A. P Cotta, M. H. Sousa, and F. A. Tourinho, H. R. Rechenberg and G. F. Goya, Journal of Applied Physics 99, 08M905 (2006).

[28] F. Gazeau *et al.*, Europhys. Lett. 40 (1997)575.

[29] J. Dormann et al., Phys. Rev. B 53 (1996)14291.

[30].Chao Liu, A. J. Rondinone and Z. J. Zhang, Pure Appl. Chem. Vol 72, Nos1- 2, (2000)pp37-45.

[31] Chao Liu, Z. John Zhang, Chemistry of materials, Volume 13, No.6, (2001)pp. 2092-2096.

[32] A. J Rondinone, A. C. S Samia, Z. J Zhang, J. Phys. Chem. B, 103 (1999) 6876.

[33] P. Mathur, A. Thakur and M. Singh, Phys. Scr. 77 (2008) 045701 (6pp)

[34] D. C. Dobson, J. W. Linnet, and M. M. Rahman, J. Phys. Chem. Solids 31(1970) 727.

[35] H. N. Ok, K. S. Baek, H. S. Lee, and C. S. Kim, *Phys. Rev*. B 41(1990) 62.

[36] M. A. Amer, Hyper. Interact,131 (2000), 29.

[37] B. J. Evans and S. S. Hafner, J. Phys. Chem. Solids 29 (1968) 1573.

[38] A. Dias, R. M. Paniago, V. T. L. Buono, J. Mater. Chem. 7 (12) (1997) 2441–2446.

[39] S. Yan, W. Ling, E. Zhou, J. Cryst. Growth 273 (2004) 226–233.

[40] N. N. Greenwood, T. C. Gibb, Mossbauer spectroscopy, Chapman &Hall, London, 1971 (Sec. 10).

[41] G. A. Sawatzky, F. van der Woude, A. H. Morrish, Phys. Rev. 187 (1969) 747.

[42] R. G. Gupta, R. G. Mendiratta, J. Appl. Phys. 48 (1977) 845.

[43] M. Arshed, N. M. Butt, M. Siddique, M. Anwar-ul-Islam, T. Abbas, M. Ahmed, Solid State Commun 84 (1992) 717.

[44] T. Kanazaki, K. Kikuchi, M. Sato, K. Nagai, T. Oowada, H. Onozuka, K. Kitayama, J. Electron Spectrosc. Relat. Phenom. 77 (1996) 221.

[45] R. Justin Joseyphus, A. Narayanasamy, K. Shinoda, B. Jeyadevan, K. Tohji, Journal of Physics and Chemistry of Solids, 67 (2006) 1510–1517

[46] L. Cser, I. Deszi, I. Gladkih, L. Keszthelyi, D. Kulgawcsuk, N. A. Eissa, E. Sterk, Phys. Stat. Sol. 27 (1968) 131.

[47] J. Z. Jiang, G. F. Goya, H. R. Rechenberg, J. Phys. Condens. Matter., 11 (1999) 406.

[48] J. Schnettler, Physics of Electronic Ceramics, Part B, Marcel Dekker, Inc, 1972 New York.

[49] A. Verma, T. C. Goel, R.G. Mendiratta, P. Kishan, J. of Magnetism and Magnetic Materials 208 (2000) 13-19.

[50] C. Radhakrisnamurty, J. Geol. Soc.India, 26(9) (1985) 640.

[51] Bruce M. Moskowitz, Hitchhikers Guide to Magnetism, workshop on 5-8 June 199 1at Institute for Rock Magnetism.

[52] R. V. Upadhaya, G. J. Baldha and R. G. Kulkarni, Mater. Res. Bull. 21 (1986) 1015.

[53] N. D. Chaudhari, R. C. Kambale, D. N. Bhosale, S. S. Suryavanshi, and S. R. Sawant, Journal of Magnetism and Magnetic materials, Vol. 322, Issue 14,(2010), pp 1999-2005.

[54] A. Globus , R. Valenzuela, IEEE Trans. Magen. MAG-11, (1975)1300

[55] A. M. Sankpal, S. V. Kakatkar, N. D. Chaudhari, R. S. Patil, S. R. Sawant, S. S. Suryavanshi, Journal of Materials Sciences, Materials in Electronics, 9 (1998) 173-179.

[56] T. Tanaka Jpn. J. Appl. Phys.17 (1978) 349.

[57] D. Stoppels, J. Appl. Phys. 51 (1980) 2789.

[58] H. E. Kaiyuan, H. U. Hui, Zhi Wang, Lizhi Cheng, J. Mater. Sci. Technol.Vol.16 No. 2, (2000).

[59] Chao Liu, Bingsou Zou, Adam J. Rondinonen and Z. John Zhang, J. of Phys. Chem. B, 104 (2000) 1141-1145.

[60] T. Nakamura, Y.Okara, J. Appl. Phys. 79 (9) (1996) 7129.

[61] K. J. Standley, 'Oxide Magnetic Materials' (oxford: claredon Press, 1972).

[62] S. H. Keluskar R. B. Tangsali , G. K. Naik, J. S. Budkuley, J. of Magnetism and magnetic Materials, 305(2006) 296-303.

[63] J. Gieraltowski, A. Globus (1977) IEEE Trans Magn 13:1359.

[64] A. Globus (1977) Proc J Phys Colloq 38:C1.

[65] Anjali Verma, Ratnamala Chatterjee, Journal of magnetism and magnetic materials, 306(2006)313-320.

[66] A Thakur, M. Singh, Ceramics International 29 (2003) 505-511.

CHAPTER VII

ELECTRICAL PROPERTIES

7.1 INTRODUCTION

Ferrites are extensively used in electronics and telecommunication industry because of their novel magnetic and electrical properties. These are used in variety of applications with operating frequency ranging from low frequency to radio frequency, high quality filters, rod antennas, transformer cores, read/write heads for high speed digital tapes, storage devices and many other devices. With development in new technology the application areas of ferrites has enhanced and are presently being tested for drug delivery and hyperthermia in medical field.

Semiconductor like behavior of resistivity of the material with high resistivity variation over large range of temperature is an ideal characteristic essential for materials in sensor application [1]. The electrical Properties of ferrites are sensitive to their composition and microstructure, which in turn are sensitive to their processing conditions [2].

The conduction mechanism in ferrites is quite different from that in semiconductors. In ferrites, temperature dependence of mobility affects the conductivity and the carrier concentration is almost unaffected by temperature variation.

In semiconductors the charge carriers occupy states in wide energy band, whereas the charge carriers in ferrites are localized at the magnetic atoms. In ferrites the cations are surrounded by closed packed oxygen anions and as a first approximation can be treated as isolated from each other. The electrons associated with a particular ion will largely remain isolated and

hence localized electron model is more appropriated in the case of ferrites rather then a Band model of electrons. These factors that differentiate the electrical behavior of ferrites from that of semiconductors led to hopping electron model [3,4].

The electrical properties of ferrites are mainly affected by cation distribution, non-magnetic and magnetic substitutions, amount of Fe^{2+} present, sintering conditions, grain size and grain growth effects.

In this chapter the following electrical properties are discussed

1. Resistivity
2. Thermoelectric power
3. Dielectric constant

7.2 RESISTIVITY

Resistivity in ferrites varies in the range of 10^{-3} to 10^{11} Ohm.cm at room temperature [5]. These low and high resistivities of ferrites are mainly explained on the basis of cations distribution in A and B sites of the spinel structure and hopping mechanism. The high value of conductivity in ferrites is due to simultaneous presence of ferrous and ferric ions in the crystallographically equivalent sites. The low resistivity in ferrites is associated with the occupation of B-sites by other divalent metal ions and trivalent iron ions. The spinel ferrites contain large number of oxygen ions and small number of metal ions in the interstitial spaces. Both Fe^{2+} and Fe^{3+} ions are at B-site and conduction takes place when electrons move from $Fe^{2+}$to Fe^{3+} ions.

The conduction mechanism in ferrites is assumed to be related to d electrons and direct electron exchange between Fe^{2+} and M^{3+} (M=metal ions) ions is neglected due to small tunneling effect of d electrons.

The resistivity of ferrites is very sensitive to temperature. The diffusion of charge carriers from one state to other is possible only when their energy exceeds a certain minimum energy called activation energy.

Different models are used to differentiate the electrical behavior of ferrites from that of semiconductors, such as hopping model of electrons, small polaron model and Phonon induced tunneling.

7.2.1 Hopping Model

Jonker [6] **(**1959), observed in Cobalt ferrite that the transport properties are different from that of normal semiconductors. In ferrites the charge carriers are not free to move through the crystal lattice, but jump from ion to ion.

Assuming the number of electrons contributing to be equal to the number of Fe^{2+} ions and the number of electron holes to be equal to the number of Co^{3+} ions Jonker has calculated from resistivity data extremely low values of mobilities for electron and holes, and showed a fairly strong exponential dependence of resistivity on temperature.

In the presence of lattice vibrations the probability of electron transfer is high as the ions come close enough to facilitate electron transfer. Thus the conduction is induced by the lattice vibrations and in consequence the carrier mobility shows a temperature dependence characterized by activation energy. The mechanism of transport phenomenon in ferrites can be represented as [6]

$$Fe^{2+} + Fe^{3+} \longleftrightarrow Fe^{3+} + Fe^{2+} + \Delta E$$

$$M^{2+} + Fe^{3+} \longleftrightarrow M^{3+} + Fe^{2+} + \Delta E$$

Where ΔE is activation energy, the energy required for transfer of electron from M^{2+} to Fe^{3+} and vice versa. The valence states of two ions get interchanged. Under the influence of an electric field these extra electrons can be regarded to constitute the current, by jumping or hopping process [7].

Thus the transport of charge carriers is achieved by hopping process through interaction with phonons. On the basis of this the temperature dependence of resistivity of ferrites is given by the relation.

$$\rho = \rho_o \exp(-\Delta E/kT)$$

where ρ_o = Temperature dependent constant

ΔE = activation energy

K = Boltzmann constant

T = Absolute temperature

The electron and hole mobilities μ are given by

$$\mu_1 = [ed^2 \gamma_1 \exp.(-q_1/kT)]/ kT$$

$$\mu_2 = [ed^2 \gamma_2 \exp.(-q_2/kT)]/ kT$$

Subscript 1 and 2 represents the parameters for electrons and holes respectively, d represents jumping length. γ_1 and γ_2 are lattice frequencies, q_1 ,q_2 are activation energies.

The general expression for the total conductivity where two types of charge carriers present is given as $\sigma = n_1 e\mu_1 + n_2 e\mu_2$ where

n_1, n_2 is concentration of electrons and Holes.

μ_1, μ_2 is mobility of electrons and Holes.

The temperature dependence of conductivity arises only due to mobility and not due to number of charge carriers in the sample [8].

7.2.2 Small Polaron Model

A small polaron is a defect created when an electron carrier becomes trapped at a given site as a consequence of the displacement of adjacent atoms or ions. The entire defect then migrates by an activated hopping mechanism. Small polaron formation can take place in materials whose conduction electrons belong to incomplete inner (d or f) shells, which due to small electron overlap; tend to form extremely narrow bands. The possibility for the occurrence of hopping conductivity in certain low mobility semiconductors, and extensive theoretical literature has been developed which considers the small polaron model and its consequences [9-14].

The small polaron model also explains the low value of mobility, temperature independent, Seeback coefficient and thermally activated hopping. In addition to these properties if the hopping electron becomes localized by virtue of its interaction within phonons, then a small polaron is formed and the electrical conduction is due to hopping motion of small polarons.

The electrical resistivity, the change in activation energy at curie temperature and the relation of activation energies with composition can be explained and discussed in the light of the mechanism of hopping of polarons, which has been successfully employed to explain the electrical properties of ferrites [15,16]. These polarons have low activation energy in magnetic region, while more activation energy in non-magnetic regions.

7.2.3 Phonon Induced Tunneling

Electrical properties of ferrites have been explained on the basis of tunneling of electrons amongst Fe^{2+} and Fe^{3+} atoms on B sites [17]. It has been assumed that the electrons, which participate in the $Fe^{2+} \rightarrow Fe^{3+} + e$ exchange process, are strongly coupled to the lattice and tunnel from one site to other due to a phonon-induced transfer mechanism.

In ferrites, the B-B distances are smaller than A-A and A-B distances. Even then, the B-B distance is much larger than the sum of ionic radii of the cations involved, indicating a little or no overlap between d-d wave functions of ions on adjacent octahedral sites. This gives rise to a situation in which electrons are not free to move through the crystal but remain fixed on B- sites, necessitating a hopping process. However, in ferrite, conductivity is decided mainly by the availability of a pair of cations that facilitate hopping mechanism [18]. Therefore conductivity in ferrites depends upon such pairs available.

7.2.4 Experimental Technique

Fine powders of $Mn_xZn_{(1-x)}Fe_2O_4$ were pressed into pellets of the size 10mm diameter and of thickness ranging between 2mm to 2.5mm under a pressure of $9.554*10^8$ Newton/m^2 applied for 8minitues. Four sets of pellets were sintered in nitrogen atmosphere at temperatures, 900^{o}C, 1000^{o}C, 1100^{o}C, 1200^{o}C and 1300^{o}C respectively for 4 hours by setting heating and cooling rate at 5 degrees centigrade per minute to obtain the bulk material. The pellets were silver pasted on both side for establishing good ohmic contacts with the electrodes. The dc resistivity measurements on these samples were then made using standard two-probe method.

The schematic block diagram in fig 7.1 (a) shows the circuit arrangement used for the resistivity measurements. The electrode assembly with the sample was then placed in the furnace for making the necessary measurements.

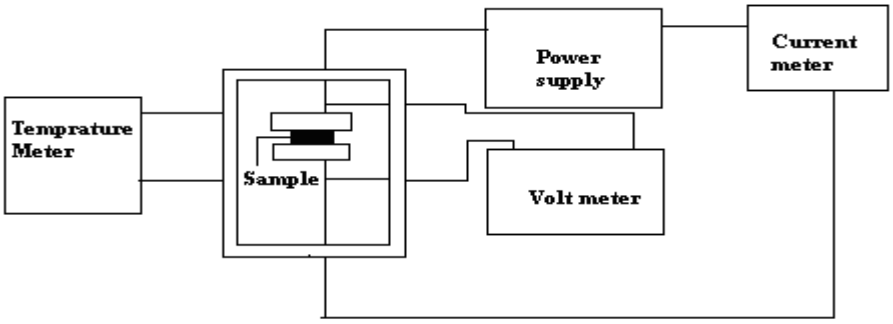

Fig 7.1 (a) Block diagram for resistivity measurement.

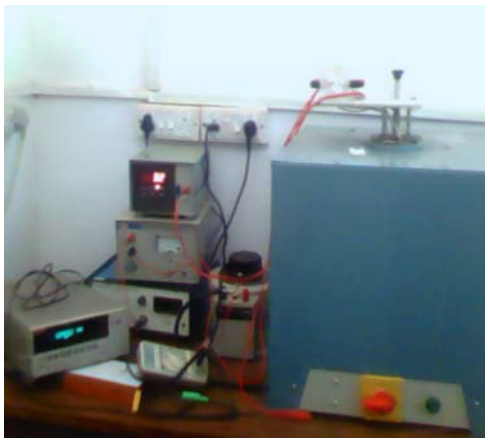

Fig7.1(b) D.C.Resistivity measurement Apparatus. Fig 7.1(c) Electrode assembly with sample

.

The constant potential of 2V was applied across the sample. Variation in the current with corresponding variation in the temperature was recorded from room temperature to 500^{o}C. The resistance (R) of the sample was calculated using the Ohms law and hence the resistivity (ρ) of the sample at different temperatures by using the formula R= ρ(t/A), where, 't' is the

thickness of the conductor, ‘A’ is area of the cross-section and ρ is the resistivity. The same procedure was then repeated for all samples.

7.3 THERMOELECTRIC EFFECT: (SEEBACK COEFFICIENT MEASUREMENTS)

If a temperature difference is maintained between two end surfaces of a semiconductor then a thermo e.m.f. (Vs) is developed across the sample. Thermoelectric property is widely used in the interpretation of the conduction mechanism in semiconductors. Thermoelectric power measurement is the best technique used in the case of low mobility materials such as ferrites**.** The thermo e.m.f. generated is given by the relation Vs = Q*(ΔT), where ‘Q’ is the seeback coefficient is also known as thermoelectric power [19]. The sign of thermo e.m. f. gives vital information about the type of conduction occurring at different temperatures in the sample or semiconductor. Another important significance of thermo e.m.f. is that it enables one to calculate the values of Fermi energy and carrier concentrations in the sample.

7.3.1 Experimental technique

The sample preparation procedure was similar to the one followed for resistivity measurements. The setup consists of two electrodes. The top one ‘A’ acts as a hot junction and the base ‘B’ acts as a cold junction on inserting the sample between the two electrodes.

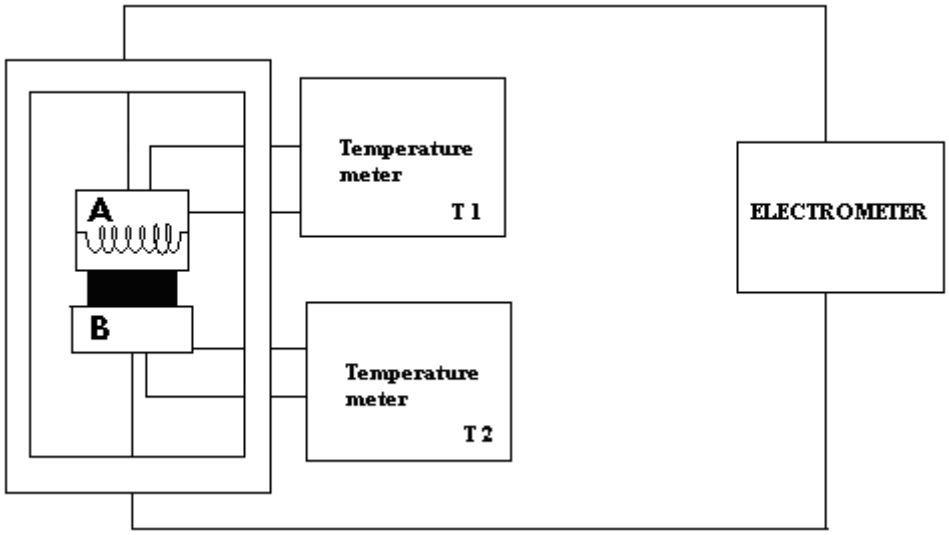

Fig 7.1 (d) Block diagram of experimental set-up to determine thermo-e.m.f. of the sample

The hot and cold electrodes are connected to electro meter for measuring thermo-e.m.f. The temperature of the hot junction is increased by keeping the temperature of the cold junction at room temperature. However the temperature of the cold junction goes on rising due to thermal conductivity of the sample which is low. The temperature of the hot junction is raised up to 300^{o}C. The difference in the temperature of the two junctions is used for the purpose of calculation of thermo emf generated by the sample and the thermopower of the sample.

7.4 DIELECTRIC CONSTANT

Ferrites are very good dielectric materials in the low frequency regions. The dielectric constant of polycrystalline ferrites depend upon operating frequency. Ferrites having very high dielectric constants are useful in designing good microwave devices such as isolators, circulators, etc. The dielectric behavior is one of the most important properties of ferrites, which depends on method of preparation, chemical composition and substitution, grain structure or size, sintering temperature and doping element [8]. Koop

[20] gave a phenomenological theory of dispersion based on the Maxwell-Wagner Theory (Interfacial polarization model).

According to this theory in an inhomogeneous dielectric structure the solid consists of well conducting grains separated by poorly conducting surface layers. This model explains a strong dispersion in dielectric constant and a relaxation peak in dielectric loss at low frequencies. Thus the dielectric constant of polycrystalline ferrites is related to the average grain size of the specimens of the same composition. The frequency dispersion studies suggest that the grains of different sizes contribute differently to the value of dielectric constant and its relaxation frequency.

The behavior of dielectric material to an alternating electric field is different from free space as it contains charge carriers that can be displaced. For an alternating field the time required for polarization shows phase retardation of the charging current instead of 90 ^{o} advanced.

It is advanced by some angle 90-δ where δ is the loss angle, which gives,

$$\text{Tan } \delta = K'' / K = \varepsilon'' / \varepsilon'$$

Where K's represent dielectric constant and ε's the permittivities. The loss factor Tan δ is the primary criterion for usefulness of dielectric as an insulating material.

Maxwell–Wagner two-layer Model or the heterogeneous model of the polycrystalline structure of ferrites can also be used to explain the dependence of dielectric constant on frequency. According to this theory the dielectric structure is composed of two layers. The first layer consists of ferrite grains of fairly well conducting (ferrous ions), which is separated by a thin layer of poorly conducting substances, which forms the grain boundary. These grain

boundaries are more active at lower frequencies; hence the hopping frequency of electron between Fe^{3+} and Fe^{2+} ion is less at lower frequencies. As the frequency of the applied field increases, the conductive grains become more active by promoting the hopping of electron between Fe^{2+} and Fe^{3+} ions, thereby increasing the hopping frequency. Thus we observe a gradual increase in conductivity with frequency. But at higher frequencies the frequency of hopping between the ions cannot follow the applied field frequency and it lags behind it. This causes a dip in dielectric constant at higher frequencies.

7 .4.1 Experimental Technique:

The sample preparation procedure was similar to the one followed for resistivity measurements. Dielectric Constant measurements were carried out on nanoparticle /bulk samples at room temperature by varying frequency from 20Hz to 3MHz. Measurements for temperature dependence of dielectric constant for nanoparticle /bulk samples were also carried out up to 500^{o} C for (20Hz, 100Hz, 500Hz, 1KHz, 10KHz, 100KHz, 500KHz, 1MHz, 2MHz, 3MHz) frequencies, using Wayne Kerr Precision component Analyzer , Model 6400.

The capacitance C was measured and the dielectric constant, was calculated using the relation

$$\varepsilon' = ct/ \varepsilon_o A$$

Where t = Thickness of pallet, A = Area of cross section and ε_o = permittivity of free space.

7.5 RESULT AND DISCUSSION

7.5.1 Resistivity

Resistance of the material from room temperature to 500°C was measured using two probe setup as mentioned in section 7.2.4. The measurements were used to evaluate the D.C. resistivity of the material. Variation of log ρ versus 1000/ T (K) for nanosamples $Mn_xZn_{(1-x)}Fe_2O_4$ (x=0.4, 0.5, 0.6, 0.65, 0.625, 0.675, 0.7, 0.8) is shown in fig 7.2 (a)

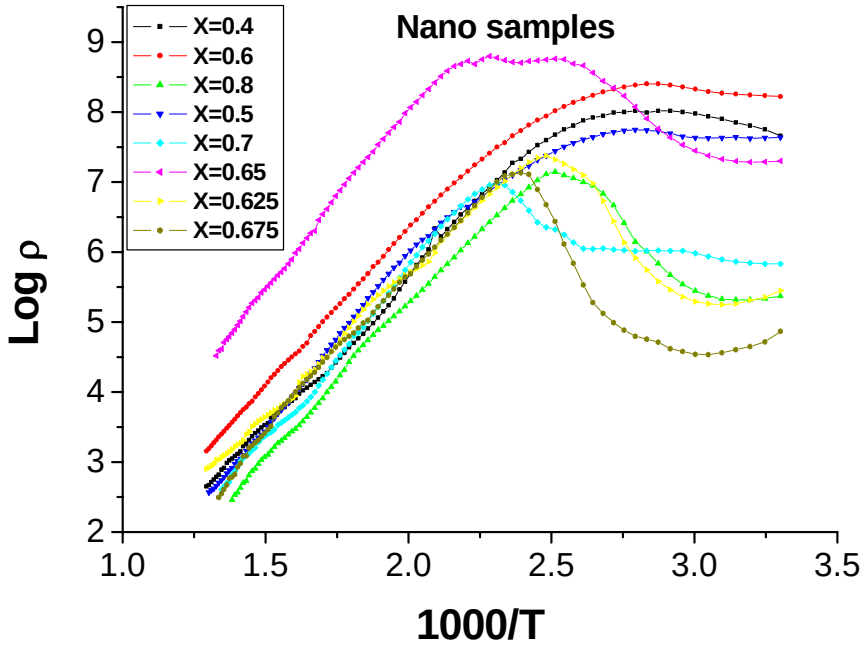

Fig. 7.2 (a) Variation of log ρ versus 1000/ T (K) for nanosamples $Mn_xZn_{(1-x)}Fe_2O_4$

The resistivity of $Mn_{0.8}Zn_{0.2}Fe_2O_4$ at room temperature is $2.38x10^5$ ohm-cm, which increases smoothly with initial minor (shallow) deep to $1.25x10^7$ ohm-cm at 390°K. Further rise in temperature lowers the resistivity value linearly and the same attains a value of 380 ohm-cm at 500°C. Similar behavior was observed for the samples with x= 0.625, 0.65 and 0.675 with initial room temperature resistivity values $2.64x10^5$ohm-cm, $1.8x10^7$ ohm-cm,

7.39 x10^4 ohm-cm and final high temperature values are 625 ohm-cm, 3.54x10^4ohm-cm, 301 ohm-cm at 500^{o}C respectively. In general all the nanosamples show increase in resistivity with increase in temperature in the range of 300 ^{o}K to 400^{o}K, beyond that resistivity decreases with increase in temperature, indicating the semiconductor nature of the ferrite. Increasing part of the resistivity with increase in temperature is dominated by the scattering of charge carriers by lattice vibrations, voids in the sample as well high resistive grain boundaries. As the temperature increases the lattice vibrations increase thereby producing more scattering of charge carriers. The broad peeks observed in the resistivity of the samples could be due to the existence of resonant phonon modes in the samples. The increase in resistivity may also be attributed to the p-type conductivity, which increases the activation energy on the basis of Verwey conduction mechanism [21].

More charge carriers appear to be injected into the conduction process with increasing temperature as a result the resistivity decreases with increasing temperature. The resistivity is seen to decrease much more rapidly with increasing temperature as the samples undergo a ferrimagnetic to paramagnetic transition. The decrease in resistivity with temperature may be attributed to the increase in drift mobility of the charge carriers. Also, conduction in ferrite is mainly due to hopping of electrons from Fe^{3+} to Fe^{2+} ions [22]. The number of such ion pairs depends upon the preparative conditions of nanoparticles which is a decisive factor for cation distribution in the material.

In ferrites, the electrons are localized and there is little overlap between the wavefunctions of ions situated on adjacent sites. In the presence

of lattice vibrations, the ions occasionally come so close that the transfer of electrons from one ion to another occurs with high probability. Hence the mobility is temperature dependent and is characterized by activation energy.

The value of activation energy in the ferromagnetic region is lower than that of the paramagnetic region. The lower activation energy in the ferromagnetic region is attributed to the magnetic spin disordering [23] due to decrease in the concentration of current carriers [24], while the change in activation energy is attributed to the change in conduction mechanism [25,26].

Fig.7.2 (b, c, d, e, f) shows plots of log ρ v/s 1000/ T (K) for bulk $Mn_xZn_{(1-x)}Fe_2O_4$ ((x=0.4, 0.5, 0.6, 0.65, 0.625, 0.675, 0.7, 0.8) samples obtained at 900^{o}C, 1000^{o}C, 1100^{o}C, 1200^{o}C,1300^{o}C. A semiconductor like general behavior is seen for all the samples as the samples undergo a second order ferrimagnetic to paramagnetic phase transition. Although the trends depend on the concentration of Mn in the sample these are more strongly dependent on the sintering temperature of the sample.

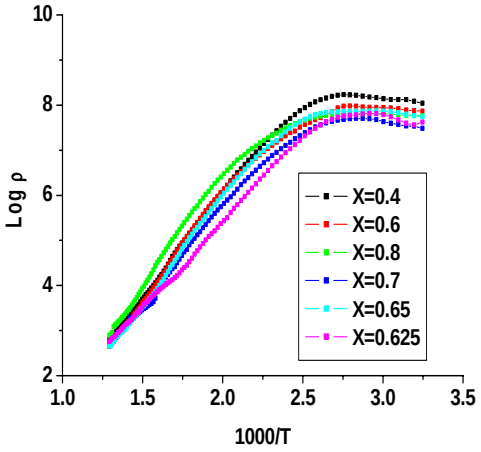

(b)

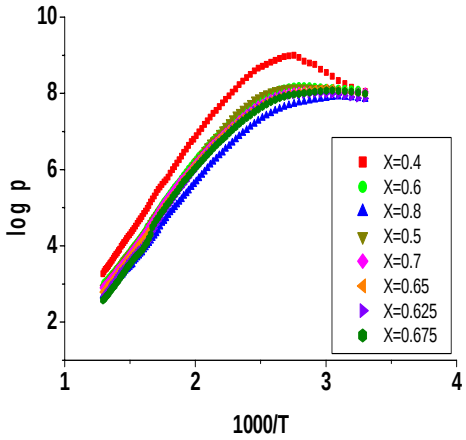

(c)

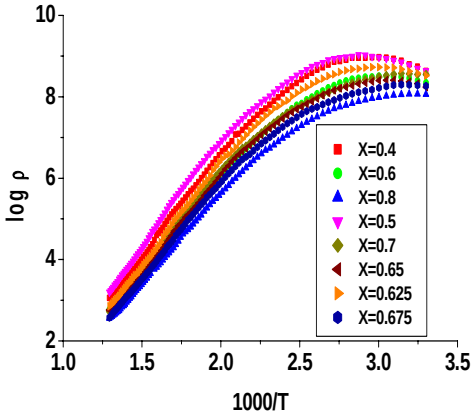

(d)

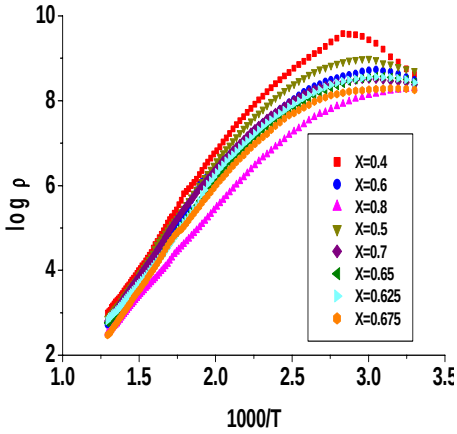

(e)

Fig. 7. 2 (b, c, d, e) : plots of log ρ v/s 1000/ T (K) for bulk samples $Mn_x Zn_{(1-x)} Fe_2O_4$ (x=0.4, 0.5, 0.6, 0.65, 0.625, 0.675, 0.7, 0.8) obtained at b)900 °C, c)1000 °C, d)1100 °C, e)1200 °C

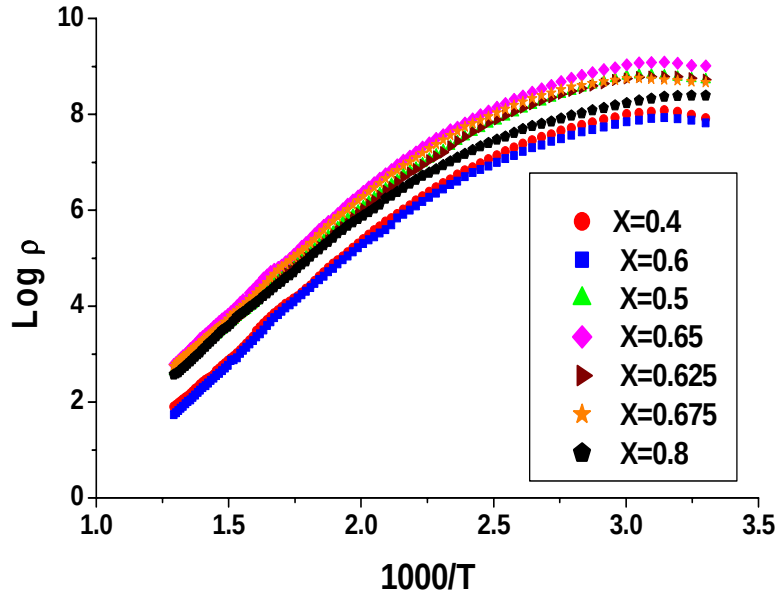

(f)

Fig.7. 2 f Plots of log ρ v/s 1000/ T (K) for bulk samples $Mn_xZn_{(1-x)}Fe_2O_4$ (x=0.4, 0.5, 0.6, 0.65, 0.625, 0.675, 0.7, 0.8) obtained at 1300°C

Room temperature resistivity values of bulk samples (900°C) are seen to vary between 2.9×10^7 ohm-cm (x=0.7) and 1.12×10^8 ohm-cm (x=0.4). Bulk samples obtained at 1000°C show highest resistivity value of $1.2x10^8$ ohm-cm and the lowest resistivity value of $6.45x10^7$ ohm-cm, observed for $Mn_{0.4}Zn_{0.6}Fe_2O_4$ and $Mn_{0.8}Zn_{0.2}Fe_2O_4$ respectively at room temperature. These values decrease to 511 ohm-cm and 380 ohm-cm at 773°K for $Mn_{0.4}Zn_{0.6}Fe_2O_4$ and $Mn_{0.8}Zn_{0.2}Fe_2O_4$ respectively. Similar trend is followed by the bulk sample obtained at 1100°C, 1200°C and 1300°C.

In general for all sintering temperature, resistivity of $Mn_{0.4}Zn_{0.6}Fe_2O_4$ is higher compared to $Mn_{0.8}Zn_{0.2}Fe_2O_4$ at room temperature. This may be due to increase in Zn content, decreases the concentration of Fe^{2+}ion. These ions

block the Fe^{3+} - Fe^{2+} pattern of conductivity [27]. Therefore an increase in resistivity is observed with increase in Zn content.

In ferrites electron conduction mechanisms have been studied by many investigators [28]. Various models were proposed; however, the thermally activated hopping model is found to be more appropriate in explaining qualitatively the electrical behavior of Mn-Zn ferrites. In the hopping process the additional electron on a ferrous (Fe^{2+}) ion requires little energy to move to an adjacent (Fe^{3+}) on the equivalent lattice sites (B sites). In presence of the electric field, these extra electrons hopping between iron ions give rise to the electrical conduction. Therefore, any change in the (Fe^{2+}) ion content in the spinel ferrite lattice and/or the distance between them is crucial to the intrinsic resistivity of Mn-Zn ferrite grains, including the intrinsic grain boundaries. If the introduction of another cation into the lattice causes a change in the valency distribution on the B sites, then the number of electrons potentially available for transfer will be altered. On the other hand, the incorporation of foreign (addition of impurity) ions can change the distance between the B lattice sites, which is crucial for the conduction mechanism. Thus, the formation of an intrinsic grain boundary in doped samples by the segregation of aliovalent ions must increase the resistivity. This gives rise to polycrystalline Mn-Zn ferrite with nonferrimagnetic grain boundary, ferrimagnetic outer grain region and ferrimagnetic conductive core. Thus the contribution to the bulk resistivity may be considered as resistivity contribution coming from three different regions. To establish a relation between the Power loss due to eddy currents and the average grain diameter a hypothetical brick wall model is applied. As per the model each layer can be

represented by a resistance –capacitance (R-C) lumped circuit of high ohmic layers. When the resistivity of the bulk is much lower than the grain boundary layers, the equivalent circuit of the ferrite can be represented by a series of lumped R-C circuits of the grain boundary layers [29].

As the samples under investigation are sintered from nanoparticle Mn-Zn ferrite in a reducing atmosphere with no additives, there is no possibility of formation of high resistivity ferrimagnetic outer grain boundary. Thus the total contribution should come only from the non-ferrimagnetic grain boundaries and ferrimagnetic conductive core.

Variation of resistivity with temperature of $Mn_{0.6}Zn_{0.4}Fe_2O_4$ and $Mn_{0.8}Zn_{0.2}Fe_2O_4$ sintered at different temperatures (Fig 7.3 c, d) and SEM of bulk $Mn_{0.6}Zn_{0.4}Fe_2O_4$ obtained at 1100^0Cand 1300^0C are shown in fig. 7.3 (a,b).

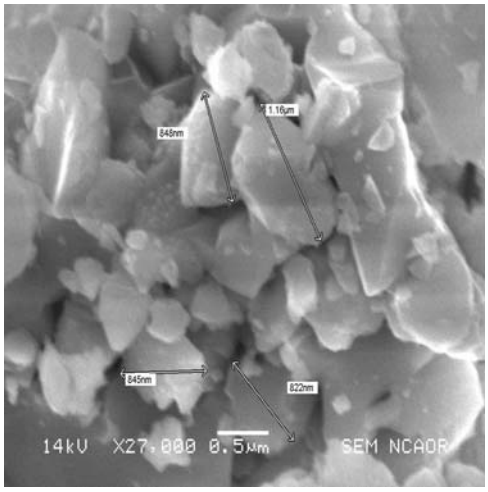

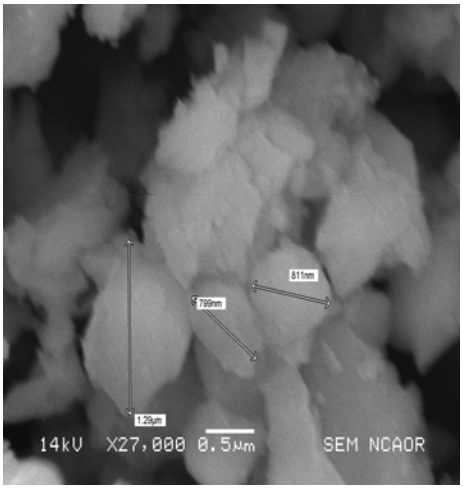

Fig 7.3 (a) $Mn_{0.6}Zn_{0.4}Fe_2O_4$ sintered at 1100^oC Fig 7. 3(b) $Mn_{0.6}Zn_{0.4}Fe_2O_4$ sintered at 1300^oC

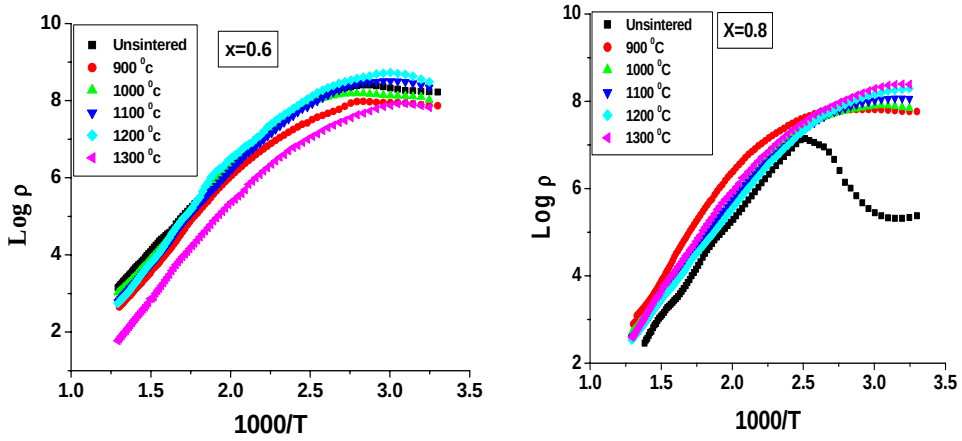

(c) (d)

Fig 7.3 (c, d) Variation of resistivity with temperature of c) $Mn_{0.6}Zn_{0.4}Fe_2O_4$ and d) $Mn_{0.8}Zn_{0.2}Fe_2O_4$ sintered at different temperatures.

Bulk sample $Mn_{0.8}Zn_{0.2}$ Fe_2O_4 (1300°C) shows maximum resistivity $2.5x10^8$ ohm-cm at room temperature and minimum value $5.6x10^7$ ohm-cm is observed for the bulk sample obtained at 900°C. Whereas the bulk sample $Mn_{0.6}Zn_{0.4}Fe_2O_4$ (1100°C) shows higher value of resistivity i.e. $2.18x10^8$ ohm-cm at room temperature, compared to the value of resistivity $6.6x10^7$ ohm-cm for the bulk sample obtained at 1300°C.

Bulk sample $Mn_{0.6}Zn_{0.4}Fe_2O_4$ (1100°C) shows small grain sizes with large nonferrimagnetic grain boundaries more over the total surface area of the sample also increases due to formation of fine crystals which results in high resistivity for the samples [30]. Whereas the samples sintered at 1300°C do not show formation of perfect crystals or small grain shapes which results in low surface area and less resistivity nonferrimagnetic grain boundaries which accounts for low value of resistivity at 300K for this samples as compared to samples sintered at 1100°C. Which is evident from the SEM Micrograph shown in Fig. 7.3 (a, b)

7.5.1.5 Analysis of Resistivity at room temperature, at resistivity maximum and at highest temperature (500^{0}C)

Variation of resistivity values with sintering temperature obtained at room temperature for nanosamples and bulk samples $Mn_xZn_{(1-x)}Fe_2O_4$ obtained at 900^{o}C, 1000^{o}C,1100^{o}C, 1200^{o}C and 1300^{o}C are shown in Fig 7.3 (e).

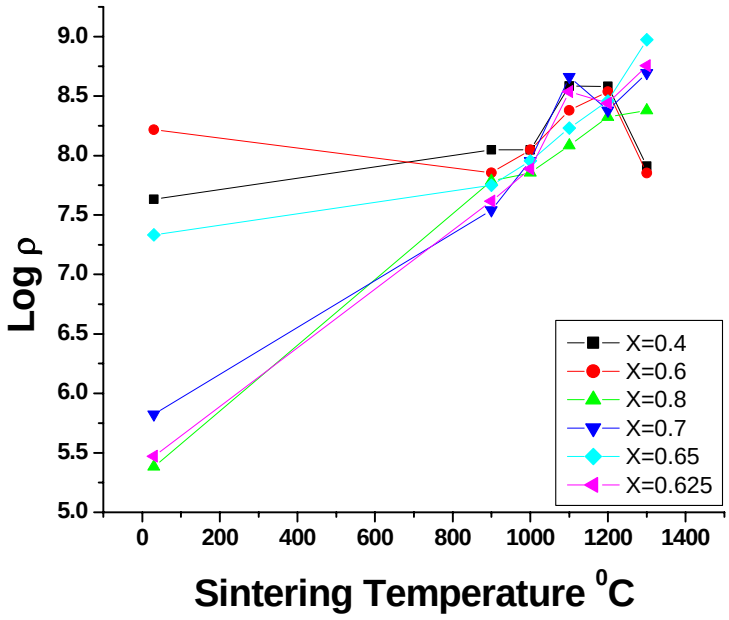

Fig 7.3 (e) Variation of room temperature values of Resistivity with sintering temperature for different concentration.

Fig 7.3 (e) shows variation of room temperature resistivity of nanosample and bulk sample against sintering temperature. Room temperature resistivity of all bulk samples is higher compared to the nanosample except for the sample with (x=0.6), the nanoparticle sample has more resistivity than the bulk sample obtained at 900^{0}C. Room temperature resistivity increases with sintering temperature for bulk sample with (x=0.6) obtained at 1000^{0}C, 1100^{0}C, 1200^{0}C, and it drops to a lower value for the bulk sample at 1300^{0}C.

Samples with (x=0.65, 0.8) show almost linear rise in room temperature resistivity values with sintering temperature.

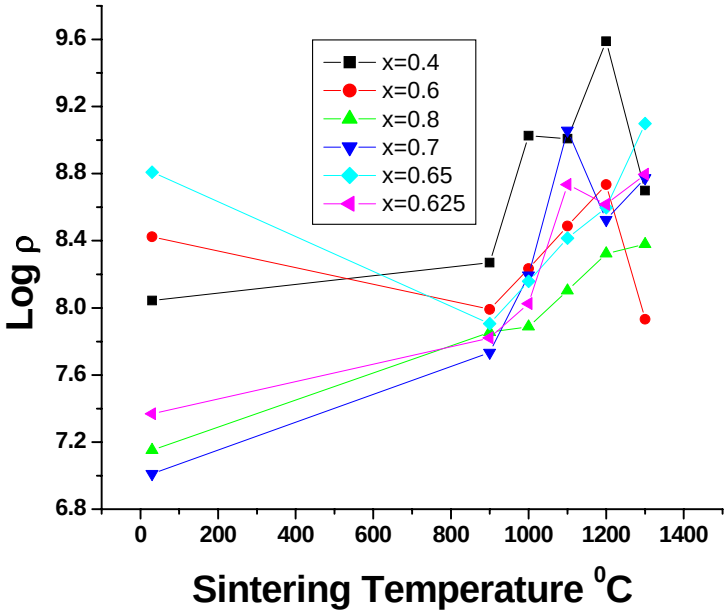

Fig 7.3 (f) Variation of Resistivity maximum of all nanoparticle and bulk samples obtained at different temperatures

The resistivity patterns of all the samples show a broad resistivity maximum at different temperatures. The maximum values of resistivity were recorded and plotted against sintering temperature in Fig 7.3 (f). It may be seen that the nanoparticle sample with x=0.6 and 0.65 exhibits a higher value of resistivity compared to corresponding resistivity values observed for the bulk sample obtained at sintering temperature 900^0C, the maximum value increases further with increase in sintering temperature except for the bulk sample (x=0.6)obtained at 1300^0C. Resistivity maximum, of nanosample (x=0.4, 0.625, 0.7,0.8) shows a lower value than the resistivity of corresponding bulk samples. In general maximum resistivity increases with increase in sintering temperature. For the bulk sample with (x=0.4, 0.6) obtained at 1300^0C, maximum resistivity values drops down to low value.

Variation of resistivity values with sintering temperature obtained at temperature 500^0C for nanosamples and bulk samples $Mn_xZn_{(1-x)}Fe_2O_4$ obtained at 900^oC, 1000^oC,1100^oC, 1200^oC and 1300^oC are shown in Fig 7.3 (g).

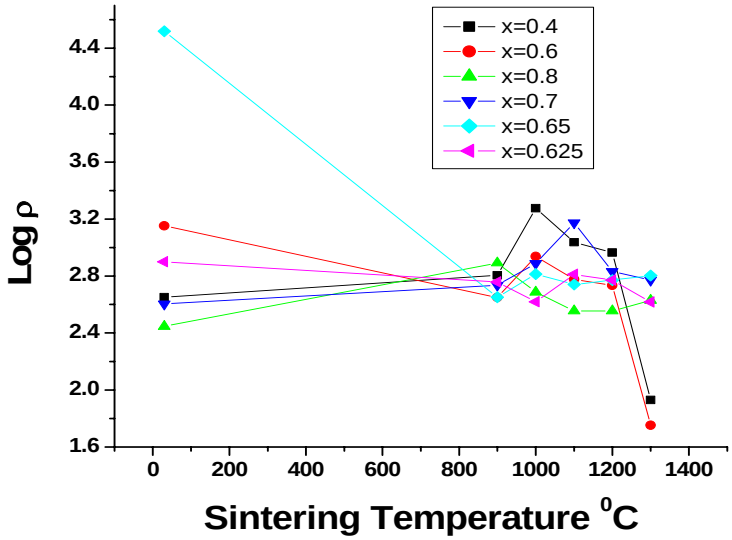

Fig 7.3 (g): Variation of resistivity minimum (at 500^oC) of nanoparticle and bulk samples with different sintering temperatures.

It can be seen that the resistivity values at 500^0C for nanosample $Mn_xZn_{(1-x)}Fe_2O_4$ (x=0.6, 0.625 and 0.65) show higher values compared to the corresponding values for bulk samples. Bulk sample $Mn_xZn_{(1-x)}Fe_2O_4$ (x=0.6) obtained at 1300^0C shows the lowest value of resistivity (at 500^0C). Bulk samples $Mn_xZn_{(1-x)}Fe_2O_4$ (x=0.65) obtained at 900^0C shows the lowest value compared to other bulk samples obtained at 900^0C. Whereas bulk sample $Mn_xZn_{(1-x)}Fe_2O_4$ (x=0.4, 0.7, 0.8) obtained at different sintering temperature exhibit higher values of resistivity (at 500^0C) compared to nanosamples. But the bulk sample $Mn_{0.6}Zn_{0.4}Fe_2O_4$ (1300^0C) shows lowest value of resistivity (at 500^0C).

7.5.2 Seeback coefficient:

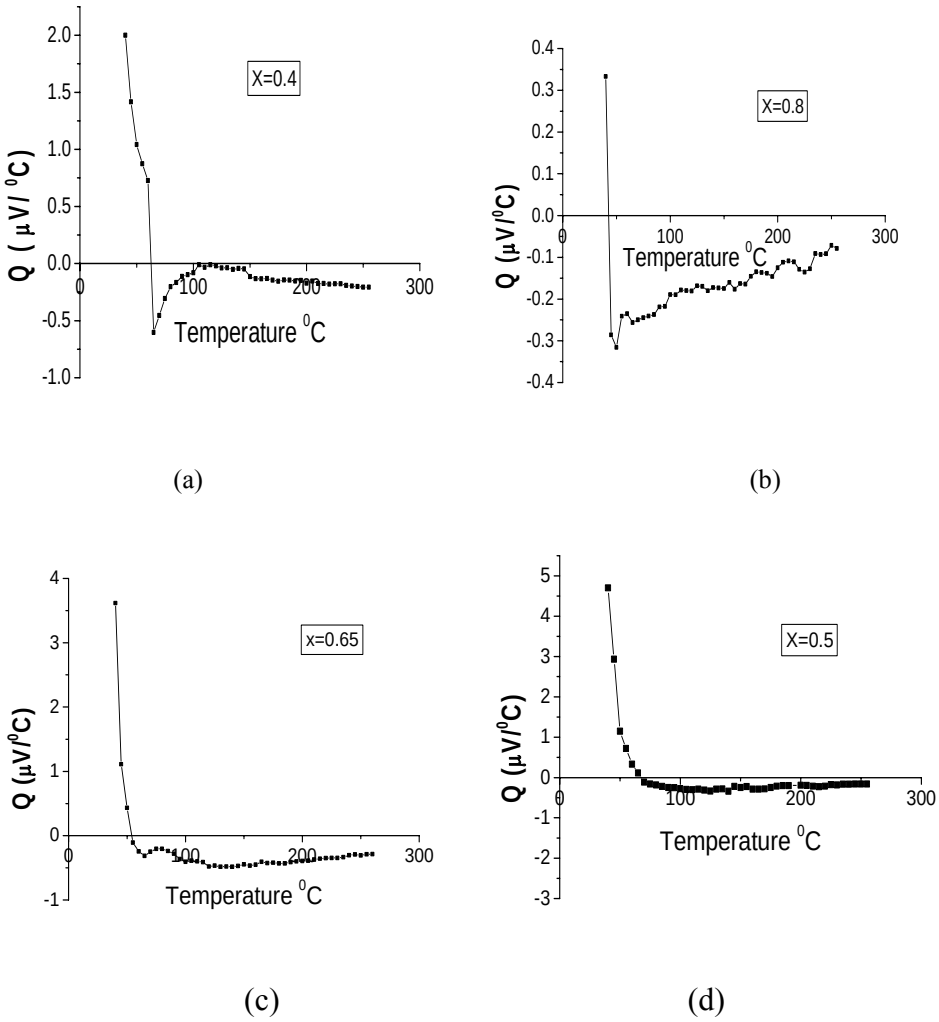

Fig7.4 (a,b,c,d) Plot of Seeback coefficient (Q) V/S Temperature for nanosample $Mn_xZ_{(1-x)}Fe_2O_4$ (with x=0.4, 0. 5, 0.65 and 0.8)

The compositional variation of the Seeback coefficient as a function of temperature is as shown in Fig 7.4 (a, b, c & d). Seebeck coefficient in all the cases is strongly dependent on temperature. The variation of the Seeback

coefficient(Q) as a function of temperature shows positive value of Q followed by negative value which confirms the dominance of p-type charge carriers at lower temperatures followed by n-type charge carriers dominating the transport phenomena at high temperatures in the samples. The samples also show second order and first order transitions during change over of the conduction mechanism.

The n-type conduction reveals that the materials have electrons as majority carriers. Generally conduction in ferrites is explained either by a hopping mechanism or a band type process [31]. The decrease in Q above a certain temperature can be understood by reference to an observation [32] where the conduction was assumed to be in the intrinsic region. In this region, the contribution to Q from electrons becomes less significant with the decrease in the hopping mechanism. Then Q becomes increasingly influenced by the mobility of holes lying far below the Fermi energy. At higher temperature the plateau of Q versus T shows that the thermoelectric power is independent of temperature. It was reported [33] that Mn-Zn ferrites belong to the degenerate type of semiconductor and that thermo-emf does not depend on temperature. Hence, in the present investigations, the materials exhibit degenerate semiconductor behaviour at higher temperature and non-degenerate semiconductor behaviour at lower temperature.

7.5.3 Dielectric constant

The variation of dielectric constant (ε^{1}) with frequency of all the nanoparticle as well as bulk samples $Mn_x Zn_{1-x}Fe_2O_4$ obtained at 900 ^{o}C,

1000 ^{o}C, 1100 ^{o}C, 1200 ^{o}C and 1300 ^{o}C. is presented in Fig. 7.5 (a, b) , Fig. 7.5 (c , d) & 7.5 (e, f)

The dielectric constant is found to decrease rapidly with increasing frequency and remain constant at higher frequencies for all nanoparticle as well as bulk samples. This is a normal dielectric behavior for mixed ferrites observed by several other investigators [34-36].

The polarization decreases with increase in frequency and the changes become insignificant beyond a certain frequency limit. This is well explained on the basis of space charge polarization model of Wagner and Maxwell [37, 38] and is also in agreement with the Koop's phenomenological theory [40]. The decrease of dielectric constant at higher frequency can be explained on the basis that the solid is composed of well conducting grains separated by insulating grain boundaries. The electrons reach the grain boundary through hopping between Fe^{+2} and Fe^{+3} and if the resistance of the grain boundary is high enough, electrons pile up at the grain boundaries and produces polarization. However, as the frequency of the applied field is increased beyond a certain value, the electron hopping can not follow the alternating field fluctuations. This decreases the probability of electrons reaching the grain boundary and the polarization becomes stagnant [38, 39]. Consequently, the dielectric constant attains a constant low value.

Frequency Dependence of Dielectric Constant

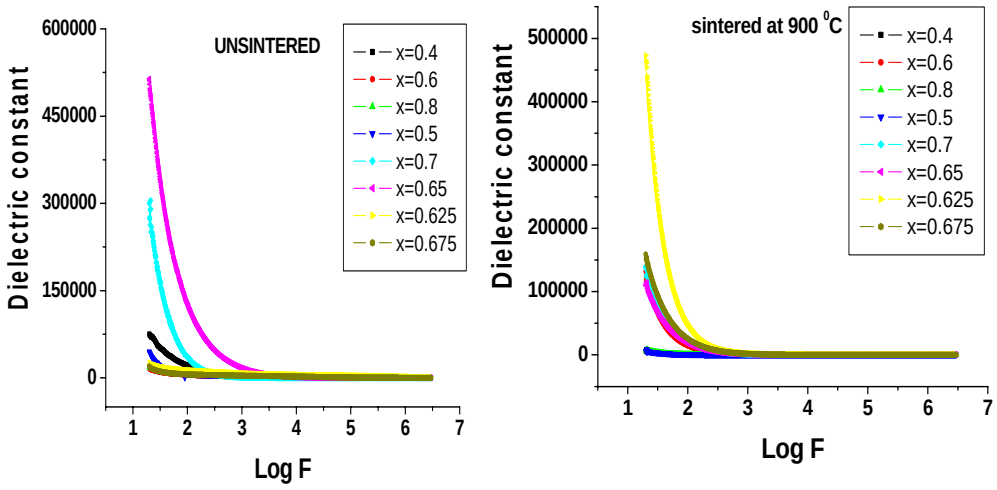

(a) (b)

Fig. 7.5 (a,b) Variation of Dielectric constant with frequency for

(a) nano sample $Mn_xZn_{(1-x)}Fe_2O_4$ (b)Bulk sample $Mn_xZn_{(1-x)}Fe_2O_4$ (900°C)

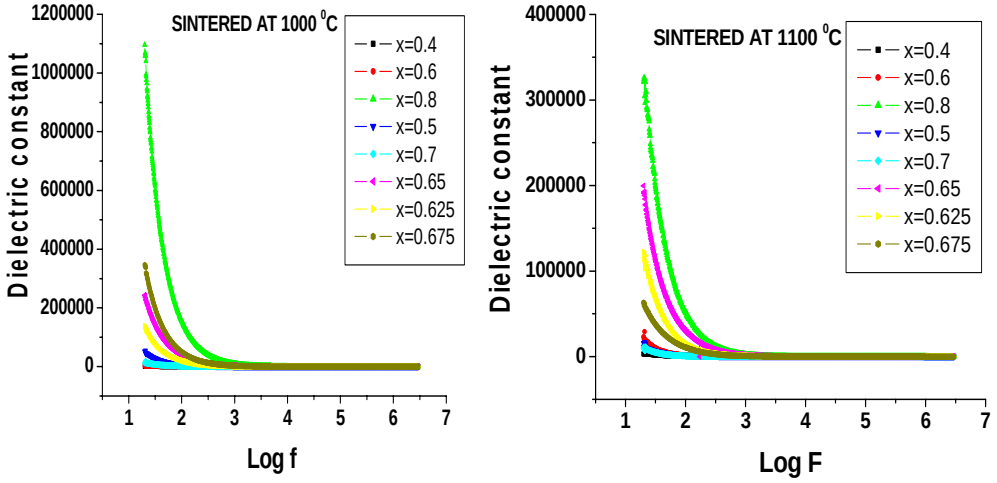

(c) (d)

Fig. 7.5 (c, d) Variation of Dielectric constant with frequency for bulk sample

$Mn_xZn_{(1-x)}Fe_2O_4$ obtained at (c) 1000°C (d)) 1100 °C

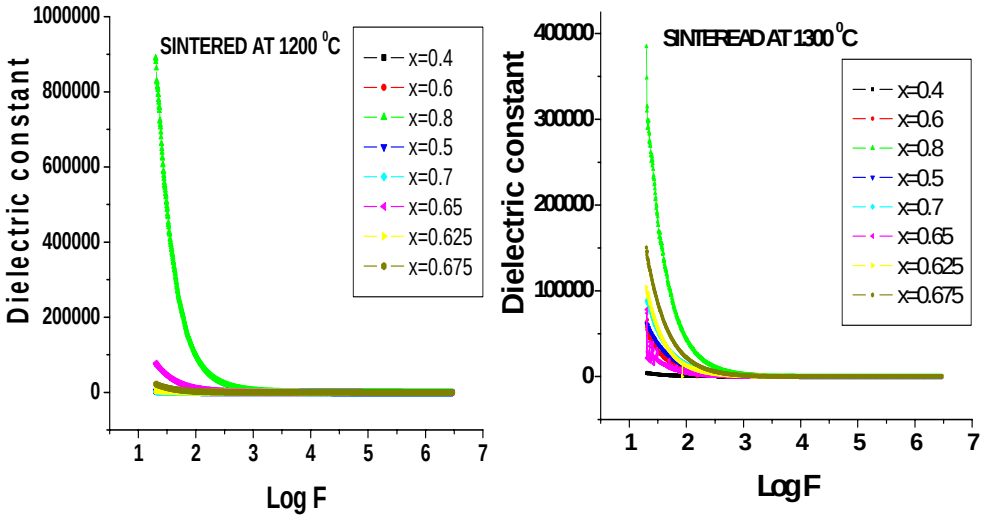

(e) (f)

Fig. 7.5 (e,f) Variation of Dielectric constant with frequency for the bulk sample $Mn_xZn_{(1-x)}Fe_2O_4$ obtained at (e) 1200 °C (f) 1300 °C

The large value of ε at lower frequency is due to the predominance of species like Fe^{2+} ions, interfacial dislocation pile ups, oxygen vacancies, grain boundary defects etc [37, 38]. According to Maxwell–Wagner theory of dielectric dispersion, the dielectric polarization had its origin in the heterogeneous structure of ferrites with grains and grain boundaries [40]. The effect of grain interfaces is more pronounced at lower frequencies, where we observe relatively large values of ε. The space charge polarization occurring at the interfaces at low frequencies can also contribute to dielectric constant at lower frequencies. According to Koops's model [39] the dielectric constant at low frequency comes from the grain boundaries which have a high dielectric constant. At high frequency $\acute{\varepsilon}$ results from the grains which have a small dielectric constant. The variation of dielectric constant with frequency for all nanoparticle samples under investigation is shown in Fig 7.5 (a). Sample $Mn_{0.65}Zn_{0.35}Fe_2O_4$ has highest value of dielectric constant $5.2x10^5$ whereas

$Mn_{0.675}Zn_{0.325}Fe_2O_4$ has lowest value of dielectric constant i.e.$1.9x10^4$ at 300^oK and 20Hz frequency. Dielectric constant for all nanosamples decreases to a low value for all higher frequencies.

The values of dielectric constant measured at 300 ^oK and 20Hz frequency are $4.7x10^5$ and $4.068x10^3$ being observed for bulk sample $Mn_{0.625}Zn_{0.375}Fe_2O_4$(900^oC) and $Mn_{0.5}Zn_{0.5}Fe_2O_4$ (900^oC) respectively. Dielectric constant for all the bulk samples (9 00^oC) beyond 1kHz is very low.

The value of dielectric constant at 300 ^oK and 20 Hz. for the bulk samples $Mn_xZn_{(1-x)}Fe_2O_4$ (1000^oC) vary between $1.08x10^6$ and 2.5×10^4. The highest and the lowest value of dielectric constant being observed for $Mn_{0.8}Zn_{0.2}Fe_2O_4$ and $Mn_{0.7}Zn_{0.3}Fe_2O_4$ respectively. At 1KHz and beyond this frequency almost all the samples have low value of dielectric constant ie.$8.19x10^2$. The low value of dielectric constant in the frequency range 1KHz. to 3MHz. is appreciable value, which makes it useful for high frequency applications.

It is observed that the bulk sample $Mn_{0.8}Zn_{0.2}Fe_2O_4$ obtained at 1100^oC exhibits the highest value of dielectric constant $3.27x10^5$ at 300^oK and 20Hz frequency. At 1KHz. this value decreases to $1.064x10^3$. The lowest value of dielectric constant $2.9X10^3$ is observed for the bulk sample $Mn_{0.7}Zn_{0.3}Fe_2O_4$ (1100^oC). The bulk sample $Mn_{0.8}Zn_{0.2}Fe_2O_4$ (1200^oC) has highest value of dielectric constant $8.8x10^5$ at 300^oK and at 20 Hz frequency, where as the lowest value of dielectric constant $8.13x10^3$ is exhibited by the sample $Mn_{0.7}Zn_{0.3}Fe_2O_4$.

The mechanism of the polarization process in ferrites is similar to that of the conduction process [41,42]. It is observed that the electronic exchange

between Fe^{2+} and Fe^{3+}, results in local displacements that determine the polarization behavior of the ferrites. The dependence of the dispersion of dielectric constant on composition can be explained on the basis of the available ferrous ions on octahedral sites [36].

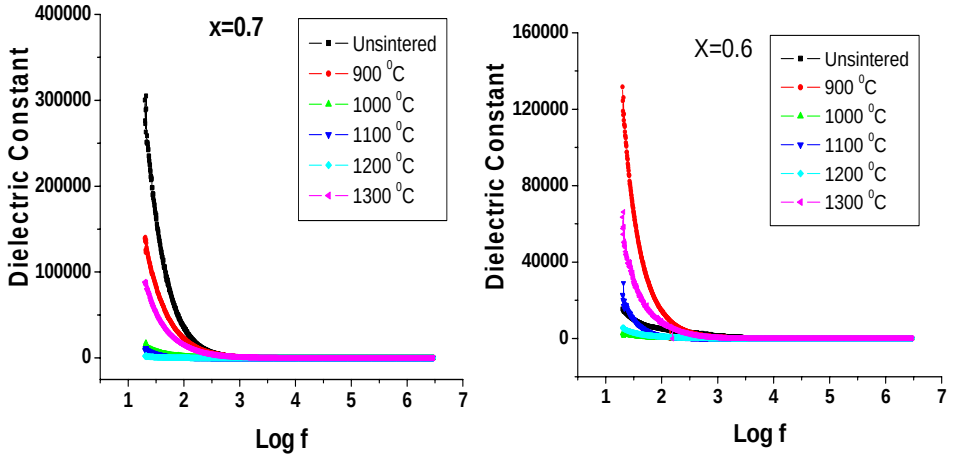

(a) (b)

Fig: 7.6 (a, b)) Variation of dielectric constant with frequency of bulk $Mn_xZn_{(1-x)}Fe_2O_4$ (x=0.7, 0.6) obtained at 900 °C, 1000 °C, 1100 °C, 1200 °Cand 1300 °C

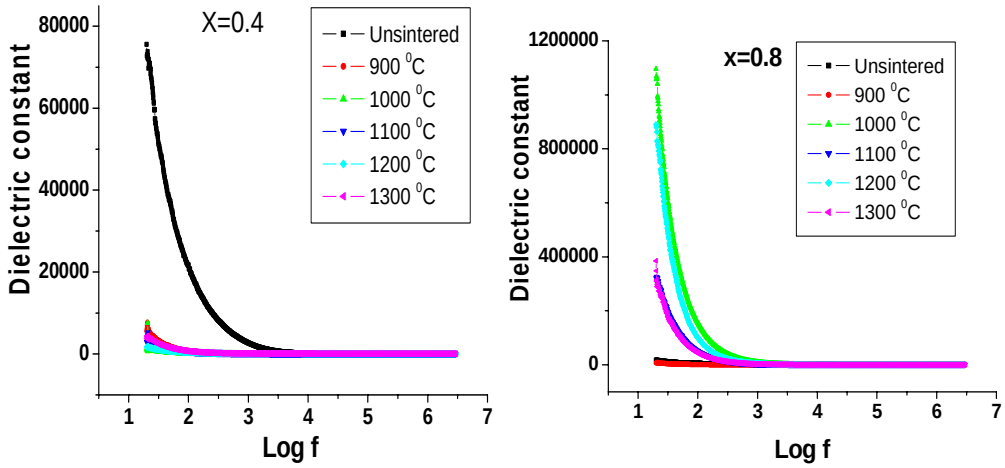

(c) (d)

Fig. 7.6 (c, d) Variation of dielectric constant with frequency of bulk $Mn_xZn_{(1-x)}Fe_2O_4$ (x=0.4, 0.8) obtained at 900 °C, 1000 °C, 1100 °C, 1200 °Cand 1300 °C

Fig. 7.6 (a, b, c, d) shows variation of dielectric constant of bulk $Mn_xZn_{(1-x)}Fe_2O_4$ (x=0.7, 0.6, 0.4, 0.8) with frequency at different sintering

temperature. The bulk sample $Mn_{0.8}Zn_{0.2}Fe_2O_4$ (1000^{o}C) has higher value of dielectric constant compared to the bulk sample $Mn_{0.8}Zn_{0.2}Fe_2O_4$ (1300^{0}C). .Dielectric constant is affected by the two factors: i) There is an inverse proportionality between resistivity and dielectric constant [43]. ii) There is an increase in homogeneous dielectric structure when the sintering temperature is increased. Because the sample sintered at 1300^{o}C and 1000^{o}C has highest and lowest value of resistivity respectively, this dielectric behavior is mainly governed by the resistivity of the sample. Similarly dielectric constant of the bulk sample $Mn_{0.6}Zn_{0.4}Fe_2O_4$ (900^{o}C) is highest and the bulk sample $Mn_{0.6}Zn_{0.4}Fe_2O_4$ (1200^{o}C**)** has lowest value of dielectric constant since bulk sample(1200^{o}C) has higher value of resistivity compared to the bulk sample obtained at 900^{o}C.

7.5.4: Temperature dependence of Dielectric constant

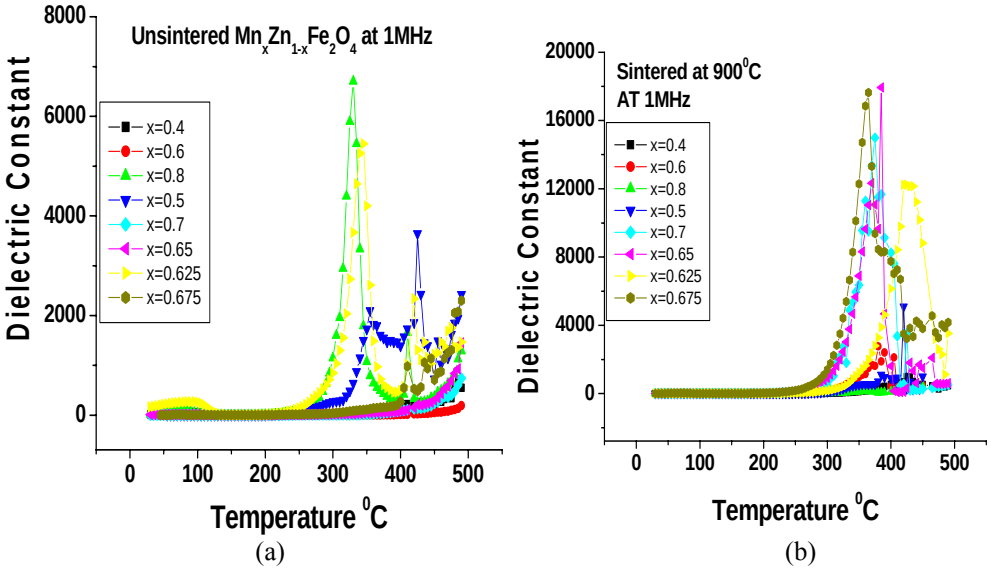

Fig. 7.7 (a, b) Dielectric constant vs Temperature at 1MHz for
a) Nano sample $Mn_xZn_{(1-x)}Fe_2O_4$ and b) bulk sample $Mn_xZn_{(1-x)}Fe_2O_4$ (900^{0}C)at 1MHz

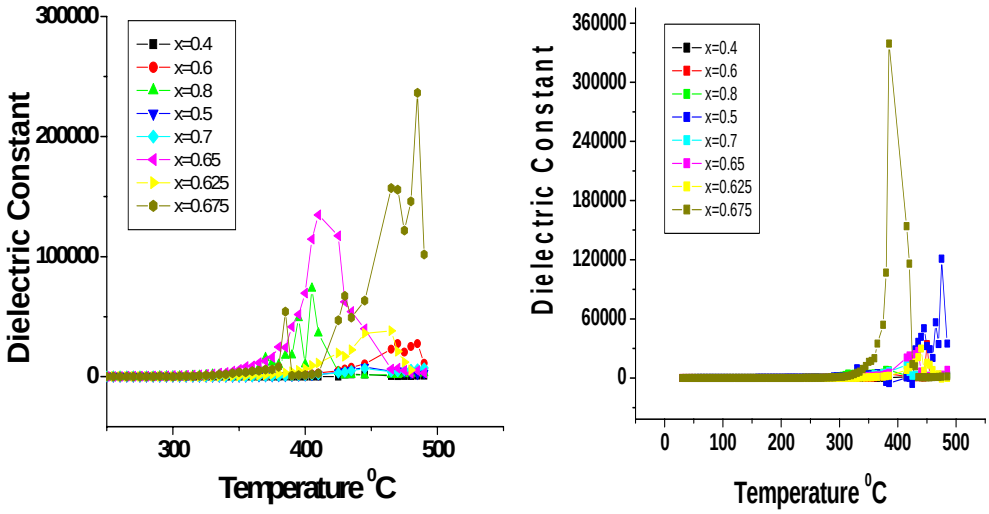

Fig. 7.7 (c, d) Dielectric constant vs Temperature at 1MHz for bulk sample c) $Mn_xZn_{(1-x)}Fe_2O_4$ (1200^{0}C) and d) $Mn_xZn_{(1-x)}Fe_2O_4$ (1300^{0}C)

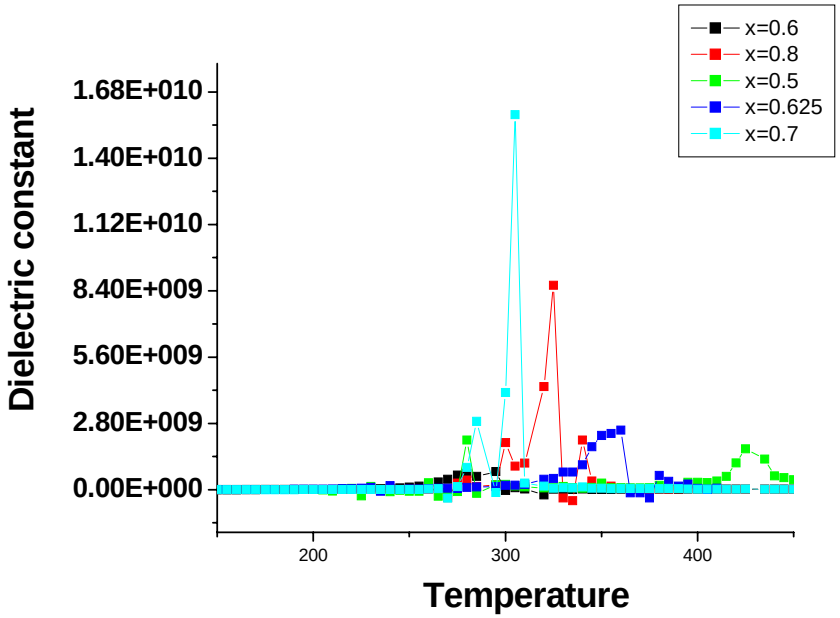

Fig. 7.7 (e) Dielectric constant vs Temperature at 500 Hz. for bulk $Mn_xZn_{(1-x)}Fe_2O_4$ (1300^{0}C)

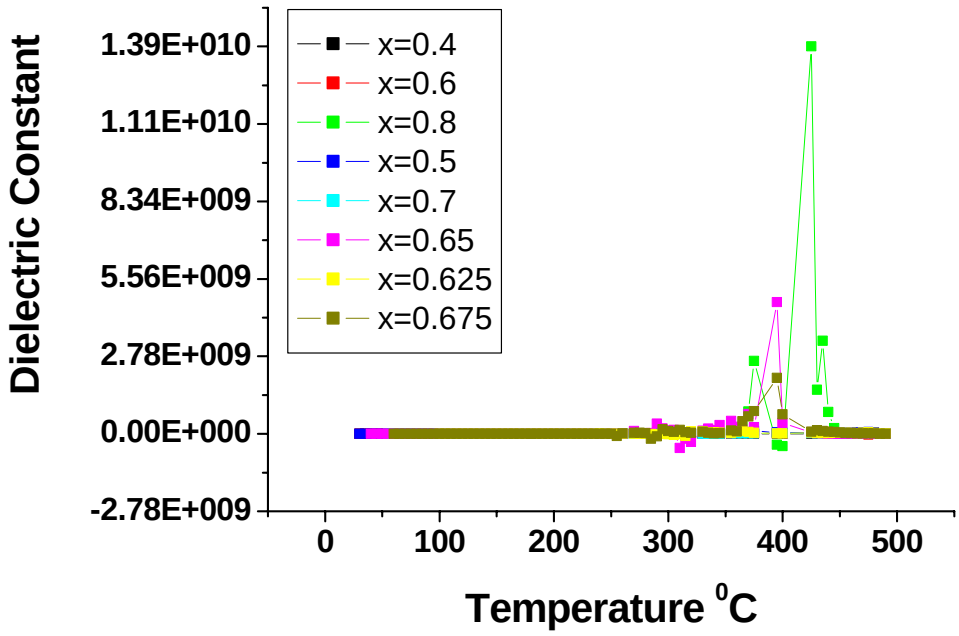

Fig. 7.7 (f) Dielectric constant vs Temperature at 100 Hz. for bulk sample $Mn_xZn_{(1-x)}Fe_2O_4$ (1300^0C)

The variation of dielectric constant with temperature for nanoparticle and the bulk samples $Mn_xZn_{(1-x)}Fe_2O_4$ (x= 0.4.0.5, 0.6, 0.625, 0.65, 0.675. 0.7, 0.8) at 1MHz. are shown in fig.7.7 (a, b, c, d).

Dielectric constant of nanosample of $Mn_{0.8}Zn_{0.2}Fe_2O_4$ remains low and constant for the temperature less than 280^0C. Beyond this temperature it starts increasing and shows a maxima peak at 330^oC, decreases to a low value of dielectric constant with further increase in temperature. Similar trend is observed in all other nanosamples.

Dielectric constant measured at 1MHz. for the bulk sample $Mn_{0.675}Zn_{0.325}Fe_2O_4$ (900^oC) shows low and constant value up to 283^oC, beyond this temperature exhibits a sharp peak at 364^oC reaching a maximum value of $1.7x10^4$ and then decreases with increasing temperature showing second peak at 463^oC**.** Whereas the bulk sample $Mn_{0.65}Zn_{0.35}Fe_2O_4$ (900^oC)

also exhibits two peak behaviors at 381^{o}C and 467^{o}C respectively. For the bulk sample $Mn_{0.675}Zn_{0.325}Fe_2O_4$ (1200^{o}C), initially dielectric constant is independent of temperature till 411^{o}C, increases with increase in temperature, followed by a sharp peak at 483^{o}C and then decreases with further increase in temperature. Similar behavior is observed in all other bulk samples. The bulk samples obtained at 1300^{o}C also exhibit similar behavior.

Fig 7.7 (d, e, f) show the variation of dielectric constant with temperature at 1MHz, 500Hz and 100Hz for bulk sample $Mn_xZn_{1-x}Fe_2O_4$ (1300^{0}C) respectively.

Initially the value of dielectric constant is low up to 300^{o}C. It increases with increasing temperature, exhibits a peak and then decreases with further increase in temperature. This trend is observed for all the frequencies. The rising temperature thermally activates the hopping of charge carriers and hence, the dielectric polarization increases thereby causing an increase in dielectric constant. It may be notices that the dielectric constant is high at low frequencies and low at high frequencies. Moreover, increase in ε with increasing temperature is frequent at low frequencies, compared to high frequencies. The dielectric constant of any material, in general, is due to dipolar, electronic, ionic, and interfacial polarizations. At low frequencies, dipolar and interfacial polarizations are known to play an important role [44]. Both these polarizations are strongly temperature dependent [45]. The interfacial polarization increases with temperature due to creation of crystal defects, whereas the dipolar polarization decreases with increase in temperature. The rapid increase in dielectric constant with increase in temperature at low frequencies suggests that the effect of temperature is more

pronounced on the interfacial than on dipolar polarization. As temperature increases, the accumulation of charges on the grain boundaries increases, which causes an increase in the interfacial polarization. This happens at lower frequencies. Therefore, the dielectric polarization and hence ε increases with temperature at lower frequency. At high frequencies, electronic and ionic polarizations are the main contributors, [44] and their temperature dependence is insignificant.

In all the nanosamples and bulk samples, measurement (carried out at different frequencies) show that there is a minor increase in dielectric constant for the temperature range of 30^{o}C to 300^{o}C. This feature can be explained on the basis of, supply of insufficient thermal energy to free the localized dipoles for oriented in the direction of applied electric field. In the temperature range 300 ^{o}C -500^{o}C the bulk sample $Mn_{0.675}Zn_{0.325}Fe_2O_4$ (1200^{o}C) shows two peaks, one at 467 ^{o}C and a dominant peak at 484^{o}C. Bulk sample $Mn_{0.65}Zn_{0.35}Fe_2O_4$ (1200^{o}C) exhibits only one peak at 409^{o}C. Above 300 ^{o}C a large number of dipoles become free due to availability of adequate thermal energy and applied electric field for required polarization. The small peak observed at 467 ^{o}C for the bulk sample $Mn_{0.675}Zn_{0.325}Fe_2O_4$ (1200 ^{o}C) is due to the migration of Fe^{3+} ions which increases electron exchange between thermally activated Fe^{3+}-Fe^{2+} at octahedral site, which results into increased polarization and dielectric constant [46]. The peak appearing at 484^{o}C is attributed to ferromagnetic (magnetically ordered) to paramagnetic (disordered) transition of sample. This is in agreement with dielectric behavior observed for other ferrites at Curie temperature [46]. The decrease in 'ε' above 484^{o}C is attributed to decrease in internal viscosity of the system giving rise to

more degrees of freedom to the dipoles with the result of increasing the disorder in the system and hence decrease in dielectric constant [46]. This is in agreement with Ahmed et. al [47].

7.5.5 Dielectric Loss Factor

The variation of dielectric loss factor with frequency for nanomaterial $Mn_xZn_{(1-x)}Fe_2O_4$ samples is shown in fig 7.8 (a). It may be seen that the Dielectric loss decreases with increase in frequency to a very low value for the sample $Mn_{0.7}Z_{0.3}Fe_2O_4$ with no resonance peak. Sample $Mn_{0.7}Zn_{0.3}Fe_2O_4$ shows highest value of tanδ i.e 20.46 at 20 Hz, which decreases to 0.6239 at 100KHz. Whereas in all other nanosamples there is an appearance of resonance peak in the frequency range 1KHz to 100KHz. The lowest value of tanδ observed is 0.458 at very high frequency. The variation of loss tangent (tan δ) with frequency for bulk samples $Mn_xZn_{(1-x)}Fe_2O_4$ (x = 0.4, 0.5, 0.6, 0.625, 0.65, 0.675, 0.7, 0.8) are shown in figure 7.8 (b, c, d, e & f).

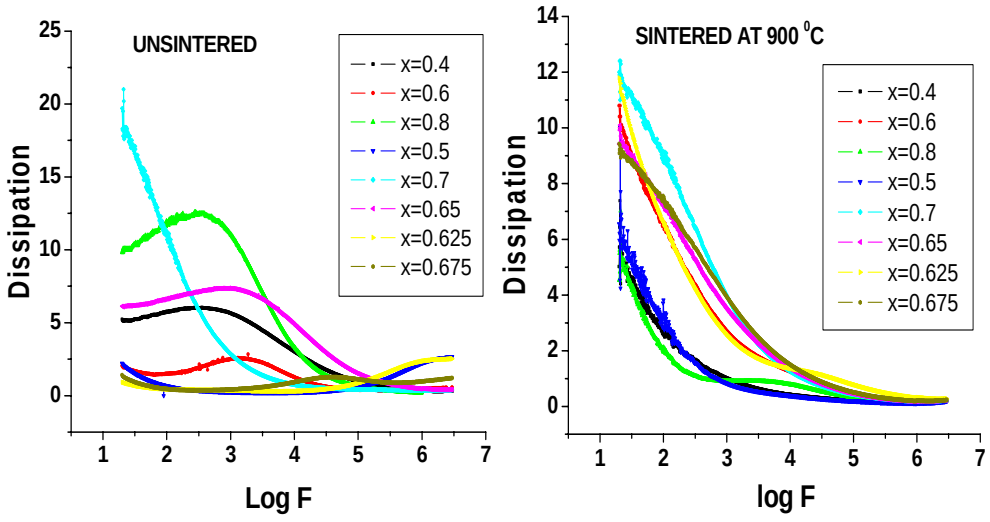

(a) (b)

7.8 (a,b) Variation of dielectric loss factor with frequency for

a) nanosample $Mn_xZn_{(1-x)}Fe_2O_4$ and b) $Mn_xZn_{(1-x)}Fe_2O_4$ (900^0C)

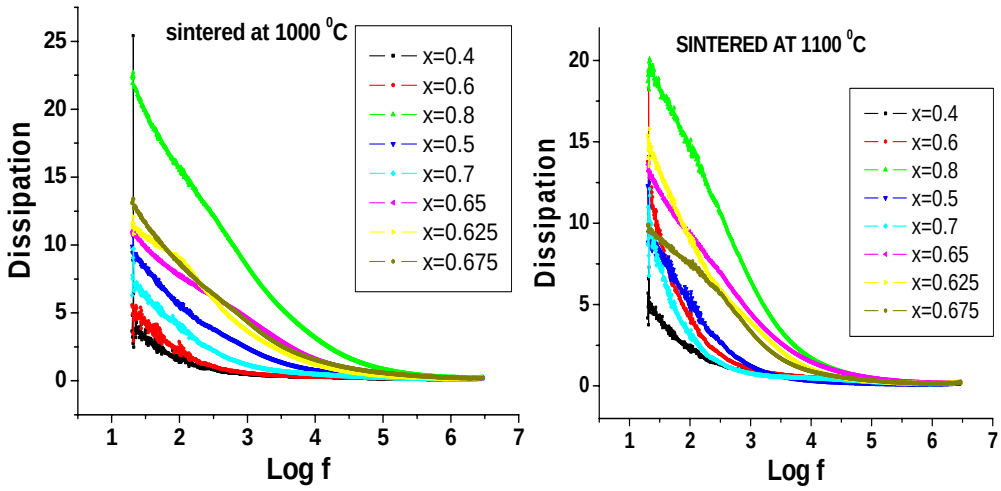

(c) (d)

Fig 7.8 (c, d) Variation of dielectric loss factor with frequency for bulk sample

c) $Mn_xZn_{(1-x)}Fe_2O_4$ (1000^0C) and d) $Mn_xZn_{(1-x)}Fe_2O_4$ (1100^0C)

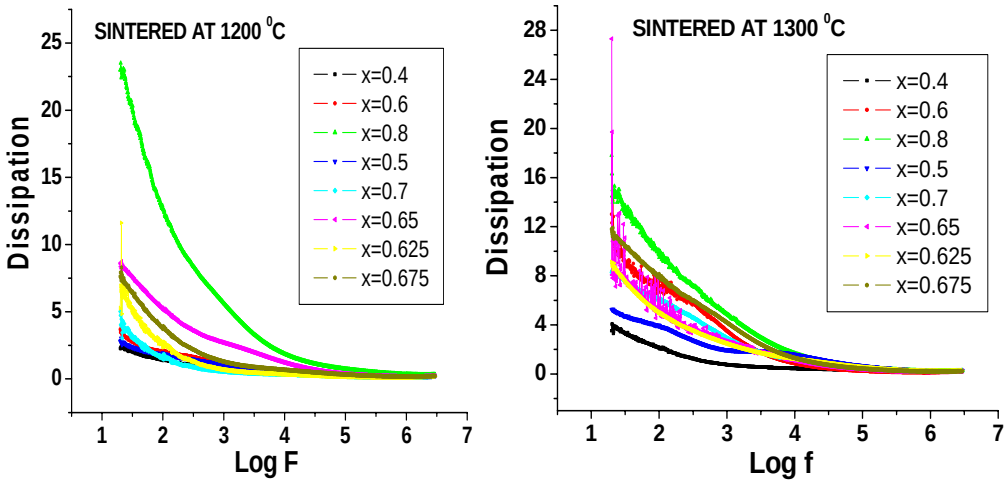

(e) (f)

Fig.7.8 (e,f) Variation of dielectric loss factor with frequency for bulk sample

e) $Mn_xZn_{(1-x)}Fe_2O_4$ (1200^0C) and f) $Mn_xZn_{(1-x)}Fe_2O_4$ (1300^0C)

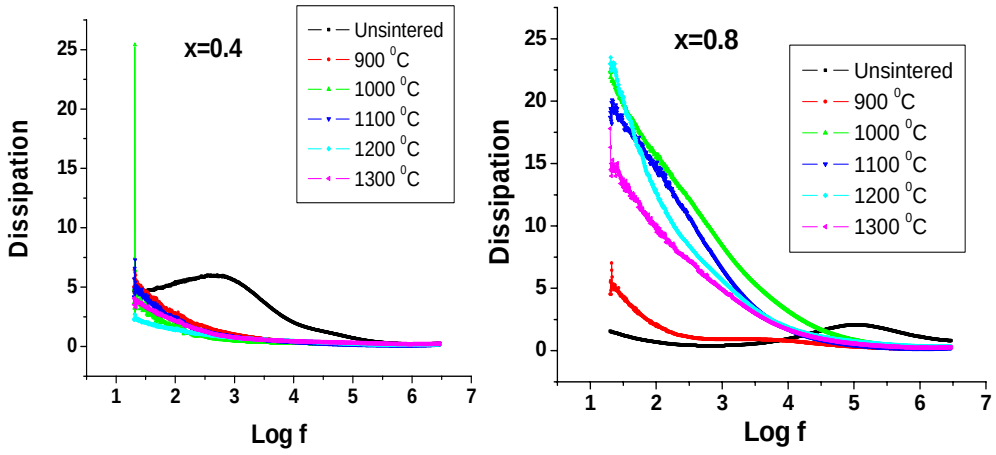

(a) (b)

Fig. 7.9 (a,b) Loss factor with frequency for a) $Mn_{0.4}Zn_{0.6}Fe_2O_4$ and b) $Mn_{0.8}Zn_{0.2}Fe_2O_4$ sintered at different temperature

It is found that for all the samples dielectric loss decreases initially with increase in frequency up to 100K Hz, beyond this frequency loss is very low and independent of frequency. None of the samples are found to exhibit any resonance peaks. The peaking behavior occurs when the hopping frequency of electrons between Fe^{2+} and Fe^{3+} matches the frequency of the applied field [48]. From the figure it is clear that tan δ decreases exponentially with increasing the frequency following the relation [49] $\tan\delta = 4\pi\sigma_{ac}/\omega\varepsilon'$. Similar results were reported by Kumar *et al* [50] in Li–Ti ferrites and Ahmed *et* al [51] in Ni ferrites. The initial decrease of dielectric loss with an increase in frequency can be explained on the basis of Koops' model [39]. In the low frequency region which corresponds to high resistivity (due to grain boundaries) more energy is required for electron exchange between Fe^{2+} and Fe^{3+} ions. Thus the energy loss is high. In the high frequency range which corresponds to low resistivity (due to the grains) a small energy is needed for electron transfer between Fe^{2+} and Fe^{3+} ions in the grains and hence the energy

loss is small [52]. Loss values vary from 11.98 to 5.3 at 20Hz for the bulk samples (900^{o}C) decreases to a very low value 0.25 above 100 KHz. For the bulk samples (1100^{o}C) the maximum value of loss is 19.8 and minimum loss is 4.8 at 20Hz. These values of losses decrease with increase in frequency to 0.47 beyond 100KHz.frequency. The value of dielectric loss observed at room temperature is only 0.596 at 100KHz. for the bulk samples (1200^{o}C).

Loss vs. temperature

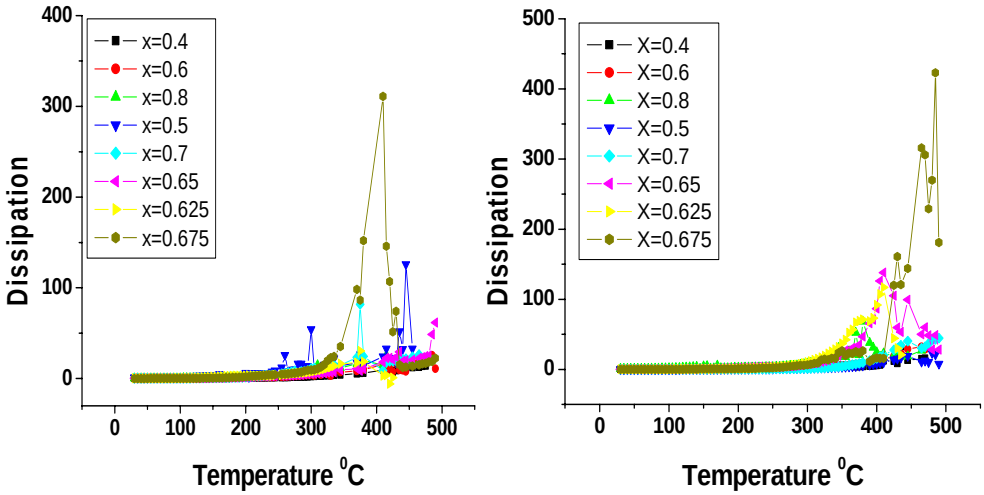

Fig.7.10 (a, b) Dissipation Vs. Temperature at 1MHz. frequency for bulk sample a) $Mn_xZn_{(1-x)}Fe_2O_4$ (1300^{0}C) and b) $Mn_xZn_{(1-x)}Fe_2O_4$ (1200^{0}C)

Fig. 7.10 (a,b) shows the variation of tan δ with temperature. It seems that tan δ in general, has small values and indicates a peak at different temperature for the samples of different Mn concentration. For the sample $Mn_{0.675}Zn_{0.325}Fe_2O_4$ peak appears at 408^{0}C whereas in the sample $Mn_{0.5}Zn_{0.5}Fe_2O_4$ it appears at 444^{0}C. The appearance of a maximum in tan δ could be explained according to Koops's model [39] in which the solid is

assumed to be composed of grains and grain boundaries. Each one has different parameters where the grains have low resistivity and large thickness while the grain boundaries have high resistivity and small thickness. Moreover, it was assumed that [53] each of the grains and grain boundaries has its characteristic peak. Thus the observed peak in tan δ may be attributed to the contribution from the grain boundaries, where the impurities reside, which take part in the conduction at low temperatures.

References

[1] D. Santosh Kumar and K. Chandra Mouli, International Journal of Nanotechnology and Applications, Volume 4, No.1 (2010) 51-59.

[2] Sangeeta Thakur and S. C. Katyal M. Singh, Applied Physics Letters, 91, (2007) 262501.

[3] A. A. Samokhvalov, A.G. Rustamov, Sov. Phys. Solid state, 6, (1964). 749

[4] A. A. Samokhvalov, A.G. Rustamov, Sov. Phys. Solid state, 7, (1965). 961.

[5] L.G.Van Uitert, Proc.I.R.E. 44 (1956) 1294.

[6] G. H. Jonker, J. Phys. Chem. Solids, 9, (1959), 165.

[7] E. J. W. Verwey and J. H. de Boer, Reauil Ches Travaux chimques des Phys. Bas(Czeckh), 55(1936) 531.

[8] B. Vishwanathan, V. R. K Murthy., Ferrites materials, Science and Technology, Narosa Publishing House, 1990, pp.58.

[9] J. Yamashita and T. Kurosawa, J. Phys. Chem. Solids, 5, 34 (1958).

[10] T. Holstein, Ann. Phys., (N.Y.) 8, (1959), 343.

[11] J.Appel, Solid state Phys., 18, (1969), 41.

[12] I.G. Austin and N. F. Mott, Adv.Phys., 18 (1969).

[13] H. L. Tuller and A. S. Nowick; J. Phys. Chem. Solids, 38 (1977) 859.

[14] B. Gillot, Mat.Res.Bull, 11 (1976) 848.

[15] N. Rezlescu and E. Rezlescu, Solid State commun., 14 (1974) 69.

[16] Z. Sisma, J. Simsova and V. A. M. Borabers, in Proc.11th Int. Conf. on progr. of semiconductors (Warsaw, Poland) 2 (1972) 1294.

[17] G. Srinivasan and C. M. Srivastava, Phys. Stat.Solidi, 108, (1981) 665.

[18] E. J. W. Verwey, P. W. Haayman, F. C. Romeijn and G. W. Van Oosterhout, Philips Res. Rep. 5 (1950) 173.

[19] A. D. P. Rao, B. Ramesh, P. R. M. Rao, S. B. Raju, Journal of Material Science, 34 (1999) 621– 623.

[20] C. G. Koops, Phys. Rev., 83(1951) 121.

[21] E. J. W. Verwey, P. W. haaijman, F. C. Romeyn, G. W. van Oosterhout, Philips Rep. 5 (1950)173-187.

[22] V. L. Mathe, R. B. Kamble, Science Direct, Material research Bulletin 43 (2008) 2160-2165.

[23] K. Barerner, P. Mandal, R. V .Heimoit. Phys. Stat. Sol. (b) 223 (2001)811-820.

[24] J. Baszsynski, Acta Phys. Polym., 35(1969)631.

[25] V. R. K. Murthy, J. Sobhandri, Phys. Stat. Sol. (A) 38(1977)647.

[26] M. Singh, S. P. Sud, Mater. Sci. Eng. B83 (2000)181.

[27] A. M. Shaikh, C. M. Kanamadi, B. K. Chougule, Material Chemistry and Physics 93 (2005) 548-551.

[28] M. I. Klinger and A. A. Samokhvalov, Phys. Status Solidi B 79 (1977)9.

[29] M. Drofenik, A. Znidarsic, I. Zajc, J. Appl. Phys. 82 (1) (1997) 333-340.

[30] R.B. Tangsali, S.H. Keluskar, G.K.Naik and J.S.Budkuley, Journal of Material science. 42.No.(3)(2007)878-882.

[31] S. A. Patil , B. L. Patil, S. R. Sawant, A. S. Jambhale and R. N. Patil, Ind. Pure & Appl. Phys., 31(1993) 904.

[32]. F. J. Morin, Phys. Rev., 93(6) (1954) 1195.

[33] B. V. Bhise, V. C. Mahajan, M. G. Patil, S. D. Lokte and S. A. Patil, Ind. J. Pure Appl. Phys., 33 (1995)459.

[34] Chandra Prakash and J. Bajal S. J. Less Common metals 51 (1985) 107.

[35] D. Ravinder Phys. Status Solidi (a) 139 K 69.

[36] Ramana Reddy, A. V. Ranga Mohan G., Ravinder D. and Boyanov B. S. J. Mater. Sci.,34, (1999), 3169.

[37] K. W. Wagner, Ann. Physik, 40 (1913) 817.

[38] J. C. Maxwell "Electricity and Magnetism",vol.1 Oxford University press, New york, 1973, (1950)pp.828.

[39] C. G. koops, Phycs., Rev., 83(1953) 121.

[40] Miles Z. P. A., West Phal W. B. and Von Hippel A., 1957 Rev. Mod. Phys.29 279.

[41] Rabinkin L. I. and Novikova Z. I. Ferrites Minsk (1960) 146.

[42] Iwauchi K., Jap. J. Appl. Phys., 10 (1971) 1520.

[43] F. G. Brockman, P.H. Dowling, W.G. Steneck, Phys. Rev., 75 (1949) 1440.

[44] L. L. Hench and J. K. West, Principles of Electronic Ceramics Wiley, New York, (1990), pp. 189.

[45] Sangeeta Thakur and S. C. Katyal, M. Singh, Applied Physics Letters 91, 262501 (2007).

[46] V. L. Mathe, R. B. Kamble, Material Research Bulletin 43(2008)2160-2165.

[47] M. A. Ahmed, E. Ateia, L. M. Salah, A. A. El-Gamal, Mater. Chem. Phys.92 (2005)310.

[48] Abo El Ata A. M. and S. M. Attia, J. Magn. Magn. Mater., 257 (2003)165

[49] J. Smit and H. Wijn, Ferrites Philips Technical Library, Cleaver-Home Press Ltd. London (1959).

[50] B. K .Kumar, G .P. Srivastava and P. Kishen, Proc. ICF-5 (Bombay) 1988 p 233.

[51] M. A. Ahmed, M. K. El Nimar, A. Tawfik and A .M. El Hasab, J. Magn. Magn. Mater., 98 (1991) 33.

[52] Samy A. Rahman, Egypt. J. Solids, Vol. (29), No. (1), (2006).

[53] A. A. Sattar and Samy A. Rahman, Phys. Stat. Sol. (a) 200, No. 2, (2003) 415 –422.

CHAPTER VIII

PRECIS AND CONCLUSIONS

8.1 SUMMARY

Present study was undertaken to establish a new mechano-chemical method using auto combustion for preparing nanoparticle Mn-Zn materials by using metal oxides as the raw material for the first time. Auto-combustion method has been used by number of investigators for preparing nanoparticle ferrite materials at low temperature with metal salts, which are water soluble as raw materials. Taming auto combustion method for oxide material is a difficult task as metal oxides used in the present preparation are insoluble substances as are formed at elevated temperatures. This was indeed a difficult task as the potential energy of oxides is quite high. Since oxides react at high temperatures it was necessary to bring down the activation energy of the reaction so that method like auto combustion which uses lower temperatures could be used for production of ferrite.

Activation energy in a chemical reaction is known to depend on several factors. One way of reducing the activation energy of the reaction is to bring the reactants as close as possible. This not only reduces the activation energy but also increases the speed of the reaction. Addition of complexing agent also helps in reducing the activation energy of the reaction by forming ligands. Ligands are Lewis bases because they always bear at least one atom having a lone pair of electrons accessible for bonding to another atom. This in turn facilitates the formation of desired compound in a much rapid manner.

The task of getting the reactants as close as possible was achieved by downsizing the grain size of the mixture of metal oxides using mechanical ball mill. This process improved the surface area to volume ratio of the material, thereby reducing the activation energy of the reaction and increasing the reactivity of the mixture. Nitrilotriacetic acid performed the function of complexing agent. The fuel, hydrazine hydrate N_4H_4 also performed the function of reducing agent.

Thus, the production of nanoparticle $Mn_xZn_{(1-x)}Fe_2O_4$ ferrite with x = 0.4, 0.5, 0.6, 0.625, 0.65, 0.7and 0.8 at low temperature was made possible by using new simple inexpensive autocombustion mechano-chemical method using metal oxides as starting material.

Materials obtained by this method were found to produce expected nanoparticle ferrite material. The formation of nanoparticle monophasic spinal ferrite was confirmed using standard methods of characterization such as

i) Chemical Analysis (Percentage yield, EDAX)

ii) FTIR spectra analysis

iii) X- ray diffraction analysis.

iv) Neutron Diffraction

Estimated percentage contents of the elements Mn, Zn, Fe and O carried out with the help of EDS analysis of all the samples are in good agreement with the theoretical estimated values thus confirming the preservation of stoichiometry. The typical IR absorption spectra obtained for the sample $Mn_xZn_{(1-x)}Fe_2O_4$ exhibits two broad bands at 600-550 cm^{-1} and 450-330 cm^{-1}, which confirm the formation of spinal structure.

The X-ray diffraction and Neutron diffraction clearly identified formation of single phase cubic spinel structure with no impurity phases. The lattice constant values calculated using the XRD data is in the range of 8.4268A^o to 8.4657A^o. Lattice constant was found to increases with increase in Mn content in the sample. X- ray density was found to be in the range of 5.094x10^3 Kg./m^3 to 5.258x 10^3 Kg./m^3 and decrease with lattice constant '**a**'. The XRD data was found to fit well to the space group Fd-3m. The average size of nanoparticle calculated using Scherrer formula after applying Williamsons Hall Plot correction was in the range of 10nm to 36nm. However, the average particle size of the same samples seen from TEM and HRTEM was in the range of 9 nm to 40 nm.

Magnetic measurements done on the samples suggest that Hysteresis loss which was low increases with increase in Mn concentration and show a peak at x = 0.625 followed by a dip at x = 0.65 and increases further with increase in Mn content. Magnetic measurements made on the nanoparticle samples using VSM and hysteresis loop tracer, show high values for M_s, very low values for coercivity, and low loss. Saturation magnetization for different Mn concentration measured using VSM for nanoparticle sample at room temperature is in good agreement with the measurements made using hysteresis loop tracer. Highest value of M_s equal to 50.92 emu/gm was recorded for the sample $Mn_{0.65}Zn_{0.35}Fe_2O_4$. Magnetic measurements carried out at room temperature as well as at low temperature using VSM showed that M_s increases with decrease in temperature. The maximum value of M_s, 47.14 emu/gm observed for $Mn_{0.6}$ $Zn_{0.4}Fe_2O_4$ at room temperature, was found to increase to 82.73emu/gm at 5K.

Temperature dependent magnetization (FC, ZFC) of $Mn_xZn_{(1-x)}Fe_2O_4$ nanoparticles indicated that the blocking temperature of the material was field and size dependent. At low applied field strength of 100 Oe, the sample was superparamagnetic at room temperature that is the blocking temperature of the samples was 300^{o}K. The blocking temperature of the samples shifts to a lower temperature, when the applied field was enhanced to 500 Oe, 1000 Oe and 5000 Oe. It is also observed that blocking temperature increases with increasing mean size of the nanoparticles for a given field strength.

The Neutron diffraction studies and Rietveld refinement of the pattern shows that there was a well defined magnetic order. The data were found to fit well to the space group Fd-3m. The magnetic Moment 3.6μB for Mn and -2.2μB for Fe were obtained for the sample $Mn_{0.6}$ $Zn_{0.4}Fe_2O_4$, with a lattice constant of 8.4564 A^o.

AC susceptibility curves of nanoparticle samples indicate that the samples are mixtures of different type's particles except for x= 0.5 and x=0.4 sample. The sample with x= 0.4, 0.5 were made up of single domain (SD) crystallites. The samples with higher values of "x" exhibited a narrow multidomain (MD) character in addition to single domain (SD) behavior. Curie temperature of nanosamples was high in the range of 350^{o}C to 500^{o}C compared to bulk samples, which is in the range 100 ^{o}C to 325 ^{o}C. It was found that, Zn concentration in the sample played a decisive factor in variation of lattice constant, particle size, Curie temperature, hystersis loss, saturation magnetization and superparamagnetic behavior of the samples.

Appearance of central doublet in Mössbauer spectra of all the samples with quadruple splitting was essentially due to the presence of

superparamagnetic particles in the samples. Whereas the occurrence of only the central doublet without any sextet in the samples $Mn_xZn_{(1-x)}Fe_2O_4$ (x=0.4, 0.5), indicated absence of long-range magnetic ordering in these samples and these samples appeared to be superparamagnetic. The Mössbauer spectra of the sample $Mn_xZn_{(1-x)}Fe_2O_4$ (x=0.6, 0.65, 0.7) showed that significant number of particles in samples are magnetically ordered. Magnetic measurements were carried out on the bulk sample obtained by sintering of the nanoparticle samples. These measurements not only confirmed conclusions drawn from the results obtained on the nanoparticle sample but provided more information on the behavior of the bulk samples.

Scanning electron micrograph of the sintered samples shows that there is an increase in particle size with increase in sintering temperature. The study of magnetic and electrical properties of the bulk samples indicate that control of Mn or Zn concentration in the sample is not only the factor that affected these properties but also the same are strongly dependent on microstructure of the sample which in turn dependent on the sintering conditions.

Saturation magnetization of all the samples was almost destroyed in bulk samples obtained at 900^0C, but at higher sintering temperature, there was a gradual reappearance of the lost magnetization. Bulk samples obtained at 1200^oC and 1300^oC exhibit high value of saturation magnetization, low loss, low coercivity, which are essential parameters for high performance Mn-Zn Ferrite.

Permeability of the bulk samples obtained at 900^0C has very low value of permeability, but it increases with increase in sintering temperature. Highest value of initial permeability observed was 26,876 for the bulk sample

$Mn_{0.675}Zn_{0.325}Fe_2O_4$ (1300^0C) measured at 20Hz. All the bulk samples exhibit high value of permeability at room temperature, which decreases with increase in temperature and drops to a very low value at Curie temperature, except for the bulk sample $Mn_{0.5}Zn_{0.5}Fe_2O_4$ obtained at 1100^0C and 1200^0C. In the bulk samples $Mn_{0.5}Zn_{0.5}Fe_2O_4$ (1100^0C, 1200^0C) permeability increases with increase in temperature exhibits a peak near Curie temperature and then drops to a very low value at Curie temperature. Permeability of all the bulk samples is high at low frequency, decreases with increase in frequency and then remains constant for a wide range of frequency. Constant behavior of μi in the frequency range 100Hz to 3 Mhz is attributed to the domain wall motion. It is observed that in all the samples, loss factor (tanδ) decrease rapidly to a extremely low value with increase in frequency from 20Hz. to 1KHz. In the frequency range from 1 KHz to 3MHz. loss remains constant to a low value. Also loss decreases with increase in sintering temperature.

Resistivity of the nanosample as well as bulk samples initially increases with increase in temperature due to various factors like phonon scattering, p-type conductivity, which increases the activation energy on the basis of Verwey conduction mechanism. Then, there is a decrease in resistivity with increase in temperature exhibiting semiconductor-like behavior.

In general for all sintering temperature, the room temperature resistivity of the bulk sample $Mn_{0.4}Zn_{0.6}Fe_2O_4$ is higher compared to $Mn_{0.8}Zn_{0.2}Fe_2O_4$. This may be due to increase in Zn content. Bulk sample $Mn_{0.4}Zn_{0.6}Fe_2O_4$ (1200^0C) exhibits highest value of resistivity maximum $4.8x10^9$ohm meter where as $Mn_{0.6}Zn_{0.4}Fe_2O_4$ (1300^0C) has lowest value of resistivity maximum i.e $2.81x10^7$ ohm meter. Bulk sample $Mn_{0.4}Zn_{0.6}Fe_2O_4$

(1000^0C) shows highest value of resistivity (at 500^0C) ie $1.87x10^3$ ohm meter and $Mn_{0.6}Zn_{0.4}Fe_2O_4$ (1300^0C) has lowest value of resistivity 570 ohm meter (at 500^0C).

Dielectric constant of nanosamples as well as bulk samples is very high of the order of 10^6 at very low frequency, but decreases rapidly to a very low value for higher frequencies, which is a normal dielectric behavior for mixed ferrites. Measurement of dielectric constant of the materials with temperature at high frequencies show that, dielectric constant of nano as well as bulk samples was low and constant below 300^0C, it increases with increase in temperature and exhibits a maxima peak at transition temperature. Dielectric loss of the materials also exhibits the similar nature. Materials have very low loss at high frequencies.

8.2 CONCLUSIONS

A simple precursor based mechano chemical auto-combustion method employed using the idea of, increase in surface area to volume ratio as well as lowering the activation energy of chemical reaction on particle size reduction of the metal oxide reactants, could successfully produced monophasic nanoparticle $Mn_xZn_{(1-x)}Fe_2O_4$ ferrite with x =0.4, 0.5, 0.6, 0.625, 0.65, 0.7and 0.8 ferrite materials with required stiocheometry from metallic oxides at low temperatures. The Mn-Zn ferrite nanoparticles obtained exhibited super paramagnetic behavior with blocking temperature as low as room temperature. Superparamagnetic particle at room temperature have large number of applications and are ideally suited for drug delivery system and hyperthermia as well as in large number for medical sensor application. The samples are

found to show optimum values of saturation magnetization, high permeability, high resistivity, high dielectric constant, with low loss, which are essential parameters for any present-day high technology electronic and electromagnetic, and biomedical applications. The bulk material obtained by sintering this nanoparticles show different behavior compare to nano particles. These materials exhibit paramagnetic, ferromagnetic as well as superparamagnetic behavior under different sintering conditions. Quenching of the magnetization has been a unique feature exhibited by these materials when they are sintered at 900 ^{o}C.

Thus the experimental investigations performed on the samples reveal that Mn-Zn ferrite materials having general formula $Mn_xZn_{(1-x)}Fe_2O_4$ ferrite where x= 0.4, 0.5, 0.6, 0.625, 0.65, 0.7, 0.8 produce high quality, high performance material in nano form as well as bulk, suitable for present-day high technology applications.

8.3 SCOPE FOR FUTURE WORK

A tremendous surge in research on nonmaterials and bulk materials produced from nanograins has been observed in the last few years since these materials are to shape the future technology. Synthesis, development and study of different properties of Mn-Zn ferrite nanomaterials using various techniques has become an interesting area of research. Since there is always a scope for improvement and widening the area of application, good amount of work can be taken up on these materials.

Similar study of these materials, synthesized using microwave decomposition could be interesting. This method could be compared with the

materials prepared using auto combustion method. XRD of the samples under investigation can be taken at various temperatures so that structural change of these materials at various temperatures can be studied.

Since there is quenching of magnetic moment of the bulk samples obtained at 900^{o}C, detailed investigative study can be taken to find the reason for quenching of magnetic moment.

Temperature dependence of magnetization of the nanosamples as well as bulk samples using SQUID can be studied in detailed, so that one can investigate the variation of blocking temperature with particle size and different applied field.

Neutron diffraction of nano as well as bulk samples obtained by present method at room temperature and at low temperature could be interesting field of research to investigate the cation distribution and to determine the magnetic moment of Mn and Fe in the samples. Study of magnetic properties at low temperature using VSM and SQUID to know about the softness of the materials or the behavior of superparamagnetism in nanosample as well as bulk samples could be interesting.

These Mn-Zn materials can be dispersed to form thin films using Pulse Laser Deposition (PLD) Technique. Further, the study of characterization and different properties of these thin films could be an interesting field of research. One can study the ageing effect of magnetic properties of these materials and also by irradiating these materials with gamma (γ) radiations.

The materials can also be studied for their applications as sensors. Also these materials can be investigated for their potential use in medical applications, especially with regard to drug delivery and hyperthermia.

Papers presented at National /International conferences:

1) **"Novel method of synthesis of ultrafine high performance magnetic material, Mn-Zn mixed metal ferrites."**

   (R. B. Tangsali, G. V. Kundaiker, J. S. Budkuley, V. J. Pissurlekar)

   Presented at International Conference on "Magnetic materials and their Applications for 21st Century" organized by National Physical Laboratory, New Delhi & Magnetic Society of India (MSI) on 21-23 October 2008.

2) **"Quenching of magnetization in Bulk material obtained from Nano-particle $Mn_xZn_{(1-x)}Fe_2O_4$ synthesized with Novel technique".**

   (G. V. Kundaiker, R. B. Tangsali, J. S. Budkuley, V. J. Pissurlekar)

   Presented at International Conference on "Nano Science & Nano Technology "(ICONN-2010) Organized By Dept. of Physics SRM University, Tamil Nadu on 24^{th} -26^{th} Feb.2010.

3) **"Transport Properties of Nanoparticles $Mn_x\ Zn_{(1-x)}\ Fe_2O_4$ Prepared by Novel Synthesis."**

   (G. V. Kundaiker, V. J. Pissurlekar, R. B. Tangsali, J. S. Budkuley)

   Presented at Internationl conference on Lasers and Advanced Materials (ICLAM-2010) Organized by Dept. of Physics, Abasaheb Garware College, Pune, on March 6-8, 2010.

4) **"Resistivity and Thermo power of nanoparticle Ferrites $Mn_xZn_{(1-x)}\ Fe_2o_4$ prepared by Innovative chemical method."**

   (G. V. Kundaiker, V. J. Pissurlekar, R. B. Tangsali, J. S. Budkuley)

   Presented at National Conference on "Mathematical Aspects of Physical Concepts and Physical Aspects Of Mathematical Concepts" Organized By

Shikshan Vikas Mandal's Shri. S. H. Kelkar College Of Arts, Commerce and Science, Devgad. on 16- 17 Jan. 2010.

5) **"Magnetic Properties of Nanoparticle Mn-Zn mixed metal Ferrites Synthesized by novel method."**

(G. V. Kundaiker, V. J. Pissurlekar, R. B. Tangsali, J. S. Budkuley).

Presented at National Seminar on "Recent trends In Nanoscience, Nanotechnology & Their Applications" Organized by Dakshin Maharashtra Shikshan Mandal's, Bhaurao Kakatkar College - Belgaum, on 20^{th} & 21^{st} Feb., 2009.

6) **"Characterization and Mossbauer study of $Mn_xZn_{(1-x)}Fe_2O_4$ Nanoparticle"**

(G. V. Kundaiker, V. J. Pissurlekar, Jaison Joseph, R. B. Tangsali, J. S. Budkuley).

Presented at Third International conference on frontiers in Nanoscience and Technology (Cochin Nano-2011) Organized by Department of Physics, Cochin University of Science and Technology on August 14 to 17, 2011

List of Publications

1. “Transport Properties of Nanoparticles $Mn_xZn_{(1-x)}Fe_2O_4$ Prepared by Novel Synthesis.” Published in Bionano Frontier Special Issue by International Society of Science and technology, (2010), 0974-0678.

2. “Synthesis of Uniform Size Superparamagnetic Grains of $Mn_XZn_{(1-X)}$ Fe_2O_4 Ferrites by precursor based autocombustion Method (Communicated).